

**Volume 3, No. 3, September 2001**

**Journal of  
Optoelectronics and  
Advanced Materials**

**20020405 053**

**Edited by INOE & INFM**

# Journal of Optoelectronics and Advanced Materials

## EDITOR-IN-CHIEF

**Mihai Popescu**

National Institute of Materials Physics,  
Bucharest, Romania  
E-mail: mpopescu@alpha1.infm.ro

## TECHNICAL MANAGER

**Maria Nedelcu**

National Institute for Optoelectronics,  
Bucharest, Romania  
E-mail: nedelcu@inoe.inoe.ro

## EDITORIAL BOARD

**Horia Alexandru**

University of Bucharest,  
Bucharest, Romania

**Roxana Radvan**

National Institute for Optoelectronics,  
Bucharest, Romania

**Roxana Savastru**

National Institute for Optoelectronics,  
Bucharest, Romania

**Valentin Teodorescu**

National Institute of Materials Physics,  
Bucharest, Romania

**Florin Vasiliu**

National Institute of Materials Physics,  
Bucharest, Romania

## CONSULTING BOARD

**Andrei Andries**

President of the Academy of Sciences,  
Chisinau, Moldova

**Costas Fotakis**

FORTH-IESL  
Heraklion, Greece

**Margareta Giurgea**

Member of the Romanian Academy,  
Bucharest, Romania

**Radu Grigorovici**

Member of the Romanian Academy,  
Bucharest, Romania

**Stanford R. Ovshinsky**

President & CEO, Energy Conversion Devices,  
Troy, Michigan, USA

**Vladimir Topa**

Correspondent Member of the Romanian Academy,  
Bucharest, Romania

## ADVISORY BOARD

**Guy Adriaenssens**

Catholic University Leuven,  
Heverlee-Leuven, Belgium

**Rafi Ahmad**

Cranfield University, UK

**Dan Apostol**

National Institute of Lasers,  
Plasma and Radiation Physics,  
Bucharest, Romania

**Vasile Babin**

National Institute for  
Optoelectronics,  
Bucharest, Romania

**Mario Bertolotti**

University La Sapienza  
Rome, Italy

**Marie-Geneviève Blanchin**

Université Claude Bernard  
Lyon I, Villeurbanne, France

**Hans Bradaczek**

EFG International,  
Berlin, Germany

**Nathan Croitoru**

Tel-Aviv University, Israel

**Eugen Curatu**

ALCON Summit Autonomous  
Orlando, Florida, USA

**Sergei Dembovsky**

Institute of General and  
Inorganic Chemistry,  
Moscow, Russia

**Ernesto Dieguez**

University of Madrid, Spain

**Stephen R. Elliott**

Cambridge University, UK

**Enrico Esposito**

University of Ancona, Italy

**Luca Fiorani**

ENEA, Frascati, Italy

**Miloslav Frumar**

University of Pardubice  
Czech Republic

**Neville Greaves**

University of Wales,  
Aberystwyth, UK

**Walter Hoyer**

Technical University Chemnitz,  
Chemnitz, Germany

**Pham V. Huong**

University of Bordeaux, France

**Ovidiu Iancu**

"Politehnica" University,  
Bucharest, Romania

**Bogdan Idzikowsky**

Institute of Molecular Physics  
Poznan, Poland

**Mihai Iovu**

Center of Optoelectronics  
Chisinau, Moldova

**Alexander Kikineshi**

Uzhgorod University, Ukraine

**Alexander Kolobov**

JRCAT-NAIR, Tsukuba, Japan

**Stefan Levai**

University of Bucharest,  
Bucharest, Romania

**Victor Lyubin**

Ben Gurion Univ. of Negev,  
Beer-Sheva, Israel

**Ion N. Mihailescu**

National Institute of Lasers,  
Plasma and Radiation Physics,  
Bucharest, Romania

**Bernardo Molinas**

Research Centre of Venezia,  
Venezia, Italy

**Ion Munteanu**

University of Bucharest,  
Bucharest, Romania

**Piet Nagels**

RUCA-University of Antwerp,  
Antwerpen, Belgium

**Diana Nesheva**

Institute of Solid State Physics,  
Sofia, Bulgaria

**Tatau Nishinaga**

Tokyo University, Japan

**Dorin Pocriciuc**

University of Bucharest  
Bucharest, Romania

**Aurel Popescu**

University of Bucharest,  
Bucharest, Romania

**Nicolae Puscas**

"Politehnica" University,  
Bucharest, Romania

**Alexandros Rigas**

Demokritos University of  
Thrace, Xanthi, Greece

**Keshra Sangwal**

Technical University of Lublin,  
Lublin, Poland

**Koichi Shimakawa**

Gifu University, Japan

**Ionel Solomon**

Ecole Polytechnique,  
Palaiseau, France

**Paul Sterian**

"Politehnica" University,  
Bucharest, Romania

**Toma Stoica**

National Institute of Materials  
Physics, Bucharest, Romania

**Keiji Tanaka**

Hokkaido University  
Sapporo, Japan

**Enrico Tomasini**

AIVELA, Ancona, Italy

**Claude Weisbuch**

Ecole Polytechnique,  
Palaiseau, France

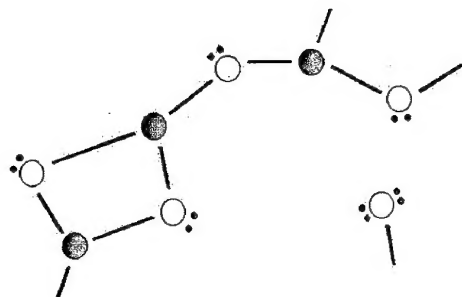
## PUBLISHING BOARD

**Teodorina Popescu**  
**Giorgiana Botea**

<http://inoe.inoe.ro/Journal.html>  
<http://alpha1.infm.ro/Journal.html>

## COVER

**Doina Nicoleta Nicolae**



**First International Workshop on  
AMORPHOUS AND NANOSTRUCTURED  
CHALCOGENIDES**

*-Fundamentals and Applications-*

Bucharest, Romania, June 25-28, 2001

Proceedings, Part II

dedicated to  
Acad. Prof. Dr. Doc. **Radu Grigorovici**  
with the occasion of his 90<sup>th</sup> anniversary

Editor: Prof. Dr. Mihai A. Popescu

AQ F02-07-1180

**Sponsors of the Workshop:**

- **Romanian Ministry of Education and Research**
- **Office of Naval Research, International Field Office, U.S.A.**
- **Rom Tech S.R.L./Bruker aXS, Romania**
- **TRANSGAZ S.A., Medias, Romania**
- **S.C. Rulmentul SA – Brasov, Romania**

**Organizers:**

- **National Institute of Materials Physics, Bucharest**
- **National Institute of Optoelectronics, Bucharest**
- **Romanian Academy**
- **University of Bucharest**
- **Romanian Materials Science-Crystal Growth Society**
- **University “Polytechnica”, Bucharest**
- **National Institute of Glass, Bucharest**

**Honorary Director: Radu Grigorovici,**  
**Romanian Academy**

**Director: Mihai A. Popescu, NIMP, Bucharest**



**REPORT DOCUMENTATION PAGE**

Form Approved OMB No. 0704-0188

Public reporting burden for this collection of information is estimated to average 1 hour per response, including the time for reviewing instructions, searching existing data sources, gathering and maintaining the data needed, and completing and reviewing the collection of information. Send comments regarding this burden estimate or any other aspect of this collection of information, including suggestions for reducing this burden to Washington Headquarters Services, Directorate for Information Operations and Reports, 1215 Jefferson Davis Highway, Suite 1204, Arlington, VA 22202-4302, and to the Office of Management and Budget, Paperwork Reduction Project (0704-0188), Washington, DC 20503.

1. AGENCY USE ONLY (Leave blank)		2. REPORT DATE September 2001	3. REPORT TYPE AND DATES COVERED June 25-28 2001 Final	
4. TITLE AND SUBTITLE International Workshop on Amorphous and Nanostructured Chalcogenides. Fundamentals and Applications (1st) held in Bucharest, Romania on 25-28 June 2001. Proceedings, Part II			5. FUNDING NUMBERS	
6. AUTHOR(S) Mihai Popescu, Editor				
7. PERFORMING ORGANIZATION NAME(S) AND ADDRESS(ES) National Institute of Material Physics Bucharest, Romania			8. PERFORMING ORGANIZATION REPORT NUMBER ISSN 1454-4164	
9. SPONSORING/MONITORING AGENCY NAME(S) AND ADDRESS(ES) Office of Naval Research, European Office PSC 802 Box 39 FPO AE 09499-0039			10. SPONSORING/MONITORING AGENCY REPORT NUMBER	
11. SUPPLEMENTARY NOTES See also ADA398590. Published in the Journal of Optoelectronics and Advanced Materials, Volume 3, No.3, September 2001. Published by the Journal of Optoelectronics and Advanced Materials, 1 Atomistilor St., P.O. Box MG.5, 76900 Bucharest-Magurele, Romania. This work relates to Department of the Navy Grant issued by Office of Naval Research International Field Office-Europe. The United States has a royalty-free license throughout the work in all copyrightable material contained herein.				
12a. DISTRIBUTION/AVAILABILITY STATEMENT Approved for Public Release; Distribution Unlimited.			12b. DISTRIBUTION CODE A	
12. ABSTRACT (Maximum 200 words)  This is Part II of the Proceedings papers presented at the First International Workshop on Amorphous and Nanostructured Chalcogenides Fundamentals and Applications held in Bucharest, Romania June 25-28, 2001				
13. SUBJECT TERMS ONRIFO, Foreign reports			15. NUMBER OF PAGES	
			16. PRICE CODE	
17. SECURITY CLASSIFICATION OF REPORT UNCLASSIFIED	18. SECURITY CLASSIFICATION OF THIS PAGE UNCLASSIFIED	19. SECURITY CLASSIFICATION OF ABSTRACT UNCLASSIFIED	20. LIMITATION OF ABSTRACT UL	

NSN 7540-01-280-5500

Standard Form 298 (Rev. 2-89)  
Prescribed by ANSI Std. Z39-18  
298-102

# Journal of Optoelectronics and Advanced Materials

(indexed in the Science Citation Index Expanded<sup>™</sup> (Scisearch<sup>®</sup>), ISI Alerting Services and Materials Science Citation Index<sup>®</sup>; abstracted in Chemical Abstracts)

Vol. 3, No. 3, September 2001

## CONTENT

---

I. Balberg <i>Transport and phototransport in amorphous and nanostructured semiconductors</i> .....	587
V. I. Arkhipov, E. V. Emelianova, H. Bässler <i>Equilibrium charge carrier mobility in disordered hopping systems</i> .....	601
T. Ohta <i>Phase-change optical memory promotes the DVD optical disk</i> .....	609
J. S. Sanghera, I. D. Aggarwal, L. B. Shaw, L. E. Busse, P. Thielen, V. Nguyen, P. Pureza, S. Bayya, F. Kung <i>Applications of chalcogenide glass optical fibers at NRL</i> .....	627
A. Pradel, O. Valls, C. Cali, G. Taillades, A. Bratov, C. Dominguez, M. Ribes <i>Chalcogenide glasses as sensitive membranes for the detection of ions in solution</i> .....	641
J. S. Romero, A. G. Fitzgerald, K. Mietzsch <i>Electron beam induced patterns in Ag/GeS<sub>4</sub></i> .....	649
C. Main, D. Nesheva <i>Transient photocurrent techniques as a mean of characterising amorphous semiconductors</i> .....	655
M. Ribes, E. Bychkov, A. Pradel <i>Ion transport in chalcogenide glasses: dynamics and structural studies</i> .....	665
I. P. Kotsalas, C. Raptis <i>Structural Raman studies of Ge<sub>x</sub>S<sub>1-x</sub> chalcogenide glasses</i> .....	675
J. M. Saiter <i>Physical ageing in chalcogenide glasses</i> .....	685
S. Krishnaswami, H. Jain, A. C. Miller <i>Effect of oxygen on the photoinduced changes in the electronic structure of As<sub>50</sub>Se<sub>50</sub> glass films</i> .....	695

## AWARD BORIS T. KOLOMIETS

P. Boolchand, D. G. Georgiev, B. Goodman <i>Discovery of the intermediate phase in chalcogenide glasses</i> .....	703
--	-----

Y. Wang, T. Nakaoka, K. Murase <i>Dynamics of Ge-Se glasses at stiffness transition .....</i>	721
N. Asha Bhat, K. S. Sangunni, K. S. R. K. Rao <i>The role of defects in carrier type reversal in Bi doped Ge-Se glasses by photoluminescence spectroscopy.....</i>	735
N. Goyal, A. Zolanvari, S. K. Tripathi <i>Effect of photo and thermal dissolution of Ag on the electrical properties of a-As<sub>2</sub>S<sub>3</sub>.....</i>	741
E. Kashchieva, Y. Ivanova, V. Ivanova, S. Nedev, Y. Dimitriev, E. Lefterova <i>Microstructure of glasses and glass-crystalline materials in the system TeO<sub>2</sub>-V<sub>2</sub>O<sub>5</sub>-Ag<sub>2</sub>O-Agl.....</i>	747
S. Asokan <i>Electrical switching in chalcogenide glasses - some newer insights .....</i>	753
M. Schieber, A. Zuck, M. Lukach <i>Non-destructive evaluation of purified HgI<sub>2</sub> starting materials .....</i>	757
F. Iacomi <i>MnS and CdS clusters encapsulated in natural zeolites.....</i>	763
A. Petris, V. I. Vlad <i>Diffraction in laser induced gratings on thin As<sub>2</sub>S<sub>3</sub> films.....</i>	769

## TRANSPORT AND PHOTOTRANSPORT IN AMORPHOUS AND NANOSTRUCTURED SEMICONDUCTORS

I. Balberg

The Racah Institute of Physics, The Hebrew University, Jerusalem 91904, Israel

The basic physical ideas, concepts and pictures that are used for the understanding of the electronic properties of crystalline and amorphous semiconductors and their nanostructures are briefly reviewed. The emphasis is put in particular on the physical ideas that are encountered in the description of the transport and phototransport in crystalline and amorphous chalcogens and chalcogenides, and their recently developed nanostructures.

(Received June 8, 2001; accepted September 3, 2001)

*Keywords:* Band tails, Percolation, Tunneling, Extended states, Localized states, Mobility edge, Hopping, Quantum confinement, Resonant tunneling and Coulomb blockade

### 1. Introduction

The strong directed covalent bond yields solids with band separations that are of the order of an electron volt (eV), which makes them then part of the family of semiconductor materials [1]. In particular, in the solid chalcogens (S, Se and Te) the  $sp_z$  bonding-antibonding and the lone-pair  $p_x$  and  $p_y$  non-bonding orbitals yield such band separations and these are also carried over to the chalcogenides, where such and other  $sp$  covalent bonds exist [2]. The low coordination number  $Z$  in these two groups of materials has profound implications on the corresponding atomic-network structures and thus on the electronic properties of these materials. To appreciate the implication of this low  $Z$  value, let us consider [3] the constraints in a covalent network with a given  $Z$ . In such a network the bond length between two adjacent atoms is fixed and so is the bond angle between two bonds of a given atom. We have then  $Z/2$  bond-length constraints and  $Z(Z-1)/2$  bond-angle constraints per atom. Hence, the location of each atom in the network is determined by  $Z^2/2$  constraints. Since in the three dimensional space the rigid structure is determined by three coordinates per atom, if  $Z^2/2 \leq 3$  we have more degrees of freedom than constraints and thus a quasi-random network can be constructed. In contrast, if  $Z > \sqrt{6}$  no random structure is possible and there may be only a few (e.g. crystalline) structures that are compatible with all the constraints. Since the low  $Z$  is a special property of the chalcogens and the chalcogenides let us examine the consequence of the above conclusion for the family of these materials. For example, in the chalcogenides the alternating  $Z = 2$  and  $Z = 3$  combinations enable a flat quasi-random network [2], while, for silicon ( $Z = 4 > \sqrt{6}$ ) a diamond-like structure is enforced [1]. In the latter case any randomness can be introduced only by lifting some of the constraints of the ideal network. Indeed, we do know that in amorphous silicon the basic tetrahedral structure is conserved and it is only the long-range order that is destroyed. The latter is thus a consequence of the accumulated effect of strained bond lengths and distorted bond angles [4]. Moreover, in the latter case the removal of constraints also brings about broken (dangling) bonds. While relatively few in their number (less than 0.01% of the atoms) the effect of these dangling bonds is very significant when one considers the electronic properties of the material, as are even lower defect concentrations in crystalline semiconductors [5]. We note then that while in the amorphous chalcogens and chalcogenides, the potential fluctuations result from fluctuations in the (ring) arrangements of the atoms, i.e. the density of the atoms, in amorphous silicon they are primarily localized on the atomic-bond scale. Hence, we would expect in the former case that the potential fluctuations spectrum will be spread over a larger length, yielding a broader energy distribution of disorder-induced quantum states. In this sense the amorphous chalcogenides provide an experimental system that is closer to the ideal picture of a disordered semiconductor with a monotonic continuous

distribution of states. In view of these considerations we will limit our discussion to this type of a disordered semiconductor, and use it to review briefly the concepts of bands, band-tails, extended states, localization, mobility gap and hopping. The fact, then, that the chalcogenides are the natural test grounds for experimental checks of the corresponding physical ideas, as well as the fact that they can yield significant applications, such as xerography [2] and switching [6], makes the latter an exciting systems to study from both the basic-physics and practical-applications points of view.

Recently, the science of semiconductors became more and more concerned with the special properties of artificial nanostructures that are based on the traditional single-phase semiconductor materials. Such are the quantum wells [7], the quantum wires [8] and the quantum dots [9]. The success in the understanding and applications of various crystalline [7-9] as well as amorphous [10] nanostructures in general, and recently on chalcogens and chalcogenides [11,12] in particular, suggests that interesting effects may be found and understood in the latter structures. This is because of their structural flexibility and the rich phenomena that can result from the combination of their properties in the crystalline and amorphous phases.

The purpose of this paper is to review then, from the electronic point of view, the main ideas in the understanding of crystalline, amorphous and nanostructured semiconductors. In view of the limited space allocated for this review, we confine ourselves to qualitative-intuitive pictures of the current understanding of the electronic structure and the electrical transport of semiconductors and their nanostructures. We will try to introduce the relevant, rather general, concepts from the point of view of the chalcogenides in order to facilitate their grasp by researchers of these materials. Also, we will show how the understanding of the above systems can be derived by analogies with, and extrapolations of, other, much more familiar systems. In particular, we will show that the concepts of tunneling and percolation are the keys to our understanding of amorphous and nanostructured semiconductors. For the interested reader we provide a list of text-books and references in which experimental data, mathematical details and illuminating discussions are given.

We start our review in Sec. 2 by considering briefly the physical picture that explains intuitively the electronic properties of crystalline semiconductors. Then, in Sec. 3, we describe how these properties are varied when we turn to the chalcogenide-like, ideal, disordered semiconductors, and we bring the new concepts that were found necessary for an adequate description of these systems. Following the recent interest and success in the understanding of nanostructures in general and the potential of their construction from chalcogenides in particular, we review in Sec. 4 the fundamental ideas in the description of the electronic structure and transport properties of semiconductor nanostructures. The conclusions of this review will be given in Sec. 5.

## 2. Concepts in the theory of crystalline semiconductors

Since in the picture of the electronic properties of a solid we consider electrons that are present in an "infinite" block, the bulk, the simplest quantum picture that we can attribute to an electron is that of a free electron. Such an electron is characterized by its quantum momentum  $\hbar\mathbf{k}$  where  $\mathbf{k}$  is its wave-vector that is associated with a wavelength  $\lambda = 2\pi/k$ , where  $k = |\mathbf{k}|$ . If the electron has a kinetic energy  $E(\mathbf{k})$  that is higher than the potential undulations on the atomic scale, the above free electron picture can be used with the potential undulations treated as a perturbation [13]. The perturbation in a crystal, i.e. when the potential is periodic, implies a periodicity of the electronic wave function throughout the bulk so that the macroscopic cyclic boundary conditions can be applied naturally. Expressing these conditions by the lattice constant yields that there are as many allowed wave-vectors (or allowed states) as there are unit cells, in the bulk. Considering the fact that the energies of interest are of the order of an eV and that the lattice constant is of the order of an angström, we can consider the energy distribution of the density of states  $g(E)$  in a macroscopic crystal to be quasicontinuous. The second observation is that the wave function of the electron is determined by the propagation and reflection of a free electron-like wave as it travels "above" the potential undulations. This yields strong interference effects as one can find in the nearly free electron-like model [13] and in the Kronig-Penny model [7]. The destructive interference of the electron waves when its wavelength matches the periodicity of the crystal lattice yields then forbidden quantum states that are known as the edges of the Brillouin zone. These states interrupt the quasi

continuous,  $E(\mathbf{k}) = \hbar^2 \mathbf{k}^2 / 2m$  spectrum of states, yielding gaps in the state distribution. The size of the gaps is determined by the magnitude of the periodic potential. Here  $\hbar (=h/2\pi)$  is Planck's constant and  $m$  is the free electron mass. The quasicontinuous distribution of states between the energy gaps are known as the allowed energy bands, and thus the energy ranges or forbidden quantum states are known as the bandgaps. It is obvious then that the smaller the magnitude of the potential undulations compared with  $E(\mathbf{k})$  the smaller will be its effect on the free electron-like state distribution. In particular, we note in passing, that if the low-amplitude potential is not periodic, the number of allowed states is not expected to change and  $g(E)$  will be very much the same as the one that is determined by the above given  $E(\mathbf{k})$  dependence. On the other hand the absence of "exact" interference conditions under non-periodic conditions will not yield forbidden states in the entire bulk, and thus no bandgap in  $g(E)$  is to be, *a priori*, expected.

When we "introduce" electrons into the solid, the allowed states are filled according to the Fermi-Dirac statistics that follows the Pauli principle. In particular, if the number of electrons in the last non-empty band is less (but not negligible) in comparison with the number of states,  $2N$  (where  $N$  is the number of unit cells), we have a metal and we call the highest occupied state, the Fermi level,  $E_F$ . If there are only fully occupied and fully empty bands the material is an insulator. In the particular case of an insulator with a small band gap, i.e. of the order of an eV or less, the material is known as a semiconductor. One particular property of semiconductors is that at room temperature it is possible to have thermally excited electrons in the (zero-temperature electron-empty) "conduction band" and thermally excited (left behind) holes in the "valence band". The above definition of  $E_F$  does not hold in this case. However a very simple generalization of it, i.e. that it is the energy level at which the occupation probability is  $1/2$ , can be carried over to the semiconductor case. The naming of a material, as an insulator, is compatible with the above picture of the electronic structure since an externally applied electric field cannot shift the distribution of the electron velocities, as all the  $\mathbf{k}$ -states in the last electron-occupied band are already filled. In contrast, in a semiconductor at a finite temperature, thermal excitation (interband or from a dopant) of some electrons and/or holes is possible and they can move (due to the availability of empty states) in their respective bands.

While the above brief description is helpful for the introduction of some concepts of the theory of the electronic structure of solids, it does not give a clue as to the calculation of the band structures, i.e. the  $E(\mathbf{k})$  dependence, in real solids. The latter is determined by the particular geometry of the structure, the special character of the atoms and, in covalent materials, the nature of the bonds. This is in particular important for semiconductor materials, where (in contrast to, say, alkali metals) the energy of the charge carriers is of the order of the amplitude of the potential undulations [5].

The breakthrough in solving the above problem in crystalline solids was made by the suggestion of Bloch that the wave function of the electron in the crystal can be presented by the product of the free electron wave function and a function that has the periodicity of the lattice [13]. While this appears at first sight as a technical tool, the Bloch theorem had far-reaching consequences on the understanding of the electronic properties of solids, beyond the above-sketched nearly free electron-like picture. First, it suggests that  $\mathbf{k}$  is always a "good quantum number in a crystalline solid" i.e. that regardless of the details of the system, the essence of the above free electron-like picture is always valid in crystals. All the specific features of a system are enclosed however in the  $E(\mathbf{k})$  dependence and an electron can be considered free except for having an  $E(\mathbf{k})$ -defined effective mass  $m^*$ . This quantity contains the resultant effect of the lattice interactions so that  $m^*$  replaces the free electron mass  $m$  and plays then the same role as  $m$  in the electron dynamics. In particular, for semiconductors [5], where one is interested in the few carriers around the extremas of the  $E(\mathbf{k})$  function the nearly free electron picture applies and all the electrons (and similarly all the holes) have practically the same  $m^*$ .

The fact that  $\mathbf{k}$  is a "good quantum number" in a periodic lattice gives us also an intuitive insight as to the motion of an electron in such a lattice. One can think then on a corresponding analogous picture as follows. Suppose there is a car moving on a straight road with periodic intersections, the traffic though which is controlled by traffic lights. If the traffic lights are synchronized, the driver can program the car to go at a fixed speed such that, on the one hand, the car does not stop at intersections, but on the other hand the driver will not be able to choose his speed, which is predetermined by the road (i.e. the  $E(\mathbf{k})$ ) conditions. In a crystal this means that on the macroscopic scale the electron moves with a constant-like velocity and that, when an electric field is



applied, the response of the electron will be determined by its effective mass. We see then that the concepts of  $\mathbf{k}$  and  $m^*$  are very helpful in describing both the electronic states structure and the adoption of the classical picture of transport. In particular, the conservation of the crystal momentum  $\hbar\mathbf{k}$  in optical and electrical interactions enables a classical analysis of the corresponding processes in crystals.

For the transport in the real crystal [13] we note that the main perturbation to the exact periodicity comes from the thermally induced vibrations of the lattice that can be described as quantum mechanical particles. These phonons, have an energy  $\hbar\omega$  and momentum  $\hbar\mathbf{k}$ , where  $\omega$  is the corresponding vibration frequency and  $2\pi/|\mathbf{k}|$  is their wave length. The conservation of energy and momentum can be used then as in the corresponding classical picture. When one considers the contribution of all the electrons one finds an average scattering time  $\tau_s$  and correspondingly one can compress all the information concerning the transport into an effective mobility,  $\mu = q\tau_s/m^*$  where  $q$  is the electronic charge. When the main interaction is with phonons, the concentration of which increases with the temperature  $T$ , the value of  $\tau_s$  is expected to decrease with increasing  $T$ . In semiconductors where the velocity is proportional to  $T^{1/2}$  this yields that  $\mu \propto \tau_s \propto T^{-3/2}$ .

Since the electrical conductivity  $\sigma$  is determined by  $\mu$  and the carrier (say, the electron) concentration  $n$ , i.e. by  $\sigma = qn\mu$ , we must, in the case of a semiconductor, where carriers are thermally excited into the bands, consider the  $n(T)$  dependence. We note that at very low temperatures (shallow defect ionization)  $n(T) \propto \exp(-E_a/k_B T)$  where  $k_B$  is the Boltzmann constant, and  $E_a$ , the activation energy, is the corresponding ionization energy. At high temperatures (band to band excitations)  $n(T) \propto \exp(-E_g/2k_B T)$  where  $E_g$  is the forbidden-gap energy. Only in the intermediate temperature range of complete defect ionization (well known as the extrinsic regime)  $n$  may be considered to be a constant.

Of course the carrier concentration in a semiconductor can be increased by optical excitation, primarily from the valence band to the conduction band. This creates electrons-hole pairs that are responsible for the well-known phenomenon of photoconductivity [14]. The corresponding steady state that results is determined by the balance between the generation rate of the charge carriers,  $G$ , and the corresponding recombination rate. For commonly applied illumination intensities the main recombination processes take place in the defects that exist within the (otherwise forbidden) band gap. The concentration of the excess, optically excited carriers  $n_{op}$  is presented via the concept of the recombination (or life) time  $\tau_r$ . This quantity is defined by the measurable ratio of  $n_{op}/G$ . The microscopic parameters that determine  $\tau_r$  via the relation  $\tau_r = 1/P_t C_t$  are the concentration of the available trapping defects  $P_t$  and their capture coefficient  $C_t$  that is determined by the special characteristics of the defect. In general, both  $P_t$  and  $C_t$  depend on the energy of the defect [14],  $E_t$ , the temperature [15] and the position of  $E_F$  [16]. In particular, we note that under a given  $E_F$  and  $T$ , the thermal release rate from  $E_t$  competes with the recombination rate of the carriers of the other type that originate from the other band. The energy,  $E_D$ , above which (for electrons) the thermal emission dominates the recombination, is known as the demarcation line. States for which  $E_t > E_D$  are called trapping centers and states for which  $E_t < E_D$  are called recombination centers. It is generally assumed that the mobility of the optically excited carriers is the same as that of the thermally excited carriers and thus the photoconductivity is given by  $\sigma_{ph} = q\mu n_{op}$ .

### 3. Electronic properties of disordered semiconductors

The relatively simple picture and concepts sketched in Sec. 1 cannot be carried over as such to the disordered semiconductors because of the loss of translational symmetry. The importance of this loss is that the resultant interference of the free carrier-like wave is not the same at the various unit cells. In particular, if a  $\mathbf{k}$  value is assigned to an electronic waves there will not be a particular  $\mathbf{k}$  value for which a total destructive interference will be found, and consequently there will be no forbidden states throughout the solid. Similarly, a relation such as  $E(\mathbf{k})$  is not well defined since different amounts of interference may yield different energy levels in the solid for an a priori assumed value of  $\mathbf{k}$ . Hence, one cannot describe the electron interactions by  $E$ - $\mathbf{k}$  conservation laws. The great advantages of having the concept of crystal momentum as introduced by Bloch are lost then and we usually summarize all these facts by saying that  $\mathbf{k}$  is no more a "good quantum number". How can we

picture then the, conceptually new, situation encountered in the disordered solids? In what follows we present the simplest picture, mainly due to Anderson and Mott [2,17], for the description of the electronic properties of a disordered solid. For that purpose let us introduce first the concepts that enabled to suggest such a picture for disordered semiconductors.

We start then by returning to the pre-Bloch area with the nearly free electron model. We recall that this model is based on the assumption that the amplitude of the potential undulations in the solid is much smaller than the kinetic energy of the electron [13]. Under these conditions the fact that the potential is not periodic should have little effect on the free-electron-like nature for quantum states that are allowed (in the corresponding crystals), i.e. for states for which no exact destructive interference occurs. We may conclude then that for energies and states "deep" in the bands of the corresponding solid the features of the free-electron-like states, will be similar to those in the crystalline solid, in spite of the fact that  $k$  is no more a "good quantum number". We can call such states band-like states. These considerations suggest, for example, that there will not be much difference between a crystalline alkaline-metal and its "amorphous" counterpart if such would exist. However, while setting the stage, the above conclusion is not too helpful for the consideration of semiconductors, where the states of interest are precisely those that (in the crystalline counterparts) lie at, or close to, the band edges. This is since the energies involved there are of the order of the potential undulation. While bearing the above consideration in mind, we see that we have to start our discussion from a different point of view. The easiest choice is to take the other extreme, i.e. the electronic states in the space-limited atomic orbitals.

The point of view we take then is that of atomic orbitals and/or bond orbitals in a covalent semiconductor. We start by adopting the  $N$  fold degeneracy of the atomic orbital within the solid (as we have for the crystalline bands) and the lifting of this degeneracy by the interaction with the other atoms [1]. These effects can simply be considered as quasicontinuous splitting of the atomic or covalent bond levels, as the inter-atomic distance is decreased, into bands [15]. Again, as in the above metallic picture, this point of view enables us to conclude that the existence of a band of allowed states is independent of the order within the structure of the solid. As the atoms come close together, the bands may even overlap and consequently split in two [1,5]. However, for disordered semiconductors, in view of the above discussion, the effect of the disorder will be important at energies around the levels that were band edges in the crystalline counterparts. We conclude then that the gross features of the band structure will be similar in the crystalline and the disordered semiconductors, and that the main difference is that in the latter systems the "edges" will be "blurred". Correspondingly, the common quantity by which we can describe the electronic structure of both types of solids is the density of states (DOS) distribution function  $g(E)$ . What we concluded already then is that in the disordered case  $g(E)$  will have a broad maximum (rather than peaks that are due to well defined interference effects in the crystalline phase) and a broad minimum. The maximum will be found in the energy interval where, in the crystalline counterpart, there was the center-of-band maximum of  $g(E)$ , and the minimum will be found in the energy interval where there was a "band" of forbidden states (i.e. the band gap where  $g(E) = 0$ ). From the conservation of the number of states and the above discussion we would expect then that  $g(E)$  between two bands that originate from two different "atomic" (or bond) orbitals, will be relatively low. We call then the region of finite  $g(E)$  in the amorphous phase, in which we had  $g(E) = 0$  in the crystalline counterpart, the pseudogap. Since the band edges and band gap are the more interesting regimes of  $g(E)$  in the crystalline semiconductors it is natural that we will be mainly interested in the regions of relatively low  $g(E)$  when we discuss amorphous semiconductors.

For a more quantitative evaluation of the shape of  $g(E)$  in the above mentioned regions we can use the following considerations. In a disordered covalent network in which  $Z^2 \geq 6$  (such as amorphous silicon) the disorder is manifested by stretched bonds or distorted bond-angles. In this case we may see the amorphous structure as a topologically distorted crystalline structure and think of the local potential fluctuation as we think of the potential of an impurity in a crystal. This approach suggests that we will have now states that lie in the energy interval that was forbidden in the crystalline state. In particular, since there are no new atoms introduced by the disorder there will be an "immigration" of states from the bands of the crystalline phase into the pseudo gap. The larger the distortion of the bond the larger will be the local potential fluctuation and thus the deeper (i.e. towards the mid-pseudogap) will lie the corresponding state. On the other hand, we expect that the larger the

concentration of the potential fluctuations the larger will be  $g(E)$  in the region for which  $g(E)$  was zero in the pseudogap. We further expect that the probability for having a distortion is smaller, the larger the distortion. Hence, fewer larger distortions and fewer deeper states are expected. This consideration suggests that there will be a decay of  $g(E)$  from the pseudogap edges towards the center of the pseudogap. Similar considerations apply for the random-like (topologically different) structures such as the structure of the chalcogens and the chalcogenides, for which  $6 \geq Z^2$ . This is since the concentration of the structural deviations from the crystalline (e.g. honeycomb decorated) structure to larger or smaller atom-membered rings will decrease [2]. Hence, in this case, we also expect that  $g(E)$  will decrease from the pseudogap edges to the pseudogap center. In fact in the chalcogenides we have, in addition to the topological disorder, a chemical disorder that may induce even larger potential fluctuations. Correspondingly, the value of  $g(E)$  around midgap is expected to be larger than in chalcogens or in the tetrahedrally-bonded semiconductors [18]. This, rather general, decrease of the function  $g(E)$  towards the center of the pseudogap makes the states distribution in the pseudogap look like "tails" of the states distribution in the bands. We thus call these DOS tails the band tails. The natural expectation from the above argument is that the tails will be characterized by an exponential decrease of the form (for the conduction band tail) of  $g_c = g_{c0} \exp[-(E_c - E)/E_{c0}]$  where  $E_c$  is the conduction band-edge,  $g_{c0}$  is roughly the density of states in the  $k_B T$  interval at the conduction band edge of the pseudogap and  $E_{c0}$  is the "width" of the tail [19]. Of course the blurring of  $g(E)$  around the pseudogap edges and the conservation of states suggest that  $g_{c0}$  is somewhat lower than the corresponding value in the crystalline counterpart. This value is usually taken then to be of the order of  $10^{21} \text{ cm}^{-3} \text{ eV}^{-1}$  [4], suggesting that the total concentration of band tail states is only about one thousand's of the band-like states in the disordered semiconductor. However, as we know for crystalline semiconductors, this is a huge number when one considers the possible contribution of the defects to the concentration of the charge transporting carriers in a semiconductor. We also note in passing that the exponential dependence of  $g(E)$  is not universal, and  $g(E)$  can be different depending on the particular energy distribution of the potential fluctuation in the amorphous semiconductor [20].

From the above discussion we saw that the overall picture and the density of states concepts are basically similar to those used for the crystalline materials, but now we have a "pseudo gap", i.e. a region of a relatively small, but not negligible, DOS. On the other hand, the above discussion did not yield a characterization of the states as we had in the crystalline case, where we were able to characterize a state by its  $\mathbf{k}$  vector. To do that let us recall that we have already concluded that deep in the bands the nature of the states should be very similar to that in the crystal since they are effected weakly by the potential undulations in the solid. This is obvious both classically and quantum mechanically, and can be well formulated by the nearly free electron model. Correspondingly we call these states band-like states. In contrast, for states deep in the pseudogap their energy is relatively low, in comparison with the features of the potential undulations, as are impurities in crystalline semiconductors. Again, both classically and quantum mechanically we would expect the electrons in these states to be limited in the spatial extent to the scale of the corresponding potential fluctuations around their location. We can, however, quantum mechanically, refine the distinction between the band-like states and the spatially limited states by noting that for the higher energies in the pseudogap quantum mechanical tunneling can enable diffusion in the lattice even when the electrons energy is lower than the features of the surrounding potential. For these states conduction can take place in a path that is classically forbidden for percolation but is allowed for "quantum mechanical" percolation [2]. This process can be described as follows. If the spatially limited equal energy states are separated in space on a scale much larger than the fluctuation confining range their tunneling probability is so small that in practice they can be assumed to be localized within the scale of the limiting fluctuation. Such states are known as localized states [17]. If however, the spatial separation of these states is small enough to enable significant tunneling between them, a continuous percolation path can form. We call these types of states extended states. Quantum mechanically we have then that as the state energy is increased from the center of the "pseudogap" towards the center of the bands the character of the states will change from localized to extended to band-like.

As pointed out above, for semiconductors the interesting states are those of the energy range in the transition between localized and extended states. This is since we know that the transport in crystalline semiconductors is taking place at the "band edges", i.e. it is expected to be somewhere in the bandtails of the disordered material. This rather more delicate, then the above rather course,

characterization of the corresponding types of states, was given by Anderson. His approach, that relies on the percolation-diffusion and quantum mechanical tunneling concepts can be presented [2,21] in the following qualitative way. We know that in the quantum theory of solids the width of the band,  $B$ , accounts for the overlap of the wave functions of two atoms in the solid. Hence, the larger the value of  $B$ , i.e. the larger the overlap of the atomic wave-functions of a given pair of atoms, the larger the tunneling probability between them. We have also mentioned above that the larger the spread in the potential fluctuations,  $W$ , the broader will be the width of the tail. Correspondingly, the larger the  $W$  the farther will be the distance between two states of the same  $E$ . Recognizing the "equal  $E$  requirement" for tunneling between two sites, the larger the  $W/B$  the lower the probability for tunneling and then for the quantum diffusion of an electron throughout the disordered solid. It is obvious also that the larger the value of  $E$ , the larger is  $g(E)$  and thus the larger the probability for the delocalization of the electrons. What is not obvious is how sharp in this delocalization transition with the increase of  $E$ . A simple picture that is helpful in considering this question is the percolation picture. We assume that two sites in the solid are connected if  $B$  is large enough to yield the requested overlap of the wave functions for an electron to belong to both of them, as in the crystalline solid. For low  $g(E)$  there will be only few such states and the average spatial distance between them will be too large to enable the above requested overlap. With the increase of  $E$  there will be more and more pairs and then clusters of "tunneling connected sites". As  $E$  is further increased there will be an energy  $E_c'$  at which a macroscopic-percolative path of "connected site" will be formed, and the "quantum diffusion" will rise abruptly from zero to a finite value. This energy is known as the conduction band mobility edge [17]. Similarly, we have for the holes the valence band mobility edge  $E_v'$ , and the energy range between  $E_v'$  and  $E_c'$  is correspondingly known as the mobility gap. As is apparent from its definition this gap differs from the optical (and the same mobility) gap in the crystalline semiconductor. On the other hand considering the exponential decay of  $g(E)$  towards the center of the pseudogap we do not expect the respective gaps in the two systems to differ too much, on the energy gap scale.

Let us turn now to the expected transport processes in the extended states and in the (finite temperature possible) localized states. Starting with the extended states we can go back to the pre-Bloch concepts of diffusive transport interrupted by scatterers, as in the Drude-model [4], except that we do not consider the interaction with atoms or lattice vibration, but rather, we assume that the dominant scattering is by potential fluctuations. This (much more) effective scattering and the low mobility that results can be accounted for by considering the Einstein relation between mobility and diffusion [22]. In particular, in the limit of potential fluctuations on the inter-atomic distance scale  $a$ , we expect that the diffusion (random-walk scattering) process [23] will yield a mobility that is given by  $\mu_e = (qa^2v)/(6k_B T)$ , where  $v$  is the "nearest neighbor hopping probability" (which is proportional to the quantum transfer probability between neighboring atoms). Since  $\mu_e$  is also the mobility in the lowest lying extended state this  $\mu_e$  is also expected to be the mobility just above the mobility edge,  $E_c'$ . Considering the fact that we are dealing with a semiconductor, the concentration of carriers at  $E_c'$  is expected to be given by  $n_c' = N_c' \exp[-(E_c' - E_F)/k_B T]$ , where  $N_c'$  is the effective DOS at the mobility edge ( $\approx g(E_c')k_B T$ ). The electrical conductivity will be given then by  $\sigma = q\mu_e n_c'$ .

Turning to the localized states, our previous discussion shows that at  $T = 0$  there will be no conduction between localized states [2,17]. However, at finite temperatures, the restriction of equal-energy tunneling is eased, since phonons may provide the difference in energy between two states that are within the above overlap-distance, thus enabling tunneling between these states. The energy of the phonon  $W_p$  is smaller than about  $k_B \theta_D$  where  $\theta_D$  is the Debye temperature of the material. This finite temperature activation can enable then a (phonon assisted hopping) percolating route at  $E > E_c''$  where  $E_c''$  is the lowest energy of localized states for which there is a sufficiently high  $g(E)$ , to provide (at a given  $T > 0$ ) conduction. This yields (assuming the expected decay of the DOS towards the center of the pseudogap) the lowest (non-zero) finite temperature mobility for localized states. The mobility then is thermally activated and is thus proportional to  $\exp(-W_p/k_B T)$ . However, for this process to take place the carrier has to be excited from the last (in a semiconductor possible) occupied level (i.e.  $E_F$  in the disordered semiconductor) to the various states above  $E_c''$ . Hence, the activation energy for the electron excitation is of the order of, but not smaller than,  $E_c'' - E_F$  ( $< E_c' - E_F$ ) and the activation energy for this conduction process is at least  $E_c'' - E_F + W_p$ . At lower temperatures, such nearest neighbor, or so-called fixed range hopping [17,24], can take place only around  $E_F$  since the concentration of the

phonons drops and probability for the phonons to provide energies beyond  $W_p$  is reduced. The low  $g(E_F)$  will limit this conduction process yielding that  $\sigma \propto \exp(-W_p/k_B T)$ . The smaller the  $g(E_F)$  the larger the spread in energy differences between states of nearest neighbors, and thus there will be fewer adjacent sites with smaller energy differences than  $W_p$ . Hence, as the temperature is lowered even further the energy of the available phonons will be too small to enable enough nearest neighbor hopping-events to open a conducting percolation path.

For such low temperatures the only option left for possible contribution to the conductivity is hopping to sites beyond the nearest neighbors. In this case the possibility to find an energy difference within the value of available phonon energies, increases the larger the hopping distance. Mott suggested for this regime the process of variable range hopping that can be described as follows [17,25]. For the electron, at a site  $i$  and at the level  $E_i \approx E_F$  (assumed to be the ground state), to find a state with energy  $E_i + W_{ij}$  it has to tunnel a relatively large distance  $R_{ij}$ . In this case the probability for the electron hop is proportional to  $\exp(-2R_{ij}/\xi - W_{ij}/k_B T)$ , where  $\xi$  is the localization length of the electrons in the localized states of the system. How far a distance  $R_h$ , on the "average" (see however below), does the electron have to go in order to find a state of energy  $E_i + W_p$  where  $W_p$  lies in the interval  $W_{ij} \leq W_p \leq k_B \theta_D$ . If we assume that  $g(E_i) \approx g(E_F) \approx g(E_F + W_p)$ , the concentration of states that can "accept" the hop in a unit volume is about  $g(E_F)W_p$ . Thus, to "secure" a hop the "average" minimum required  $R_h$ , has to be given by  $(4\pi/3)R_h^3 g(E_F)W_p = 1$ . Considering this relation the value of  $R_h$  that will yield the highest hopping probability (i.e. the minimum value of  $(2R_h/\xi + W_p/k_B T)$ ) will be  $R_h = \{\xi/8\pi k_B T g(E_F)\}^{1/4}$  (or when "properly" [24,25] averaged  $\{9\xi/8\pi k_B T g(E_F)\}^{1/4}$ ). Considering the above probability this yields the famous Mott's  $T^{-1/4}$  law, i.e. the conclusion that the hopping conductivity will have the  $\exp[-(T_h/T)^{1/4}]$  dependence [24] where  $T_h = (5\xi^3)/(18\pi k_B g(E_F))$ . This process describes then a variable range of the hopping with the variation of temperature. The "properly derived" expression was found [26] by noting that the resultant resistance of the network is determined by the largest resistor that participates in the percolative network, and not by an unspecified "average" resistor [26]. This derivation was shown, however, to effect the exact value of  $T_h$  and the prefactor of the macroscopic conductivity [25], but not the temperature dependence which is a result of the optimization of the individual "resistors" that participate in the conduction process. For our purpose of an intuitive picture the important finding is that it is, at least in principle, possible to distinguish between different conduction mechanisms by the different temperatures dependencies of the electrical conductivity.

For the phototransport, the excitation of the carriers is provided by external illumination so that usually one considers the transport in extended states, and thus the photoconductivity is given by the extended-states mobility and, as mentioned in Sec. 2, by the concentration of the carriers  $n_{op} \approx \tau_r G$ . In the present case, however, the interesting effective state distribution that determines  $\tau_r$  is that of the tail states [14,15]. The occupancy of these states is determined then as follows. For states, below, but close to  $E_c$  the occupation is determined by thermal equilibrium of the localized state with the conduction band. For the deeper states the occupation is determined, as explained above, by the recombination in states that lie below the demarcation line [14]. Now we know that as the temperature is lowered the demarcation lines move towards the mobility edges and thus we have an increasing number of recombination centers that bring about a lower value for  $\tau_r$ . The same role is played by the increase of the illumination i.e. the electron-hole generation rate, as to be expected from the larger recombination rate for a larger concentration of electrons and/or holes [27]. In the case of an exponential band tail the effect of the shift of the demarcation line will be particularly strong yielding an exponential-like decrease of  $\tau_r$  with decreasing temperature [14]. For the photoconductivity,  $\sigma_{ph}$ , we note that its dependence on the optical generation rate is usually characterized by an exponent  $\gamma$  that is defined by the relation  $\sigma_{ph} \propto G\tau_r \propto G^\gamma$ . In the case of present interest, i.e. the case of the band tails, one correspondingly obtains [14] a value of  $\gamma = E_{ct}/(E_{ct} + k_B T)$  where  $E_{ct}$  is the width of the bandtail, when the DOS of the latter is assumed to be given by  $N_c \exp[-(E_c - E)/E_{ct}]$ . Hence, the measured temperature dependence of  $\gamma$  can reveal the value of  $E_{ct}$ . It turns out that the temperature dependence of  $\gamma$  is also sensitive to deviations from the exponential bandtail shape, and as such its measurement can provide a tool for the mapping of the  $g(E)$  map.



#### 4. Electronic properties of semiconductor nanostructures

As we saw above the well understood electronic structure of crystalline semiconductors is quite a good starting point for the analysis of the electronic properties of non-crystalline semiconductors. For the understanding of the electronic structure and electrical transport in nanostructures we begin then again with the Bloch-picture. This is in artificially made structures for which the scale is larger than the atomic or macromolecular scale ( $\leq 10 \text{ \AA}$ ) but smaller than the macroscopic-bulk scale ( $\geq 100 \text{ \AA}$ ) for which the electronic properties are independent of the size of the structure.

The most important fundamental effect that takes place in the nanostructures is that of the simple quantum confinement which is an immediate result of the uncertainty principle [28]. This principle in the present context can be understood as the consequence of limiting an a priori free electron into a space region of diameter  $d$ , say, in the  $x$ -direction, as can be done by infinitely high potential barriers. Here we assume, however, that  $d$  is not only larger than the lattice constant  $a$ , but is such that the carrier can be assumed to be well described by the Bloch wave function, i.e. that it can be assumed to behave a priori as a free particle with the same effective mass that it has in the bulk. This above confinement of the electron yields then an increase of the electron momentum by  $\hbar/d$ , and consequently, its kinetic energy increases by about  $(\hbar/d)^2/(2m^*)$  or, more precisely [8], by  $\Delta = (\hbar^2/2m^*)(\pi/d)^2$ . It is important to note that if the electron has a mean free path  $\ell$  such that  $\ell < d$ , a dephasing of the electron wave will take place and its amplitude will decrease within the distance  $\ell$ , thus making the above picture inappropriate. This aspect of the confinement can also be discussed using the uncertainty principle by noting that if the electron has a mean free time for scattering  $\tau_s$ , such that  $\ell < d$ , its energy is broadened by the amount of  $\Gamma = \hbar/\tau_s$ . Hence, the quantum confinement effect is expected to be observed only if  $\Delta > \Gamma$ , i.e. only if  $\ell > d$ . This is the reason that the fascinating phenomena associated with quantum confinement take place in high mobility semiconductors and in particular at low temperatures [28,29]. As a consequence we would expect that for a disordered solid these phenomena will be found for smaller nanostructures than in their crystalline counterparts [30]. We note in passing that over the scale of  $\ell$ , the concept of  $m^*$  (though not with the same value) appears to be useful for the extended states in a disordered semiconductor. In what follows we discuss then the electronic structure in nanostructures of crystalline semiconductors, recalling that for small enough structures of disordered materials the results are expected to be qualitatively the same. On the other hand since  $\ell$  is a statistical concept the potential fluctuations in disordered semiconductors, over their scales, will cause the smearing of the sharper features associated with the electronic properties of crystalline nanostructure even for  $\ell > d$ . Indeed, clear manifestations of the quantum confinement, i.e. the dependence of the electronic structure and transport on the size of structure, in the above  $10 \leq d \leq 100 \text{ \AA}$  range, have been reported for chalcogenes [11], chalcogenides [12] and tetrahedrally bonded [30] amorphous semiconductors.

In addition to the increase of the electrons' energy there is another consequence of the confinement, i.e. the quantization of the states according to their standing waves in the potential well. To appreciate these effects let us start by a brief review of the electronic levels in a quantum well [8], i.e. in a two-dimensional geometry where the confinement takes place between two infinite barriers, the distance between which is  $d$ , and the direction of which is  $x$ . A particle within such a well is described by the product of the Bloch wave function for the  $y$ - $z$  plane and the envelope wave function  $\Xi(x)$  of the standing-wave that is determined by the corresponding solution of the one dimensional Schrödinger equation in the  $x$ -direction [9,28]. The solutions for  $\Xi(x)$  yields then the energies  $E_n = n^2\Delta$  where  $n = 1, 2, 3, \dots$ . In the more realistic case of a finite-depth well these value change somewhat but the main consequences of the confinement, i.e. energy shifts and discrete levels in the confinement direction, remain [8,28].

As in our discussion in Sec. 3 the most general and informative feature of the electronic structure is the DOS. Let us examine then this property in the nanostructures. We do know that for the simple parabolic bands the density of states (per unit, of the corresponding dimensional, volume) within a band (the bottom of which lies at  $E = 0$ ) is:  $\rho_3 = [(2m^*)^{1/2}/(\pi^2\hbar^3)]E^{1/2}$  in three dimensions,  $\rho_2 = (m^*/\pi\hbar^2)$  in two dimensions and  $\rho_1 = (2/\pi\hbar)(m^*/2E)^{1/2}$  in one dimension [7,8]. We note here that the DOS is finite at the band edge in two-dimensional systems and that it diverges at the bottom of the



band in one-dimensional systems. In the simple quantum well-like structures we will have then that the energies are given by  $E_n(\mathbf{k}_\perp) = n^2\Delta + \hbar^2|\mathbf{k}_\perp|^2/2m^*$ , where  $\mathbf{k}_\perp$  is the wave-vector in the y-z plane. The corresponding DOS will be then a "steps" function where at each  $n$  the DOS "jumps" by  $m^*/\hbar\pi$ . It is obvious then that as  $d$  increases, the separation between the  $E_n$  levels will be reduced and that the overall DOS will approximate that of the three dimensional system [8]. This is to be expected since with the increase of  $d$  the system approaches the situation of the Bloch's macroscopic crystal where we consider the fact that  $d = aN_d$ , where  $N_d$  is the number of unit cells in the well. Indeed we mentioned above that  $E_n = (\hbar^2/2m^*)(\pi n/aN_d)^2$ . As  $d$  increases we get two simultaneous effects. First, the separation between the levels (the confinement energy) becomes smaller, and second, the number of allowed states ( $2N_d$ ) becomes larger. Consequently the increase of  $d$  yields a transition from that of well-separated discrete states distribution to a quasicontinuous distribution as in the crystalline band. The states change their nature from standing waves to traveling-Bloch waves. Since for the latter states the crystal momentum is a good quantum number, we have that for a wide enough quantum well the expected three-dimensional crystalline DOS will be found.

In general, we are familiar with the evolvement of the electronic structure from that of the atom to that of the molecule to that of the crystalline solid. Let us follow then, in a similar way, the evolvement of the electronic structure when adjacent quantum wells are introduced, say, along the above x-direction. The double well structures, in which a barrier of finite height and finite width enables the tunneling of an electron from one well to the other, in a manner that is reminiscent of the hydrogen molecule, is expected to yield the removal of the double degeneracy of the original well states by the perturbation that is due to the effect of one potential well on the electron energy in the other potential well.

As we go to an array of finite-depth quantum wells, with a barrier width  $b$  we encounter the periodic situation of the well-known Kronig-Penney model [7] with a periodicity of  $d+b$ . The smaller the  $b$  the larger the overlap of the wave functions in adjacent wells and the broader the corresponding minibands that form by the broadening of the discrete confinement levels of the isolated well. The degeneracy of the states in each band will be  $N_w$  where  $N_w$  is the number of wells in the one-dimension arrays. We can use here exactly the same considerations that we have used for the broadening of the atomic levels into bands, in the crystalline bulk. When  $d+b$  becomes so small to approach the lattice periodicity, the corresponding atomic potential becomes dominant and  $g(E)$  transforms to the expected three-dimensional density of states of the original semiconductor bulk. One of the interesting outcomes of this "superlattice" is that the width of the Brillouin zone of the minibands is  $2\pi/(b+d)$ . Since the superlattice crystal momentum is conserved up to the reciprocal lattice vector  $\pi/(b+d)$ , the corresponding wave vector behaves as a zero wave vector and we can look at the original crystalline zone edge  $\pi/a$  to be folded into smaller zones. This view is known as the "zone folding" picture [7]. The significant effect of this folding is that it enables to transfer a chosen effective mass in the crystalline bulk band to the minimum of the next miniband, yielding an "effective mass engineering" [7,28]. In fact, by choosing the sequence of quantum well and quantum barrier materials, one can engineer many of the electronic properties of the semiconductor. In particular, one can tailor the properties of the electrons and the holes in the system to yield high efficiency light emitting diodes (LED's) and solid-state lasers [8]. The reason for the higher efficiency, in comparison with the older pn-diodes, is that in the quantum wells we have both a wave guide-like structure due to the different refractive indices of the well and barrier materials and to the geometrical confinement of both electrons and holes that increases the overlap of their wave-functions and thus the probability for their radiative recombination.

Turning to lower dimensions, we find that in the one-dimensional system in the x-direction we have standing wave-like states due to the confinement in the y and z directions. For a wire with a rectangular cross section  $L_y \times L_z$  this will yield the discrete levels to be given by  $E_{x,y} = (\hbar^2\pi^2/2m^*)[(n_y/L_y)^2 + (n_z/L_z)^2]$  where  $n_y$  and  $n_z$  are the states of the confined wave function. Only in the x-direction we have then a free electron-like behavior. In the latter case, we can have elastic scattering only from the  $-k_x$  to the  $k_x$  or the  $-k_x$  states and vice versa. This, as we show below, yields then the interesting phenomenon of the quantization of the conductance [29]. An interesting result that we have mentioned before is the diverging of the DOS at the band edge. We note however that for a "quantum wire" of a finite length the separation of the energy levels and the control of the states occupation by the Fermi-Dirac statistics will cause the conduction to take place at a finite value

of  $k_x$ , as is the case of the Bloch metal. Consequently, we refer to the corresponding largest occupied  $k_x$  as the Fermi wave vector and denote it by  $k_F$ .

Further reduction of the dimensionality brings us to the quantum dot of which we can think of as a cubical box, or a sphere with radius  $R$ , where  $R$  is in the range considered above for quantum structures [9]. Following the above consideration this will yield discrete states such as  $E_{e,n,l} = E_g + (\hbar^2/2m^*)(\kappa_{n,l}/R)^2$  for the electrons in the "conduction" band, and  $E_{h,n,l} = (\hbar^2/2m_h^*)(\kappa_{n,l}/R)^2$  for the holes in the "valence" band. Here, the  $E_g$  is the bandgap of the original crystalline bulk and  $\kappa_{n,l}$  are the quantum numbers of the confined states that are characterized by the integers  $n$  and  $l$ . The sum of the confinement energies gives then the increment in the widened "forbidden gap" that consists now of discrete states. In the ground state the "band gap" becomes then  $E_g + E_R$ , where  $E_R = (\hbar^2/2m_r^*)(\pi/R)^2$  and  $m_r^*$  is the reduced electron-hole mass. In this simple treatment we ignore of course the Coulomb interactions, the importance of which will be considered below. It is obvious that as the size of dot increases, the above level separation and the confinement energies decrease, yielding again a smooth transition from the discrete, quantum confined states, behavior to that of the Bloch-bulk traveling-wave behavior. We note that as a consequence of the discreteness of the energy levels one defines the energy "band gap" in such a system by the energetic distance between the highest energy DOS peak in the valence band and the lowest DOS peak in the conduction band [31].

Turning to the transport properties we start by mentioning the most conspicuous transport phenomenon in each of the various dimensions, leaving the other phenomena to be found in the cited literature [8,29]. Starting with the two-dimensional quantum well structures the most known special feature is the resonant tunneling [8,28]. The essence of this very famous effect is quite simple considering the two requirements for tunneling as we presented them already in the context of hopping conduction. First, tunneling can take place from a given state to another state at the same energy level, and second, the latter state must be empty so that the electron can tunnel into it. Let us consider then a five-layer semiconductor structure such that the first and the last layers are made of a bulk semiconductor with a conduction band edge  $E_c$ . The second and fourth layers, made of another semiconductor, serve as the tunnel barriers. The third layer is a quantum-well semiconductor with say, a conduction band edge  $E_w$  and a confinement energy  $E_d$ . The carrier concentration in the well is usually lower than that of the bulk semiconductor. The assumption then is that in the semiconductor bulks  $E_c$  is occupied by electrons so that these states can be considered to be discrete occupied levels above which there are empty levels. Before a voltage  $V$  is applied,  $E_w + E_d > E_c$  and thus no tunneling is possible throughout the structure. Upon the application of a voltage  $V$  the conduction band edge of the "left" bulk is raised to  $E_c + V/2$  and that of the "right" bulk is lowered to  $E_c - V/2$ . Now, tunneling is not possible (at  $T = 0$ ) as long as  $E_w + E_d > E_c + V/2$ . With further increase of  $V$  the alignment of  $E_c + V/2$  with  $E_w + E_d$  yields a strong increase of the tunneling current. Then, as  $E_c + V/2$  is made larger than  $E_w + E_d$  the tunneling probability drops again, and the current drops in spite of the rise in  $V$ . This provides then a region of  $V$  for which there is a "negative differential resistance". The importance of this feature is that it is a condition for current instability. In particular this feature enables oscillations in the circuit [8] or even self-excited oscillations [32] as do (by other mechanisms) the Gunn [28] or the acoustoelectric [33] effects. It is interesting to note that such an effect has also been observed in double barrier structures of amorphous semiconductors [34], indicating the validity of the nearly free electron picture in small enough structures of these systems.

For the one-dimensional system of quantum wires the most striking feature is the quantization of the conductance [8,29]. As we saw in this case the only way for an elastic scattering process to take place is that of an electron in the  $k_x$  state to be scattered to the  $k_x$  state or the  $-k_x$  state, or vice versa. In the "channels" (or the subbands, i.e. the two-dimensional confinement energies,  $E_{x,y}$ ), if they are well separated (e.g. for  $L_y \approx L_z \approx 100$  Å the separation between the confinement levels is 50 meV) this motion, with only elastic scattering, can yield very high mobilities. In the ideal case this motion yields a quantized (minimum) conductance as can be concluded from the following considerations. The conduction takes place at  $k_F$  such that the velocity of an electron contributing to the current is  $v_e = (\hbar k_F/m^*)$ . The time it takes to travel through a wire of length  $L_x$  is  $L_x/v_e$  and thus the current contributed by each electron at  $k_F$  is given by  $qv_e/L_x$ . The number of such electron states within the interval  $qV/2$  (see below) is  $L_x \rho_1(E_F) qV/2$ . Considering the fact that  $\rho_1 = (2/\pi\hbar)m^*/\hbar k_F$  we get then that the total current is  $I = (2q^2/h)V$ . Hence, each occupied channel contributes a quantized conductance of  $2q^2/h$ . In a system where only a single channel is occupied this quantized conductance

will be manifested by the corresponding quantized jumps in the conductance. In this simple picture the non-trivial point is that we considered  $V/2$  rather than the intuitively expected  $V$ . The reason for that is that a system of only elastic collisions has no resistance and thus the voltage drops at the contacts [9]. Hence the quasi-Fermi level in the wire is shifted up on the "average" by only  $V/2$ .

As for the two-dimensional and the one-dimensional systems the transport in an array of quantum dots is expected to be controlled by the tunneling between adjacent quantum dots. Hence, the effective mobility of the carrier propagation  $\mu_t$  is expected to be proportional to the inter-dot tunneling probability  $\exp(-2\chi s)$  where  $\chi$  is the tunneling (say, WKB) exponent and  $s$  is some typical (see however below) inter-dot distance. A priori then, the conditions for transport in the array resemble those between adjacent quantum wells. However, there is one significant difference that follows the relatively small size of the dots, i.e. the non-negligible charging energy of a dot which is a result of placing a single electronic charge on the dot. The dot size is typically a few tens of Å and thus, this energy is typically of the order of a tenth of an eV [35]. A rough upper estimate of that energy can be obtained as follows. The energy needed to be supplied by a single electron addition to a dot is  $E_{cb} = q^2/2C$  where  $C$  is the capacitance of the dot within its environment. Assuming an isolated spherical dot, with a radius  $R$ , that is embedded in a dielectric with a constant  $\epsilon\epsilon_0$ , the capacitance is given by  $C = 4\pi\epsilon\epsilon_0 R$ . For a dot with  $R = 20$  Å in a quartz matrix ( $\epsilon = 3.9$ ) one gets that  $E_{cb} = 0.175$  eV. Correspondingly, for a single electron to be injected to a system of dots an activation process that supplies the energy  $E_{cb}$  is required. Similarly, for the thermal "generation" of an electron-hole pair i.e. a negatively charged dot and a well-separated positively charged dot, from an a priori two neutral dots, the energy to be supplied is  $2E_{cb}$ . The latter situation can be viewed as the thermal electron-hole pair generation in an intrinsic semiconductor with an energy gap of  $E_g$ , for which we saw that the carrier concentration is proportional to  $\exp(-E_g/2k_B T)$ . Thus, in both cases mentioned here, the concentration of carriers available for tunneling is given by  $n_{cb} \propto \exp(-E_{cb}/k_B T)$ . Hence, conduction can take place only if the energy  $E_{cb}$ , to overcome this electrostatically-imposed Coulomb blockade, is provided. The conductivity will be given then by  $\sigma_t = q\mu_t n_{cb} \propto \exp(-\chi s - E_{cb}/k_B T)$ . This expression has simple consequences in two cases. If we have an ordered array of the same  $s$  and the same  $R$ , the conductivity  $\sigma_t$  will be activated in the same way as  $n_{cb}$ . This analogy can be carried over also to the case of a disordered array of dots if there is a continuous path of very small (of the order of atomic spacing) dot-separation. In the latter case, that resembles impurity-band-like conduction, this optimal conduction path shunts the other possible conduction routes and the conductivity of the system will be the same as that of the optimal conduction path [36]. In the other extreme of large  $s$  or very low temperature (so that there is a low probability for the supply of  $E_{cb}$ ) we encounter the situation similar to that of variable range hopping and the expected  $\exp(-T_0/T^{1/4})$  dependence, but of course with a  $T_0$  that corresponds to the dots rather than to atoms [37]. The most interesting case takes place however for some distributions of  $s$  and  $R$  [37] and in particular for the simple correlated case for which the  $s/R$  ratio is assumed to be a constant [35]. Such a situation is a priori expected to occur in a composite where the fractional content of the material of which the dots are made (the other is the dielectric in which the dots are embedded) is a constant. In the latter case a region with larger dots is also expected to have large  $s$  values, and a region of smaller dots is expected to have small  $s$  values. There is here the obvious competition between the smaller barrier, that enhances the tunneling, and the smaller dot that requires higher activation energy. In that case the optimal conduction path will be determined by the  $s$ - $R$  combination that will yield the highest conductivity. It is easy to see then that the maximum of  $\sigma_t$  for a given temperature will be determined by the  $s$ - $R$  combination that will minimize the term  $(\chi s + E_{cb}/k_B T)$ . In the simple case of a constant  $s/R$  this will be obtained for  $s \propto R \propto T^{-1/2}$ , yielding that  $\sigma_t \propto \exp(-AT^{-1/2})$ , where  $A$  is a corresponding constant. Thus, there will be a shift of the optimal conduction path as a function of temperature. It is to be noted that while this argument resembles Mott's argument for variable range hopping [17] which is a pure mobility argument, in the present case there is an interplay between the mobility and the carrier concentration, that yields the optimal path shift [35]. Here again there is a participation of relatively very few (as low as 1%) quantum dots in the effective conduction process [36].

Summarizing the above picture one would expect for a disordered system of quantum dots a temperature dependence of the type  $\log(\sigma_t) \propto T^{-\alpha}$ , where  $1/4 \leq \alpha \leq 1$ , for various systems of quantum dots. In particular a transition from  $\alpha = 1/4$  to  $\alpha = 1/2$  is to be expected with increasing temperature. If a

path of close enough adjacent dots is present a transition from  $\alpha = 1/2$  to  $\alpha = 1$  is also to be expected [37]. We should remark in passing that while the above ideas have been developed for granular metals their essence are valid for semiconductor quantum dots [38], for which the additional refined effects associated with the quantized levels in the dot have also been observed [39]. In particular deconfinement effects accompanied with [40,41] or without [42] their effect on the photoluminescence have been observed in disordered arrays of semiconductor quantum dots.

## 5. Conclusions

The fact that semiconductor chalcogens and chalcogenides can come with crystalline or amorphous forms and the fact that they can be made to have various nanostructures, make them a very good testing grounds for the ideas and concepts introduced into semiconductor physics in the second half of the 20<sup>th</sup> century. In addition they have the prospects of providing structures for various electronic and optoelectronic applications which benefit from their very special properties. The most notable example of the latter is of course the xerography.

It appears, following the above review, that the Bloch and the localized states pictures are very good starting points for the understanding of the electronic properties of disordered and nanostructured semiconductors. To better understand these systems one must apply the concepts and the theories of tunneling and percolation. The important new concepts, as well as some analogies and extrapolations from the theory of crystalline semiconductors and situations of other quantum systems, are found to be very helpful for the construction of pictures of the electronic properties of the above systems in general and for chalcogens and chalcogenides in particular. These concepts are in fact necessary tools for quantitative characterization of the latter systems.

## Acknowledgement

This work was supported by the Israel Science Foundation.

## References

- [1] J. C. Philips, *Bonds and Bands in Semiconductors*, Academic, New York (1973).
- [2] R. Zallen, *The Physics of Amorphous Solids*, John Wiley, New York (1983).
- [3] D. Adler in *Amorphous Semiconductors*, Eds. H. Fritzsche, D. Han, C. C. Tsai, World Scientific, Singapore, 1987, p. 3.
- [4] S. R. Elliot, *Physics of Amorphous Materials*, Longman, Hong Kong (1990).
- [5] C. M. Wolfe, N.J. Holonyak Jr. and G.E. Stillman, *Physical Properties of Semiconductors*, Prentice Hall, Englewood Cliffs (1989).
- [6] I. Balberg, *Appl. Phys. Lett.*, **16**, 491 (1970).
- [7] J. Singh, *Physics of Semiconductors and their Heterostructures*, McGraw Hill, New York (1993).
- [8] C. Weisbuch, B. Vinter, *Quantum Semiconductor Structures: Fundamentals and Applications*, Academic, Boston (1991).
- [9] L. Ba'enjai, S. W. Koch, *Semiconductor Quantum Dots*, World Scientific, Singapore (1993).
- [10] For a collection of papers see, *Optical Effects in Amorphous Semiconductors*, Eds. P.C. Taylor and S. G. Bishop, AIP, New York, 1984.
- [11] E. Vateva, I. Georgieva, *J. Non Cryst. Solids*, **164-166**, 865 (1993).
- [12] See for example, I. Z. Indutnyi, P. E. Shepeljavy, *J. Non Cryst. Solids*, **227-230**, 700 (1998), and V. Palyok, M. Malyovanik, *J. of Opt. and Adv. Mater.*, **1**, 77 (1999).
- [13] J. Ziman, *Principles of the theory of Solids*, Cambridge University, Cambridge (1965).
- [14] A. Rose, *Concepts in Photoconductivity and Allied Problems*, Wiley Interscience, New York (1963).
- [15] R. H. Bube, *Photoelectronic Properties of Semiconductors*, Cambridge University, Cambridge (1992).

- [16] I. Balberg, *J. Appl. Phys.*, **75**, 914 (1994).
- [17] N. F. Mott, E. A. Davis, *Electronic Processes in Non-Crystalline Materials*, Oxford University, Oxford (1979), and N. F. Mott, *Conduction in Non-Crystalline Materials*, Oxford University, Oxford (1993).
- [18] M. H. Cohen, H. Fritzsche, S. R. Ovshinsky, *Phys. Rev. Lett.*, **22**, 1065 (1969).
- [19] A. A. Klochikhin, S. G. Ogloblin, *Phys. Rev. B*, **48**, 3100 (1993).
- [20] See for example, E. N. Economou, C. M. Soukoulis, M. H. Cohen, A. D. Zdetsis, *Phys. Rev. B*, **31**, 6172 (1985), and S.K. Oleay and P.K. Lim, *Solid State Commun.*, **101**, 513 (1997).
- [21] J. M. Ziman, *Models of Disorder*, Cambridge University, Cambridge (1979).
- [22] R. A. Smith, *Semiconductors*, Cambridge University, Cambridge (1961).
- [23] H. C. Berg, *Random Walk in Biology*, Princeton University, Princeton (1983).
- [24] O. Madelung, *Introduction to Solid State Theory*, Springer, Berlin (1978).
- [25] B. I. Shklovskii, A. L. Efros, *Electronic Properties of Doped Semiconductors*, Springer, Berlin (1984).
- [26] A. Ambegaokar, B. I. Halperin, J. S. Langer, *Phys. Rev. B*, **4**, 2612 (1971).
- [27] Y. Lubianiker, I. Balberg, L. Fonseca, *Phys. Rev. B*, **55**, R15997 (1997).
- [28] P. Y. Yu, M. Cardona, *Fundamentals of Semiconductors*, Springer, Berlin (1999).
- [29] S. Datta, *Electronic Transport in Mesoscopic Systems*, Cambridge University, Cambridge (1995).
- [30] As an example see B. Abeles, T. Tiedje, *Phys. Rev. Lett.*, **51**, 2003 (1983, and for a review see M. Hirose, S. Miyazaki, N. Murayama, in *Tetrahedrally-Bonded Amorphous Semiconductors*, Eds. D. Adler and H. Fritzsche, Plenum, New York, 1985, p. 441.
- [31] See for example, N. A. Hill, K. B. Whaley, *J. Elect. Mater.*, **25**, 269 (1996), and S.V. Nair, L. M. Ramaniah and K. C. Rustagi, *Phys. Rev. B*, **45**, 5969 (1992).
- [32] P. Zhao, H. L. Cui, D. L. Wooland, *Phys. Rev. B*, **63**, 075302 (2001).
- [33] A. Many, I. Balberg, *Physics Letters*, **21**, 486 (1966).
- [34] Z. R. Yu, I. Pereyral, M. N. P. Carreno, *Jpn. J. Appl. Phys.*, **38**, 1317 (1999).
- [35] B. Abeles, *Applied Solid State Science*, **6**, 1 (1974).
- [36] G. A. Levin, *Physics Letters A*, **142**, 405 (1989).
- [37] P. Sheng, J. Klafter, *Phys. Rev. B*, **27**, 2583 (1983).
- [38] G. Y. Yu, R. F. O'Connel, Y. L. He, M. B. Yu, *J. Appl. Phys.*, **78**, 3945 (1995).
- [39] X. Gu, H. Qin, H. Lu, J. Xu, K. Chen, *Mater. Res. Soc. Symp. Proc.*, **467**, 367 (1997).
- [40] Y. Posada L. Fonseca, O. Resto, S. Z. Weisz, I. Balberg, *Mater. Res. Soc. Symp. Proc.*, to be published (2001).
- [41] Y. Lubianiker, I. Balberg, *Phys. Rev. Lett.*, **78**, 2433 (1997).
- [42] Y. He, Y. Wei, G. Zheng, M. Yu, d M. Liu, *J. Appl. Phys.*, **82**, 3408 (1997).

## EQUILIBRIUM CHARGE CARRIER MOBILITY IN DISORDERED HOPPING SYSTEMS

V. I. Arkhipov, E. V. Emelianova,<sup>a</sup> H. Bässler

Institute of Physical, Nuclear and Macromolecular Chemistry and Material Science Center, Philipps-Universität Marburg, Hans-Meerwein-Strasse, D-35032 Marburg, Germany

<sup>a</sup>Semiconductor Physics Laboratory, University of Leuven, Celestijnenlaan 200D, B-3001 Heverlee-Leuven, Belgium

It is shown that the charge carrier mobility in a positionally and energetically disordered hopping system can be evaluated by averaging either hopping rates or hopping times over the thermally equilibrium energy distribution of localized carriers. However, at variance with averaging hopping rates, averaging hopping times can be correct only if the energy dependence of the carrier energy relaxation time is also taken into consideration. The equilibrium carrier mobility was calculated by averaging hopping rates as a function of the temperature and concentration of localized sites. The obtained results prove that, in good quantitative agreement with both Monte Carlo simulations and experimental data, the temperature and concentration dependences of the mobility can be factorized, i.e. that the mobility can be represented as a product of two functions. The first function depends almost solely upon the temperature and reveals only a weak concentration dependence while the second one mainly governs the concentration dependence of the mobility and is almost independent of the temperature.

(Received June 25, 2001; accepted September 3, 2001)

**Keywords:** Disordered semiconductors, Carrier mobility, Hopping conductivity

### 1. Introduction

Basic characteristics of charge carrier transport in non-crystalline semiconducting materials are well known to be controlled by positional and energy disorder inherent in these materials [1-6]. Due to the disorder effects, most carriers are permanently localized in amorphous materials and the only feasible mode of charge transport is carrier jumps either directly between localized states or via a band of extended states if such states do occur in a given material. It is worth noting that the occurrence of the positional disorder will almost inevitably give rise to the energy disorder via the dependence of the potential energy of interaction upon the distance between interacting particles [7,8]. Nonetheless, charge carrier hopping can be simulated as  $r$ -hopping in a random system of localized states ignoring the energy disorder [9]. Trap-controlled transport implies a negligible contribution of direct tunneling jumps of carriers between localized states and, therefore, this transport mode can be considered as the energy-controlled hopping or  $\varepsilon$ -hopping. In most disordered materials both positional and energy disorder affect the carrier jump rate and this transport mode is described by models of  $r\varepsilon$ -hopping.

Most such models are based on the Miller-Abrahams [10] expression for the rate of carrier jumps,  $\nu(r, E_{st}, E_t)$ , over the distance  $r$  between a starting state of the energy  $E_{st}$  and the target site of the energy  $E_t$ . This expression can be written as,

$$\nu(r, E_{st}, E_t) = \nu_0 \exp[-u(r, E_{st}, E_t)] \quad , \quad u(r, E_{st}, E_t) = 2\gamma r + \frac{\eta(E_t - E_{st})}{kT} \quad , \quad (1)$$

where  $u$  is the hopping parameter,  $\nu_0$  the attempt-to-jump frequency,  $\gamma$  the inverse localization radius,  $T$  the temperature,  $k$  the Boltzmann constant, and  $\eta$  the unity step-function. Although the distance and



the energy difference between the starting and target sites almost similarly affect the jump rate there is one important difference that makes very different  $r$ - and  $\varepsilon$ -hopping modes.

The distance-dependent factor in Eq. (1) is completely symmetric, i.e. the distance between hopping sites similarly affects the rate of forth and back jumps. If a site, remote from any other site in a positionally random system of monoenergetic hopping sites, could be considered as a trap for carriers, the trapping time will be exactly equal to the release time. It means that it is equally difficult for a carrier to be released and to be trapped by such an isolated localized state. However, it is not the case for an energetically random system. While energetically upward jumps require thermal activation downward jumps imply dissipation of the excess energy via phonon emission. The former process is much slower than the latter and, therefore, the rates of forth and back jumps between two fixed states of different energies are normally very different. Consequently, a deep localized state can promptly capture a carrier and keep it localized over a long time. It is the strong asymmetry of trapping and release times that makes the energy disorder much more important as far as charge transport characteristics are concerned.

In the present paper we concentrate on the role of energy disorder in  $\varepsilon$ - and  $r\varepsilon$ -hopping. It will be shown that the carrier release time from deep localized states does control the effective carrier mobility in an energetically disordered system with a broad density-of-states (DOS) distribution under the non-equilibrium dispersive transport conditions. However, it is not the case for the equilibrium non-dispersive transport regime. Once the thermally equilibrium energy distribution of localized carriers is established the transport is controlled by both trapping and release of carriers whose energies are around the maximum of this distribution. Averaging the carrier hopping rates yields the equilibrium mobility which is in agreement with the exact analytic results obtained for  $\varepsilon$ -hopping [11] as well as with the results of Monte-Carlo simulations [12] and predictions of the effective medium theory [13-15] for  $r\varepsilon$ -hopping.

## 2. Equilibrium charge carrier mobility in an energetically disordered system

Mathematically,  $\varepsilon$ -hopping can be described as a set of multiple-trapping equations which relate the density of localized carriers to the density of carriers in extended states [11]. This is possible because the time carrier spends in extended states is typically by orders of magnitude shorter than the total jump time such that the sequence of carrier release, motion in the extended states, and trapping can be considered as a single jump. The  $\varepsilon$ -hopping equations for the localized carrier distribution,  $\rho$ , and the free carrier density,  $p_c$ , then read,

$$\frac{\partial \rho}{\partial t} = \frac{1}{\tau_0} p_c g(E) - \nu_0 \rho \exp\left(-\frac{E}{kT}\right), \quad (2)$$

$$\frac{\partial p}{\partial t} + \mu_c F \frac{\partial p_c}{\partial x} = 0, \quad (3)$$

where  $p$  is the total density of carriers which is practically equal to the density of localized carriers,

$$p = p_c + \int_{-\infty}^0 dE \rho(E) \approx \int_{-\infty}^0 dE \rho(E), \quad (4)$$

$t$  the time,  $x$  the coordinate,  $g(E)$  the normalized DOS energy distribution,  $\mu_c$  the mobility of carriers in extended states,  $F$  the electric field,  $\nu_0$  the attempt-to-jump frequency, and  $\tau_0$  the lifetime of carriers in extended states. Solving Eq. (2) under the thermal equilibrium conditions ( $\partial \rho / \partial t = 0$ ) yields the equilibrium distribution  $\rho_{eq}$  as,

$$\rho_{eq} = \frac{1}{\nu_0 \tau_0} p_c g(E) \exp\left(-\frac{E}{kT}\right). \quad (5)$$

Substituting Eq. (5) into Eq. (4) leads to the following relation between the total density of carriers and the density of carriers in extended states:

$$p_c = v_0 \tau_0 \left[ \int_{-\infty}^0 dE g(E) \exp\left(-\frac{E}{kT}\right) \right]^{-1} p \quad (6)$$

This relation together with Eq. (3) allows to obtain a transport equation for the total density of carriers:

$$\frac{\partial p}{\partial t} + \mu F \frac{\partial p}{\partial x} = 0 \quad (7)$$

with the equilibrium carrier mobility in an energetically disordered system of localized states,  $\mu$ , defined as [11],

$$\mu = \mu_c v_0 \tau_0 \left[ \int_{-\infty}^0 dE g(E) \exp\left(-\frac{E}{kT}\right) \right]^{-1} \quad (8)$$

In the following, we shall use this *exact* expression for the mobility as a reference for different approximate methods.

Now we consider two possible approaches to estimating the equilibrium mobility. The carrier mobility appears in the expressions for the current,  $j = \mu F p$ , and for the carrier transit time,  $t_T = L / \mu F$ , where  $L$  is the distance crossed by carriers over the time  $t_T$ . These two definitions are absolutely equivalent to each other once carriers are thermally equilibrated. Experimentally, it is rather difficult to evaluate the mobility from the current measurements because the density of drifting carriers is normally a poorly known value. Therefore, the mobility is usually determined from the time-of-flight measurements. However, theoretical evaluation of the mobility may be based on either of these two definitions and both must, of course, yield the same result.

The trap-controlled current can be estimated as the total rate of carrier jumps,  $v_t$ , multiplied by the average distance crossed by a carrier during a single jump. The former should be calculated as the jump rate averaged over the energy distribution of localized carriers, while the latter is the mean free path of carriers in extended states,  $\mu_c F \tau_0$ . The normalized thermally equilibrium distribution function,  $f_{eq}$ , takes the form,

$$f_{eq}(E) = g(E) \exp\left(-\frac{E}{kT}\right) \left[ \int_{-\infty}^0 dE g(E) \exp\left(-\frac{E}{kT}\right) \right]^{-1} \quad (9)$$

Averaging the hopping rate over this distribution leads to the following expression for the equilibrium current,

$$j = \mu F p = \mu_c F \tau_0 v_0 \left[ \int_{-\infty}^0 dE g(E) \exp\left(-\frac{E}{kT}\right) \right]^{-1} p \quad (10)$$

where  $\sigma$  is the surface carrier density. Equation (10) yields exactly the same formula for the equilibrium mobility as was obtained from the exact analytic solution of the multiple-trapping equations. For a Gaussian DOS distribution,

$$g(E) = \frac{1}{\sqrt{2\pi}\sigma} \exp\left(-\frac{E^2}{2\sigma^2}\right) \quad (11)$$

with the variance  $\sigma \gg kT$  both Eq. (8) and Eq. (10) yield,

$$\mu = \mu_c v_0 \tau_0 \exp\left[-\frac{\sigma^2}{2(kT)^2}\right] \quad (12)$$

At first glance this result seems to be puzzling if one tries to rationalize it as a carrier packet drift mobility. According to Eq. (9) the equilibrium distribution of localized carriers is also described by a Gaussian distribution of the same variance  $\sigma$  with the maximum of the distribution located at the energy  $E_{max} = -\sigma^2/(kT)^2$ . The value of  $E_{max}$  is two times larger than the activation energy of the equilibrium drift mobility  $E_a = \sigma^2/2(kT)^2$ . The implication is that jumps of an *absolute minority* of carriers, which are localized in states with energies around  $-E_a$ , seem to be responsible for the drift of

a carrier packet as a whole while the majority of carriers, localized around  $E_{max}$ , do not apparently participate in this process.

To resolve this puzzle one should consider the carrier release time *together with* following up equilibration. The average carrier release time,  $\langle t_r \rangle$ , is determined as,

$$\langle t_r \rangle = \frac{1}{v_0} \int_0^\infty dE \exp\left(-\frac{E}{kT}\right) f_{eq}(E) . \quad (13)$$

For a Gaussian DOS distribution Eq. (13) yields,

$$\langle t_r \rangle \propto \exp\left[\frac{3}{2}\left(\frac{\sigma}{kT}\right)^2\right] . \quad (14)$$

The average distance,  $\Delta x$ , which a carrier have crossed before it got trapped again must be proportional to the equilibration time,  $t_{eq}$ . The latter can be estimated as the carrier release time from a localized state of the energy  $E_m$  as,

$$\Delta x \propto t_{eq} \propto \exp\left[\left(\frac{\sigma}{kT}\right)^2\right] . \quad (15)$$

The average carrier velocity during the round trip,  $\langle v \rangle$ , can be written as,

$$\langle v \rangle = \Delta x / \langle t_{eq} \rangle \propto \exp\left[-\frac{1}{2}\left(\frac{\sigma}{kT}\right)^2\right] . \quad (16)$$

Equation (16) indicates that the average round-trip velocity is determined by the interplay of the carrier release and equilibration times. The result of this interplay strongly depends upon the DOS function. For an exponential DOS,  $g(E) = (1/E_0) \exp(E/E_0)$  the round-trip velocity monotonously decreases with increasing depth of the starting site. This implies that carriers are always accumulated in deep states and that the regime of thermally equilibrium transport can never be established. This proves that, under equilibrium transport conditions, the drift mobility is controlled not only by the time of thermally activated jumps of carriers but also by the time of carrier trapping by states that are equally deep or deeper than the starting site. The latter time increases with energy even steeper than an exponential function. This is in contrast with predictions of  $r$ -hopping models in which the mobility and the current are shown to be controlled by the most difficult single carrier jump. In models of  $\varepsilon$ - and  $\varepsilon r$ -hopping in disordered systems, neglecting the trapping time (or, equivalently, the time of downward jumps) as compared to the release time (or the time of upward jumps) is possible only under the dispersive transport conditions. The use of this approximation for the analysis of equilibrium transport characteristics leads to exponentially incorrect results [16].

It is worth noting that the integral in the right-hand side of Eq. (8) is formally equivalent to the carrier release time averaged over the DOS distribution rather than over the distribution of localized carriers. In the first place, it should be emphasized that such averaging has no physical meaning. The similarity is simply caused by the fact that the carrier release time is governed by the same Boltzmann exponential as the thermally equilibrium energy distribution of localized carriers. This similarity is specific for  $\varepsilon$ -hopping but is not valid in systems with both energy and positional disorder. For instance, an attempt to use such averaging in variable range hopping [16] is hardly justifiable. The results of this section prove that the equilibrium carrier mobility can be evaluated by averaging either hopping rates or hopping times. However, averaging hopping times should also account for the energy relaxation time while averaging hopping rates is not subject to this additional complication. In the following section we apply the latter approach for calculating the equilibrium carrier mobility in a positionally and energetically disordered hopping system.

### 3. Equilibrium mobility in a positionally random and energetically disordered hopping system

In a diluted random system of hopping sites most carriers will jump to nearest hopping neighbors i.e. to target sites characterized by minimum values of the hopping parameter  $u$  as counted

from starting sites. For a starting site of energy  $E_{st}$ , the average number,  $n(E_{st}, u)$ , of hopping neighbors, whose hopping parameters are not larger than a given value  $u$ , is given by,

$$n(E_{st}, u) = 4\pi N_t \int_0^{u/2\gamma} dr r^2 \int_{-\infty}^{E_{st} + kT(u-2\gamma r)} dE_t g(E_t) =$$

$$= \frac{\pi N_t}{6} \left( \frac{u}{\gamma} \right)^3 \left[ \int_{-\infty}^{E_{st}} dE_t g(E_t) + \int_{E_{st}}^{E_{st} + kTu} dE_t g(E_t) \left( 1 - \frac{E_t - E_{st}}{kTu} \right)^3 \right], \quad (17)$$

where  $N_t$  is the total density of hopping sites. The probability density,  $w(E_{st}, u)$ , of finding a nearest hopping neighbor of the hopping parameter  $u$  is determined by the Poisson distribution as,

$$w(E_{st}, u) = \exp[-n(E_{st}, u)] \frac{\partial n(E_{st}, u)}{\partial u}. \quad (18)$$

Equation (18) forms a basis for calculating the average hopping parameter,  $\langle u \rangle(E_{st})$ , for carrier jumps from a starting site of energy  $E_{st}$ . Using Eq. (18) as a distribution function for averaging the hopping parameter yields,

$$\langle u \rangle(E_{st}) = \int_0^\infty du u \exp[-n(E_{st}, u)] \frac{\partial n(E_{st}, u)}{\partial u} = \int_0^\infty du \exp[-n(E_{st}, u)]. \quad (19)$$

Evaluating the typical jump distance as  $\langle u \rangle/2\gamma$  and averaging over  $E_{st}$  under thermal equilibrium conditions leads to the following expression for the equilibrium mobility,

$$\mu = \frac{e v_0}{kT(2\gamma)^2} \left[ \int_{-\infty}^\infty dE_{st} g(E_{st}) \exp\left(-\frac{E_{st}}{kT}\right) \right]^{-1}$$

$$\times \int_{-\infty}^\infty dE_{st} \exp[-\langle u \rangle(E_{st})] [\langle u \rangle(E_{st})]^2 g(E_{st}) \exp\left(-\frac{E_{st}}{kT}\right). \quad (20)$$

Temperature dependence of the mobility, calculated from Eq. (20) for a Gaussian DOS distribution, is shown in Fig. 1 for different values of the total density of localized states. All the curves feature almost perfect straight lines if plotted as  $\log \mu$  vs  $1/T^2$ . Although the absolute value of the mobility does strongly decrease with decreasing  $N_t$ , the slopes of  $\log \mu$  vs  $1/T^2$  curves increase by only less than 15 % when the density of hopping sites decreases by four orders of magnitude. This implies that the equilibrium mobility can be rather accurately represented in a factorized form as,

$$\mu = \mu_0 \varphi(N_t) \exp\left[-\left(\frac{c\sigma}{kT}\right)^2\right], \quad (21)$$

with the numeric parameter  $c$  changing from 0.59 at  $N_t = 10^{22} \text{ cm}^{-3}$  to 0.68 at  $N_t = 10^{18} \text{ cm}^{-3}$ . Both the form of Eq. (21) and the value of the parameter  $c$  are in good quantitative agreement with the results of Monte Carlo simulations ( $c = 0.67$ ) and predictions of the effective medium model ( $c = 0.64$ ). It is worth noting that a simpler model, based on averaging hopping rates and employing configurational averaging, also yielded the mobility of the form given by Eq. (21) with  $c = 0.5$ . This value seems to be the lower limit of  $c$  that can be reached at high densities of localized states.

The dependence of the equilibrium mobility upon the total density of hopping sites is illustrated in Fig. 2 parametric in the temperature. The curves plotted in this figure indicate that the concentration dependence of the mobility does obey typical for hopping transport an exponential law,

$$\varphi(N_t) = \exp\left(-\frac{b\gamma}{N_t^{1/3}}\right), \quad (22)$$

with the numeric parameter  $b$  being rather weakly dependent upon the temperature. The values of this parameter are indicated for each curve in Fig. 2.

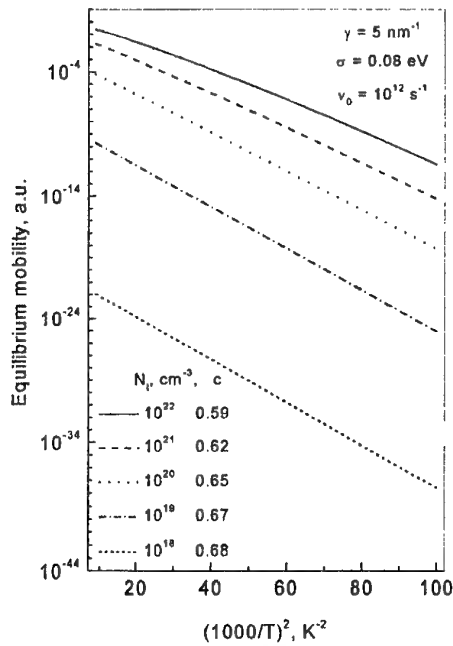


Fig. 1. Temperature dependence of the equilibrium drift mobility calculated from Eq. (20) for a hopping system with a Gaussian DOS distribution of localized states.

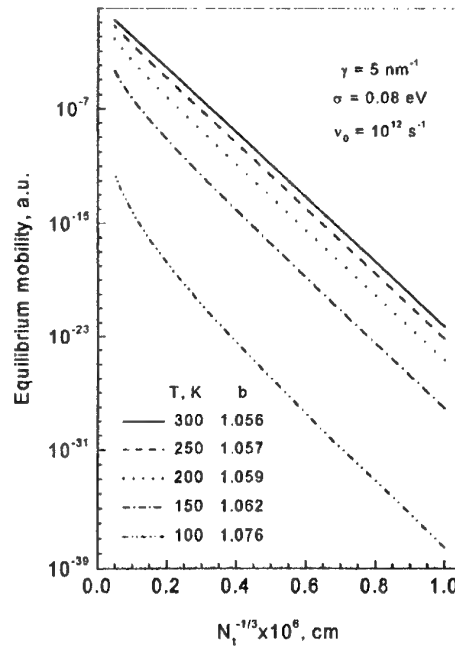


Fig. 2. Concentration dependence of the equilibrium drift mobility calculated from Eq. (20) for a hopping system with a Gaussian DOS distribution of localized states.

The above consideration disregards repeated carrier jumps between two accidentally close hopping neighbors both of which are isolated from other localized states. Although such jumps are important as far as ac conductivity is concerned they do not contribute to the dc current and, concomitantly, to the equilibrium carrier mobility. Accounting for isolated pairs and, more general, for isolated clusters of hopping sites would result in decreasing effective density of states  $N_t$  and, therefore, to increasing values of the coefficients  $b$  and  $c$ .

#### 4. Effective transport energy

The first term in the right-hand side of Eq. (17) gives the number of target states which are deeper than the starting site and the second one describes the number of shallower states. The former is important as far as downward carrier jumps are concerned while the latter governs the rate of upward jumps. In the present paper we consider the equilibrium transport conditions under which both drift and diffusion are controlled by upward hopping and, concomitantly, in the following we concentrate on consideration of this hopping mode. Making out the replacement of variables,

$$u = \frac{E_{tr} - E_{st}}{kT}, \quad (23)$$

yields the following expression for the number of shallower hopping neighbours of a starting site of energy  $E_{st}$ :

$$n(E_{st}, E_{tr}) = \frac{\pi}{6} (\gamma kT)^{-3} \int_{E_{st}}^{E_{tr}} dE_t g(E_t) (E_{tr} - E_t)^3. \quad (24)$$

An upward carrier jump from a starting site is possible if there is at least one such hopping neighbour, i.e. from  $n(E_{st}, E_{tr}) = 1$  on. The use of this condition in Eq. (24) leads to the following transcendental equation for the energy of the most probable upward jumps:

$$\int_{E_{st}}^{E_{tr}} dE_i g(E_i) (E_{tr} - E_i)^3 = \frac{6}{\pi} (\gamma kT)^3. \quad (25)$$

If the DOS distribution decreases with energy faster than  $|E|^{-4}$  than (i) the value of the integral in the left-hand side of Eq. (25) is practically independent of the lower bound of integration for sufficiently deep starting sites and (ii) a major contribution to the integral comes from states with energies around  $E_{tr}$ . Physically, it means that target sites for thermally assisted upward carrier jumps are located around the energy  $E_{tr}$  independent of the energy of starting sites and, therefore, Eq. (5) reduces to:

$$\int_{-\infty}^{E_{tr}} dE_i g(E_i) (E_{tr} - E_i)^3 = \frac{6}{\pi} (\gamma kT)^3. \quad (26)$$

In order to illustrate the efficiency of the transport energy concept we apply it to the calculation of the equilibrium carrier mobility,  $\mu$ , in a positionally random hopping system with a Gaussian DOS distribution at weak external electric fields. Estimating the equilibrium diffusivity as a squared typical jump distance multiplied by the average jump frequency and using the Einstein relation yields,

$$\begin{aligned} \mu_{eq} &= \frac{e v_0}{kT} \left[ \int_{-\infty}^{\infty} dE g(E) \exp\left(-\frac{E}{kT}\right) \right]^{-1} \left[ \int_{-\infty}^{E_{tr}} dE g(E) \right]^{-2/3} \int_{-\infty}^{E_{tr}} dE g(E) \exp\left(-\frac{E}{kT}\right) \exp\left(-\frac{E_{tr} - E}{kT}\right) = \\ &= \frac{e v_0}{kT} \left[ \int_{-\infty}^{\infty} dE g(E) \exp\left(-\frac{E}{kT}\right) \right]^{-1} \left[ \int_{-\infty}^{E_{tr}} dE g(E) \right]^{1/3} \exp\left(-\frac{E_{tr}}{kT}\right) \end{aligned} \quad (27)$$

Equation (27) is remarkably similar to the expression for the trap-controlled equilibrium carrier mobility. The only two differences are: the occurrence of a temperature-dependent transport energy instead of a fixed mobility edge and a weakly temperature-dependent mean jump distance instead of a fixed mean free path of delocalized carriers. For a Gaussian DOS function Eq. (27) reduces to,

$$\mu_{eq} = \frac{e v_0}{\sqrt[3]{2kTN_t}} \exp\left[-\frac{\sigma^2}{2(kT)^2}\right] \left[1 + \text{Erf}\left(\frac{E_{tr}}{\sqrt{2}\sigma}\right)\right]^{1/3} \exp\left(-\frac{E_{tr}}{kT}\right), \quad (28)$$

where Erf is the error function. Further simplification of this equation is possible at high  $T$  and/or low  $N_t$ . Substituting the high-temperature/low-concentration expression for  $E_{tr}$  from Eq. (26) into Eq. (28) yields,

$$\mu_{eq} = \frac{e v_0}{kTN_t^{2/3}} \exp\left[-\left(\frac{6\gamma^3}{\pi N_t}\right)^{1/3}\right] \exp\left[-\frac{\sigma^2}{2(kT)^2}\right]. \quad (29)$$

Equation (29) once again proves that the temperature and concentration dependencies of the mobility are factorized at high temperatures and/or in diluted hopping systems. This result does suggest that these dependencies will also be almost factorized at lower temperatures and in systems with higher concentrations of hopping sites.

## 5. Conclusions

Charge carrier mobility in disordered hopping systems can be evaluated by averaging either hopping rates or hopping times over the thermally equilibrium energy distribution of localized carriers. However, at variance with averaging hopping rates, averaging hopping times can be correct only if the energy dependence of the carrier energy relaxation time is also taken into consideration. Neglecting this relaxation would lead to exponentially incorrect expressions for the equilibrium mobility and diffusivity.

The equilibrium carrier mobility was calculated by averaging hopping rates as a function of the temperature and concentration of localized sites in an energetically disordered and positionally



random hopping system. The obtained results prove that, in good quantitative agreement with both Monte Carlo simulations and experimental data, the temperature and concentration dependences of the mobility can be factorized, i.e. that the mobility can be represented as a product of two functions.

The first one depends almost solely upon the temperature and reveals only a weak concentration dependence while the second one mainly governs the concentration dependence of the mobility and is almost independent of the temperature. These results support the predictions of the simpler models based on the effective medium approximation and configurational averaging.

### Acknowledgments

V. I. Arkhipov is grateful to the Volkswagen Foundation for financial support under the grant No. VW I/76147. E. V. Emelianova acknowledges financial support from the Flemish National Science Foundation. This work was supported by the *Fond der Chemischen Industrie*.

### References

- [1] H. Scher, E. W. Montroll, *Phys. Rev. B*, **12**, 2455 (1975).
- [2] A. I. Rudenko, *J. Non-Cryst. Solids*, **22**, 215 (1976).
- [3] M. Pollak, *Philos. Mag.*, **36**, 1157 (1977).
- [4] D. Lakin, L. Marks, J. Noolandi, *Phys. Rev. B*, **15**, 5834 (1977).
- [5] F. W. Schmidlin, *Phys. Rev. B*, **16**, 2362 (1977).
- [6] A. I. Rudenko, V. I. Arkhipov, *J. Non-Cryst. Solids*, **30**, 163 (1978).
- [7] A. Dieckmann, H. Bässler, P. M. Borsenberger, *J. Chem. Phys.*, **99**, 8136 (1993).
- [8] D. H. Dunlap, P. E. Parris, V. M. Kenkre, *Phys. Rev. Lett.*, **77**, 542 (1996).
- [9] B. I. Shklovskii, A. L. Efros, *Electronic Properties of Doped Semiconductors* (Springer, Berlin, 1984).
- [10] A. Miller, E. Abrahams, *Phys. Rev.*, **120**, 745 (1960).
- [11] A. I. Rudenko, V. I. Arkhipov, *Philos. Mag. B*, **45**, 177 (1982).
- [12] H. Bässler, *Phys. Stat. Sol. (b)*, **175**, 15 (1993).
- [13] B. Movaghar, W. Schirmacher, *J. Phys. C*, **14**, 859 (1981).
- [14] W. Schirmacher, *Solid State Commun.*, **39**, 893 (1981).
- [15] B. Movaghar, B. Grünwald, B. Pohlmann, D. Würtz, W. Schirmacher, *J. Stat. Phys.*, **30**, 315 (1983).
- [16] S. D. Baranovskii, H. Cordes, F. Hensel, G. Leising, *Phys. Rev. B*, **62**, 7934 (2000).

## PHASE-CHANGE OPTICAL MEMORY PROMOTES THE DVD OPTICAL DISK

T. Ohta

Optical Disk Systems Development Center, Matsushita Electrical Industrial Co., Ltd.  
1006 Kadoma, Kadoma City, 571-8501 Osaka, Japan

The progress in phase-change optical disk memory, based on amorphous chalcogenide materials is presented. High density recording of around 100 Gb/in<sup>2</sup> was reached. The basic effect of the ultra short laser pulse of femto second response on phase-change film for the future Tb/s data rate recording is discussed.

(Received June 26, 2001; accepted September 11, 2001)

*Keywords:* Phase-change memory, Optical disk, Amorphous chalcogenide

### 1. Introduction

Great advances have been made in memory devices such as magnetic tapes, floppy disks, hard disks (HDDs) and semiconductor memory such as memory cards. The density growth rate of HDDs is around 60% /year but the upper limit of density due to paramagnetic stability is thought to be around 50 Gbits/in<sup>2</sup>. Hard disks have high speed data transfer rates but are generally not removable.

Optical disk memory has its own unique feature of read-only media performance, which is also compatible with the rewritable function and is different from HDD technology. Recordable optical disk market such as CD-R is growing recently and the shipment becomes 3 billions disks/year. Rewritable optical disk technology was first commercialized in the form of the magneto-optical (MO) disk. With the increasing use of multimedia, phase-change rewritable (PCR) optical disks are becoming more popular due to their CD and DVD (digital versatile disk) compatibility.

In 1968, S. R. Ovshinsky discovered a new memory phenomenon in chalcogenide film materials. This order-disorder phase-change memory effect came to be called the "Ovonic memory" [1]. In developing this storage medium, the main issues have been the stability of the film materials, the stability of the reversible cycle characteristics and the recording sensitivity. The author and his colleagues were the first to achieve a breakthrough in these areas, which led to the commercialization of phase-change optical disk products. The first version phase-change optical disk product was shipped in 1990 from Matsushita/Panasonic. The PD (phase-change dual) and CD-RW (rewritable) followed, and now rewritable DVD with 4.7 GB capacity and 3.4 Gbit/in<sup>2</sup> density is being produced.

Blue laser technology, large numerical aperture lens, volumetric recording and multilevel recording technologies are candidates for the future of high-density phase-change nanometer scale mark recording technology.

This paper describes the breakthroughs achieved, the progress on phase-change optical disk memory of the candidate of the high-density recording with a density of around 100 Gbits/in<sup>2</sup> and more, and discusses the basic effect of the ultra short laser pulse of femto second response on phase-change film for the future Tbit/s data rate recording.

### 2. Principle of overwrite phase-change memory

#### 2.1. Phase-change optical memory phenomena

Prior technologies developed for optical disk memory in 1972 utilized thin film materials of either the thermal deformation type or ablation pit mark forming type. These methods, however, require rather high laser power, while is difficult to provide rewritable performance. In the first stage I

proposed sub-oxide thin film phase-change memory by  $\text{TeO}_x$  and developed W/O (write-once) optical disk products for video image file optical disk system in 1982 [2]. Then I have started development of rewritable phase-change optical disk which is compatible with the W/O optical disk having the multifunction optical disk system.

There have been many kinds of rewritable thin film materials in sub-oxide system such as  $\text{GeO}_x$ ,  $\text{SbO}_x$ ,  $\text{MoO}_x$  and so on, and the chalcogenide system. As deposited films are in amorphous state and after heating, they show the darkening effect. Fig. 1 shows the optical transmission change through the heating process of the rewritable chalcogenide film.

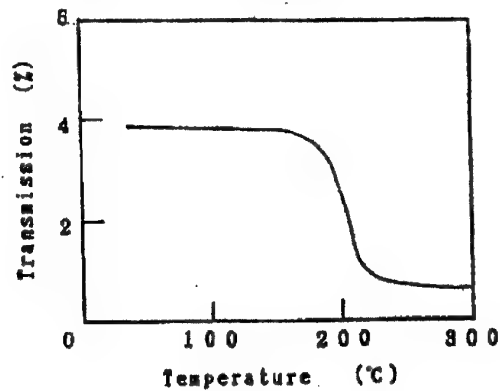


Fig. 1. Transmission ( $d = 633 \text{ nm}$ ) change of  $\text{GeTe-Sb}_2\text{Te}_3\text{-Sb}$  ( $g = 2.0$ ,  $b = 0.5$ ) film when heated in air at a heating rate of  $100^\circ\text{C/min}$ .

## 2.2. Model of the phase-change memory

Fig. 2 shows the model of phase-change memory. The enthalpy of the amorphous state and the crystalline states are different. It is higher in the amorphous phase than in the crystalline phase. When the structure changes from the amorphous state to the crystalline state, the optical absorption edge of the material shifts to shorter wavelength region. Then, the optical constant of complex refractive index  $N = n + ik$  ( $n$  is refractive index and  $k$  is extinction coefficient) changes. And the reflectivity of the film changes, which shows the optical memory effect. So, the information can be detected by the reflectivity change just like the CD disk playback method. When a high power level laser spot irradiates the crystalline film at "a", the temperature of the portion goes over the melting temperature  $T_m$ , the state changes "b" to "c" and "d".

After the laser spot moves away, the temperature goes down rapidly through super cooling state between "c" and "e" to room temperature "f". When the cooling rate is above the critical cooling rate ( $3.4 \text{ K/ns}$ ), the portion of the film at "f" becomes the amorphous phase. When a low power level laser spot irradiates on the amorphous mark portion "f", the temperature goes up to above "e" at the glass temperature  $T_g$ , then the amorphous portion transforms to the crystalline phase and the mark is erased.

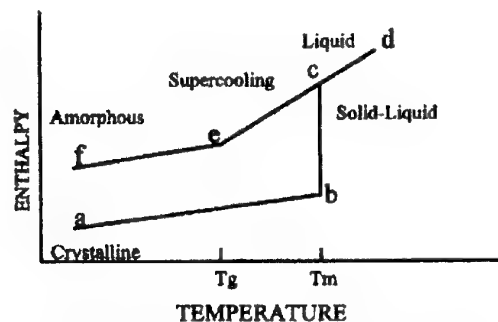


Fig. 2. Model of the phase-change memory.

### 2.3. Phase-change overwriting method

Fig. 3 illustrates the operating principle of phase-change overwriting [3, 4]: a) shows a laser power modulation waveform, b) shows written marks on a track before and after overwriting, c) shows a readout signal after overwriting.

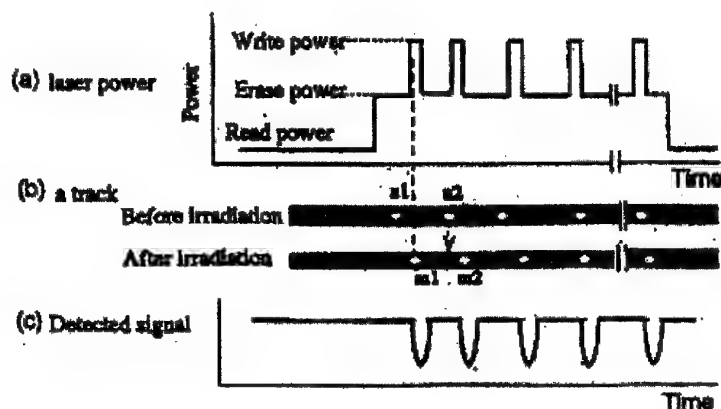


Fig. 3. Direct overwriting method by optical mean only on phase-change optical disk.

The critical cooling rate has been estimated to be 3.4 K/ns from our experiments [5]. The critical cooling rate depends on the atomic elements and their compositions [6].

The portion on the track irradiated by the recording high laser power is melted and after the laser spot moves away from that portion, it is quenched immediately. This quenching process changes the portion to be an amorphous mark portion. If irradiated by the erase laser power, the temperature goes up over the crystallizing temperature and the former recording mark portion changes to the erased crystalline phase. Fig. 4 shows TEM observations of the overwritten marks on the phase-change optical disk. The amorphous mark portion (a) shows halo diffraction pattern and the erased mark portion (b) shows fcc crystalline structure diffraction pattern. The track pitch  $T_p$  is 1.2  $\mu\text{m}$  in the figure. This method achieves one-pass overwriting by using only the laser power modulation scheme. The read out signal is obtained by detecting the reflectivity change between the amorphous mark portion and the crystalline area, which is the same method as the CR-ROM signal detection method.

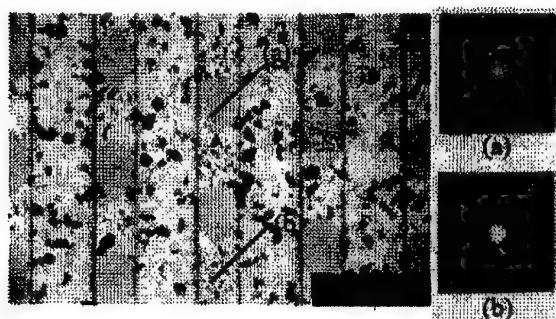


Fig. 4. TEM observation of overwritten marks.  
(a) amorphous mark, (b) erased mark.

## 3. Phase-change materials for optical memory

### 3.1. Bonding features of chalcogenide phase-change materials

Chalcogenide compounds have characteristics of easy transition from crystalline state to amorphous state. The compounds are composed of Te, Se and/or S elements which are the 6<sup>th</sup> group

elements in the Periodic Table. Fig. 5 shows the variations of the bonding structures of chalcogenide compounds.

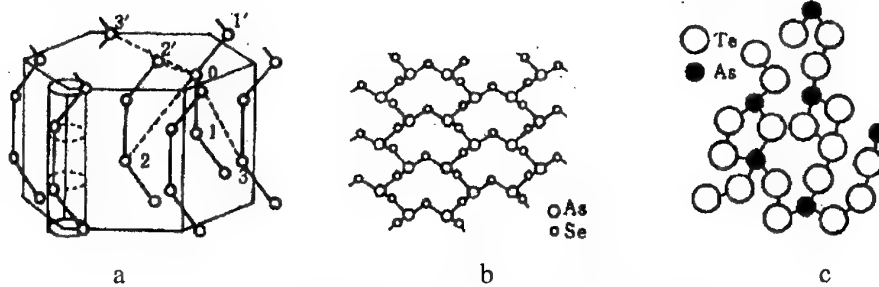


Fig. 5. Bonding structures of chalcogenide materials  
 (a) Hexagonal chain structure of Te and Se [7]  
 (b) Ring structure of  $\text{As}_2\text{Se}_3$  [8]  
 (c) Amorphous structure of  $\text{As}_{25}\text{Te}_{75}$  [9].

Fig. 5(a) shows the chain structure of Te and Se crystalline [7]. Fig. 5(b) shows the network structure of the ring bonding structure produced by adding As component [8]. Fig. 5(c) shows the amorphous network structure of  $\text{As}_{25}\text{Te}_{75}$  compound [9].

The reason why these compounds are easy to transform to the amorphous state is related to the fact that the elements such as Te and Se have chain-like bonding structure.

There are two types of bonding forces, the one is covalent bonding and the other is the rather weak van der Waals force which appears in chain-chain bindings. These two different types of bonding forces are considered to relate to easy amorphizing characteristics of chalcogenide materials.

The crystalline structures of the chalcogenide materials belong to hexagonal or monoclinic systems. The former forms a spiral chain bonding structure and the later often forms a ring bonding structure with eight corners. Additive elements such as Sb and As generate bridges between chains or transform them to network structures.

### 3.2. Phase-change disk materials for optical disk memory

The rewritable optical memory phenomena has been observed in  $\text{Te}_{81}\text{Ge}_{15}\text{Sb}_2\text{S}_2$  composition material [10]. This material was modified from  $\text{Te}_{85}\text{Ge}_{15}$  eutectic composition by adding Sb and S elements. Fig. 6 shows the phase diagram of the Ge-Te system [11]. At the eutectic composition, the melting temperature goes down to 375 °C.

The melting temperature shows a minimum at the eutectic composition, and it is expected that the viscosity increases also. Then, it is easy to freeze the bonding structure in the disordered liquid phase through the cooling process. Though many materials having easy amorphizing characteristics, were proposed in this early stage, these were typical samples for only the observation of phase-change write-erase phenomena.

In the next stage, applicable materials were found which have rather high speed crystallization characteristics. There are three kinds of phase-change material systems such as In-Sb-Te [12], Ge-Te-Sb [13] and Ag-In-Sb-Te [14]. Fig. 7(a), (b), (c) shows the phase-diagrams of In-Sb-Te, Ge-Te-Sb,  $\text{Te}_3\text{-(Sb)}$  and the thin film structure of Ag-In-Sb-Te [14].

They exhibit different crystallization processes.

<In-Sb-Te>

This material shows that the crystalline growth phenomena overcome the nucleation rate phenomena. When erase laser power irradiates the mark written track, whose power just melts the In-Sb-Te film, then recrystallizes the portion from the mark edge and the erase ratio increases. The In-Sb-Te film and the special overwrite laser power level leads to very high erase ratio. In this case, the difference of the write peak power and the erase power is small, both are situated at the melt power level and the power tolerance of writing and erasing becomes small.

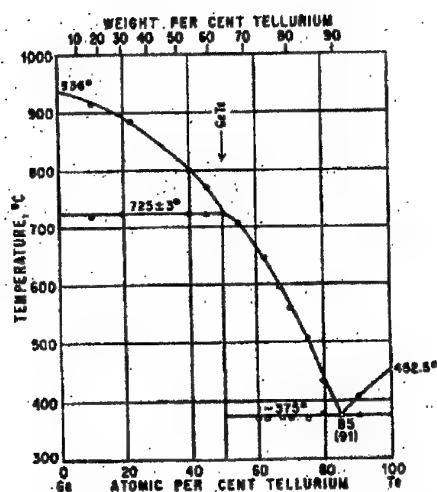


Fig. 6. Phase diagram of Ge-Te system.

### <GeTe-Sb<sub>2</sub>Te<sub>3</sub>-Sb>

The phase-change processes of the Ge-Sb-Te amorphous material were examined by DSC (differential scanning calorimetry) measurement. Fig. 8 shows that there are two exothermal peaks and one endothermal peak.

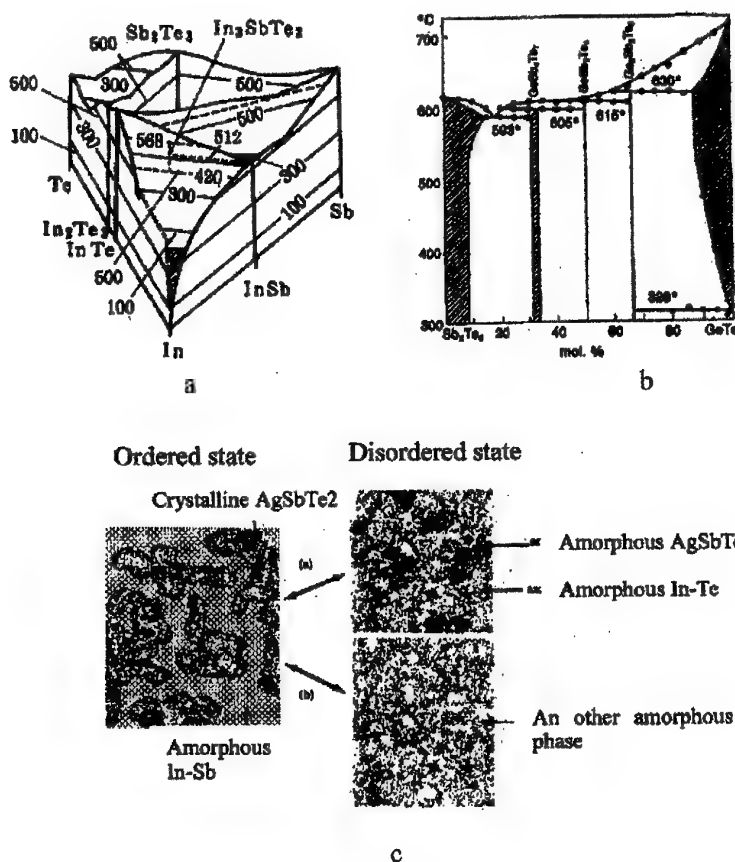


Fig. 7. Phase-change active layer materials for optical disks.

(a) In-Sb-Te ternary alloy

(b) GeTe-Sb<sub>2</sub>Te<sub>3</sub>-(Sb) system

(c) Phase-change model for Ag-In-Sb-Te system.



The first exothermal peak corresponds to the crystallization phase-change and the second to the fcc to hexagonal crystalline structure change, and the third endothermal peak corresponds to melt phase transition [15]. The latent heat for the transformation crystalline to liquid (16.3 kcal/kg) and amorphous to liquid (8.5 kcal/kg) were obtained experimentally.

The nucleation rate overcome the crystalline growth. The erased (crystallized) state of the GeTe-Sb<sub>2</sub>Te<sub>3</sub>-Sb film shows a lot crystalline grains. It shows two steps of the erase process: in the first step, a high number of the crystalline nuclei appears and in the second step the crystalline grain growth occurs and the amorphous mark can be erased. The erase process is in the solid state and the power tolerance becomes rather wide and applicable but the erase ratio is lower than In-Sb-Te films.

Phase-change materials for overwriting by one laser spot need to have high-speed crystallizing characteristics. High-speed crystallizing materials such as the In-Se system were discovered [3].

We found a GeTe-Sb<sub>2</sub>Te<sub>3</sub>-<Sb> system, one of the group of Ge-Te-Sb compositions, and the parameters  $g = \text{GeTe} / \text{Sb}_2\text{Te}_3$ ,  $b = \text{<Sb>} / \text{Sb}_2\text{Te}_3$ , which control the crystallizing speed around 100 ns to 30 ns and the crystalline grain size smaller, and the residual Sb element in the system is <Sb> [16], [17], [18].

Recently at ODS2001, there were proposed for high density and high data rate recording, phase-change optical disks, with small amorphous mark forming, several crystallizing growth dominant compositions at the eutectic composition system such as Sb<sub>69</sub>Te<sub>31</sub> were proposed [CAPut!], [20]. Last years, the density of the phase-change optical disk was increased, when the mark became small (<200 nm), and in the growth dominant case the mark can crystallize rapidly. The eutectic composition of Sb<sub>69</sub>Te<sub>31</sub> is the point ( $\lambda$ ) on the line of Sb<sub>2</sub>Te<sub>3</sub> to Sb of Fig. 9, the composition point is that of 0.18 (Sb<sub>2</sub>Te<sub>3</sub>) and 0.82 Sb. The reason why this eutectic composition shows the rapid crystallization characteristics is now under discussions.

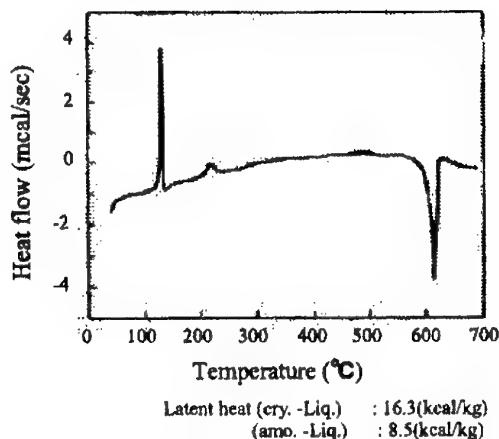


Fig. 8. DSC (differential scanning calorimeter) analysis of Ge-Sb-Te film at a heating rate of 10 °C/min.

#### <Ag-In-Sb-Te>

The Ag-In-Sb-Te system has two kinds of typical composition area, one is (AgSbTe<sub>2</sub>+In-Sb) system and the other is (AgInTe<sub>2</sub>+Sb) system. The phase-change model of this system is that the former composition shows that a part of the compound such as AgSbTe<sub>2</sub> crystallizes in amorphous In-Sb. This composition has large erase ratio characteristics. The origin of the erase ratio is discussed as it has low thermal conductivity components in thin film structure which is composed of the mixture of AgSbTe<sub>2</sub> phase-change component and amorphous In-Sb. The overwrite cycle performance of Ag-In-Sb-Te system is reported as around 10,000 or more and the limitation of this overwrite cycle is discussed now.

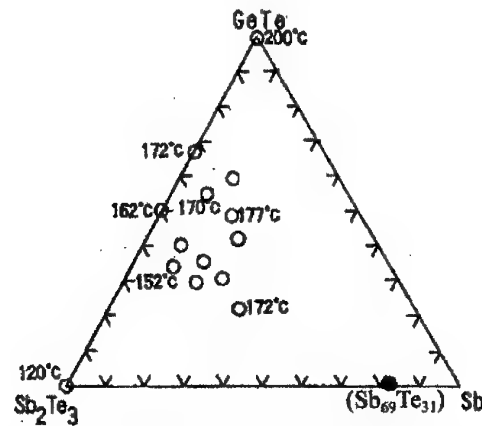


Fig. 9 The crystallizing temperature of the system. This material system shows nucleation dominant crystallizing characteristics.

#### 4. Key technologies of the phase - change disk media

In the early phases of its development, the most important subject of phase-change optical disk was cycle degradation. Fig. 10 shows a cross-sectional TEM (transmission electron microscopy) image of the basic 4-layer structure of a phase-change optical disk. The layers comprise a bottom dielectric layer (155 nm), an active layer (24 nm), an upper dielectric layer (45 nm) and a reflection layer (100 nm).

Fig. 11 shows a high resolution TEM image of ZnS and the new ZnS-SiO<sub>2</sub> mixture dielectric protection films. The grain size of ZnS-SiO<sub>3</sub> film is very small, at around 2 nm [21]. The new ZnS-SiO<sub>3</sub> dielectric layer is thermally stable and does not show grain growth even after annealing at 700° C, 5 min. Grain growth in the ZnS layer was one reason the phase-change optical disks degraded after many rewrites. The newly developed materials of GeTe-Sb<sub>2</sub>Te<sub>3</sub>-Sb active layer and ZnS-SiO<sub>2</sub> protective layer have resolved one of the cycle issue of variations of signal amplitude and noise level. The other cycle degradation model is that of the sub-nanometer level space deformation of the disk layers, which works as the motive force of the sub-nanometer displacement of the active layer components. The deformation occurs by thermal expansion of the layers along the thermal diffusion process. The deformation is generally asymmetrical along the laser scanning direction, the forward edge and the backward edge.

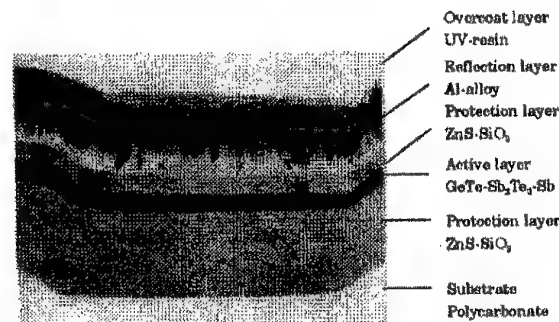


Fig. 10. Cross-sectional TEM observation of the basic 4-layer phase-change optical disk.

The space deformation becomes the motive force of the sub-nanometer displacement of the liquid phase active layer components. The thermal expansion coefficient of SiO<sub>2</sub> is  $5.5 \times 10^{-7}$ , and of ZnS-SiO<sub>2</sub> is  $6.1 \times 10^{-6}$ . When forming an additional SiO<sub>2</sub> layer, the thermal deformation of the space between the bottom upper dielectric layer is reduced.

Subsequently, in 1989, dynamic overwrite cycle characteristics over more than  $2 \times 10^6$  cycles were achieved by the development of new layer materials and a new disk structure [22, 23]. The first phase-change optical disk product was shipped in 1990 by Matsushita. In 1995, a new concept, the dual function PD disk, arrived on the multimedia scene which system can operate both a CD-ROM and a phase-change optical disk PD [24] and now rewritable CD-RW is following.

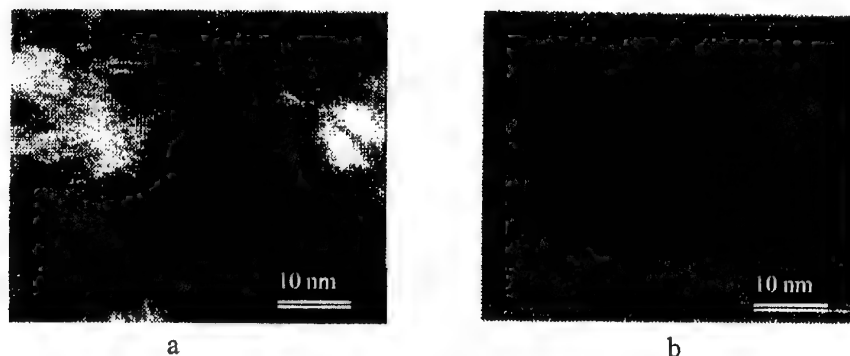


Fig. 11. High resolution TEM (Transition electron microscope) observation of ZnS (a) and new ZnS-SiO<sub>2</sub> mixture dielectric films (b).

The first version phase-change optical disk product with 4-layer structure showed more than 100,000 overwrite cycle performance. The new 5-layer structure, which has the additional SiO<sub>2</sub> layer shows more than 1,000,000 overwrite cycles. Fig. 12 shows more than 2-million cycle characteristics of the phase-change optical disk with the additional SiO<sub>2</sub> layer.

The sensitivity of the phase-change optical disk was rather low at the first version disk of the laser power of 21mW on the disk. For amorphous mark forming, it needs melting process and the melting temperature of GeTe-Sb<sub>2</sub>Te<sub>3</sub>-Sb active layer materials were around 600 °C, a rather high temperature. But the recording layer thickness was around 20 nm and the heat capacity of the layer was very small. Table 1 shows the optical, thermal and mechanical properties of the phase-change optical disk layers. The heat capacity of the thin active layer (24 nm) of the 1μm<sup>2</sup> mark is roughly calculated as the value of  $2.5 \times 10^{-5}$  nJ/μm<sup>2</sup> and the laser spot energy supply is much larger than this value even at 10 mW laser power level irradiation.

The sensitivity of the phase-change optical disk is controlled by the disk layer structure. The reflection metal layer of Al works as the quenching layer of the recording phase-change layer for amorphous mark formation and the upper protection dielectric layer thickness control the cooling rate and also the disk sensitivity.

Table 1. Optical, mechanical and thermal properties of materials.

Material	Refractive index $\lambda=830\text{nm}$	Density (kg/m <sup>3</sup> )	Young's modulus (N/m <sup>2</sup> )	Poisson's ratio	Specific heat (J/(kg · K))	Thermal conductivity W/(m·K)	Coefficient of linear expansion
GeTe-Sb <sub>2</sub> Te <sub>3</sub> -Sb (Amorphous)	4.6+1.0i	-----	-----	-----	-----	-----	-----
GeTe-Sb <sub>2</sub> Te <sub>3</sub> -Sb (Crystal)	5.7+3.0i	6150	$5.49 \times 10^{10}$	0.33	$0.209 \times 10^3$	0.581	$1.1 \times 10^{-5}$
2 : 1 : 0.5 (mol ratio)							
ZnS-SiO <sub>2</sub>	2.0	3650	$7.81 \times 10^{10}$	0.2	$0.263 \times 10^3$	0.657	$7.4 \times 10^{-6}$
4 : 1 (mol ratio)							
SiO <sub>2</sub>	1.46	2202	$7.81 \times 10^{10}$	0.2	$0.753 \times 10^3$	1.313	$5.5 \times 10^{-7}$
Al Alloy	2.2+7.5i	2750	$7.03 \times 10^{10}$	0.345	$0.892 \times 10^3$	$0.215 \times 10^3$	$2.2 \times 10^{-5}$
Polycarbonate	1.58	1200	$2.26 \times 10^9$	0.3	$0.126 \times 10^2$	0.223	$7.0 \times 10^{-5}$

Latent Heat (Crystal  $\leftrightarrow$  Liquid)  $0.682 \times 10^5$  (J/kg), (Amorphous  $\leftrightarrow$  Liquid)  $0.356 \times 10^5$  (J/kg)

For the disk rotation linear velocity of 10 m/s, the cooling rate becomes more than the critical cooling rate of amorphous formation of 3.4 K/ns. We obtained that the overwrite cycle characteristics and the disk sensitivity are not the trade-off relation. Then we developed the high sensitivity PD

phase-change optical disk which has 4-layer structure and more than 500,000 overwrite capability by layer thickness improvement.

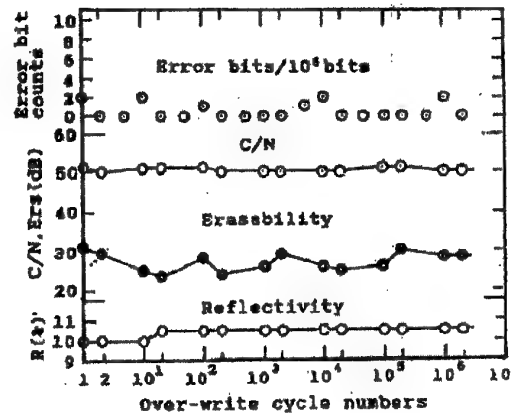


Fig. 12. Two million overwrite cycle test results of phase-change optical disk with additional  $\text{SiO}_2$  protection layer.

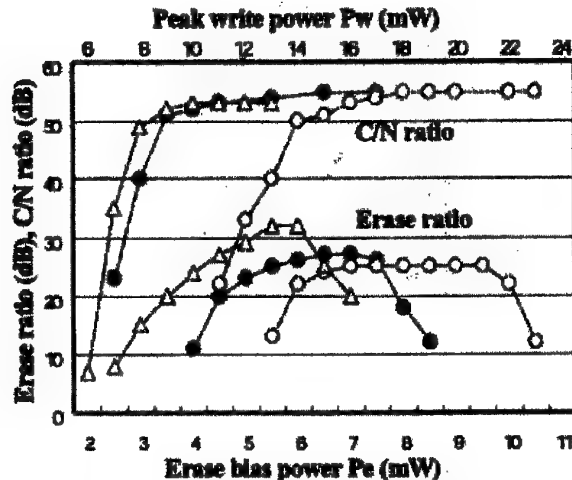


Fig. 13. The sensitivity of phase-change optical disk products ○: First version phase-change optical disk (1990), ( $\lambda=830\text{nm}$ ,  $\text{NA}=0.5$ ,  $V=12\text{m/s}$ ); ●: PD disk (1995), ( $\lambda=780\text{nm}$ ,  $\text{NA}=0.5$ ,  $V=12\text{m/s}$ ); △: Rewritable DVD-RAM (4.7GB), (2000), ( $\lambda=650\text{nm}$ ,  $\text{NA}=0.6$ ,  $V=6\text{m/s}$ ).

Phase-change optical disk sensitivity was improved by the use of a basic 4-layer structure. Fig. 13 shows the overwrite sensitivity characteristics of three phase-change optical disk products. The first version phase-change optical disk needs around 21 mW laser power on the disk (1990).

At that time the sensitivity of MO disk was around 10 mW, but the laser source power was almost the same as for phase-change optical disk drive. Optical transmission efficiency of MO drive was lower than that of the phase-change optical disk drive applying BS (beam splitter) or PBS (polarized beam splitter) in the optical pass.

The sensitivity of PD disk was subsequently improved by decreasing the heat capacitance and cooling rate by the disk layer structure (1995). Then the sensitivity became almost the same for MO and phase-change optical disk.

## 5. Technology comparisons of CD-ROM, phase-change and MO (magneto - optical) disk

Only the optical disk technology has the ROM function other than the HDD technology, which is suitable for multimedia applications.

It has long been a topic of discussion in optical disk memory research and development worlds as to which method best meets multimedia optical disk applications, the magneto-optical (MO) technology or the phase-change optical disk technology.

Table 2 shows comparisons of three technologies: the first is ROM (Read only CD disk), the second is phase-change optical disk and the third is MFM (Magnetic field modulation) recording magneto-optical (MO) disk.

The main advantage of phase-change optical disk technology is that signal reading process is the same as ROM disk. After overcoming the issues such as cycle performance and sensitivity of the phase-change optical disk technology, we proposed a new concept of "PD" system which can play both CD-ROM and rewritable phase-change optical disks in one drive, the same as rewritable CD (CD-RW). Today, rewritable DVD system can operate CD-ROM, DVD-ROM and also rewritable DVD.

Table 2. Technology comparison of CD, phase-change and MO disks.

Term/ Media	CD Disk	Phase-change Disk	Magneto optical Disk (MFM)
Read/Write Head	Optical Head	Optical Head	Optical Head & Magnetic Head
Write Mechanism	Emboss-Pit	Amorphous Mark	Magnetization Domain
Read Mechanism	Diffraction	Optical Constant Change	Polarization Change
Signal Detection	Reflectivity Change	Reflectivity Change	Kerr Rotation Change
Readout Amplitude Signal	1.0	1/4	1/80
	(normalized reflectivity)		
Disk Track Structure	$\lambda/4$ Emboss-Pit	$\lambda/8$ Pre-Groove $\lambda/8$ Emboss-Pit	$\lambda/8$ Pre-Groove $\lambda/8$ Emboss-Pit
Optical Path	P.B.S $\lambda/4$ -Plate	P.B.S $\lambda/4$ -Plate	B.S P.B.S Analyzer
Disk Materials	Polycarbonate	Polycarbonate	Polycarbonate
Substrate	Al-alloy	Al-alloy	Al-alloy
Reflection layer	-	Ge-Te-Sb	Tb-Fe-Co
Active layer	-	ZnS-SiO <sub>2</sub>	SiN
Dielectric layer			
Function	Read-Only	Overwrite	Overwrite

## 6. Thin substrate technology of phase-change optical disk promotes DVD

The general method of high density recording for optical disks is to introduce large numerical aperture (NA) lens to form the smaller laser spot. But the large numerical aperture lens is strongly affected by the disk substrate tilt angle for forming the small spot. We first reported that a thin disk substrate is effective for resolving the disk tilt problem during high density recording. We developed a high density 90 mm diameter phase-change optical disk for an ISO standardization proposal in 1995 [25]. It featured top-level technologies such as a red light laser diode, a large numerical aperture NA (0.6) lens and thin disk substrate (0.6 mm) at that time [26, 27]. Fig. 14 shows the crosstalk characteristics of two types of disks, disk substrate thickness  $t=1.2$  mm and  $t=0.6$  mm when using large numerical aperture lens (NA=0.6). The thin substrate disk of 0.6mm thickness shows lower crosstalk characteristics than the thick substrate disk under conditions of large tilt angle.

The conventional optical disk CD has the capacity of 650 MB and for the next generation optical disk, the capacity requirement was 4.7 GB for recording 2 hour high quality cinema title. Then, next generation DVD (Digital versatile disk) specifications demand a thin disk substrate ( $t=0.6$  mm), a bonded disk structure, a large numerical aperture lens (NA=0.6) and red laser diode wavelength of 650 nm. A simple overwrite disk function and ROM disk compatibility of the phase-

change optical disk is also featured in the rewritable DVD specifications of DVD-RAMs and DVD-RWs.

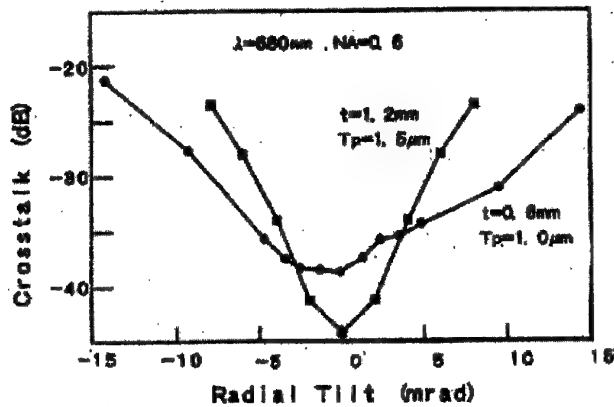


Fig. 14. Comparison of the tilt angle dependency of crosstalk for substrate thickness of  $t=1.2$  mm and thin substrate of  $t=0.6$  mm. Lens numerical aperture :  $NA=0.6$ .

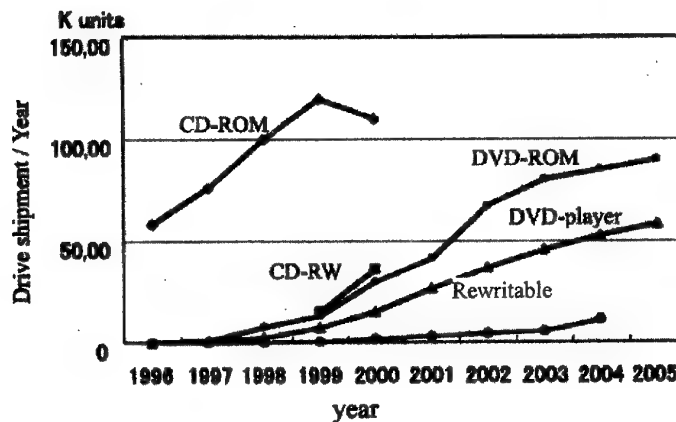


Fig. 15. Optical disk drive market growth.

The disk format life is around 15 years and these years, the new DVD-ROM replaces the conventional CD-ROM market in 2000. Fig. 15 shows the market change of CD-ROM and DVD-ROM drives. Rewritable phase-change CD-RW drive shipment increases these years.

## 7. High density recording technologies of phase-change optical disks

### 7.1. Short wavelength blue laser high density recording

The phase-change recording layer also has the advantages of high signal output and response to a wide spectrum of wavelength. Table 3 shows the wavelength dependency of the complex refractive index of the phase-change material film in the amorphous and crystalline state. Though both the refractive index and the extinction coefficient are decreasing at short wavelength, the difference of the value between amorphous state and crystalline state keeps large. Then the signal output by the reflectivity change is large.

Fig. 16 shows the blue laser recording marks, the track pitch  $T_p$  is  $0.6 \mu\text{m}$ , land and groove recording marks. The recording density was estimated to be  $9 \text{ Gbit/in}^2$ , the laser wavelength was  $425\text{nm}$ , the lens numerical aperture was  $0.6$ .



Table 3. Wavelength dependency of complex refractive index ( $N=n+ix_k$ ) of phase-change material GeTe-Sb<sub>2</sub>Te<sub>3</sub>-SB film.

Wavelength	Refractive index	
	Amorphous	Crystal
830 nm	4.61+1.05i	5.67+3.01i
780 nm	4.47+1.04i	5.07+3.42i
650 nm	4.21+1.89i	4.56+4.23i
430 nm	3.08+2.51i	2.21+3.77i
405 nm	2.90+2.51i	2.03+3.58i

Three main approaches have been proposed to increase the recording density of phase-change optical disks. The first is to combine a short wavelength laser with a large NA lens, recently DVR technology is proposed, which is applying larger numerical aperture lens of NA=0.85 and the new disk structure of thin cover-layer, the thickness is 0.1 mm for 0.6 mm disk substrate. This new DVR-blue system shows the recording capacity of 22.4 GB/ side, the disk diameter is 120mm, the laser diode wavelength is 405 nm [28]. The other large numerical aperture recording is SIL (solid immersion lens) recording, the lens numerical aperture is NA=1.5, the recording density is increasing to 45G bit/in<sup>2</sup> by blue laser diode on the phase-change optical disk [29].



Fig. 16. TEM photograph of blue (SHG) laser recording marks. Wavelength = 425 nm, NA = 0.6, MI = 300 nm, Signal:  $f=6.6$  MHz,  $v=8.2$  m/s.

## 7.2. Dual-layer recording technology

The second approach is dual layer recording, creating volumetric rather than two-dimensional surface recording. The dual layer optical disk DVD is read out from one side, which has been commercialized for 8.5 GB dual layer DVD cinema titles. The phase-change rewritable dual layer optical disk of 8.5 GB technology was announced, which achieves nearly double the previous density [30]. The phase-change optical disk system is composed with laser optical head only other than MO MFM (magnetic field modulation) system, which has two heads, optical head and magnetic head. The phase-change optical disk, optical head only system can record volumetric data by focus position choice in vertical direction and the MO magnetic head system can record data on only media surface. The former achieves increased recording capability by techniques such as multi-layer structures. The dual-layer phase-change optical disk shows a density of 6.4 Gbit/in<sup>2</sup> using a conventional optical system (laser wavelength of  $\lambda=650$  nm, lens numerical aperture NA=0.6) and disk structure. This technology has the advantage of the feature of enhanced density and compatibility with DVD head.

Fig. 17 shows a cross sectional view of a blue laser dual-layer rewritable phase-change optical disk. The first medium has a high transmission characteristic of around 45% in the crystalline state with a recording reflectivity difference of 7%. The second medium has a high reflectivity characteristic. As a result, the signal output of the second medium becomes  $24 \times 0.5 \times 0.5 = 6\%$  by the absorption of the first medium, which closely matches the value of the first medium [31]. The capacity is increasing to 27 GB.

DVD technology and DVR technology, both can be used to realize dual-layer phase-change optical disk and the combination increases the density more.

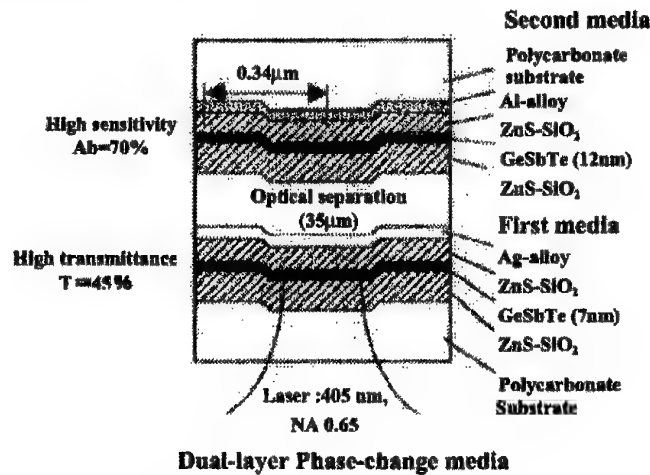


Fig. 17. Cross-sectional view of the blue laser dual-layer rewritable phase-change optical disk.

### 7.3. New proposal of MRWM (mark radial width modulation) concept of multi-level recording

The third is the possibility of multi-level recording on phase-change optical disks. Multi-level recording was first announced in a phase-change electrical switching memory (Ovonic memory) device in 1997, which showed 16 switching levels [32]. Multi-level recording, for example 4-ary recording gives  $\log_2 4 = 2$  bits per mark, doubling the recording density of conventional binary recording.

The phase-change optical recording layer has a large reflection difference characteristic between the crystalline state (around  $R_{\text{cry}} = 30\%$ ) and the amorphous state (around  $R = 7\%$ ) of the same order as in CD-ROM pit signal output. M. P. O'Neil showed 8-level phase-change recording technology at ODS2000 and announced 2 GB capacity of CD-RW capacity capability [32]. Multi level recording on phase-change media, 4 to 8 level optical recording technologies are announced and the recording density increase is expected around 1.5 to 3 times.

We propose to subdivide this large signal output into multi-level (ML) signals on a phase-change optical disk using the MRWM (mark radial width modulation) method [33].

Binary recording is 2-level: an unchanged state and a changed state, which translate into 0 and 1. M-ary recording is M-level, giving an unchanged state and multi-amplitude states such as 0, 1, 2, ..., (M-1). With level 0 mark unchanged, the mark radial width increases from level 1 to level 3 to deliver 4-level recording.

Fig. 18 shows an outline diagram of MRWM recording marks on a phase-change optical disk. The mark radial widths are 1/3, 2/3 and 1 for level 1, level 2 and level 3 respectively. The assigned laser power is low for level 1 marks but the assigned laser pulse width is long compared to Level 3 marks.

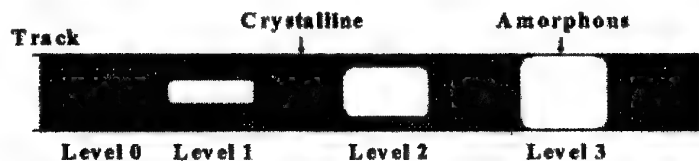


Fig. 18. Outline diagram of MRWM (Mark Radial Width Modulation) 4-level recording on phase-change optical disk.

ML recording requires a high C/N ratio for accurate detection of the M-ary signal. The phase-change optical recording method realizes a greater C/N ratio than the MO disk. Four-level recording gives (0, 1, 2, 3) and gives 4 different states.

Y. Honguh et al. [35] proposed the run-length-limited (RLL) code for multi-level recording introducing the spacing in addition to the minimum and maximum run-length constraints. It showed a magnification factor of 1.76 for (1, 7) code when applied to multi-level recording [34].

The idea of MRWM recording is to assign a specific laser pulse width and power level to a specific mark level. For example, for level 1 mark, since at low laser power, using a long pulse width, the mark length becomes long and becomes the same mark length as Level 3, and increasing the C/N ratio. The minimum mark length of these three levels of marks are designed by the optical head resolution.

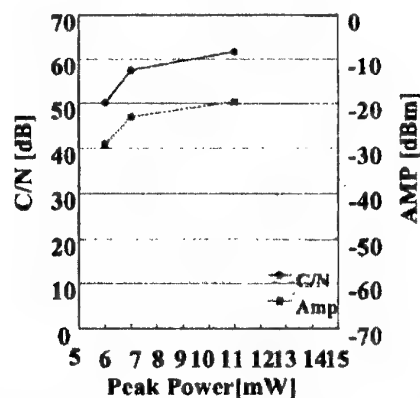


Fig. 19. Pulse width and power assigned MRWM recording characteristics of phase-change optical disk.

Level 1 (113.3 ns, 6 mW)  
 Level 2 (83.1 ns, 7 mW)  
 Level 3 (45.3 ns, 11 mW)  
 Signal:  $f = 6.6$  MHz,  $v = 8.2$  m/s.

The assigned laser pulse widths are 114 ns, 84 ns and 46 ns, and the assigned laser power is 6 mW for Level 1, 7 mW for Level 2 and 11 mW for Level 3. Fig. 19 shows C/N and amplitude of MRWM recording method with various pulse widths and power conditions. The C/N value is 50.1 dB, 57.5 dB and 61.5 dB for the Level 1, Level 2 and Level 3 marks, respectively. Fig. 20 shows the TEM observation of MRWM recording marks on a phase-change optical disk. The mark radial widths are 200 nm, 400 nm and 600 nm for level 1, level 2 and level 3, respectively.

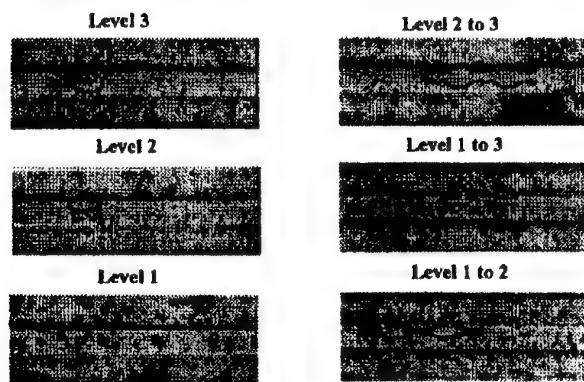


Fig. 20. TEM observation of MRWM recording marks (Track width: 600 nm) Each marks, Level 1, 2, 3 and the set recording marks (1 to 2), (1 to 3), (2 to 3).

## 8. Combination technology of high density recording

There are two strategies of high density recording of phase-change optical disk, the first is the DVD compatible method which has the optical head,  $NA = 0.6$  and 0.6 mm disk substrate. The second method uses a large numerical aperture head of  $NA = 0.85$  combined with a new disk structure of 0.1 mm transparent overcoat layer.

The recording density increases to double that of a conventional DVD by the ratio of the large numerical aperture lens  $(0.85/0.6)^2 = 2$ . Short wavelength increases the density by the ratio of the wavelength  $(650/405)^2 = 2.6$ .

Rewritable DVD of the 4.7 GB version holds the density of 3.4 Gbit/in<sup>2</sup>. A dual-layer phase-change rewritable disk whose capacity is 8.5 GB has an effective density on one side of 6.4 Gbit/in<sup>2</sup>.

By introducing the magnification factor of the multi-level recording of  $M = 4$  ( $\times 1.76$ ), the recording density will further increase. Using the combination with the dual layer technology, the density becomes 30 Gbit/in<sup>2</sup> at 405 nm with an  $NA = 0.6$  lens. This technology also is expected to have the blue laser DVD head compatibility.

Another density increasing strategy is to apply a large numerical aperture lens of  $NA = 0.85$  and a 0.1 mm thin overcoat layer disks for 0.6 mm substrate. The recording density will increase to double and the recording density is predicted to be 60 Gbit/in<sup>2</sup> and the capacity will rise to 83 GB/120 mm/side. By magnifying the multi-level recording from  $M = 4$  to  $M = 8$ , the density is expected to increase to more than 100 Gbit/in<sup>2</sup>. Fig. 21 shows the area recording density growth of phase-change optical disks.

J. Tominaga has announced phase-change Super-RENS (super-resolution near-field structure) recording technology, which achieves 13 Gbit/in<sup>2</sup> using the conventional optical head system (laser wavelength = 640 nm, lens numerical aperture  $NA = 0.6$  [35]. The disk structure is composed with additional super-RENS mask layer of AgOx on the bottom dielectric layer. The layer works as the near-field light emission. The super-RENS effect can be combined with the above technologies, resulting in the potential for increasing the density by around 4 times to achieve 240 Gbit/in<sup>2</sup> in the future.

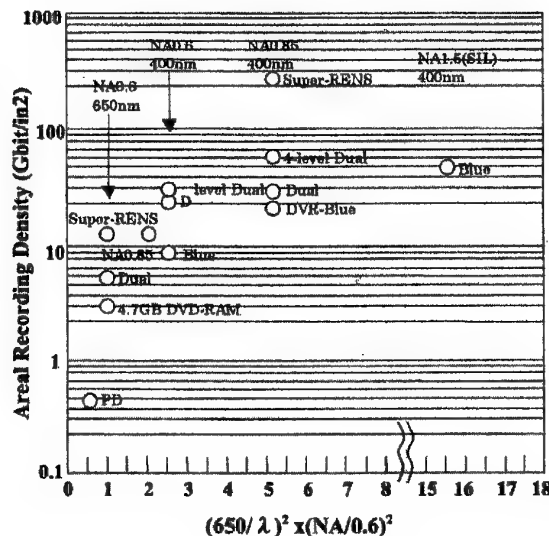


Fig. 21. Areal recording density growth of phase-change optical disk. PD ( $\lambda = 780$  nm,  $NA = 0.5$ ), 4.7 GB DVD-RAM ( $\lambda = 650$  nm,  $NA = 0.6$ ), 8.5 GB Dual-layer disk, Blue wavelength 27 GB Dual-layer disk, DVR, SIL ( $NA = 1.5$ ), Multi-level recording, Super-RENS (640 nm,  $NA = 0.6$ ).

## 9. Ultra short pulse femto second laser response on phase-change media

Recently, short pulse width laser such as femto to pico second pulse laser have become popular. In high-speed fiber communication, the high-resolution laser processing field and ultra-high-speed time-resolution measurement technology, these femto lasers have achieved ultra-high-speed chemical reactions and bio-molecular dynamics. A 120 fs laser pulse of laser wavelength 800 nm in silicate glass demonstrated a photo-induced refractive index change, which is considered by multi-photon absorption process [36]. Laser processing on the metal or ceramics is done almost in laser ablation process by femto second laser irradiation.

Both are important characteristics, the recording density and the recording data rate. The recording speed on phase-change optical disk is advancing recently from 10 Mbt/s to 100 Mbit/s [36]. It is unknown that the speed limitation of amorphous mark formation and this paper tries to obtain the femto second response of the phase-change films.

Conventional optical disk recording is performed by laser spot irradiation on the rotational disk. In this case, the laser irradiation time on the portion of the disk is around 10 ns to 100 ns, a rather long time compared with the femto second laser spot irradiation. The recording process includes the heat diffusion in the layers. The temperature increasing area is wider than the laserspot size, which means the mark size and the position of the mark are determined by not only the beam factor ( $\lambda/NA$ ) but also the disk thermal characteristics and the pulse duration. Heat diffusion of the conventional laser recording limits the performance of future high-density and high-data rate optical disk.

This time I first examined the response of the femto second laser pulse on the phase-change thin media to obtain the features of the ultra short pulse laser recording.

The experimental condition of the femto laser irradiations were the wavelength  $\lambda = 800$  nm, the pulse width = 120 fs and the lens numerical aperture of  $NA = 0.95$ . The sample disk structure is the polycarbonate substrate/ZnS-SiO<sub>2</sub> 155 nm/ GeSbTe 24 nm/ ZnS-SiO<sub>2</sub> 45 nm/ Air, without reflection layer. The femto laser incident side is the air side. Fig. 22 shows the TEM (transmission electron microscope) observation of the mark formed by the femto second laser exposure (120 fs). The diffraction pattern shows only halo pattern of amorphous phase and this experiment shows that order to disorder phase-change occurs by one-shot 120 femto second laser pulse. The mark edge is clear without heat diffusion influence.

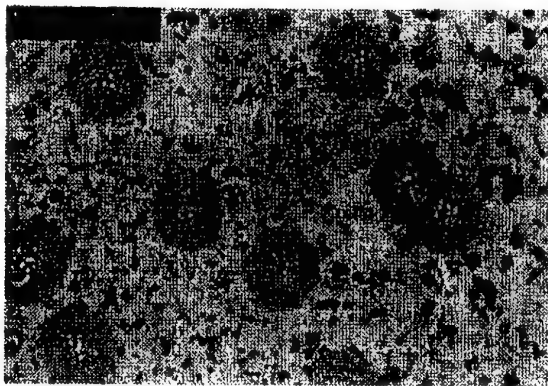


Fig. 22. TEM observation of amorphous marks formed by femtosecond laser pulse on the phase-change optical disk media.

This experiment shows the amorphous mark recording data rate of phase-change optical disk is expected to be more than T bit/s.

## 10. Conclusion

Key technologies obtained by materials research and disk structure development have achieved multimedia phase-change rewritable 4.7 GB DVD products. The application of blue laser

light ( $\lambda = 405$  nm), large numerical aperture lens ( $NA = 0.85$ ), volumetric (dual layer) recording and multilevel recording shows the potential recording density of the phase-change optical disk to exceed 60-100 Gbits/in<sup>2</sup>. Ultra short laser pulse recording experiment shows that even femtosecond pulse (120 fs) forms amorphous mark on the phase-change material film and gives more than 1 Tbit/s data rate capability. The mark shows one of the method to resolve the heat diffusion limitation of the conventional laser recording.

## Reference

- [1] S. R. Ovshinsky, Phys. Rev. Lett., **21**, 1450 (1968).
- [2] T. Yoshida, T. Ohta, S. Ohara, Proc. SPIE, **329**, 40 (1982).
- [3] M. Terao, N. Nishida, Y. Miyauchi, S. Horigome, T. Kaku, N. Ohta, Proc. SPIE, **659**, 105 (1986).
- [4] T. Ohta, T. Nakamura, N. Akahira, T. Yamasita, Japanese patent No. 1668522.
- [5] T. Ohta, K. Inoue, S. Furukawa, T. Akiyama, M. Uchida, S. Nakamura, Electro. & Comun. Technical Research Meeting Rep. CPM 89-84, 41 (1989).
- [6] M. Okuda, H. Naito, T. Matsushita, Proc. Int. Symp. on optical memory, 73 (1991).
- [7] R. Grigorovici, Amorphous and liquid semiconductors, ed. by J. Tauc, Plenum Press, London, chapter 2 (1974).
- [8] J. Cornet, D. Rossier, J. Non-Cryst. Solids, **12**, 95 (1973).
- [9] R. Grigorovici, Amorphous and liquid semiconductors, ed. by J. Tauc, Plenum Press, London, 46 (1974).
- [10] J. Feinleib, J. de Neufville, S. C. Moss, S. R. Ovshinsky, Appl. Lett., **18**, 254 (1971).
- [11] W. Klemm, G. Frischmuth, Z. anorg. Chem. **218**, 249 (1934).
- [12] Y. Maeda, H. Andoh, I. Ikuta, M. Nagai, Y. Katoh, H. Minemura, N. Tsuboi, Y. Satoh, Appl. Phy. Lett., **54**, 893 (1989).
- [14] H. Iwasaki, Proc. SPIE, **3109**, 12 (1997).
- [15] N. Yamada, E. Ohno, K. Nishiuchi, N. Akahira, J. Appl. Phys., **69**, 5, 2849 (1991).
- [16] N. Yamada, E. Ohno, N. Akahira, K. Nishiuchi, K. Nagata, m. Takao, Proc. Int. Symp. on optical memory, 61 (1987).
- [17] M. Suzuki, I. Doi, K. Nishimura, I. Morimoto, K. Mori, Proc. Optical memory Symposium '88, 41 (1988).
- [18] T. Ohta, M. Uchida, K. Yoshioka, K. Inoue, T. Akiyama, S. Furukawa, K. Kotera, S. Nakamura, Proc. SPIE, **1078**, 27 (1989).
- [19] G. F. Zhou, H. J. Borg, J. C. N. Rijpers, M. H. R. Lankhorst, J. J. L. Horikx, Proc. SPIE, **4090**, 108 (2000).
- [20] M. Horie, T. Ohno, N. Nobukuni, K. Kioyo, T. Hashizume, M. Mizuno, Tech. Digest, ODS2001, MC1, 37 (2001).
- [21] T. Ohta, K. Inoue, S. Furukawa, K. Yoshioka, M. Uchida, S. Nakamura, Electro. & Comun. Technical Research Meeting Rep. CPM90-35, 43 (1990).
- [22] T. Ohta, M. Uchida, K. Yoshioka, K. Inoue, T. Akiyama, S. Furukawa, K. Kotera, S. Nakamura, Proc. SPIE, **1078**, 27 (1989).
- [23] T. Ohta, K. Inoue, M. Uchida, K. Yoshioka, T. Akiyama, S. Furukawa, K. Nagata, S. Nakamura, Jpn. J. Appl., Phys. **28**, 123 (1989).
- [24] T. Ohta, K. Yoshioka, H. Isomura, T. Akiyama, R. Imanaka, Proc. SPIE, **2514**, 302 (1995).
- [25] 1.3 GB 90mm Phase-change optical disk, ISO/IEC JTC, Project 1.23.14760 (19985).
- [26] T. Ohta, K. Inoue, T. Ishida, Y. Gotoh, I. Satoh, Jpn. J. Appl. Phys., **32**, 5214 (1993).
- [27] T. Sugaya, T. Taguchi, K. Shimura, K. Taiara, Y. Honguh, H. Satoh, Jpn. J. Appl. Phys., **32**, 5402 (1993).
- [28] M. J. Dekker, N. Pfeffer, M. Kuijper, I. P. D. Ubbens, W. M. J. Coene, E. R. Meinders, H. J. Borg, Proc. SPIE **4090**, 28 (2000).
- [29] K. Kishima, I. Ichimura, K. Yamamoto, K. Osato, Y. Kuroda, A. Iida, K. Saito, Proc. SPIE, **4090**, 50 (2000).



- [30] K. Nagata, K. Nishiuchi, S. Furukawa, N. Yamada, N. Akahira, *Jpn. J. Appl. Phys.*, **38**, 1679 (1999).
- [31] T. Akiyama, M. Uno, H. Kitaura, K. Narumi, K. Nishiuchi, N. Yamada, *Jpn. J. Appl. Phys.*, **40**, 1598 (2001).
- [32] S. R. Ovshinsky, *Proc. The 9<sup>th</sup> Symp. On Phase Change Recording*, **44** (1997).
- [33] M. P. O'Neill, T. L. Wong, *Tech. Digest ODS 2000*, EB2, 170 (2000).
- [34] T. Ohta, K. Nishiuchi, K. Narumi, Y. Kitaoka, H. Ishibashi, N. Yamada, T. Kozaki, *Jpn. J. Appl. Phys.*, **39**, 770 (2000).
- [35] Y. Honguh, T. Murakami, *Electron. & Commun. Jpn. Part 3*, **77**, 85 (1994).
- [36] K. Miura, J. Qiu, H. Inoue, T. Mitsuyu, K. Hirao, *Appl. Phys. Lett.*, **71**, 3329 (1997).

## APPLICATIONS OF CHALCOGENIDE GLASS OPTICAL FIBERS AT NRL

J. S. Sanghera, I. D. Aggarwal, L. B. Shaw, L. E. Busse, P. Thielen, V. Nguyen, P. Pureza, S. Bayya, F. Kung

Naval Research Laboratory, Code 5606, Washington, DC 20375, USA

Chalcogenide glass fibers based on sulphide, selenide, telluride and their rare earth doped compositions are being actively pursued both at the Naval Research Laboratory (NRL) and worldwide. Great strides have been made in reducing optical losses using improved chemical purification techniques, but further improvements are needed in both purification and fiberization technology to attain the theoretical optical losses. Despite this, chalcogenide glass fibers are enabling numerous applications which include laser power delivery, chemical sensing, imaging, scanning near field microscopy/spectroscopy, IR sources/lasers, amplifiers and optical switches.

(Received July 26, 2001; accepted September 3, 2001)

*Keywords:* Chalcogenide glass, Optical fibers, Optical losses

### 1. Introduction

Chalcogenide glasses are based on the chalcogen elements S, Se and Te and the addition of other elements such as Ge, As and Sb leads to the formation of stable glasses [1]. The addition of halides leads to the formation of chalcohalide glasses [2]. Examples of stable glasses include  $\text{As}_2\text{S}_3$  [1],  $\text{Ge}_{20}\text{S}_{40}\text{Br}_{40}$  [2],  $\text{As}_2\text{Se}_3$  [1] and  $\text{Ge}_{30}\text{As}_{10}\text{Se}_{30}\text{Te}_{30}$  [3]. More recent efforts have reported on rare earth doping for active applications and consequently alternative glasses have been developed. Examples of these glass systems include Ge-Ga-S [4], Ge-As-Ga-S [5], Ga-La-S [6], Ga-Na-S [7], Ge-S-I [8] and Ge-As-Se [9].

Since the chalcogenide glasses transmit to longer wavelengths in the IR than silica and fluoride glasses (Fig. 1), there are numerous potential applications in the civil, medical and military areas. These can be essentially divided into two groups, namely "passive" and "active" applications. The passive applications utilize chalcogenide fibers as a light conduit from one location to another without changing the optical properties, other than that due to scattering, absorption and end face reflection losses associated with the fiber. Active applications of chalcogenide glass fibers are where the initial light propagating through the fiber is modified by a process other than that due to scattering, absorption and end face reflection losses associated with the fiber. Examples of these include fiber lasers, amplifiers, bright sources, gratings and non-linear effects.

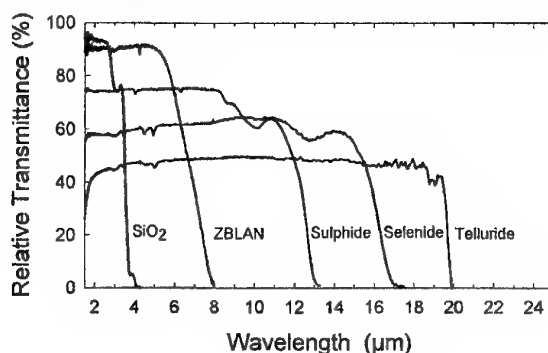


Fig. 1. Transmission spectra for several glasses (thickness of about 2-3 mm).

This paper describes some of the applications being developed in our laboratory as well as a review of the literature describing where chalcogenide fibers are being used and where they could potentially be used.

## 2. Experimental techniques for preparing fibers

Chalcogenide glasses are either melted directly in quartz ampoules or in vitreous carbon crucibles located within quartz ampoules. Typical melt temperatures range from 600°C to 1100°C, depending upon composition. The liquids are quenched and the glass rods annealed at temperatures around the appropriate softening temperatures. The optical fibers are obtained by heating preforms fabricated via rod-in-tube type processes [10,11] or by double crucible (DC) processes [11,12,13]. The cladding tubes can be obtained via an in-situ casting process, which is preferred due to less contamination and higher quality surfaces, or by core drilling from larger samples which typically leads to a rough surface quality. The preforms can also be obtained by extrusion of core and cladding glass billets [7]. The DC process enables adjustments to be made in the core/clad diameter ratio during fiber drawing by independent pressure control above each melt. Therefore both multimode and single mode fibers can be drawn with relatively fewer processing steps using the DC process.

There has been much work on determining the origin of the extrinsic scattering centers and absorption impurities and consequently numerous purification techniques based on distillation and sublimation of precursors and glasses have been developed to reduce their contribution to the total optical loss of the fiber [14,15,16].

## 3. Results and discussion

### 3.1. Properties of fibers

Table 1 lists some physical, mechanical and optical properties of two chalcogenide glasses used in making optical fibers [17]. Compared to the more traditional oxide glasses, they can be described as having lower  $T_g$ 's, higher CTE's, lower hardness and higher indices of refraction [17]. From a practical viewpoint, the most important difference is their longer wavelength transmission. Figs. 2a and b show the transmission spectra of three chalcogenide fibers made in the authors' laboratory as a function of precursor quality.

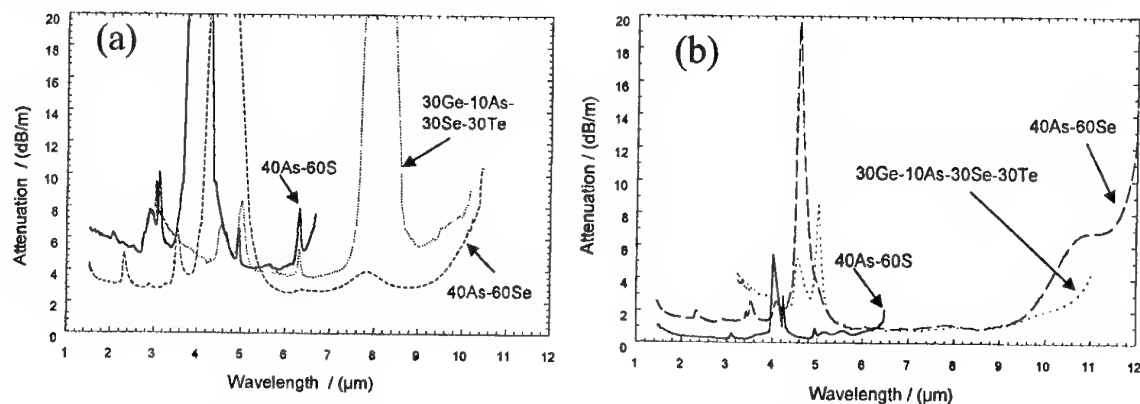


Fig. 2. Transmission loss spectra of chalcogenide glass fibers, (a) without purification of chemicals and (b) after purification of chemicals.

The fibers in Fig. 2b were made using distillation and sublimation of the precursors [16]. Depending upon composition, the sulphide, selenide and telluride based fibers transmit between about 0.8-7 μm, 1-10 μm, and 2-12 μm, respectively. Therefore, the practical applications dictate the type of fiber to be used. The As-S fibers have received the most attention to-date in our laboratory and so the loss routinely achieved is about 0.1-0.2 dB/m in fiber lengths in excess of 100 meters. Comparing Figs. 2a and b, it is apparent that both purification and composition play an important role in making low loss fibers. Fig. 3 compares the losses routinely obtained for a couple of chalcogenide glasses along with the lowest ("champion") losses reported in the literature [3,15].

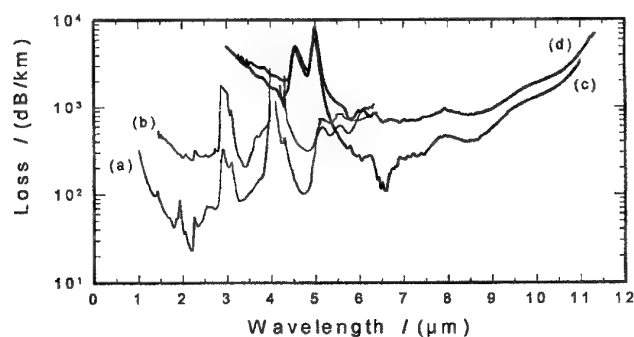


Fig. 3. Transmission loss spectra of (a) lowest loss sulphide fiber, (b) typical sulphide fiber, (c) lowest loss telluride fiber, and (d) typical telluride fiber.

Table 1. Some physical, mechanical and optical properties of chalcogenide glasses used for making optical fibers [17].

	$\text{As}_{40}\text{S}_{60}$	$\text{Ge}_{30}\text{As}_{10}\text{Se}_{30}\text{Te}_{30}$
<b>Physical Properties</b>		
$T_g / (^{\circ}\text{C})^a$	197	265
$\text{CTE} / (10^{-6}/^{\circ}\text{C})^b$	21.4	14.4
Thermal Conductivity / ( $\text{W}/\text{m}\cdot^{\circ}\text{C}$ )	0.17	$\sim 0.2$
<b>Mechanical Properties</b>		
Density / ( $\text{g}/\text{cm}^3$ )	3.20	4.88
Knoop Hardness / ( $\text{kg}/\text{mm}^2$ )	109	205
Fracture Toughness / ( $\text{MPa}\cdot\text{m}^{1/2}$ )	$\sim 0.2$	$\sim 0.2$
Poisson's Ratio	0.24	$\sim 0.26$
Young's Modulus / (GPa)	16.0	21.9
<b>Optical Properties</b>		
Refractive Index <sup>c</sup>	2.415 (3.0)	2.80 (10.6)
$dn/dT / (10^{-5}/^{\circ}\text{C})^{c,d}$	+0.9 (5.4)	+10.0 (10.6)
Bulk transmission / (:m)	0.6 - 10.0	1.0 - 17.0
Fiber transmission / (:m)	0.8 - 6.5	3.0 - 11.0
Lowest Loss / ( $\text{dB}/\text{km}$ ) <sup>c</sup>	23 (2.3)	110 (6.6)
Typical Loss / ( $\text{dB}/\text{km}$ ) <sup>c</sup>	100-200 (2.2-5.0)	500-1000 (6.0-9.0)
Estimated minimum loss / ( $\text{dB}/\text{km}$ ) <sup>c</sup>	1.0	nd

<sup>a</sup>  $T_g$  is the glass transition temperature.

<sup>b</sup> CTE is the coefficient of thermal expansion.

<sup>c</sup> Wavelength in  $\mu\text{m}$  given in parenthesis.

<sup>d</sup>  $dn/dT$  is the change in refractive index with temperature.

nd – not determined

The question arises as to what is the origin of the extrinsic scattering and absorption losses, and furthermore, how can these impurities be removed. The scattering centers have been previously identified as bubbles and particles of  $\text{SiO}_2$  and carbon and their contribution to the scattering loss has been rigorously analyzed [14]. Despite this, the concentration of these species has not been experimentally determined. On the other hand, the absorbing species have been quantitatively characterized [16]. Table 2 lists the estimated concentration of typical absorbing impurities found in sulphide and telluride fibers [16]. Although the losses of the fibers are routinely higher than the champion values, it is worthwhile to estimate the theoretical minimum loss. This has been done for an arsenic sulphide glass [16] and the results are shown in Fig. 4.

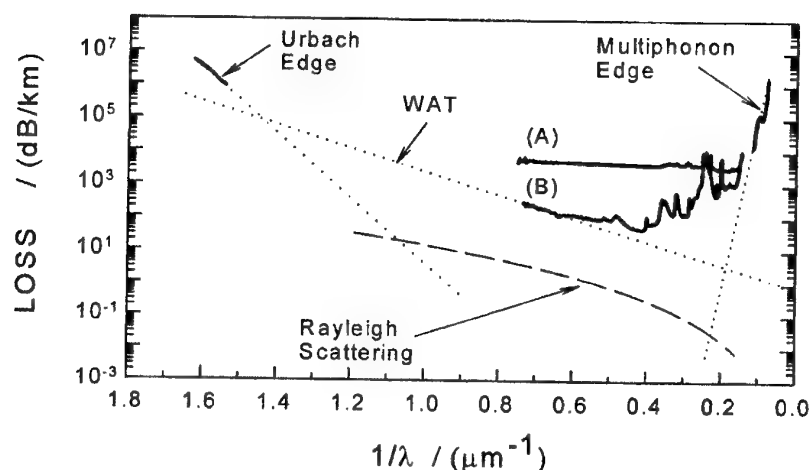


Fig. 4. Estimation of theoretical minimum loss in a sulphide fiber. A and B represent poor and high quality glasses, respectively [16].

Table 2. Estimated concentration of typical impurities in sulphide and telluride fibers [16].

Impurity Absorption	Wavelength (μm)	Absorption Loss (dB/m)	Extinction Coefficient (dB/m/ppm)	Impurity Concentration (ppm)
<b><u>Sulphide Fibers</u></b>				
H-S	4.0	10	2.3	4.3
O-H	2.9	0.3	5.0	0.06
<b><u>Telluride Fibers</u></b>				
H-Se	4.5	3.0	1.1	2.7
Ge-H	5.0	6.0	---	---
H <sub>2</sub> O	6.3	0.07	34.0	0.002
Ge-O	7.9	0.16	2.6	0.06

The minimum loss is estimated to be about 4 dB/km at 5.0 μm [16]. Although the losses of the sulphide fibers are routinely higher than both the "champion" and the estimated theoretical values, these fibers can, and are being used in numerous applications. Unfortunately, theoretical estimates are not available for other glass systems, but despite this, the selenide, telluride and rare earth doped glass fibers are being fabricated and utilized in numerous applications. The minimum loss obtained for a 400 ppm Dy doped unclad selenide glass fiber was 0.8 dB/m at 6.6 μm and 3 dB/m at 1.3 μm. Multimode fiber has been drawn with a loss of 6 dB/m at 1.33 μm and a minimum loss of about 3 dB/m at approximately 6 μm. The losses for Pr doped fibers are similar. Undoped samples have been fabricated into singlemode fibers (core / cladding diameters = 4 / 110 μm) with losses of 3 dB/m at 1.55 μm. In general, typical measured losses for the rare earth doped glasses are >0.5 dB/m and so improvements in purification and fiberization technology are still needed to reduce the measured optical losses.

Tables 3 and 4 list the passive and active applications of chalcogenide glass fibers, respectively, that have been demonstrated or are being investigated. These will be discussed in more detail in the next section.

Table 3. Passive applications of IR transmitting chalcogenide glass fibers.

Applications	References
<b>Laser Power Delivery</b> <ul style="list-style-type: none"> <li>• 5.4 <math>\mu\text{m}</math> (CO)</li> <li>• 10.6 <math>\mu\text{m}</math> (CO<sub>2</sub>)</li> <li>• Atmospheric 2-5 <math>\mu\text{m}</math> region</li> <li>• Medical Free Electron Laser (2-10 <math>\mu\text{m}</math>)</li> <li>• Anti-reflection (AR) coatings</li> </ul>	18,19 18,19 20,21 22,28 18,20
<b>Chemical Sensing</b> <ul style="list-style-type: none"> <li>• Aqueous, non-aqueous, toxic chemicals</li> <li>• Polymers, paints, pharmaceuticals</li> <li>• Condition Based Maintenance (CBM)</li> <li>• Cone Penetrometer System</li> <li>• Active Coatings</li> <li>• Bio-medical</li> </ul>	24-28 11,27,29 27 30 31 22,32
<b>Temperature Monitoring</b> <ul style="list-style-type: none"> <li>• Grinding ceramics</li> </ul>	33
<b>Thermal Imaging &amp; Hyperspectral Imaging</b> <ul style="list-style-type: none"> <li>• Coherent fiber bundles</li> </ul>	34, 35,36,38
<b>Near Field Microscopy</b> <ul style="list-style-type: none"> <li>• Imaging and spectroscopy</li> </ul>	39-41
<b>Fiber Multiplexing</b> <ul style="list-style-type: none"> <li>• Fiber couplers</li> </ul>	42

Table 4. Active applications of IR transmitting chalcogenide glass fibers.

Applications	References
<b>Rare Earth Doped Fibers</b> <ul style="list-style-type: none"> <li>• Fiber Lasers - 1.08 <math>\mu\text{m}</math> (Nd)</li> <li>• Amplifiers - 1.08 <math>\mu\text{m}</math> (Nd)</li> <li>                    - 1.34 <math>\mu\text{m}</math> (Pr)</li> <li>                    - 1.34 <math>\mu\text{m}</math> (Dy)</li> <li>• Infrared Scene Simulation (IRSS)</li> <li>• Chemical Sensing</li> <li>• Gratings - 1.5 <math>\mu\text{m}</math></li> </ul>	54 55 7 53 58 22 59
<b>Non-linear</b> <ul style="list-style-type: none"> <li>• Optical switching</li> <li>• Second Harmonic Generation</li> <li>• Frequency mixing</li> <li>• Electrical Poling</li> </ul>	62 64 --- ----

### 3.2. Passive Applications

#### 3.2.1. Laser Power Delivery

High power CO and CO<sub>2</sub> lasers operating at 5.4  $\mu\text{m}$  and 10.6  $\mu\text{m}$ , respectively, are readily available and can be used for industrial welding and cutting. Transmitting the laser power through fibers enables remote operation. Small core diameter (<200  $\mu\text{m}$ ) fibers have demonstrated tolerance to power densities of  $\sim 125 \text{ kW/cm}^2$  at 5.4  $\mu\text{m}$  and  $\sim 54 \text{ kW/cm}^2$  at 10.6  $\mu\text{m}$  without damage [19] (Fig. 5). Telluride glass fiber losses at 10.6  $\mu\text{m}$  lie in the range of 1.5 dB/m to 3 dB/m, depending upon composition and purity [3,18].



The arsenic sulphide fibers transmit in the atmospheric 2 to 5  $\mu\text{m}$  region and can be used for transmission of laser power in this region [20]. Pulsed laser power delivery has been demonstrated (Fig. 5). The average power is about 2.69 Watts but the peak power is 26.9 kW, which corresponds to a peak power density of  $1.07 \text{ GW}/\text{cm}^2$  without fiber damage for up to  $1.5 \times 10^7$  pulses [21]. This remarkable threshold to damage is close to the predicted value of about  $3.0 \text{ GW}/\text{cm}^2$  due to dielectric breakdown at the surface. This threshold to damage is obtained by control of fiber polishing, otherwise the fiber end face undergoes damage at relatively lower powers.

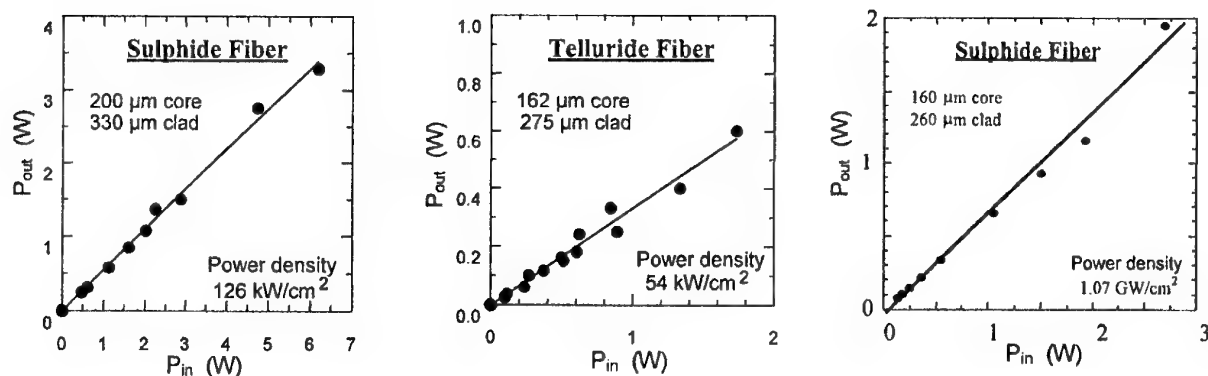


Fig. 5. (a) CO laser transmission, (b)  $\text{CO}_2$  laser transmission and (c) pulsed high energy laser transmission in the 2-5  $\mu\text{m}$  region.

Recent efforts have considered delivery of energy from a medical free electron laser (MFEL) operating between 2 and 10  $\mu\text{m}$  through chalcogenide fiber [22]. The MFEL can emit more than 10 MW of power in a femtosecond pulse which relates to an average power of greater than 10 Watts. While not all this power is needed, it has been shown [23] that in certain cases, surgery at 6.45  $\mu\text{m}$  based on cleaving of protein bonds is more efficient and leads to less denatured tissue and scarring than with conventional Er:YAG lasers at 2.94  $\mu\text{m}$  based on OH absorption [23]. Current efforts are underway to perform surgery using chalcogenide fibers at 6.45  $\mu\text{m}$ . Nevertheless, ophthalmic surgery requires operation at 2.94  $\mu\text{m}$ , with an energy requirement of 1-2 mJ. This has been demonstrated using chalcogenide fibers. Harder tissue will require up to 30 mJ and consequently larger core diameter (900  $\mu\text{m}$ ) fiber is currently being developed. Output energy from an Er:YAG laser operating at 2.94  $\mu\text{m}$  has been transmitted through sulfide fiber. Up to  $271 \text{ kW}/\text{cm}^2$  power density has been transmitted without damage to the fiber. It is conceivable that laser power can be used for machining numerous materials and biological samples by tuning the wavelength and transmitting the laser power through the chalcogenide fibers to remote areas.

The end face reflection losses decrease the overall throughput of laser power. For example,  $\text{As}_{40}\text{S}_{60}$  and  $\text{Ge}_{30}\text{As}_{10}\text{Se}_{30}\text{Te}_{30}$  glasses have refractive indices of about 2.4 and 2.8, for which reflection losses are about 17% and 22% per face, respectively. Consequently, AR coatings are being developed for both discrete wavelengths as well as broad band operation [18,20]. Reflection losses have been reduced to about 1 % per face for sulphide fibers at some IR wavelengths [20].

### 3.2.2. Chemical Sensing

Chalcogenide fibers are well suited for chemical sensing applications since practically most molecular species vibrate in the infrared region. The chalcogenide fibers can be used in fiber optic chemical sensor systems for quantitative remote detection and identification as well as detecting chemicals in mixtures. Examples of different sensing techniques include evanescent/ATR (attenuated total reflectance) [24-26], diffuse reflectance and absorption spectroscopy [27-29]. The diffuse reflectance and evanescent/ATR techniques are useful for samples that scatter or are opaque at the IR wavelengths. Numerous systems have been studied and many species have been detected including aqueous, non-aqueous and toxic liquids as well as solids [24-29]. Examples include oil, freon, soap, paints, polymer curing reactions, glucose/water, benzene and derivatives, chlorinated hydrocarbons,

alcohols, carboxylic acids, aqueous acids, perfumes and pharmaceutical products. Fig. 6 shows some representative spectra. Condition based maintenance (CBM) is becoming increasingly important and uses the approach, "if it isn't broken, don't fix it". For example, changes of oil in motor vehicles are routinely performed every 3000 miles or so, but are not necessarily needed and therefore the incurred costs can be quite significant. A fiber optic dipstick probe could potentially monitor the quality of the oil and consequently save large amounts of money in preventing unnecessary oil changes in the military and civil sector. For example, there is an additive package used to inhibit viscosity breakdown of engine oil. Unfortunately, the environmental breakdown of the additive package occurs and leads to viscosity breakdown of the oil.

A fiber optic dipstick can be used to monitor the by-products of degradation of the additive package (Fig. 6b). The alarm bells sound when these reach a pre-determined threshold value, signaling an oil change.

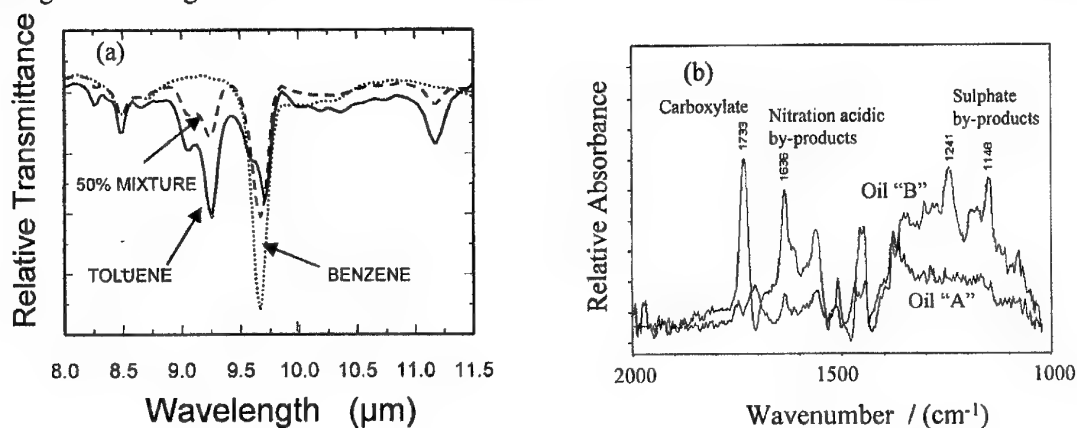


Fig. 6. Chemical sensing using IR fibers for (a) mixture of benzene and toluene and (b) difference spectra of degraded oil (after 27).

A fiber optic based reflectance probe has been used to detect contaminants in soil (Fig. 7) [30]. The detection was accomplished with the probe deployed in a cone penetrometer and tested in the field. Detection limits of 130 ppm of marine diesel fuel in sea sand have been demonstrated using a 20 meter length of cable [30].

Chalcogenide fibers with a glass cladding have been used for evanescent sensing of a few 10's of ppm of benzene (and derivatives) and chlorinated hydrocarbons. The low detection limits were achieved by etching the cladding glass and re-covering with specific polymer coatings which preferentially enrich one phase in them near the core surface [31]. Polydimethylsiloxane (PDMS) preferentially enriched benzene (and derivatives) and low-density polyethylene enriched the chlorinated hydrocarbons on the core surface while preventing water from penetrating the coating.

Recently, a chalcogenide fiber ATR probe has been used to show the spectral differences between various tissues and organs in bio-medical samples. Fig. 8a shows the IR spectra for various organs/tissues from a dead chicken, while Fig. 8b shows the IR spectrum recorded from the liver of an anaesthetized sheep [22]. Similar IR spectra have been recorded from an anaesthetized mouse with a malignant (cancer) human breast tumor grown near the surface.

While these data were recorded using chalcogenide glass in contact with tissue, alternative IR transmitting and bio-compatible probes will most likely be needed for human testing. However, the chalcogenide fibers can be utilized to generate a bio-medical database for medical diagnostics such as tissue evaluation and early detection of cancer [32]. Currently, sections are cut out of the body, prepared into thin sections and desiccated before FTIR analysis is performed. Obviously, the flexible fiber optic approach is minimally invasive. While silica fibers are available they are inappropriate for infrared spectroscopy in the 2-10 μm region.

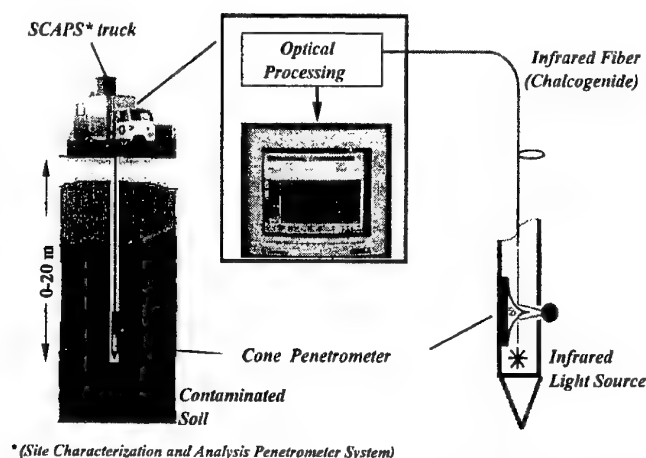


Fig. 7. The cone penetrometer system using chalcogenide fiber for detection of contaminants and water in soil.

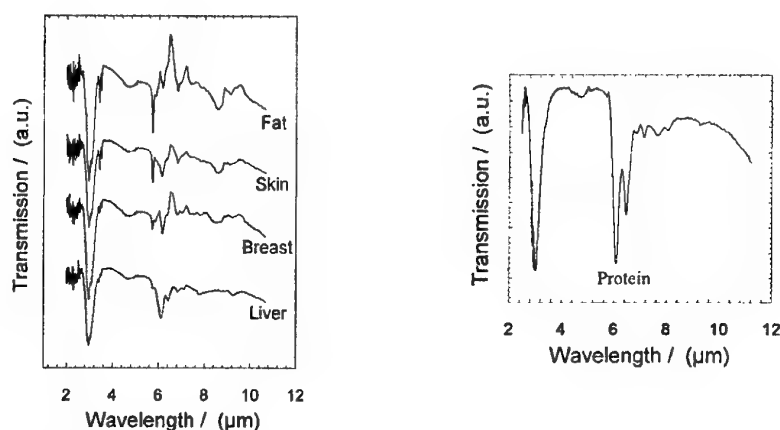


Fig. 8. Attenuated Total Reflection (ATR) spectra of (a) chicken tissue/organs and (b) liver of living sheep.

### 3.2.3. Temperature monitoring, thermal imaging and hyperspectral imaging

Ueda et al. [33] have used As-S fibers with a Teflon cladding to measure temperature increases of up to 200°C on the surface layer of ceramic plates during grinding.

Kapany and Simms first suggested the use of chalcogenide fibers for thermal imaging [34]. Saito et al. [35] recorded the image of an electric iron at 773 K, with some degree of coherency through a 1000 fiber bundle. Nishii et al. [36] fabricated a flexible fiber bundle containing 8400 Teflon coated fibers and recorded the thermal image of an operating integrated circuit in the 3 to 5.4  $\mu\text{m}$  region using an InSb detector. Techniques are needed for the fabrication of coherent and registered fiber bundles containing small diameter fiber but with tight tolerances and high precision.

The area of hyperspectral imaging can be exploited by coupling coherent fiber bundles to focal plane array (FPA) detectors based on InSb (2-5.4  $\mu\text{m}$ ) or MCT (3-11  $\mu\text{m}$ ). The focal plane array detectors are extremely sensitive and can be used for performing both spatial and spectral analysis in the infrared [37]. In other words, one can derive an IR spectrum from each pixel thereby performing chemical spectroscopy at every pixel. FPA detectors have been used for obtaining spectral and spatial information about the environment for a number of years, but without fibers. The only report in the literature pertaining to IR fibers is a 10x10 fiber bundle of As<sub>2</sub>S<sub>3</sub> fiber with a Teflon cladding which was reformatted to a 1x100 array and the output analyzed using a grating spectrometer [38]. The intensity contour of a Xenon lamp was recorded. Coupling to FPA's requires high precision diameter and high quality fiber bundles so that each fiber in the bundle couples to only one pixel on the

detector otherwise the images will be blurred. We are currently involved in the development of coherent and registered fiber bundles.

### 3.2.4. Near field microscopy

Sub-diffraction limit resolution has been demonstrated using single mode silica fibers by pulling and/or etching the fiber ends from a diameter of 125  $\mu\text{m}$  to below 100 nm at the fiber tip. Preliminary results were obtained using multimode chalcogenide fiber micro-tips with about 1  $\mu\text{m}$  resolution [39]. More recently, the authors have used high quality singlemode and multimode chalcogenide fibers to demonstrate about 20 nm topographic resolution and about 200 nm spectral resolution for different samples such as polycrystalline diamond [40], pancreatic cells [41], biofilms and semiconductor samples. Figs. 9 and 10 show the topographic and optical images for a polycrystalline diamond film and pancreatic cells, respectively. In our opinion, this is a promising technique for imaging and performing spectroscopy of semiconductor and biological samples with sub-micron resolution.

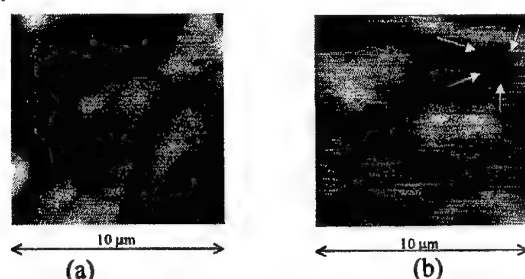


Fig. 9. The scanning near field IR microscopic (SNIM) data for a polycrystalline diamond film using a sulphide fiber micro-tip. The (a) topographic and (b) optical spectra (at  $\lambda = 3.5 \mu\text{m}$ ) were recorded with a resolution of about 200 nm.

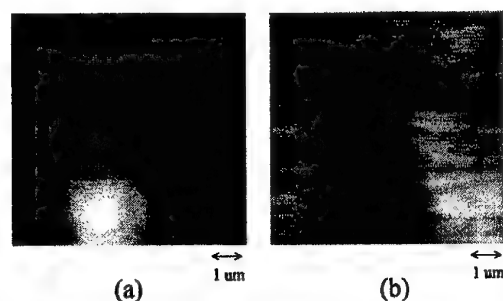


Fig. 10. The scanning near field IR microscopic (SNIM) data for pancreatic cells using a selenide fiber micro - tip. The (a) topographic and (b) optical spectra (at  $\lambda = 6.1 \mu\text{m}$ ) were recorded with a resolution of about 25 nm and 200 nm, respectively.

### 3.2.5. Fiber multiplexing

Fused fiber couplers are important since they enable fiber multiplexing. For example, they might be used in IR fiber optic chemical sensing systems and data transmission systems. A preliminary fused taper fiber coupler has been fabricated using a multimode arsenic sulphide fiber with a coupling ratio of 3:1 at 2.65  $\mu\text{m}$  [42], but it should be possible to use singlemode fibers.

## 3.3. Active applications

### 3.3.1. Rare earth doped fibers

Rare earth ions possess characteristic electronic energy levels which are only slightly influenced by the host matrix due to the screening effect of the d-electrons. When pumped with the

appropriate energy, the electrons are excited into upper levels from which they can subsequently decay to lower levels. Certain transitions become increasingly more efficient in longer wavelength transmitting hosts such as the chalcogenide glasses due to less multiphonon quenching and IR fluorescence emissions beyond 2  $\mu\text{m}$  are only seen in chalcogenide glasses and not in silica. Table 5 lists the IR emission wavelengths found in chalcogenide glasses [43-53]. The only laser oscillation observed in chalcogenide fibers has been from Nd at 1.08  $\mu\text{m}$  [54] while amplification has been demonstrated using Nd at 1.08  $\mu\text{m}$  [55] and Pr at 1.34  $\mu\text{m}$  [7]. These results were obtained in sulphide glass hosts. The 1.3  $\mu\text{m}$  wavelength is of interest for telecommunications [56]. The gain coefficient obtained from the singlemode sulphide (Ga-Na-S) fiber at 1.34  $\mu\text{m}$  was a remarkable 0.8 dB/mW and the efficiency was about 30 %. The fiber loss at 1.34  $\mu\text{m}$  was about 1 dB/m [56].

Table 5. The IR emission wavelengths in chalcogenide glasses and wavelengths which have exhibited laser oscillation and amplification in chalcogenide fibers.

Rare Earth Ion	IR Emission Wavelengths ( $\mu\text{m}$ )	Laser Oscillation Wavelength ( $\mu\text{m}$ )	Amplification Wavelength ( $\mu\text{m}$ )
Nd	0.786, 0.919, 1.08, 1.37 [42,43]	1.08 [54]	1.08 [55]
Er	0.822, 0.860, 0.987 [44,45], 1.54 [46], 2.7, 3.5, 4.5 [47]	-----	-----
Tm	1.21, 1.45, 1.81, 2.35 [48]	-----	-----
Ho	0.76, 0.91 [45], 1.2, 2.9, 3.9[49]	-----	-----
Pr	1.3, 1.6, 2.9, 3.4, 4.5, 4.8, 4.9, 7.2* [50,51]	-----	1.34 [7]
Dy	1.3, 1.8, 2.3, 4.3 [52]	-----	-----
Tb	3.0, 4.8, 8.0* [47]	-----	-----

\* Indirect evidence

The numbers in [ ] are references.

Recent work has shown that Dy doped selenide glasses are better candidates for 1.3  $\mu\text{m}$  fiber amplifiers due to the lower phonon energy of the host glass, and the larger absorption and emission cross-sections for Dy [53]. Consequently, the efficiency is expected to be about 90% and the gain coefficient approximately double the value for the best Pr doped sulphide fiber [53]. Modeling has shown that the Dy doped selenide fiber can tolerate higher losses compared with the Pr doped sulphide fibers. Therefore, device lengths will be shorter, such that a 45 cm length of doped selenide fiber with a loss of about 10 dB/m can give almost 40 dB gain at 1.34  $\mu\text{m}$ . Table 6 shows some of the properties. Preliminary multimode fibers have been drawn with losses of about 6 dB/m at 1.3  $\mu\text{m}$  and less than 3 dB/m at about 6  $\mu\text{m}$  [57]. Unclad fibers have been fabricated with losses of about 3 dB/m at 1.3  $\mu\text{m}$  and less than 1 dB/m at 6  $\mu\text{m}$ . Preliminary single mode fibers have been drawn with minimum losses of about 3 dB/m [57].

Since the rare earth doped chalcogenide fibers emit in the 2 to 5  $\mu\text{m}$  region [66], an array of the fibers can be used for infrared scene simulation (IRSS) for characterization of focal plane array detectors (e.g. InSb) [58]. Fig. 11 shows the emission spectrum of a Pr doped selenide glass fiber, demonstrating broad band emission between about 3 and 5  $\mu\text{m}$ . Prototype bundles have been fabricated and mid-IR emission measured from the pixels [58]. Black body temperatures of up to 900 K have been simulated in single pixel pumping indicating that these fibers are capable of providing bright sources in the IR [58].

It is possible to use these fiber sources in chemical sensor systems [22]. For example, figure 12 shows the IR transmission spectrum of a thin film of toluene between two  $\text{CaF}_2$  plates recorded using a Pr-doped selenide fiber (pumped at 1.064  $\mu\text{m}$ ) as a mid-IR source.

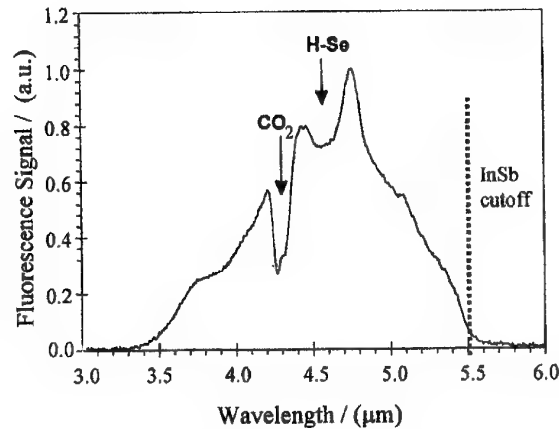


Fig. 11. The broad band mid-IR emission from a Pr doped GeAsGaSe glass fiber.

Table 6. Branching ratios ( $\beta$ ), quantum efficiencies ( $\beta\eta$ ), lifetimes ( $\tau$ ), emission cross-sections ( $\sigma$ ) and gain coefficients ( $\sigma\tau$ ), for potential 1.3  $\mu\text{m}$  fiber amplifier systems.

Glass System	$\beta$	$\eta$ (%)	$\beta\eta$ (%)	$\tau$ (ms)	$\sigma$ ( $\times 10^{-20} \text{ cm}^2$ )	$\sigma\tau$ ( $\times 10^{-26} \text{ cm}^2\text{s}$ )
Pr: ZBLAN	0.6	3.4	2.0	110	0.35	38.5
Pr: GaLaS	0.52	58	30	295	0.84	250
Pr: GaNaS	0.52	58	30	370	1.08	400
Dy: GaLaS	0.93	29	27	59	2.8	165
Dy: GeAsSe*	0.93	95	88	310	2.7	837

\* based on Ge-As-Se system

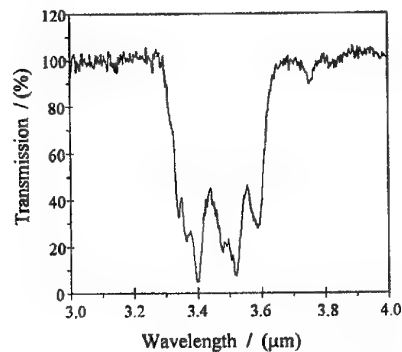


Fig. 12. Transmission spectrum of toluene using the mid-IR emission from a Pr-doped GeAsGaSe glass fiber.

The ability to write gratings in chalcogenide fibers will enable smart compact devices including lasers and dispersion compensators. Some work has been performed on writing gratings in chalcogenide glass fibers [59]. Asobe et al. [59] have fabricated an  $\text{As}_2\text{S}_3$ -based fiber Bragg grating for 1.55  $\mu\text{m}$  wavelength operation by the transverse holographic method using a He-Ne laser. A reflectivity of  $> 90\%$  was obtained with an estimated change in refractive index of about  $10^{-4}$ .

### 3.3.2. Non-linear effects

Glasses possessing high third order non-linearities ( $X^3$ ) are required for ultra-fast switching, especially for time division multiplexing (TDM) in telecommunications systems. It is well established that the values of  $X^3$  for chalcogenide glasses are about two orders of magnitude larger than silica [60,61]. To our knowledge, the number of papers reporting the use of this phenomenon in actual switching applications is not extensive. M. Asobe et al. [62] demonstrated efficient optical Kerr shutter (OKS) switching operation with pico-second response time using a 1 meter length of elliptical core fiber and a 100 GHz signal operating at a wavelength of about 1.5  $\mu\text{m}$ .

Since glasses lack a center of inversion symmetry and thus have no second order nonlinear susceptibility ( $\chi^2$ ) then they should not exhibit second harmonic generation (SHG) [63]. However, undoped and Pr-doped GaLaS glasses have exhibited SHG [64]. This SHG may be due to crystallization or the effect of frozen-in electric fields. The latter arises from the relationship  $\chi^2 = E_{dc}\chi^3$ , where  $E_{dc}$  is the frozen-in electric field [63]. Electric poling has been successfully used to produce SHG in silica based fiber systems [65]. It is not unreasonable to expect similar results in chalcogenide fibers. While  $\chi^3$  is about 2 orders of magnitude larger in chalcogenides compared with silica, we expect larger SHG efficiencies in electrically poled chalcogenide glasses. However, the question arises as to whether the electric fields can be frozen-in for chalcogenide glasses. We have observed preliminary second harmonic generation using electrically poled chalcogenide glasses. At the present time the magnitude appears comparable to silica glass but the mechanism is unknown.

#### 4. Conclusions

Tremendous progress has been made in reducing the optical losses of the chalcogenide glass fibers in the past several years resulting in numerous applications. We strongly believe that IR fiber optics will become increasingly more important in the future as further improvements are made to the quality of the fibers and new compositions developed. One of the most exciting developments in the future is going to be in the area of rare earth ion doping of fibers for IR fluorescence emission. The IR light sources, lasers and amplifiers developed using this phenomenon will be very useful in civil, medical and military applications. Remote IR spectroscopy and imaging using flexible fibers will be realized for medical and military applications. Other future research areas which will inevitably be explored include the gratings and non-linear optical properties of the IR glasses. The authors strongly believe that chalcogenide glass fiber optics will grow due to the numerous and potentially extensive applications. The availability of high quality, low loss and high strength singlemode and multimode fibers will undoubtedly improve the capabilities of existing technologies as well as enable new technologies. In summary, the future of chalcogenide glasses and fibers looks very bright.

#### Acknowledgements

The authors would like to acknowledge M. Druy (Sensiv Inc.), R. Waynant (FDA), Z. Bhatalwalla (Johns Hopkins U.), G. Edwards, N. Tolk, J. M. Gilligan, D. Jansen (Vanderbilt U.), M. Luce, R. Generosi, P. Perfetti, A. Cricenti (Istituto di Struttura della Materia), G. Margaritondo (Ecole Polytechnique Federale) and D. Schaafsma (Tetra Tech Data Systems).

#### References

- [1] Z. U. Borisova, "Glassy Semiconductors", Plenum Press, NY 1981.
- [2] J. S. Sanghera, J. Heo, J. D. Mackenzie. 1988. Chalcogenide Glasses. *J. Non-Cryst. Solids* 103-155.
- [3] J. S. Sanghera, V. Q. Nguyen, P. C. Pureza, F. H. Kung, R. Miklos, I. D. Aggarwal, *J. Lightwave Tech.* 12 (5) 737 (1994).
- [4] E. Snitzer, K. Wei. 1995. Glass compositions having low energy phonon spectra and light sources fabricated therefrom. US Patent No. 5, 379, 149.
- [5] B. Aitken, M. A. Newhouse, Ga- and/or In-containing AsGe sulphide glasses. US Patent # 5, 389, 584 (1995).
- [6] D. W. Hewak, R. S. Deol, J. Wang, G. Wylangowski, J. A. Medeiros Neto, B. N. Samson, R. I. Laming, W. S. Brocklesby, D. N. Payne, A. Jha, M. Poulain, S. Otero, S. Surinach, M. D. Baro. Low phonon-energy glasses for efficient 1.3  $\mu\text{m}$  optical fiber amplifiers. 1993. *Electronics Letters* 29 [2] 237.
- [7] H. Tawarayama, E. Ishikawa, K. Itoh, H. Aoki, H. Yanagita, K. Okada, K. Yamanaka, Y. Matsuoka, H. Toratani. 1997. Efficient amplification at 1.3  $\mu\text{m}$  in a  $\text{Pr}^{3+}$ -doped Ga-Na-S fiber. Optical Fiber Conference, Victoria, Canada, PD1-1, published by Optical Society of America, Washington, DC.
- [8] V. Krasteva, A. Yurkina, D. Machewirth, G. Sigel Jr.,  $\text{Pr}^{3+}$ -doped Ge-S-I glasses as candidate materials for 1.3  $\mu\text{m}$  - optical fiber amplifiers. *J. Non-Cryst. Solids* 213 & 214-304 (1997).
- [9] D. A. Turnbull, S. Q. Gu, S. G. Bishop. 1996. Photoluminescence studies of broadband excitation mechanisms for  $\text{Dy}^{3+}$  emission in  $\text{Dy:As}_{12}\text{Ge}_{33}\text{Se}_{55}$  glass. *J. Appl. Phys.* 80 [4] 2436.



- [10] J. Nishii, T. Yamashita, T. Yamagishi. 1989. Chalcogenide glass fiber with a core-cladding structure. *Appl. Optics* 28, 5122.
- [11] J. S. Sanghera, I. D. Aggarwal, L. Busse, P. Pureza, V. Nguyen, R. Miklos, F. Kung, R. Mossadegh, Development of Low-Loss IR Transmitting Chalcogenide Glass Fibers. *SPIE* 2396-71 (1995).
- [12] T. Kanamori, Y. Terunuma, S. Takahashi, T. Miyashita, Chalcogenide glass fibers for mid-infrared transmission. *J. Lightwave Technol.* 2, 607 (1984).
- [13] A. V. Vasil'ev, G. G. Devyatykh, E. M. Dianov, A. N. Gur'yanov, A. Yu. Laptev, V. G. Plotnichenko, Yu. N. Pyrkov, G. E. Snopatin, I. V. Skripachev, M. F. Churbanov, V. A. Shipunov, Two layer chalcogenide glass optical fibers with optical losses below 30 dB/km. *Quant. Electron.* 23, 89 (1993).
- [14] J. S. Sanghera, L. E. Busse, I. D. Aggarwal, Effect of scattering centers on the optical loss of  $As_2S_3$  glass fibers in the infrared. *J. Appl. Phys.* 75, 4885 (1994).
- [15] M. F. Churbanov, Recent advances in preparation of high purity chalcogenide glasses in the USSR. *J. Non-Cryst. Solids* 140, 324 (1992).
- [16] J. S. Sanghera, I. D. Aggarwal. Development of chalcogenide fibers at NRL. *J. Non-Cryst. Solids* 213 & 214, 63 (1997).
- [17] J. S. Sanghera, I. D. Aggarwal, Chapter 9 in "Infrared Fiber Optics", eds. J. S. Sanghera and I. D. Aggarwal (CRC Press Inc., Boca Raton, FL, 1998).
- [18] J. Nishii, S. Morimoto, I. Inagawa, R. Iizuka, T. Yamashita, T. Yamagishi, Recent trends and advances in chalcogenide glass fiber technology: a review. *J. Non-Cryst. Solids* 140, 199 (1992).
- [19] L. E. Busse, J. A. Moon, J. S. Sanghera, I. D. Aggarwal, Chalcogenide Fibers Enable Delivery of Mid-Infrared Laser Radiation. *Laser Focus World* 32, 143 (1996).
- [20] L. Busse, J. Moon, J. S. Sanghera, I. D. Aggarwal, J. Harrington, K. K. Lum. 1995. High Optical Power Transmission Through Glass Clad Infrared Fiber. *Proc. of 1995 IRIS Specialty Group on Materials* (publ. by Erim, Ann Arbor, MI, 1995) pp. 237.
- [21] I. D. Aggarwal, L. E. Busse, L. B. Shaw, B. Cole, J. S. Sanghera. 1998. IR transmitting fiber and applications: High-power delivery, sources, and amplifiers. *Proc. Diode Laser Technology Review*, March 2-4, Albuquerque, NM.
- [22] J. S. Sanghera, I. D. Aggarwal. 1998. Active and Passive Applications of Chalcogenide Glass Optical Fibers. *Proceedings of the 18<sup>th</sup> Int. Congress on Glass*, July 5-10, San Francisco, CA.
- [23] Dr. Glen Edwards. 1996. In "Research at Vanderbilt".
- [24] J. Heo, M. Rodrigues, S. Saggese, G. H. Sigel Jr., Remote fiber optic chemical sensing using evanescent wave interactions in chalcogenide glass fibers. *Appl. Optics* 30, 3944 (1991).
- [25] J. S. Sanghera, F. H. Kung, L. E. Busse, P. C. Pureza, I. D. Aggarwal, Infrared Evanescent Absorption Spectroscopy of Toxic Chemicals Using Chalcogenide Glass Fibers. *J. Am. Ceramic Soc.* 78, 2198 (1995).
- [26] X. H. Zhang, M. V. Duhamel, H. L. Ma, C. Blanchetiere, J. Lucas, Application of the TeX glass fibers as chemical sensor. *J. Non-Cryst. Solids* 161, 547 (1993).
- [27] M. Druy, Chapter 8 in "Infrared Fiber Optics", eds. J. S. Sanghera and I. D. Aggarwal (CRC Press Inc., Boca Raton, FL 1998).
- [28] P. Melling (Rempec Inc.). Commercial Literature.
- [29] M. Saito. 1985. Tech. Digest 1st Workshop on Optical Fiber Sensors (Japan Soc. of App. Phys.) pp. 113.
- [30] G. Nau, F. Bucholtz, K. J. Ewing, S. T. Vohra, J. S. Sanghera, I. D. Aggarwal, Fiber Optic Reflectance Sensor for the Cone Penetrometer. *SPIE* 2504, 291 (1995).
- [31] J. S. Sanghera, G. Nau, P. C. Pureza, I. D. Aggarwal. 1996. Selective multi-chemical fiber optic sensor. *US Patent # 5, 525, 800*.
- [32] B. Rigas, P. T. T. Wong, Human colon adenocarcinoma cell lines display infrared spectroscopic features of malignant colon tissues. *Cancer Research* 52, 84 (1992).
- [33] T. Ueda, K. Yamada, T. Sugita, *J. Eng. Ind.* 114, 317 (1992).
- [34] N. S. Kapany, R. J. Simms, *Infrared Phys.* 5, 69 (1965).
- [35] M. Saito, M. Takizawa, S. Sakuragi, F. Tanei, *Appl. Optics* 24, 2304 (1985).
- [36] J. Nishii, T. Yamashita, T. Yamagishi, C. Tanaka, H. Stone, Coherent infrared fiber image bundle. *Appl. Phys. Letts.* 59, 2639 (1991).
- [37] Raytheon IR Center of Excellence. Product 256x256 InSb VISMIR FPA.
- [38] H. Suto, Chalcogenide fiber bundle for 3D spectroscopy. *Infrared Physics and Technology* 38, 93 (1997).

- [39] M. K. Hong, S. Erramilli, P. Huie, G. James, A. Jeung, Scanning near-field infrared microscope with a free electron laser illumination source. *SPIE* 2863, 54 (1997).
- [40] D. T. Schaafsma, R. Mossadegh, J. S. Sanghera, I. D. Aggarwal, J. M. Gilligan, N. H. Tolk, M. Luce, R. Generosi, P. Perfetti, A. Cricenti, G. Margaritondo, Singlemode chalcogenide fiber infrared SNOM probes. *Ultramicroscopy* 77, 77 (1999).
- [41] J. S. Sanghera, L. B. Shaw, L. E. Busse, D. Talley, I. D. Aggarwal, Infrared Transmitting Fiber Optics for Biomedical Applications. Accepted for publication in *SPIE* 1999.
- [42] D. T. Schaafsma, J. A. Moon, J. S. Sanghera, I. D. Aggarwal, Fused Taper Infrared Optical Fiber Couplers in Chalcogenide Glass. *J. Lightwave Tech.* 15 [12] 2242 (1997).
- [43] R. Reisfeld, A. Bornstein, *Chem. Phys. Lett.* 47 [1] 194 (1997).
- [44] A. Bornstein, R. Reisfeld, Laser emission cross-section and threshold power for laser operation at 1077 nm and 1370 nm; chalcogenide mini-lasers doped by  $\text{Nd}^{3+}$ . *J. Non-Cryst. Solids* 50, 23 (1982).
- [45] R. Reisfeld, A. Bornstein, *J. Non. Cryst. Sol.* 27, 143 (1978).
- [46] R. Reisfeld, *Ann. Chim. Fr.* 7, 147 (1982).
- [47] C. C. Ye, D. W. Hewak, M. Hempstead, B. N. Samson, D. N. Payne, Proposal for an  $\text{Er}^{3+}$ -doped chalcogenide glass fiber upconversion laser operating at 980 nm and pumped at 1480 nm. *J. Non. Cryst. Solids* 208, 56 (1996).
- [48] J. Moon, B. B. Harbison, J. S. Sanghera, I. D. Aggarwal, Rare Earth Doped Chalcogenide Glasses for use in Mid-IR Sources. J. Moon, B. B. Harbison, J. S. Sanghera, I. D. Aggarwal. *Proc. of Photonics'96*, Dec. 9-13, Madras, India 1996.
- [49] Y. B. Shin, W. Y. Cho, J. Heo, Multiphonon and cross-relaxation in Ge-As(or Ga)-S glasses doped with  $\text{Tm}^{3+}$ . *J. Non. Cryst. Solids* 208, 29 (1996).
- [50] Y. B. Shin, J. N. Jang, J. Heo, Mid-infrared light emission characteristics of  $\text{Ho}^{3+}$ -doped chalcogenide and heavy-metal oxide glasses. *Opt. and Quant. Electron.* 27, 379 (1995).
- [51] L. B. Shaw, B. H. Harbison, B. Cole, J. S. Sanghera, I. D. Aggarwal, Spectroscopy of the IR transitions in  $\text{Pr}^{3+}$  doped heavy metal selenide glasses. *Optics Exp.* 1 [4] 87 (1997).
- [52] T. Schweizer, D. W. Hewak, B. N. Samson, D. N. Payne, *J. Luminescence* 72-74, 419 (1997).
- [53] L. B. Shaw, B. J. Cole, J. S. Sanghera, I. D. Aggarwal, D. T. Schaafsma, Dy-doped Selenide Glass for 1.3  $\mu\text{m}$  Optical Fiber Amplifiers. *Optical Fiber Communications*, paper WG8, San Jose, CA 1998.
- [54] T. Schweizer, B. N. Samson, R. C. Moore, D. W. Hewak, D. N. Payne, *Electron. Lett.* 33 [5] (1997) 414.
- [55] A. Mori, Y. Ohishi, T. Kanamori, S. Sudo, Optical amplification with neodymium-doped chalcogenide glass fiber. *Appl. Phys. Lett.* 70 [10] 1230 (1997).
- [56] M. Yamada, M. Shimizu, Y. Ohishi, J. Temmyo, M. Wada, T. Kanamori, M. Horiguchi, S. Takahashi, *IEEE Photonics Technol. Lett.* 9, 994 (1992).
- [57] B. Cole, L. B. Shaw, P. C. Pureza, R. Mossadegh, J. S. Sanghera, I. D. Aggarwal, Rare Earth Doped Selenide Glass Fibers. Accepted for publication in *J. Non-Cryst. Solids* (1999).
- [58] L. B. Shaw, D. T. Schaafsma, B. J. Cole, B. Harbison, J. S. Sanghera, I. D. Aggarwal, Rare Earth Doped Glass Fibers as Infrared Sources for IRSS. *SPIE* 3368, 42 (1998).
- [59] M. Asobe, T. Ohara, I. Yokohama, T. Kaino, Fabrication of Bragg grating in chalcogenide glass fiber using the transverse holographic method. *Electron. Lett.* 32, 1611 (1996).
- [60] H. Nasu, Y. Ibara, K. Kubodera, Optical third-harmonic generation from some high index glasses. *J. Non-Cryst. Solids* 110, 229 (1989).
- [61] K. A. Richardson, J. M. McKinley, B. Lawrence, S. Joshi, A. Villeneuve, Comparison of non-linear optical properties of sulfide glasses in bulk and thin film form. *Opt. Mats.* 10, 155 (1998).
- [62] M. Asobe, T. Kanamori, K. Kubodera, Ultrafast all-optical switching using highly nonlinear chalcogenide glass fiber. *IEEE Photonics Technol. Letts.* PIL4, 362 (1992).
- [63] E. M. Dianov, P. G. Kazansky, D. Yu. Stepanov, Problem of the photoinduced second harmonic generation in optical fibers. *Sov. J. Quant. Electron.* 19, 575 (1989).
- [64] M. T. de Arujo, M. V. D. Vermelho, A. S. Gouveia-Neto, A. S. B. Sombra, J. A. Medeiros Neto, Efficient second-harmonic generation in praseodymium doped Ga-La-S glass for 1.3  $\mu\text{m}$  optical fiber amplifiers. *IEEE Photonics Technol. Letts.* 8, 821 (1996).
- [65] P. G. Kazansky, P. S. J. Russell, H. Takabe, Glass fiber poling and applications. *J. Lightwave Tech.* 15, 1484 (1997).
- [66] B. B. Harbison, J. S. Sanghera, J. A. Moon, I. D. Aggarwal, Infrared transparent selenide glasses. US Patent # 5, 846, 889 (1998).

## CHALCOGENIDE GLASSES AS SENSITIVE MEMBRANES FOR THE DETECTION OF IONS IN SOLUTION

A. Pradel, O. Valls, C. Cali, G. Taillades, A. Bratov<sup>a</sup>, C. Dominguez<sup>a</sup>, M. Ribes

Laboratoire de Physicochimie de la Matière Condensée UMR 5617 CC3

Université Montpellier II 34095 Montpellier cedex 5 France

<sup>a</sup>Instituto de Microelectronica de Barcelona Campus UAB 08193, Bellaterra Barcelona Spain

The sensing properties of two chalcogenide materials, i. e. a glass ceramic of composition  $\text{Cu}_{10}(\text{As}_{0.4}\text{S}_{0.6})_{90}$  and an amorphous thin film obtained by RF sputtering of a composite target  $\text{Cu} / \text{Ge}_{28}\text{Sb}_{12}\text{Se}_{60}$  glass, were investigated. The glass ceramic was shown to be sensitive to both sulphide and copper in solution while the thin film only shows a response to  $\text{Cu}^{2+}$  ions. The  $\text{Cu}_{10}(\text{As}_{0.4}\text{S}_{0.6})_{90}$  membrane was included in a module which allowed continuous monitoring of sulphide in thermal waters. A miniaturised device for the detection of  $\text{Cu}^{2+}$  ions was developed by depositing the film  $\text{Cu} - \text{Ge} - \text{Sb} - \text{Se}$  onto the gate of a pH ISFET.

(Received July 12, 2001; accepted September 3, 2001)

**Keywords:** Ion selective electrode, ISFET,  $\text{Cu}^{2+}$  detection, Sulphide detection, Cu-Ge-Sb-Se film

### 1. Introduction

In the last years the need for analytical devices to be used for environmental, industrial or medical controls has been growing very quickly. Depending upon the concerned field two main requests can be noticed : 1) one for systems which could be used continuously on line and 2) one for miniaturised systems. Laboratory techniques involving conditioning of the sample to be analysed are not well adapted to these requirements. Even though they usually do not give as precise data as the above cited techniques chemical sensors could bring some interesting solutions. In particular chemical sensors based upon chalcogenide materials are well adapted to the detection of chemical species in solution. They can reach the present needs for in situ use and miniaturisation since they are very durable in particular in neutral and acidic media and they can be easily shaped in thin films by the usual techniques of microelectronics. Moreover their very versatile composition allows the fabrication of specific membranes for many different types of ions (heavy metals such as  $\text{Cu}^{2+}$ ,  $\text{Cd}^{2+}$ ,  $\text{Pb}^{2+}$ ,  $\text{Hg}^{2+}$ , anions such as  $\text{S}^{2-}$ , halide ions...) [1-5].

The present work is related to the use of two different chalcogenide membranes for the detection of ions in solution, i. e. a glass ceramic of composition  $\text{Cu}_{10}(\text{As}_{0.4}\text{S}_{0.6})_{90}$  and an amorphous thin films obtained by RF sputtering of a composite target  $\text{Cu} / \text{Ge}_{28}\text{Sb}_{12}\text{Se}_{60}$  glass. An autonomous monitoring system for sulphide in solution including an ion selective electrode based upon the first material has been developed in the framework of the work. The  $\text{Cu} / \text{Ge-Sb-Se}$  thin film has been used to modify the gate of a pH ISFET and thus to produce miniaturised devices for the detection of copper in solution.

### 2. Experimental

#### 2. 1. Preparation and characterisation of ion sensitive materials

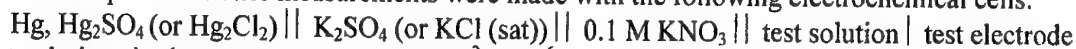
The compound  $\text{Cu}_{10}(\text{As}_{0.4}\text{S}_{0.6})_{90}$  was synthesised by melting appropriate amount of  $\text{As}_2\text{S}_3$  and copper metal (99.99%, Aldrich) in silica tubes evacuated to  $10^{-5}$  Pa at  $950^\circ\text{C}$  for 24 h and further water quenching. Cu-Ge-Sb-Se glassy thin films were obtained by RF sputtering of a composite target comprising a 50mm copper metal disk with 10mm  $\text{Ge}_{28}\text{Sb}_{12}\text{Se}_{60}$  glassy disks stuck on the top of it.

The films were deposited either directly on a Si / Si<sub>3</sub>N<sub>4</sub> substrate (ISFET gate) or after deposition of a thin Cr layer on the Si / Si<sub>3</sub>N<sub>4</sub> substrate (ISE structure). The obtained materials, either bulk or thin films, were characterised by X ray diffraction (Seifert) and scanning electron microscopy (Cambridge 360). Chemical analysis was performed using an EDS probe. Conductivity measurements were performed with a HP4192A impedance meter in the temperature range 25-130°C.

## 2. 2. Preparation and characterisation of ion selective electrodes (ISE)

In the case of bulk Cu<sub>10</sub>(As<sub>0.4</sub>S<sub>0.6</sub>)<sub>90</sub> the ion selective electrodes were prepared from discs (1 mm in thickness and 10 mm in diameter) cut from the melts and polished. A platinum layer was then deposited on a face of the disk by sputtering. The microelectrode comprised two parts: the Cu-Ge-Sb-Se glassy thin film as the sensitive membrane and a Cr layer as a collector. In both cases a wire was attached to the metallised face with silver micro-adhesive. This inner part of the electrodes was isolated from the external medium with an epoxy resin.

The potentiometric measurements were made with the following electrochemical cells:



Test solutions in the concentration range  $10^{-2} - 10^{-6}$  M were prepared by successive tenfold dilutions of 1 M Cu(NO<sub>3</sub>)<sub>2</sub> or 1 M Na<sub>2</sub>S<sub>9</sub>H<sub>2</sub>O solutions by the supporting electrolyte (0.1 M potassium nitrate) for copper and sulphide calibrations respectively. The selectivity of the sensors was tested using the mixed solution method with a constant concentration in interfering ion.

The determination of sulphide in solution was also carried out by employing a potentiometric titration with mercuric chloride and end point determination with a selective silver electrode type ISE25S-9 (Radiometer, Denmark).

## 2.3. Preparation and characterisation of microsensors based upon an ion sensitive field effect transistor (ISFET)

The ISFET based sensors sensitive to Cu<sup>2+</sup> ions were obtained by first depositing the Cu-Ge-Sb-Se sensitive membrane onto the whole surface of Si wafers containing ISFET structures initially designed for the fabrication of pH ISFET at the Centro Nacional de Microelectronica in Barcelona [6]. The film was then selectively removed so that it covered only the surface of the gate (Si<sub>3</sub>N<sub>4</sub>). Removal of the chalcogenide film was achieved either by chemical etching and by lift off. In both cases the optimisation of the process was carried out on test samples. Masks used for chemical etching allowed the design of four plots of 1mm in diameter on Si<sub>3</sub>N<sub>4</sub> substrates. Several acid and/or oxidising etching solutions were tested. The test samples for lift off were silicon nitride substrates covered with a photoresist layer into which hexagonal motives were opened.

The electrical characterisation of the Cu<sup>2+</sup> sensitive ISFET sensors was carried out using a HP 4145B semiconductor parameter analyser allowing the measurement of current as low as 1000 pA with a 1 pA resolution. The electrochemical characterisation of the ISFETs were performed using an home-made ISFET meter developed at CNM. It consisted in measuring the variations of the gate voltage while dipping the sensors in solutions containing different concentrations of copper nitrate. Identical test solutions as those used for the electrochemical characterisation of the Cu<sup>2+</sup> ISE were used for the calibration of ISFET.

## 2.4. Fabrication of a prototype for continuous on line detection of sulphide

The Cu<sub>10</sub>(As<sub>0.4</sub>S<sub>0.6</sub>)<sub>90</sub> electrode, a commercial pH electrode (Heito) and a temperature sensor (Pt100) were included in a measurement module developed by the company TMI-Orion in order to monitor the variation in sulphide concentration in two thermal springs. The programmable module could be immersed at a depth of 1 meter and allowed measurement and data storage over periods of several months.

## 3. Results and discussion

### 3.1. Characterisation of ion sensitive materials

The two selected chalcogenide membranes have very different characteristics. Indeed while the X ray diffraction pattern of the Cu-Ge-Sb-Se films deposited by RF sputtering is that of an

amorphous material, the X-ray diffraction pattern of bulk  $\text{Cu}_{10}(\text{As}_{0.4}\text{S}_{0.6})_{90}$  indicated partial crystallisation with the presence of sinnerite  $\text{Cu}_6\text{As}_4\text{S}_9$  in its triclinic form. In agreement SEM observations of  $\text{Cu}_{10}(\text{As}_{0.4}\text{S}_{0.6})_{90}$  material indicated the presence of an heterogeneous multiphase system with a crystalline material distributed throughout an amorphous matrix while the surface of the Cu-Ge-Sb-Se thin films observed by SEM was very smooth. In that case EDS measurements helped in knowing the film composition i. e.  $(\text{Sb}_{11}\text{Ge}_{29}\text{Se}_{60})_{50}\text{-Cu}_{50}$  with variation of about 5% in copper from one film to the other. We can note that the relative amount of Ge, Sb, Se is close to that existing in the bulk glass used for the target. It is noteworthy that the material the richer in copper is amorphous while the poorer shows partial crystallisation. It is attributed to the very different procedures of preparation, RF sputtering inducing easily disorder.

It is known that materials with very low conductivity cannot be used successfully as sensitive membranes for the detection of ion in solution since it induces very long response times and unstable electrochemical characteristics [1]. In our case the room temperature conductivity for both samples, i.e.  $2 \times 10^{-2} (\Omega \text{ cm})^{-1}$  for  $\text{Cu}_{10}(\text{As}_{0.4}\text{S}_{0.6})_{90}$  and  $3 \times 10^{-2} (\Omega \text{ cm})^{-1}$  for  $(\text{Sb}_{11}\text{Ge}_{29}\text{Se}_{60})_{50}\text{-Cu}_{50}$  film, should be large enough to overcome such drawbacks. We also noted in the course of the experiment the absence of polarisation phenomena (a single circle in the Cole-Cole plots) which is indicative of a large part of electronic conduction in both samples.

### 3.2. Ion selective electrodes (ISE)

#### (i) ISE for the detection of $\text{Cu}^{2+}$ ions in solution

Both chalcogenide membranes, i. e.  $\text{Cu}_{10}(\text{As}_{0.4}\text{S}_{0.6})_{90}$  material and  $(\text{Sb}_{11}\text{Ge}_{29}\text{Se}_{60})_{50}\text{-Cu}_{50}$  film, were tested as sensitive membrane for the detection of  $\text{Cu}^{2+}$  ion in solution.

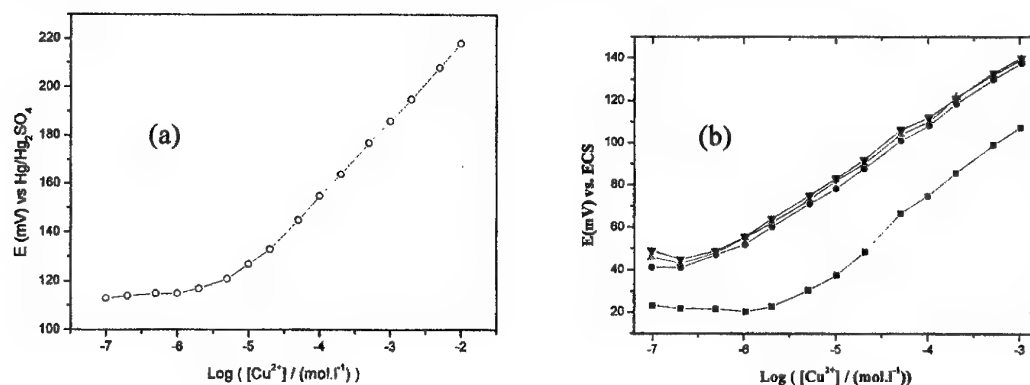


Fig. 1. Potentiometric response of (a) the  $\text{Cu}_{10}(\text{As}_{0.4}\text{S}_{0.6})_{90}$  membrane sensor and (b) the  $(\text{Sb}_{11}\text{Ge}_{29}\text{Se}_{60})_{50}\text{-Cu}_{50}$  microsensor.

Typical calibration curves are shown in figure 1. Both sensors exhibited a fast  $\text{Cu}^{2+}$  ion response. As shown in Fig. 1 for the  $(\text{Sb}_{11}\text{Ge}_{29}\text{Se}_{60})_{50}\text{-Cu}_{50}$  microsensor the result of the first calibration previous to conditioning differed from the subsequent ones by lower values of both standard potential and slopes. After few measurements the sensor characteristics became more stable. For both materials the potentiometric response obeyed the Nernst law with a slope of about 30 mV / pCu above pCu = 5. The limit of detection was close to  $10^{-6} \text{ M Cu}^{2+}$ .

The microsensor based upon the  $(\text{Sb}_{11}\text{Ge}_{29}\text{Se}_{60})_{50}\text{-Cu}_{50}$  film alone was investigated more thoroughly since we were looking more specifically for a miniaturised device for the  $\text{Cu}^{2+}$  detection to be used in a multisensor array in the future.

The  $(\text{Sb}_{11}\text{Ge}_{29}\text{Se}_{60})_{50}\text{-Cu}_{50}$  sensors showed good long term stability over periods of several weeks as shown in Fig. 2. However a slight drift in absolute potential with time, i. e. a change of about 1.5 mV per day, was observed.

Selectivity coefficients of the sensors against several interfering ions were measured and are given in Table 1. A high selectivity in the presence of alkali and alkaline-earth ions was observed whereas the only heavy-metal ion to interfere significantly with the sensors is  $\text{Fe}^{3+}$ . These results are

comparable to those already reported for similar sensitive membranes based upon bulk or thin film chalcogenide glasses [7,8].

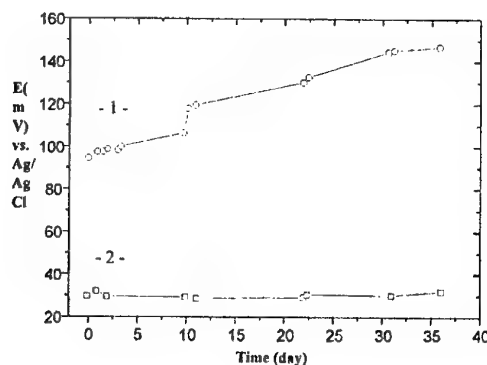


Fig. 2. Changes in time in the potential (1) and the slope (2) of the  $(\text{Sb}_{11}\text{Ge}_{29}\text{Se}_{60})_{50}\text{-Cu}_{50}$  membrane electrode in  $\text{Cu}(\text{NO}_3)_2$   $10^{-4}$  M solution.

Table 1. Selectivity coefficients against several interfering ion species for the Cu-Ge-Sb-Se membrane.

Interfering ion	Log $K_{\text{Cu}^{2+}/\text{M}^{2+}}$
$\text{K}^+$	-5.1
$\text{Na}^+$	-5.3
$\text{Ca}^{2+}$	-5.1
$\text{Ni}^{2+}$	-4.1
$\text{Cd}^{2+}$	-4.1
$\text{Pb}^{2+}$	-2.5
$\text{Mn}^{2+}$	-3.4
$\text{Fe}^{3+}$	-1.3

#### (ii) ISE for the detection of sulphide ions in solution

$\text{H}_2\text{S}$  is a diprotic acid ( $\text{pK}'_1 = 7$  and  $\text{pK}'_2 = 14$ ), so the concentration of the three sulphide species depend strongly of pH.

A first series of calibrations was based on the  $S_T = [\text{S}^{2-}] + [\text{HS}^-] + [\text{H}_2\text{S}]$  variation using pH 7 buffered solutions. While the electrodes based upon  $(\text{Sb}_{11}\text{Ge}_{29}\text{Se}_{60})_{50}\text{-Cu}_{50}$  films always gave unstable response whatever the conditioning the electrodes based upon  $\text{Cu}_{10}(\text{As}_{0.4}\text{S}_{0.6})_{90}$  material revealed to be interesting sensors for the detection of sulphide ions in solution. Indeed after conditioning in a solution of 0.01 M  $\text{Na}_2\text{S}$ ,  $9\text{H}_2\text{O}$  the electrodes gave stable electrochemical characteristics. A typical calibration curve is shown in Fig. 3. The potentiometric response displayed a near-Nernstian slope of about 55 – 65 mV /  $\text{pS}_T$ . The limit of detection was close to  $2 \times 10^{-6}$  M  $S_T$ . It corresponds to a high sensitivity to total sulphide concentration since the limitation of the standard method (as described in the experimental section) is reached for  $S_T = 10^{-4}$  M. Note that similar results for the standard method and the  $\text{Cu}_{10}(\text{As}_{0.4}\text{S}_{0.6})_{90}$  electrode were obtained for solutions where the total sulphide concentration lies in the range  $10^{-4} - 10^{-2}$  M.

A second set of electrochemical measurements for the  $\text{Cu}_{10}(\text{As}_{0.4}\text{S}_{0.6})_{90}$  electrode was based on the  $\text{S}^{2-}/\text{HS}^-$  ratio variation using pH modification with constant  $S_T$ .

Calibrations were performed in solutions containing concentrations in total sulphide equal to  $10^{-4}$ ,  $10^{-3}$ ,  $10^{-2}$  M. The pH of the solutions was monitored in the range 3 – 12 by adding adequate amount of HCl (1M) or NaOH (1M). A constant voltage drop close to 60 mV between the different curves as shown in figure 4.a demonstrates that the sensor is sensitive in the entire pH range investigated. Moreover, the variation of potential is nearly constant for  $\text{pH} > 7$  while a Nernstian behaviour was observed in the 3-7 pH range. These variations are closely correlated with the variation of  $\text{HS}^-$  concentration with pH. Indeed according to the equilibrium between the different sulphide

species (Fig. 4.b) for a given  $S_T$ , the  $HS^-$  concentration increases linearly versus pH in the range 3–7 then reaches a nearly constant value above pH 7. Such a correlation might indicate that the electrode is sensitive to  $HS^-$  species.

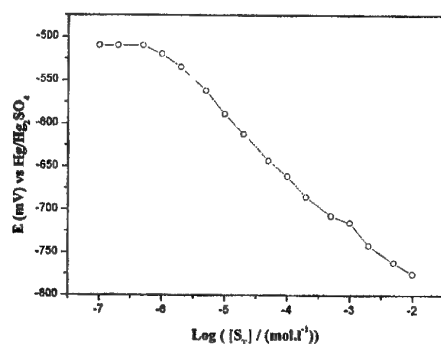


Fig. 3. Potentiometric response of a  $Cu_{10}(As_{0.4}S_{0.6})_{90}$  membrane electrode vs total sulphide concentration.

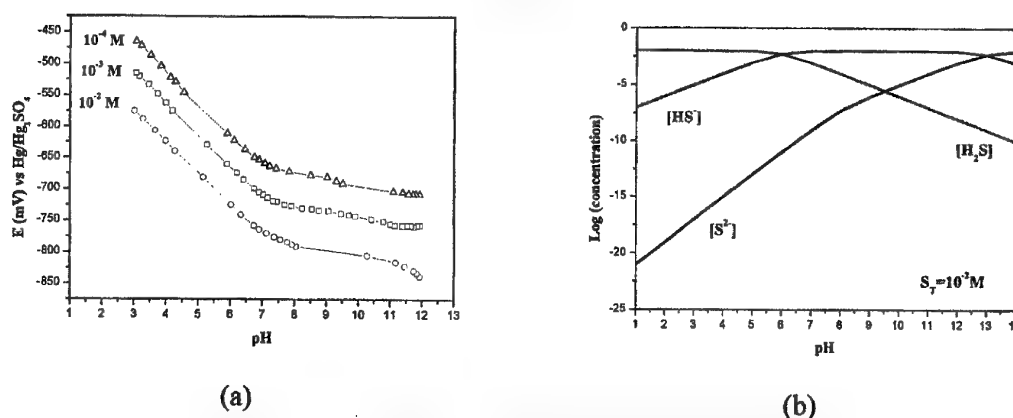


Fig. 4. (a) pH influence on potentials in different total sulphide concentration and (b) pH influence on the concentration of the different sulphide species.

Table 2. Selectivity coefficients against several interfering ion species for the Cu – As – S membrane electrode.

Interfering ion	Log $K_{Cu^{2+}/Mz^{+}}$
$Cl^-$	-5.1
$I^-$	-5.3
$NO_3^-$	-5.1
$SO_4^{2-}$	-4.1
$CH_3COO^-$	-4.1

The selectivity of the  $Cu_{10}(As_{0.4}S_{0.6})_{90}$  electrode against several interfering anions was tested. The results are summarised in table 2.  $10^3$ – $10^6$ -fold amounts of sulphate, chloride, iodide, nitrate and acetate do not influence the electrode potential. These results are comparable to those already reported for glassy-crystalline sensors sensitive to bromide [4]. The sensor was also shown to be insensitive to alkali and alkaline-earth ions. Obviously as shown in the previous section the sensor is sensitive to copper ions.

### 3.3. ISFET sensors for the detection of $Cu^{2+}$ in solution

#### (i) Preparation of modified ISFET

Owing to the interesting electrochemical characteristics of the  $(Sb_{11}Ge_{29}Se_{60})_{50}-Cu_{50}$  film, we considered them as potential candidates for the fabrication of ISFET sensors sensitive to  $Cu^{2+}$  ions in solution. The gate of ISFET structures had to be modified by deposition of the chalcogenide film. The



procedure that was developed to achieve this goal was to deposit the film on the whole surface of wafers containing the ISFETs then to remove the film selectively so that only the gate remained covered. Two photolithography processes were developed. First chemical etching of the film was considered since it usually leads to high resolution of the desired pattern. Because of the high copper content in the film strong oxidising acid etching solutions were tested at once. In fact the first solution used is that developed for chemical polishing of InSb. It contains  $\text{CH}_3\text{COOH}$ ,  $\text{HNO}_3$ ,  $\text{HF}$ ,  $\text{H}_2\text{O}$  and  $\text{K}_2\text{Cr}_2\text{O}_7$ . Many trial and error tests showed that  $\text{HF}$  and  $\text{CH}_3\text{COOH}$  could be discarded. Adjustment of the volume ratios of the remaining components in order to obtain reasonable etching time and high resolution of the patterns led to the following optimised solution :  $\text{HNO}_3$  /  $\text{K}_2\text{Cr}_2\text{O}_7$  /  $\text{H}_2\text{O}$  in volume ratio 1 / 4 / 45.

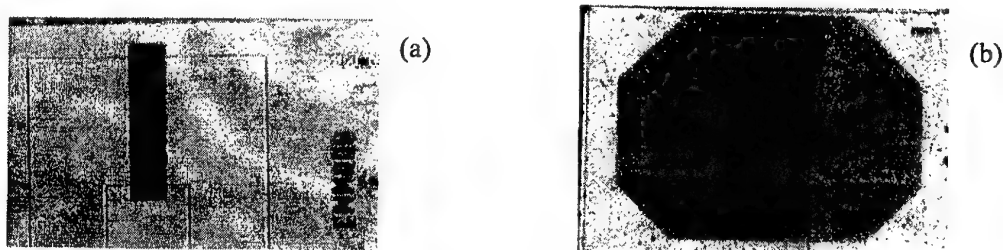


Fig. 5. Preparation of modified ISFET by (a) chemical etching and (b) lift off process.

While the chemical etching gave excellent resolution of the pattern on the gate as shown in Fig. 5 (a) it appeared impossible to remove the chalcogenide film from the Al current collector of the ISFET. Obviously the Cu-Ge-Sb-Se films had reacted with the Al current collectors and the resulting Al/Cu alloy could not be removed by etching. An additional step had then to be added to the original design of the ISFET structure. It consisted in protecting the Al current collector by an epoxy layer previous to the deposition of the Cu chalcogenide film.

The lift off process was then considered since in that case the Si wafer and thus the Al current collectors were already protected by the photoresist previous to the deposition of chalcogenide film. The hexagonal patterns observed on Fig. 5 (b) correspond to the chalcogenide glass over the gate of the ISFET (dark rectangular). The resolution of the pattern is very good. After deposition of the chalcogenide films the best resolution of the patterns was obtained by immersing the sample in an ultrasonic bath containing acetone for 30 seconds.

Even though chemical etching can be used it appeared that the lift off process was preferable since 1) it helps in reducing the number of steps in the photolithography procedure and 2) it can be used as such for the development of other modified ISFET using other types of chalcogenide films.

### (ii)Electrical characterisation of the modified ISFET

The electrical characteristics of the modified ISFETs prepared by lift off were checked before to perform the electrochemical characterisation. As a matter of fact it was not possible to discard at once eventual damage which could occur during the deposition of the chalcogenide films due to some polarisation effect for example.

A typical  $I_{gs}$ - $V_{gs}$  curve for a  $(\text{Sb}_{11}\text{Ge}_{29}\text{Se}_{60})_{50}\text{-Cu}_{50}$  modified ISFET prepared by lift off when  $V_{ds} = 500$  mV is shown in figure 6. The maximum remaining current  $I_{gs}$  is 0.65 nA which is negligible and will not affect the ISFET behaviour. The characteristics  $I_{ds}$ - $V_{gs}$  for several modified ISFETs measured with  $V_{gs} = 500$  mV are given in Fig. 7. Threshold voltages (obtained by extrapolation of the linear part of the curves) are largely smaller than the upper acceptable limit of  $\pm 3$  V. All ISFETs are sensitive to changes in gate voltage and therefore should be sensitive to any change in the  $\text{Cu}^{2+}$  ion concentration of the solution in contact with the gate.

### (iii) Electrochemical characterisation of the modified ISFET

The electrochemical characterisation of several ISFET prepared by lift off was carried out. A typical calibration curve obtained after conditioning the sensor in a  $10^{-3}$  M  $\text{Cu}(\text{NO}_3)_2$  is reported in figure 8. A near-Nernstian response with a slope of 28 mV per pCu was obtained. The limit of detection was close to  $10^{-6}$  M. The response time was about 5 seconds. These characteristics are very

similar to those obtained with the ISE prepared with the same membrane and somewhat comparable to the two other modified ISFETs for the detection of copper ion in solution described to date and based upon a  $\text{Cu-As}_2\text{Se}_3$  layer on one hand [9] and a calix[11]arene grafted gate on the other [10]. The main drawback of the present ISFETs is a very short lifetime, 20 to 40 hours in the average. The ISFETs fail by detachment of the membrane from the gate. It seemed to be due to constraints induced in the film during the drying and hardening of the encapsulation layer. Such a technological problem is currently being considered and should be settled down soon.

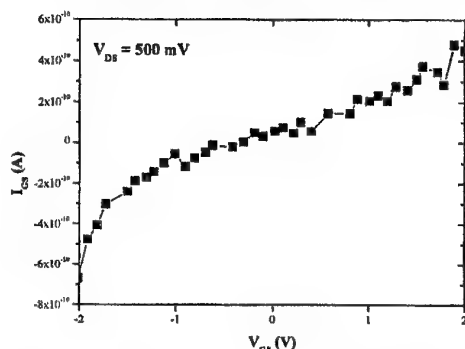


Fig. 6.  $I_{gs} - V_{gs}$  curve for a  $(\text{Sb}_{11}\text{Ge}_{29}\text{Se}_{60})_{50}\text{-Cu}_{50}$  modified ISFET.

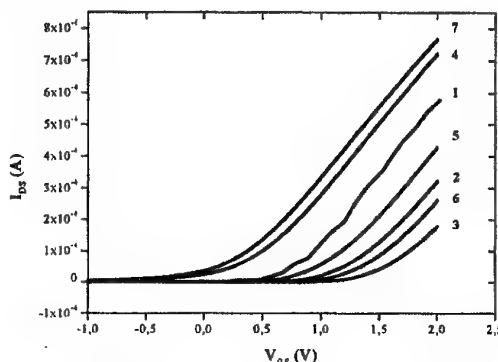


Fig. 7. characteristics  $I_{ds} - V_{gs}$  for several modified ISFET from the same wafer.

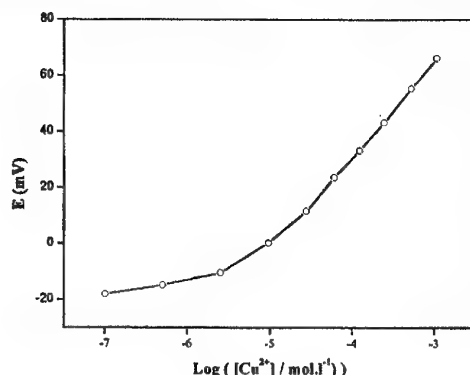


Fig. 8. Typical calibration curve of the ISFET in  $\text{Cu}(\text{NO}_3)_2$  solution.

### 3.4. Fabrication of a prototype for continuous on line detection of sulphide

The main interest for developing new ISE lies in original properties and experimental advantages that existing systems would not have. To date commercial electrodes for the detection of sulphide in solution work only at basic pH. The sensors based upon the  $\text{Cu}_{10}(\text{As}_{0.4}\text{S}_{0.6})_{90}$  can work at neutral and slightly acidic media which is the case of most natural media. Therefore these sensors could be considered for continuous in situ control of sulphide in natural solution e. g. in thermal water. To test the validity of the concept a programmable module was developed in collaboration with the company TMI-Orion and tested for several months in two thermal waters, i. e. where the sulphide concentration lies in the range 90 – 100  $\text{mg.l}^{-1}$  for a temperature of about 17°C and where the sulphide concentration lies in the range 1 – 3  $\text{mg.l}^{-1}$  for a temperature of about 40°C.

Fig. 9 depicts the profiles of electrode potential and temperature recorded for a period of 5 days in thermal water containing significant amounts of sulphate (1g.l<sup>-1</sup>), chloride (9.4  $\text{mg.l}^{-1}$ ) and fluoride ions (1.3  $\text{mg.l}^{-1}$ ). The fluctuations in potential, i. e. in sulphide concentration, are closely related to the pumping cycles. As a matter of fact the sensor potential increases (i.e. the sulphide concentration decreases) when the pumping system is turned off which corresponds to out gassing of  $\text{H}_2\text{S}$ . Note that it corresponds also to nights which is in agreement with the lower temperature. This results indicated the good sensitivity of the sensor to sulphide. The sensor was tested continuously during more than 3 months. It remained sensitive for such a long period of time in this medium and showed high long term stability.

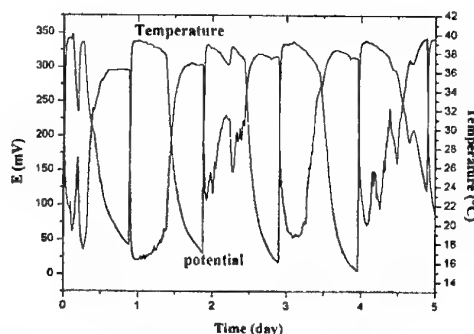


Fig. 9. Profiles of electrode potential and Temperature in thermal water.

## 5. Conclusion

Two chalcogenide materials were studied for their ion sensing properties. One is a glass ceramic of composition  $\text{Cu}_{10}(\text{As}_{0.4}\text{S}_{0.6})_{90}$ , the second is an amorphous thin film obtained by RF sputtering of a composite target  $\text{Cu}/\text{Ge}_{28}\text{Sb}_{12}\text{Se}_{60}$  glass.

Even though they are very different materials both proved to be sensitive to  $\text{Cu}^{2+}$  ion in solution.

The  $\text{Cu}_{10}(\text{As}_{0.4}\text{S}_{0.6})_{90}$  glass ceramic was also shown to be sensitive to sulphide in solution. The ability of such a sensor to work in neutral and slightly acidic medium led us to develop an in situ on line monitoring system for sulphide in thermal water.

On the other hand the sensitivity of the amorphous  $(\text{Sb}_{11}\text{Ge}_{29}\text{Se}_{60})_{50}\text{-Cu}_{50}$  thin film to copper ion in solution led us to use them as the sensitive membrane of modified ISFET. The good electrical and electrochemical characteristics of the ISFET obtained in this work show the potentiality of these films even though technological problems need still to be solved before having devices with satisfying lifetime.

In conclusion we have shown in this work the ability of chemical sensors based upon chalcogenide membranes to bring interesting solutions for the current needs for 1) devices which could be used continuously on line and 2) which could be miniaturised.

## Acknowledgments

The authors wish to thank the CNRS and the "région Languedoc – Roussillon" for financial support. TMI Orion is gratefully acknowledged for its participation in on site measurements.

## References

- [1] Yu. G. Vlasov, E. A. Bychkov, Ion-Selective Reviews, vol. 9, p 5-93 (1987).
- [2] Yu. G. Vlasov, E. A. Bychkov, A. V. Legin, Chalcogenide glass chemical sensors research and analytical applications, *Talanta* 41 (6), 1059-1063 (1994).
- [3] C. Bohnke, J. P. Malugani, A. Saida, G. Robert, Conductivité électrique et sélective des verres  $\text{AgPO}_3 - \text{MI}_2$  avec  $\text{M} = \text{Pb}, \text{Hg}$ , *Electrochim. Acta*, 26, 1137 (1981).
- [4] Y. G. Vlasov, L. N. Moskvina, E. A. Bychkov, D. V. Golikov, Silver Bromide Based Chalcogenide Glassy – Crystalline Ion-selective Electrodes, *Analyst*, 114, 185-190 (1989).
- [5] C. Cali, G. Taillades, A. Pradel, M. Ribes, Determination of sulfur species using a glassy – crystalline chalcogenide membrane, *Sensors and Actuators B* 76, 560-564 (2001).
- [6] S. Alegret, J. Bartroli, C. Jimenez, M. del Valle, C. Dominguez, E. Cabruja, A. Merlos, pH-ISFET with NMOS technology, *Electroanalysis* 3, 355-360 (1991).
- [7] E. A. Bychkov, M. Bruns, H. Klewe-Nebenius, G. Pfenning, W. Hoffmann, H. J. Ache,  $\text{Cu}^{2+}$  selective thin films for chemical microsensors based on sputtered copper-arsenic-selenium glass, *Sensors and Actuators B* 24-25, 733-736 (1995).
- [8] G. Taillades, O. Valls, A. Bratov, C. Dominguez, A. Pradel, M. Ribes, ISE and ISFET microsensors based on a sensitive chalcogenide glass for copper ion detection in solution, *Sensors and Actuators B* 59, 123-127 (1999).
- [9] Yu. A. Tarantov, et al., *Sensors and Actuators*, B1, 390-394 (1990).
- [10] Ben-Ali, M., et al., *Thin Solid Films*, 383, 292-295 (2001).

## ELECTRON BEAM INDUCED PATTERNS IN Ag/GeS<sub>4</sub>

J. S. Romero, A. G. Fitzgerald, K. Mietzsch

Carnegie Laboratory of Physics, Department of Electronic Engineering and Physics,  
University of Dundee, Dundee DD1 4HN, UK

The results of a systematic study of the formation of patterns by an electron beam in GeS<sub>4</sub> are reported. A scanned electron beam has been shown to induce the dissolution of silver into the chalcogenide matrix in the irradiated areas. The dissolution produces an expansion of the material in the irradiated region that is believed to be due to the fact that the density of the reaction product is less than the average density of the silver and chalcogenide layers [11]. Once the chemical reaction was completed, no further migration of silver towards the irradiated area was observed in the Ag/GeS<sub>4</sub> thin films.

(Received June 6, 2001; accepted September 3, 2001)

*Keywords:* Ag/GeS<sub>4</sub>, Electron beam irradiation, Silver dissolution and diffusion

### 1. Introduction

Glassy Ge<sub>x</sub>S<sub>1-x</sub> exhibits interesting properties in the presence of metals upon electron beam irradiation [1-3]. The dissolution of silver into chalcogenides assisted by UV light has been extensively studied by a number of researchers [1-4]. The most widely accepted model suggests that the incorporation of silver occurs as a result of the presence of a negative charge in the undoped region. The negative charge arises as a consequence of the generation of electron-hole pairs by UV light absorption. The holes, which have a higher mobility in chalcogenide glasses, diffuse towards the non-irradiated area, while the electrons are trapped in localized states. This gives rise to an electric field in the film, which then enables cationic migration to occur [5].

Although much attention has been devoted to the dissolution of the metal by UV light, to the best of our knowledge few studies have been performed on the dissolution of silver in Ge<sub>x</sub>S<sub>1-x</sub> by electron beams [6,7]. Yoshikawa et al. [6] and Oldale and Elliot [7] have reported lateral diffusion of silver, dendritic deposition, crystallization and structural changes but the dissolution of silver in the amorphous matrix induced by electrons is still not well understood. This effect has potential applications in the patterning of GeS<sub>4</sub> by electron beams, because the doped compound is resistant to acid and alkaline solutions [8] making it easy to fabricate lines of sub-micrometre dimensions. The use of this system as an electron resist for mask fabrication is also possible.

### 2. Experimental

The chalcogenide glass was obtained by synthesis from the elements Ge and S (purity 99.99%) heated at 1000 °C for 18 hours in an evacuated silica ampoule and cooled by rapid quenching in an ice-water mixture [9]. A JEOL T220 secondary electron microscope (SEM), in which the electron beam was controlled by a computer, was used for electron beam writing, while the chemical composition of the material was analysed by energy dispersive x-ray analysis (EDX) in a JEOL T300 SEM equipped with an ANS 400 x-ray microanalysis system. Thin films of the chalcogenide were obtained by physical vapor deposition. These films were investigated using a JEOL 100C transmission electron microscope (TEM) and were found to be amorphous.

Thin films of GeS<sub>4</sub> were deposited on a variety of substrates: silicon wafers, silicon wafers coated with silver, silica and silica coated with silver. The silica substrates were obtained through the reaction of oxygen with a polished silicon wafer, which resulted in a silicon substrate with a 0.5 µm thick silica film on top. To study the effect of the electron gun setup on the formation of the patterns, thin films were evaporated onto the substrates at a pressure of about 10<sup>-5</sup> torr. The film thicknesses were about 200 nm for the chalcogenide and 20 nm for the silver layer. To study the characteristics of the silver dissolution into the chalcogenide matrix, more complex samples were produced. GeS<sub>4</sub> films

of 100 nm thickness were deposited on top of a 15 nm thick silver film, whereby the silver film was only underlying half of the  $\text{GeS}_4$  film. For the removal of the chalcogenide film and the silver coating, a 0.1 M NaOH bath and 40%  $\text{HNO}_3$  was used respectively. UV light exposures were performed using a high-pressure 200 W mercury lamp with the principal emission lines of around 370 nm and 435 nm. All patterns were analysed using a Dimension 3000 atomic force microscope (AFM).

### 3. Results and discussion

#### 3.1 Silver dissolution in Ge-S assisted by electron irradiation

Two experiments have been designed in order to determine the mechanism of pattern formation on chalcogenide thin films that have been deposited onto silicon or silica substrates.

In the first experiment 15 nm of silver and 80 nm of  $\text{GeS}_4$  were deposited in this order onto a silica substrate. The chemical composition of the chalcogenide films was analysed by x-ray microanalysis and confirmed to be  $\text{Ge}_{20}\text{S}_{80}$ . Patterns were written for different exposure times and with different electron gun set-ups. The chemical composition in the irradiated area was monitored during the electron beam irradiation and in all cases no change was observed in the silver concentration during the exposure. After the irradiation a set of line patterns could be observed on the surface.

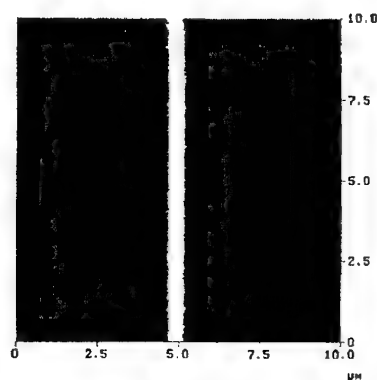


Fig. 1. AFM top view of a pattern written on a silica substrate after etching (Width = 0.4  $\mu\text{m}$ ).

The samples were then immersed in a NaOH bath for a few seconds. The material in the non-irradiated area was dissolved in the solution leaving the patterns unaffected. To remove the remaining silver, the surface was treated with a  $\text{HNO}_3$  solution, which did not affect the structures. The dimensions of the patterns were measured in the AFM. Fig. 1 presents a top view of such a pattern created within 30 seconds at 15 kV and 0.5 nA.

It is believed that the electron beam induces a chemical reaction between silver and the chalcogenide in the irradiated area. The reaction product was found to be resistant to NaOH and  $\text{HNO}_3$  solutions. Oldale et al. [4] and Eneva et al. [11] performed similar experiments using UV light and found that the reaction product has a fixed stoichiometry. This explains why no further increase in silver concentration was detected after the chemical reaction was completed.

For the second experiment a sample with the structure presented in Fig. 2 (10 nm silver and 130 nm  $\text{GeS}_4$ ) was prepared. The chemical composition of the chalcogenide was  $\text{Ge}_{20}\text{S}_{80}$ . The sample was illuminated for 2 hours by a mercury lamp. After that time the sample experienced a colour change in the area where the silver was deposited (photodissolution [2-4]). A careful x-ray microanalysis was undertaken at the interface between the silver/chalcogenide and the chalcogenide. Silver x-ray peaks appeared only in the area where silver had been deposited but not in the areas where no silver had been deposited. It can therefore be concluded that UV radiation cannot induce lateral migration of silver towards the undoped region.

Subsequently, a set of lines was written across the interface using an electron beam of 20 kV accelerating voltage and 0.8 nA beam current. Exposure times for the lines were varied between 5 and 30 minutes. The whole sample was then introduced into a NaOH bath. The lines were not removed by the NaOH but all of the surrounding material was removed. This leads to the conclusion that the

scanned electron beam has induced a lateral migration of the silver towards the undoped region. The silver then reacted with the chalcogenide directly beneath the irradiated area and formed a reaction product which is resistant to alkaline solutions.

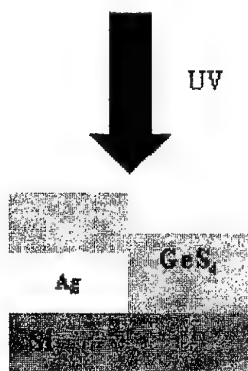


Fig. 2 Experimental setup to determine the lateral diffusion effect of silver.

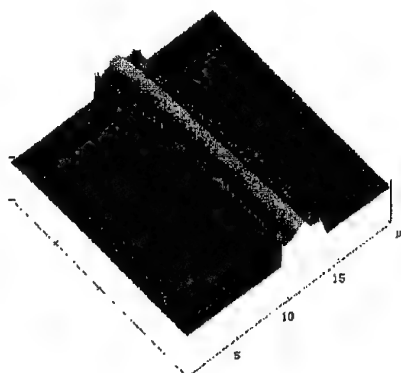


Fig. 3 AFM surface image of a pattern on a silica substrate after etching with NaOH. Width 4.3  $\mu\text{m}$ , Height 154 nm.

Fig. 3 presents an AFM image of such a pattern written for 40 minutes after etching. Fig. 4 shows a section analysis from two patterns, the first one written for 5 minutes and the second one written for 30 minutes. All images were taken after the removal of the surrounding material. Fig. 3 and Fig. 4 show the effect of the electrons in the chalcogenide film. From these pictures it can be seen that there are two stages of the pattern formation. During the first stage silver is dissolved into the material without preserving the density. The second stage begins when the chemical reaction between the chalcogenide and the silver is completed. No more silver can be dissolved in the matrix and the deformation of the material occurs with the density being preserved. The first stage can be identified in the first picture of Fig. 4 and the second stage in the second picture of the same figure. The peripheral depression and the central expansion can be clearly distinguished in this picture.

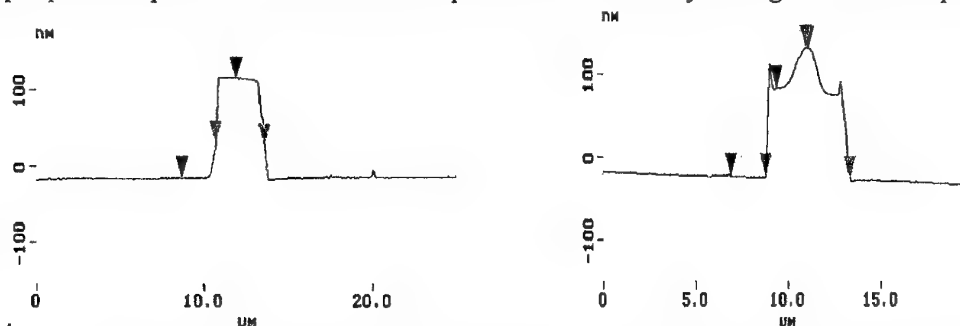


Fig. 4. AFM section analysis of line patterns drawn for 5 min and 30 min after etching in NaOH solution.

In order to clarify whether the continued irradiation with the electron beam could produce the precipitation of silver on the top of the features the sample was introduced into HNO<sub>3</sub>, which can remove silver but not the doped material. The features were subsequently measured in the AFM but no changes in the dimensions of the lines were observed. This demonstrates that the electronic charge due to the electron beam can produce dissolution of silver but cannot attract silver ions to the surface of the pattern.

Fig. 5 shows the dependence of the thickness, the width and the volume of the patterns on the exposure time. In all the three cases it can be seen that the data can be fitted to a linear dependence. The slopes of the three graphs were calculated to be:

Width	2 nm/s
Thickness	0.02 nm/s
Volume	$2.7 \cdot 10^{-4} \mu\text{m}^3/\text{s}$

This data shows that the increase in the volume of the patterns results principally from the increase in width. The observed results agree very well with the model proposed by Kokado et al. [5] for the dissolution of metals in amorphous chalcogenides assisted by UV light. In this model the metal-chalcogenide junction is considered to be a Schottky contact in which the silver cations are promoted into the chalcogenide when the junction is negatively biased by excited electrons that are trapped at dangling bonds. Similarly, the presence of electrons in the undoped chalcogenide film can bias the junction negatively, reinforcing the threshold field and attracting silver ions to the negative contact.

On the basis of this model and assuming that the interaction volume represents the negative contact, the increase in size of the patterns must be a consequence of the diffusion of electrons over time. From Fig. 5 it can be seen that the increase in width is the main cause of the increase of volume of the patterns. Since all lines, regardless of their exposure time, have the same length, which is very much larger than the width, the silver must migrate very quickly towards the irradiated area. Hence, the time constant for the recombination of silver ions with the electrons is much shorter than the exposure times used in the experiments. If it is assumed that once a steady state is established the incoming electrons produce a constant negative space charge in the film (interaction volume) and that the silver cations migrate towards this area in a very short time, then, the increase in the volume of the patterns must be a consequence of the spread of that space charge. From Fig. 5 it is clear that this space charge or interaction volume (mainly the width of this region) increases slowly with exposure time. This increase could be due to two mechanisms, the deflection of the main beam as a result of the surface being charged or the diffusion of the electrons towards the undoped region. The former mechanism has a low probability since the electrons have a high energy, the chalcogenide films are too thin and the silicon substrates have a relatively good conductivity. This makes the capacity for retaining charge limited. The latter effect is the more likely main mechanism for the increase in width of the features. It is believed that in the steady state the difference in electron density between the interaction volume and the surroundings will incur the diffusion of electrons into the surroundings, thereby increasing the size of the interaction volume and causing more silver to migrate into the newly created regions of electronic charge. This effect then leads to the broadening of the lines with exposure time.

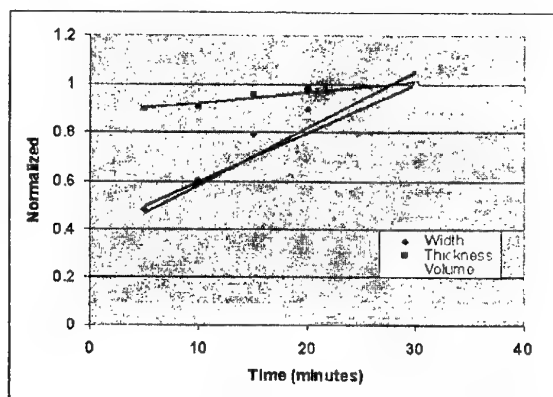


Fig. 5. Time dependence of the thickness, the width and the volume of the patterns.

### 3.2. Effect of accelerating voltage and beam current on the pattern formation

Thin films of 200 nm of  $\text{GeS}_4$  and 20 nm of silver were deposited onto a silica substrate with the silver film underlying the  $\text{GeS}_4$ . A set of patterns was written on the surface using different electron gun set-ups. These patterns were subsequently measured in the AFM. All patterns were written for 5 minutes with an electron beam of 0.45 nA beam current. Fig. 6 shows the dependence of the thickness, the width and the volume of the patterns on the accelerating voltage. The y-axis is



normalized. The maximum values are 32 nm for the thickness and 820 nm for the width. The figure shows that the volume of the patterns decreases with increasing accelerating voltage. The specimen current was monitored during the exposure and is shown in Fig. 7. This figure shows that at 5 kV accelerating voltage the specimen current is only 30% of the beam current but this percentage increases at higher accelerating voltages. This indicates that at low accelerating voltages more electrons are retained in the sample increasing the density of electrons in the interaction volume, thus creating a stronger electrostatic field inside the film, which in turn increases the migration of silver ions towards the irradiated area. The minimum width obtained was around 0.5  $\mu\text{m}$ .

Patterns were also written using different beam currents for the range of accelerating voltages used. Generally the volume of the lines has a maximum at a beam current of about 0.5 nA. This can be understood on the basis of the following model. Beam currents below about 0.5 nA cannot create a strong enough electric field to produce an effective dissolution of silver, whereas higher beam currents can overheat the sample and partially evaporate the material. The latter effect has been confirmed by irradiating samples with beam currents of high intensity. All features written with currents above 4 nA were valleys rather than hills for all accelerating voltages used.

Common characteristics of all patterns are that the thickness does not increase very much during long exposures and that the density does not remain constant as implied from the shapes of the electron beam generated patterns. These facts suggest that the formation of the patterns could be due to the expansion of the doped material. The incoming electrons induce the silver reaction with the chalcogenide. This chemical reaction is well-defined [4] and produces deformation of the surface because the density of the reaction product is lower than the average density of the initial silver and chalcogenide layers.

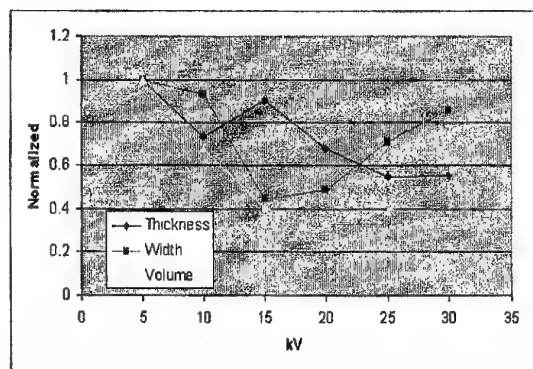


Fig. 6. Dependence of the thickness, the width and the volume on the accelerating voltage at a beam current of 0.4 nA and 5 minutes of irradiation.

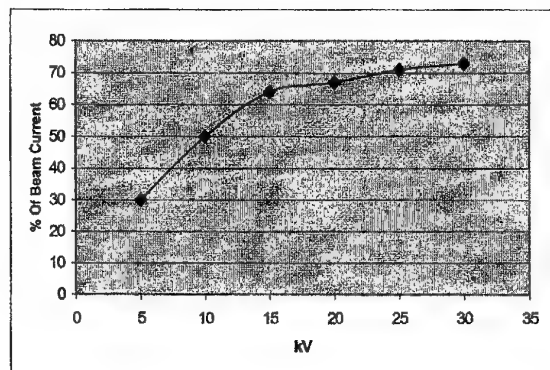


Fig. 7. Dependence of the specimen current on the accelerating voltage.

If this explanation is accepted then it appears logical that the use of a lower accelerating voltages produces the largest features. Lower accelerating voltages also give lower specimen currents [Fig. 7] and can therefore accumulate more charge for the same time of exposure and can hence produce the largest features.

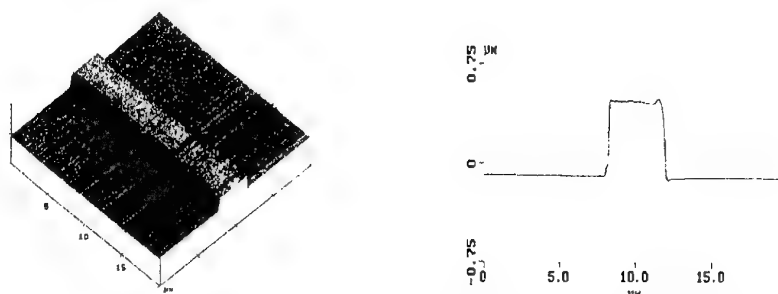


Fig. 8. Surface and profile of a pattern written on silicon with 5 minutes at 15 kV of accelerating voltage and 0.5 nA of electron beam current. Width 4  $\mu\text{m}$ , Height 570 nm.

#### 4. Conclusions

It has been shown that silver can be dissolved in  $\text{GeS}_4$  by irradiation with UV light or by electron beam irradiation. Although the effects appear very similar, some important differences were observed. During UV light exposure, no lateral diffusion of silver was observed, while during electron beam exposure a lateral diffusion of silver took place.

It was demonstrated that fine line structures could be produced by scanning a focused electron beam across the surface of a  $\text{Ag/GeS}_4$  sample. The formation of these patterns occurs in two stages. During the first stage the silver dissolves into the chalcogenide and forms a reaction product of fixed stoichiometry, which is resistant to alkaline and acid solutions. The density of the reaction product in the irradiated area is less than the average density of the initial  $\text{Ag/GeS}_4$  films and an expansion of the irradiated area occurs. Once the reaction between the chalcogenide and the silver is completed, the second stage commences. A further expansion of the irradiated area is observed, but now the density of the expanded area remains constant, and the expansion is now accompanied by a peripheral depression. During this stage no further migration of Ag was observed.

It was found that the highest features could be produced when using low accelerating voltages and an electron beam current of about 0.45 nA. The produced features were found to be resistant to alkaline and acid solutions. Therefore, these solutions can be used to remove the surrounding material, leaving the patterns unaffected and strongly attached to the substrate.

The effects described above demonstrate the potential application of the  $\text{Ag/GeS}_4$  system in the fabrication of line structures.

#### Acknowledgements

The authors would like to thank EPSRC for the financial support of this project.

#### References

- [1] C. P. McHardy, A. G. Fitzgerald, P. A. Moir, M. Flynn, *J. Phys. C: Solid State Phys.* **20**, 4055 (1987).
- [2] A. V. Kolobov, S. R. Elliot, *Advances in Physics*, **40** (N 5), 625 (1991).
- [3] A. V. Kolobov, S. R. Elliot, M. A. Taguizdzhyanov, *Philosophical Magazine B*, **61**, (N 5), 859 (1990).
- [4] J. M. Oldale S. R. Elliot, *Journal of non crystalline solids*, 255 (1991).
- [5] H. Kokado, I. Shimizu, E. Inoue, *J. non Crystalline Solids*, **20**, 131 (1976).
- [6] T. Kawaguchi, S. Maruno, K. Masai, *J. non Crystalline Solids* **77&78**, 1141-1144 (1985).
- [7] J. M. Oldale, S. R. Elliot *Appl. Phys. Lett.* **63** (13) (1993).
- [8] I. Shimizu, H. Sakuma, H. Kokado, E. Inoue, *Photogr. Sci. Eng.* **16**, 291 (1972).
- [9] K. Tanaka, Y. Ksanuki, A. Odajima, *Thin solids films* **117**, 251 (1984).
- [10] K. Tanaka, *Appl. Physics Letters* **70** (2) 1997.
- [11] J. Eneva, A. Gusterov, B. Tomerova, B. Mednikarov, *Journal of materials science: Materials in Electronics* **10**, 529-531 (1999).

## TRANSIENT PHOTOCURRENT TECHNIQUES AS A MEANS OF CHARACTERISING AMORPHOUS SEMICONDUCTORS

C. Main, D. Nesheva<sup>a</sup>

University of Abertay Dundee, Bell Street, Dundee DD1 1HG, UK.

<sup>a</sup>Institute of Solid State Physics, Bulgarian Academy of Sciences  
Boul. Tzarigradsko chaussee 72, Sofia 1784, Bulgaria

We describe techniques to study electronic transport and localized state distributions in amorphous semiconductors from their photocurrent response to steady and impulse excitation. The response to impulse excitation contains information on distributions of trapping and release times for localized states in the mobility gap of the material; the problem is to determine a unique density of states (DOS) from such data. One technique is applicable to cases in which both trapping and release processes are significant. A second 'post-transit' analysis is restricted to situations where only carrier release processes are significant. In both cases we derive analytical DOS spectroscopies capable of fine energy resolution. We also report on studies of transport and DOS distributions, in thin films of several representative chalcogenides, including recent studies of surface defect states in CdSe nanocrystals in SiO<sub>x</sub> matrix. We also report on interpretation of steady state and transient measurements on thin film amorphous As<sub>2</sub>Se<sub>3</sub>.

(Received June 25, 2001; accepted September 3, 2001)

**Keywords:** Transient photocurrent, Amorphous chalcogenides, CdSe nanocrystals

### 1. Introduction

In 'transient photocurrent' experiments, a semiconductor is excited with a short pulse of light, and the photocurrent response  $i(t)$  is measured. Two possibilities are discussed below. The first is the transient photocurrent (TPC) experiment in which a gap-cell is used, with ohmic contacts. The second is the post – transit experiment in which a high reverse field is applied to non-injecting contacts on 'sandwich' device. Either method may be used to determine the energy distribution of various species of gap states which influence carrier mobilities and lifetimes in the semiconductor, under the assumption that the response is controlled by multi-trapping processes. A reliable method would represent a valuable diagnostic tool for material quality.

The TPC method avoids extraction of charge at contacts, and the response may be considered to be a complex function of trapping and release involving the whole ensemble of localised states, and also recombination processes [1]. On the other hand, the post-transit response is a much simpler process, determined only by the collection of charge being released from successively deeper traps [2,3]. Thus the analytical approaches to determination of the gap-state distribution are necessarily very different.

Recently there has been much interest in the electronic transport and optical properties of semiconductor nanoparticles, in particular CdSe nanocrystals in SiO<sub>x</sub>/CdSe multilayer and composite SiO<sub>x</sub>-CdSe films [4,5]. Defect states in these films have been studied by sub-band absorption and thermally stimulated currents. It would be very useful to complement such studies using the ability of TPC to probe a wide energy range in a single measurement. In this study, we report on preliminary work on such materials.

Work on steady state and transient photoconductivity in amorphous As<sub>2</sub>Se<sub>3</sub> has been reported by the author [6,7] and others [8]. Such measurements have been interpreted as revealing a broad featureless exponential tail of states above the valence band mobility edge (TPC) [9], or in contrast, a fairly well defined set of recombination centres in the gap [7]. In this paper, we return to the topic, in the light of the more recent findings from TPC analysis methods, in an attempt to reconcile these differences, perhaps speculatively.

## 2. DOS spectroscopy

### 2.1 TPC Theory

A continuous  $g(E)$  may be represented by a finely spaced ladder of  $m$  discrete levels, of spacing  $\delta E$  and density  $N_{ii} = g(E_i)\delta E$ . The basic multi-trapping equations are,

$$\frac{dn(t)}{dt} = -\sum_i^m \frac{dn_{ii}(t)}{dt} - \omega_R n(t) + N_0 \delta(t), \quad (1)$$

and

$$\frac{dn_{ii}(t)}{dt} = -\omega_{ei} n_{ii}(t) + \omega_{ii} n(t), \quad (2)$$

where  $n(t)$  is the free carrier density at time  $t$ ,  $n_{ii}(t)$  is the instantaneous trapped carrier density at the  $i^{\text{th}}$  level localized state below the mobility edge,  $\omega_R$  is the recombination rate constant,  $N_0$  is the initial generated excess density,  $\omega_{ei} [= \exp(-E_{ii}/kT)]$  is the release rate constant and  $\omega_{ii} [= \nu s g(E_i)\delta E]$  is the capture rate constant for the  $i^{\text{th}}$  localized state. Energy  $E_{ii} = i\delta E$  is the depth of the  $i^{\text{th}}$  level,  $\nu$  is the attempt to escape frequency,  $s$  is the capture cross-section and  $v$  is the thermal velocity.

Applying a Fourier transform to Eqs. (1) and (2), gives in the frequency domain,

$$\hat{n}(\omega) = \int_0^\infty n(t) [\cos(\omega t) - j \sin(\omega t)] dt = \frac{N_0}{(A_\omega + jB_\omega)}, \quad (3)$$

where, treating the density of states (DOS) as continuous in energy,

$$A_\omega = \omega_R + \int_0^{E_f} \nu \sigma g(E) \left( 1 + \exp\left(-\frac{2(E_\omega - E)}{kT}\right) \right)^{-1} dE \quad (4)$$

and

$$B_\omega = \frac{i(0) \sin(\phi(\omega))}{|\hat{I}(\omega)|} = \omega + \int_0^{E_f} \frac{\nu \sigma}{2} g(E) \operatorname{sech}\left(\frac{E_\omega - E}{kT}\right) dE. \quad (5)$$

In the above,  $\hat{I}(\omega)$  represents the frequency domain photocurrent associated with  $\hat{n}(\omega)$ ,  $i(0)$  is the initial value of the transient photocurrent – i.e. when all  $N_0$  excess carriers are free, and  $E_f$  is the Fermi energy. The term  $k$  is Boltzmann's constant, and  $T$  is the absolute temperature.

Eq. (5) is a Fredholm integral equation of the first kind, and is 'ill-conditioned'. A simple approximate solution used by the authors [10] replaces the peaked sech function with a delta function, to give

$$g(E) \approx \frac{2}{\nu \sigma \pi kT} \left( \frac{i(0) \sin(\phi(\omega))}{|\hat{I}(\omega)|} - \omega \right). \quad (6)$$

This approximation results in an effective ' $kT$  broadening' effect – see section 3.1 below. More rigorous solutions for the analogous integral equation obtained by Laplace transformation have been attempted by Gueorguieva *et al.* [11], Naito and co-workers, using specialized techniques such as Tikhonov regularization [12, 13]

In our proposed approach, the high-resolution FT method (HFT) we convert Eq. (5) back to a summation over a fine ladder  $g(E_{ij})\Delta E$  of discrete traps, to give,

$$\frac{i(0) \sin(\phi(\omega))}{|\hat{I}(\omega)|} - \omega = \sum_j \frac{\nu \sigma}{2} g(E_{ij}) \Delta E \operatorname{sech}\left(\frac{E_\omega - E_{ij}}{kT}\right). \quad (7)$$

The left hand side of Eq. (7) represents information obtained from experiment, although  $i(0)$  may not be observable in practice. The discrete array of energies  $E_{ij} = j\Delta E$  need not coincide with the original  $E_{ii}$  above. The magnitude of the second term  $\omega$ , is not significant in the frequency range encountered experimentally. The right side, with the DOS implicit in a summation, is obtained from

multi-trapping theory. In our proposed HFT method, we solve Eq. (7) for  $g(E_{ij})$ , fitting the right side of Eq. (7) to the experimental data, whilst retaining the sech function of Eq. (5). We use a finely spaced set of model functions,  $A_j \frac{\nu\sigma}{2} \Delta E \operatorname{sech}((E_\omega - E_{ij})/kT)$ , with a general least-squares fitting technique LMDIF1 [14], where the  $A_j [= g(E_{ij})]$  are the adjustable fitting parameters. Specific values of  $w$  are selected at intervals to give equi-spaced  $E_\omega [= kT \ln(\nu/\omega)]$ , over the related energy range. In general a very good fit for the amplitude parameters  $A_j$  and hence  $g(E_{ij})$  may be obtained, with overall standard error values of  $< 1\%$ .

We note that the analysis performed on Eq. (7) does not require knowledge of the recombination constant  $\omega_R$ , and hence the recombination time  $t_R [= 1/\omega_R]$ . The important consequence of this is that the proposed analysis can be applied to  $i(t)$  data which span both pre- and post-recombination (or post-transit) time regimes.

## 2.2 'Post - Transit' theory

Fig. 1 compares the computed relative distribution of excess trapped charge in an exponential band-tail under conditions with no extraction (*pre-transit*) and with extraction (*post-transit*), after the same elapsed time ( $10^{-4}$  s) from initial excitation. The sharp variation in occupation in the latter case presents the possibility of improvement in resolution, over the methods of the previous section.

We consider again that the continuous density of states may be represented by a very fine ladder of discrete trapping levels  $N_{ii}$ ,  $i = 1, 2, \dots, m$ , at associated energies  $E_i$ . Of the initial excess electron density  $N_0$  introduced by pulsed excitation, a fraction  $N'$  is trapped, and the remainder is removed by collection, so that

$$N' = N_0 \frac{t_0}{t_0 + \tau_t}, \quad (8)$$

where  $t_0$  is the transit time of free electrons and  $t_t$  is the trapping time into the ensemble of traps, of total density  $N_T$ . The initial trapped fraction  $n_{ii}(0)$  is distributed according to the density of trapping states, assuming an energy-independent capture coefficient, so we may write for the trapped electron distribution

$$n_{ii}(0) = N_{ii} N' / N_T. \quad (9)$$

In the post-transit situation, the multi-trapping rate equation for free electron density  $n$  reduces to

$$\frac{dn}{dt} = \sum_i n_{ii}(t) \nu \exp\left(\frac{E_i}{kT}\right) - \frac{n}{t_0}, \quad (10)$$

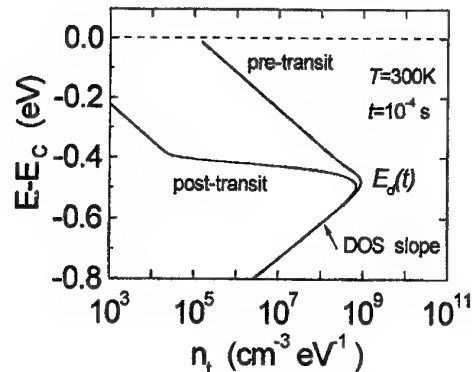


Fig.1 Computed distributions at time  $10^{-4}$  s after excitation, of excess trapped charge in an exponential band - tail of characteristic energy 50 meV, for pre - transit and post-transit cases.

The sharp edge in occupation caused by trap - stripping in the post-transit case is evident.

where the summation is necessarily only over deep-lying states whose combined trapping time is greater than the transit time. Retrapping terms are considered by definition to be negligible, so we can also write

$$n_i(t) = n_i(0) \exp\left(-\frac{t}{\tau_i}\right), \quad (11)$$

where  $t_i$  is the average thermal release time from states at level  $i$ .

The solution to Eq. 10 is

$$n(t) = n(0) \exp\left(-\frac{t}{t_0}\right) + \sum_i n_i(0) \nu \exp\left(\frac{E_i}{kT}\right) \frac{\exp\left(-\frac{t}{\tau_i}\right) - \exp\left(-\frac{t}{t_0}\right)}{1/t_0 - 1/\tau_i}, \quad (12)$$

which under post-transit conditions ( $t, t_i \gg t_0$ ), gives to a good approximation,

$$i(t) = e\mu\mathcal{E}An(t) \approx e\mu\mathcal{E}A \sum_i n_i(0) \frac{t_0}{\tau_i} \exp\left(-\frac{t}{\tau_i}\right), \quad (13)$$

where  $e$  is the electronic charge,  $\mu$  is the electron mobility,  $\mathcal{E}$  is the applied field, and  $A$  is the conduction cross sectional area of the sample. At this point, the 'standard' analysis [2] converts the summation to an integral over a continuous distribution, to the form of a Laplace transform, and replaces the exponential trap release time distribution factor in Eq. (13) with a delta function  $t_i \delta(t-t_i)$ . This approximation is equivalent to the assumption that all traps at a given depth release at the same time. The result is

$$g(E) \approx ti(t) \left( \frac{N_T}{N'e\mu\mathcal{E}At_0kT} \right). \quad (14)$$

The *alternative* proposed here, is to *retain* the trap release time distribution function of Eq. (13) and simply perform a *fit* to the photocurrent  $i(t)$  of Eq. (13), with a finely spaced set of model functions,  $(A_j/\tau_j) \exp(-t/\tau_j)$ , again using the least-squares fitting technique LMDIF1 [14], where the set  $A_j$  are the adjustable fitting parameters. Values of  $t_j$  are pre-selected so that the energy range covered is appropriate to the time range of the  $i(t)$  data set. Normally values are again chosen to give a uniform spacing  $\Delta E$  ( $< kT$ ) between levels on the energy scale. We note that since the distribution of states is assumed to be continuous, the choice of  $t_j$  is arbitrary, and thus not necessarily identical to  $t_i$ , as long as the energy spacing is very close ( $< kT$ ). In general a very good fit may be obtained, with overall standard error value of  $< 1\%$ . The amplitude parameters  $A_j$  are equated with  $e\mu\mathcal{E}An_{ij}(0)$  giving the HPT result,

$$g(E_j) \approx A_j \left( \frac{N_T}{N'e\mu\mathcal{E}At_0\Delta E} \right), \quad (15)$$

for the density of states at energy  $E_i$ .

### 2.3. Experimental

Preliminary TPC measurements have been made on  $\text{SiO}_x/\text{CdSe}$  multilayer and composite  $\text{SiO}_x$  -  $\text{CdSe}$  films ( $x \sim 1.5$ ) having varying  $\text{CdSe}$  sublayer thicknesses and average nanocrystal sizes. The total film thickness is about  $0.2 \mu\text{m}$  for the multilayers and  $1.5 \mu\text{m}$  for the composite films. The samples were fabricated as sublayers from  $\text{SiO}_x$  and  $\text{CdSe}$  on Corning 7059 glass substrates by thermal evaporation of powdered  $\text{CdSe}$  and granular  $\text{SiO}$  from two independent sources. Details of the films, preparation, charge transport measurements and structure are given in earlier publications [4,5]. Coplanar sputtered gold electrodes about  $10\text{mm}$  long, with  $1 \text{mm}$  gaps were deposited on the surface of the samples.

The TPC measurements were made using applied voltages of  $100\text{V} - 500\text{V}$ , and a temperature range of  $293 - 423 \text{K}$ . A nitrogen pumped dye laser (Laser Science VSL-337) was used to produce photogeneration pulses of width  $4\text{ns}$  at a wavelength of  $500 \text{nm}$ . Incident photon densities were approximately  $10^{14} \text{cm}^{-2}$ . Special purpose wideband DIFET current-mode op-amp circuits were used to process the sample current, the decay curves presented in this work being composites of the response at several instrumental bandwidths. The current data were sampled and averaged using a fast digitizing oscilloscope (Tektronix TDS3052), before storage and processing by PC. The transient

current component  $i(t)$  was calculated by subtracting the steady state current  $I_{ss}$  sampled immediately prior to each laser firing. Time was allowed for relaxation between each firing.

We note that any calculation of a 'density of states' from the TPC data obtained in this way will at present only result in an effective DOS for the sample as a whole. However, the relative energy profile of gap states is returned, and this should be of use in determining film quality, and in studying the effects of structural variation.

### 3. Results and discussion

#### 3.1. TPC simulation

To evaluate the HFT method, we computed the  $i(t)$  response to impulse excitation for several representative distributions of traps, using a numerical procedure developed by the authors [9]. We then performed a numerical Fourier transform on  $i(t)$  to obtain  $\hat{I}(\omega)$ , and calculated the density of states using a fitting procedure with Eq. (7). In addition to this comparison, we calculated the density of states from the  $i(t)$  data, using the approximate expression of Eq. (6).

In Fig. 2, we show the computed  $i(t)$  vs  $t$  on log-log axes, at temperature 300K for exponential tail distributions with a range of characteristic slope energies  $E_{ct}$ , from 50 meV down to 10 meV. This covers cases in which the distribution is broader than  $kT$  (25 meV) to those in which the distribution is much narrower than  $kT$ .

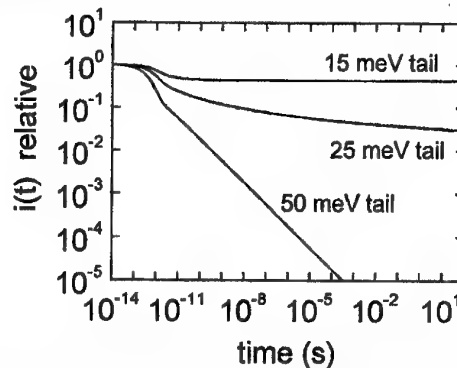


Fig. 2. Simulated transient photocurrent decays for exponential band-tails of various characteristic energies. Simulation temperature: 300K.

The broad distribution,  $E_{ct} = 50$  meV results in an  $i(t)$  which follows the well known power law form  $i(t) \propto t^{-(1-\alpha)}$  where  $\alpha = kT/E_{ct}$ . It is often assumed that such a power law automatically indicates the existence of an exponential band-tail, but this is not necessarily true, as we show below.

In Fig. 3, we display the DOS distributions obtained using the approximate FT method of equation 6, and our precise method of equation 7. It can be seen that the approximate method cannot reproduce the DOS in cases where the tailing is steep, i.e. where  $E_{ct} < kT$ . In such cases, the method returns a spurious DOS with characteristic energy broadened to a value of about  $kT$ . On the other hand, our high-resolution HFT method can recover the DOS quite well, even when the tail energy is much less than  $kT$ .

In Fig. 4, we show the reproduced  $g(E)$  when the original distribution is a steep exponential tail of characteristic energy  $E_0 = 35$  meV, with superimposed, a sharp Gaussian feature peaking at  $E_b = 0.3$  eV of form  $g_b(E) = D \exp(-((E - E_b)/E_1)^2)$ . The energy  $E_1 = 25$  meV (FWHM = 41.6 meV) and the factor  $D$  is chosen to give a peak 100 times the background tail density at the center of the feature. Now we see the ' $kT$  broadening' of the approximate FT method, which almost obscures any structure, while the HFT method follows the original density well on both sides of the Gaussian feature.



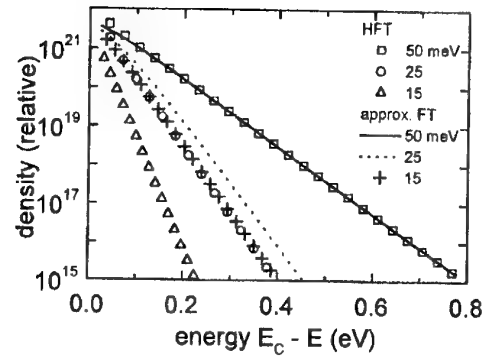


Fig.3 Density of states  $g(E)$  recovered from computed  $i(t)$  at 290K, for three exponential tails, Comparison of FT and HFT methods. Note: the HFT method returns a DOS of the correct slope, while the FT method fails for slopes  $< kT$ .

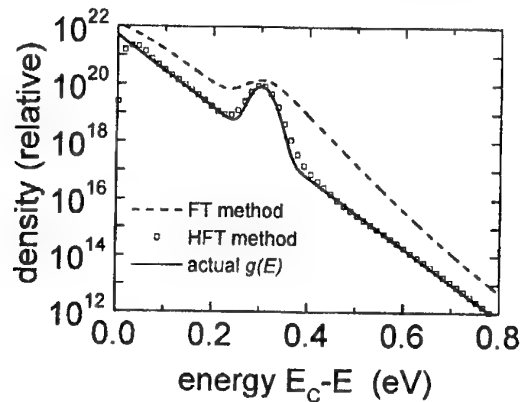


Fig. 4. Density of states  $g(E)$  recovered from computed  $i(t)$  at 290K, for an exponential tail, with a sharp Gaussian feature. Comparison of FT and HFT methods.

In Fig. 5, we test the method using two *discrete* levels of equal density,  $1.0 \times 10^{17} \text{ cm}^{-3}$ , at depths 0.3 and 0.5 eV, flanking a *third* discrete level of *lower* density,  $1.0 \times 10^{16} \text{ cm}^{-3}$  at 0.4 eV depth. We note that the discrete levels are represented now by a  $g(E)$  distribution, which when integrated should represent the same total density. The approximate FT method results in broadening, of FWHM = 67 meV ( $\sim 2.6 kT$ ) obscuring the presence of the low density middle level, and introducing also a spurious band-tailing effect closer to the band edge. It is clear that the HFT method gives a much sharper reproduction, FWHM = 27 meV ( $\sim kT$ ) also allowing ready identification of the centre level.

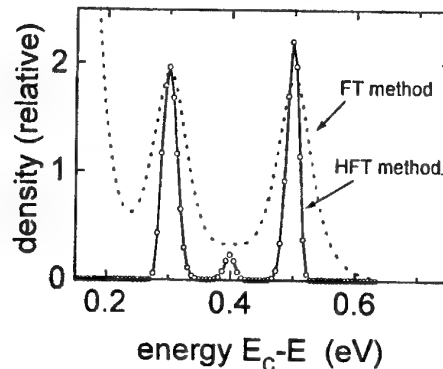


Fig. 5. Density of states  $g(E)$  recovered from computed  $i(t)$  at 290K, for Two discrete levels at 0.3 and 0.5 eV depth flanking a third discrete level of 1/10 density at 0.4 eV depth Comparison of FT and HFT methods.

### 3.2. Post – transit simulation

To evaluate the proposed method, we computed the  $i(t)$  response under post-transit conditions for several representative distributions of traps, using the numerical procedure mentioned in 3.1, ensuring that the value of  $t_0$  in the simulation was short enough to include any important features in the trap distribution within the post-transit time regime. We then calculated the density of states from the  $i(t)$  data using the relations of Eq. (14) and Eq. (15) respectively. In addition to this comparison, we calculated the density of states from *pre-transit*  $i(t)$  data for the same representative distributions, using the basic FT method described in 2.1. We note that the FT method also involves a delta function approximation to simplify an integration, and so is also subject to a broadening effect.

In Fig. 6, we show the reproduced  $g(E)$  when the original distribution is the same steep exponential tail with superimposed, sharp Gaussian feature, as in section 2.2 above. The very substantial broadening of the FT method is evident, particularly at energies below the Gaussian peak. The approximate post-transit expression of Eq. (14), is significantly better, as expected. However, the HPT method proposed in the present work follows the original density well, including the Gaussian feature, with a fit which is rather better than the HFT result shown in Fig. 4.

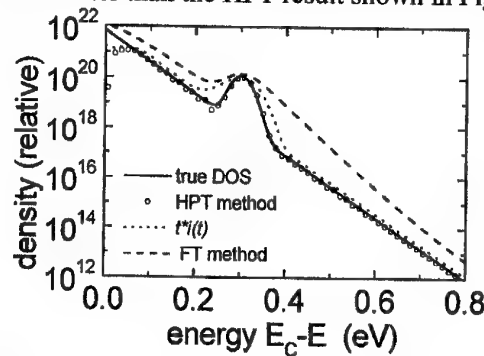


Fig. 6. DOS recovered from computed  $i(t)$  at 290K for an exponential tail of characteristic energy  $E_0 = 35$  meV, with a sharp Gaussian feature at 0.3 eV with FWHM = 41.6 meV. Comparison of approximate and proposed post transit analyses and FT method.

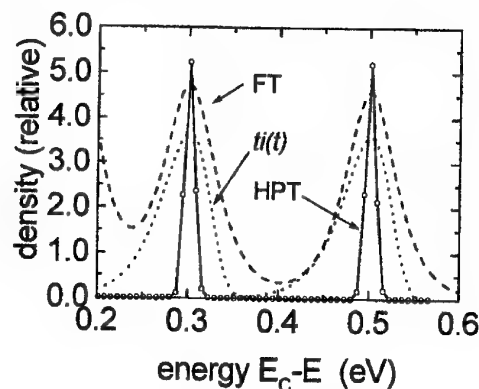


Fig. 7. Density of states recovered from computed  $i(t)$  at 290K for two discrete trap levels at 0.3 and 0.5 eV depth. While both approximate methods exhibit some  $kT$  broadening in the recovered DOS, the proposed post-transit analysis resolves the levels as sharp features, upon a very low noise base.

Next the extreme case is considered of a DOS consisting of two *discrete* levels of equal density,  $1.0 \times 10^{17} \text{ cm}^{-3}$ , at depths 0.3 and 0.5 eV. Computing the DOS from  $i(t)$  curves gives the results shown in Fig. 7, where we have scaled the results to ease comparison. We note that the discrete levels are represented now by a  $g(E)$  distribution, which when integrated should represent the same total density. The symmetrical broadening is evident in the FT method, which gives, as before, a FWHM of 67 meV ( $2.6 kT$ ) while the approximate post-transit analysis is only marginally sharper, and asymmetrically broadened. At the shallow energy side of the recovered DOS for each level,

broadening is evident, similar to that of the FT method, while the deep energy side is rather sharper in form as expected from the observations of Fig. 1. This is a consequence of fitting the asymmetric exponential release time distribution function with a delta function. It is clear however, that the proposed HPT method gives a much sharper and symmetrical reproduction, with FWHM estimated as  $\sim 12$  meV, or  $0.48 kT$  in this case.

### 3.3. Experimental - multilayers

Fig. 8 shows measured TPC in a multilayer  $\text{SiO}_x(10\text{nm})/\text{CdSe}(10\text{nm})$  film. At 293 K and 323K the  $i(t)$  decay displays a clear power-law form  $i(t) \propto t^{-(1-\alpha)}$ , over several decades of time, after an initial faster short-time fall at about 100ns. At 293K the slope index  $(1-\alpha)$  is  $-0.75$ , which might be (wrongly) interpreted as arising from a broad exponential tail of characteristic energy  $E_{\text{ct}} = 100$  meV. At 423 K a further feature appears at longer times, which is as yet unexplained.

Fig. 9 shows the relative DOS computed from the  $i(t)$  data, for all three temperatures. Also shown is a line with slope representing a characteristic energy of 100 meV. The DOS appears to be a broad, almost flat, distribution, over several tenths on an eV. It is evident also that the distribution is far from an 100 meV tail predicted from the power law of the  $i(t)$  decay. This is a striking and surprising result at first sight, but a similar effect has been observed experimentally by the authors in other materials, such as a-Si:H, and also discussed in detail, with the aid of simulations [14]. Essentially the departure from the expected exponential DOS form arises from the contribution of the short - time 'pre-power-law' section of  $i(t)$  to the relevant Fourier integral. Although the highest resolution is not required for this case, we note that application of the simple *approximate* result of equation (6) produced a calculated DOS with a spurious band tail of slope energy equal to  $kT$  in the range 0.2 - 0.4 eV depth.

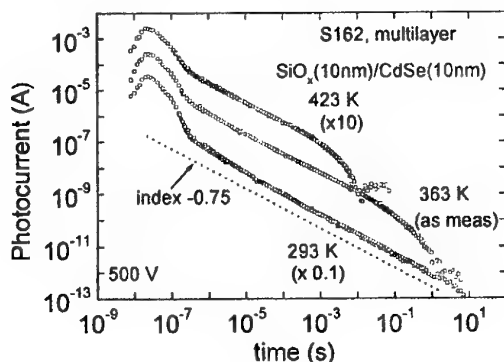


Fig. 8. TPC in a multilayer  $\text{SiO}_x(10\text{nm})/\text{CdSe}(10\text{nm})$  film at 293 K, 363 K and 423 K. Excitation: 4ns pulsedwidth, 500 nm,  $10^{14}$  photons  $\text{cm}^{-2}$  incident. Power law of index  $-0.75$  is shown.

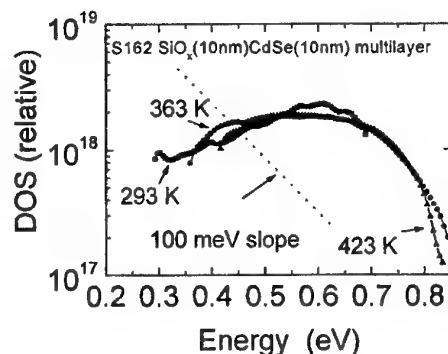


Fig. 9. DOS calculated from TPC data of Figure 8. Also shown is expected tail slope of 100 meV, expected (incorrectly) from the power law observed at 293 K in Fig. 8.

Similar results have been obtained from TPC measurements on composite  $\text{SiO}_x$  - CdSe films, where we had hoped to identify defect states observed in TSC measurements. Further work is needed to access by TPC, the energy range related to these states.

### 3.4. Experimental - arsenic triselenide

TPC in  $\text{As}_2\text{Se}_3$  is normally manifested as a featureless decay in  $i(t)$ , following a power law over many decades of time, with typically an index of  $-0.5$ , at room temperature [9]. This usually leads to an interpretation involving an extensive and featureless exponential tail (above the valence band). On the other hand,  $\text{As}_2\text{Se}_3$  exhibits bimolecular *steady state* photoconductivity, which has a reasonably well defined activation energy of  $0.33$  eV [7]. A simple analysis involving valence alternation pair defect centres with negative correlation energy then would 'place' such defects (in the doubly-negative charged state) at around double this value –  $0.66$  eV into the gap. These two interpretations seem to be incompatible. We speculate here that there may well be some structure in the defect DOS, which peaks at  $0.66$  eV above the mobility edge. We believe that it has become evident from the present study, and a previous study on a-Si:H, that a power law decay of  $i(t)$  over many decades of time, may not be incompatible with DOS distributions which are other than exponential. Further work on this is required.

## 4. Conclusions

We have shown that simple analytical procedures may be applied to the photocurrent decay observed in the general TPC case and to post-transit pulse photocurrent data to reveal the density of localized states with high resolution. The work shows that the resolution obtained is not limited by  $kT$  broadening effects. The broadening associated with earlier methods arises because of the approximation of a distribution function, using a delta function, in order to simplify an integral. The best resolution is provided by the new post-transit analysis, while both new methods exhibit versatility in handling cases with either distributed traps or with discrete traps. This means that they can be applied to disordered materials or to crystalline materials with well-defined defect levels.

Experimental results on multilayer  $\text{SiO}_x/\text{CdSe}$  films, indicate a very broad flat energy distribution of localized states exists in the material. The spatial location of such states is not identified by the method, but they may be associated with both the nanoparticle-nanoparticle and nanoparticle-matrix interfaces. The results also demonstrate the pitfalls associated with interpreting a power law TPC in terms of an exponential band-tail. This point was further used in speculating that the power-law TPC decay usually observed in  $\text{As}_2\text{Se}_3$  films may not in fact indicate a featureless exponential distribution of states, and may not be incompatible with some defect structure in the DOS.

## Acknowledgments

The authors acknowledge the Royal Society for financial support via a joint collaboration grant. One of the authors (CM) also acknowledges EPSRC for financial support through research grant GR/M 16696, which allowed development of the analytical methods.

## References

- [1] C. Main, Proc. MRS Symposium A, Vol. **467**, Eds. M. Hack, E. A. Schiff, S. Wagner, A. Matsuda, R. Schropp, MRS, Warrendale PA, 1997, Ch.143, p.167.
- [2] G. F. Seynhaeve, R. P. Barclay, G. J. Adriaenssens, J. M. Marshall, Phys. Rev. B, **39**, 10196 (1989).
- [3] S. Usala, G. J. Adriaenssens, Ö. Öktü, M. Nesladek, Appl. Surface Science, **50**, 265 (1991).
- [4] D. Nesheva, Z. Levi, Z. Aneva, V. Nikolova, H. Hofmeister, J. Phys.:Condens. Matter., **12**, 751 (2000).
- [5] D. Nesheva, Z. Levi, V. Pamukchieva, J. Phys.: Condens. Matter., **12**, 3967 (2000).
- [6] C. Main, D. P. Webb, R. Brüggemann et al, J. Non Cryst. Solids, **137**, 951 (1991).

- [7] C. Main, A. E. Owen, *Electronic and Structural Properties of Amorphous Semiconductors*, Eds. P. G. LeComber, J. Mort, Academic Press, London (1972).
- [8] M. Hammam, G. J. Adriaenssens, W. Grevendonk, *J. Phys. C: Solid State*, **18**, 2151 (1985).
- [9] D. Monroe, M. A. Kastner, *Phys Rev B*, **33**, 8881 (1986).
- [10] C. Main, R. Brüggemann, D. P. Webb, S. Reynolds, *Solid State Commun.*, **83**, 401 (1992).
- [11] M. J. Gueorguieva, C. Main, S. Reynolds, *Proc. MRS Symposium A*, Volume 609, Eds. R. W. Collins, H.M. Branz, S. Guha, H. Okamoto, M. Stutzmann, MRS, Warrendale PA, 2000.
- [12] T. Nagase, K. Kishimoto, H. Naito, *J. Appl. Phys.* **86**, 5026 (1999).
- [13] N. Tikhonov, A. V. Goncharsky, V. V. Stepanov, A. G. Yagola, *Numerical Methods for the Solution of Ill-Posed Problems*, Kluwer Academic Publishers, Netherlands (1995).
- [14] S. Garbow, K. E. Hillstom, J. J. More, Argonne National Laboratory MINPACK Project (1980).
- [15] C. Main, R. Brüggemann, D. P. Webb et al., *J. Non-Cryst Solids*, **166**, 481 (1993).
- [16] C. Main, R. Brüggemann, *Electronic and Optoelectronic Materials for the 21st Century*, Eds. N. Kirov, A. Vavrek, World Scientific Press, Singapore, 1993, p. 270.

## ION TRANSPORT IN CHALCOGENIDE GLASSES: DYNAMICS AND STRUCTURAL STUDIES

M. Ribes, E. Bychkov<sup>a</sup>, A. Pradel

Laboratoire de Physicochimie de la Matière Condensée UMR 5617 Université Montpellier II cc003, 34095 Montpellier cedex 5, France

<sup>a</sup>Laboratoire de Physicochimie de l'Atmosphère UMR 8101 Université du Littoral 145, Avenue Maurice Schumann, 59140 Dunkerque, France

In this paper we attempt to summarise the state of our knowledge on ionic conductive chalcogenide glasses. The silver chalcogenide glass family has been chosen as an example. Measurements of <sup>110</sup>Ag tracer diffusion experiments ( $D_{Ag}$ ) and electrical measurements ( $\sigma_i$ ) carried out over an extremely large composition range elucidate the dc conductivity which depends on diffusion over long distances. The results show three distinctly different transport regimes: i) below the percolation threshold at  $x_c \approx$  few silver ppm the glasses are ionic insulators, ii) just above the percolation threshold ( $x_c < x < 1-3$  at % Ag)  $\sigma_i$  and  $D_{Ag}$  are very well described by a modified geometrical percolation model using a single parameter, the critical temperature  $T_0$ :  $\sigma_i(x) \propto x^{T_0/T}$ ,  $D_{Ag}(x) \propto x^{(T_0/T)-1}$ ,  $E(x) \propto k T_0 \log(x/x_c)$ . This critical temperature, reflecting interconnectivity of "infinite" percolation clusters embedded in the glassy matrix depends on the structural organisation of the host matrix, iii) far above the percolation threshold the  $Ag^+$  ion transport depends on the Ag content but not on the host matrix. Accordingly only at low mobile ion content structure or, more precisely, dimensionality of the vitreous matrix seems to play a role in ionic transport properties of glasses. Concerning the ac conductivity the complete conductivity spectra ( $\log \sigma(\omega)$  vs  $\log f$  (Hz)), obtained in a very broad temperature and frequency ranges can be perfectly fitted by  $\sigma(\omega) = \sigma_{dc} + A\omega^{0.5} + B\omega^1 + C\omega^2$ . Thus at high frequencies (GHz range) and high temperatures the superlinear frequency dependence of the conductivity recently evoked to describe the data can be discarded. Moreover the existence of a high frequency plateau postulated by many models can be questioned.

(Received June 25, 2001; accepted September 3, 2001)

**Keywords:** Ion transport, Dc and ac conductivity

### 1. Introduction

The ionic mobility in glasses is at the origin of many applications in various domains (ion-exchange strengthening, chemical (micro) sensors, solid state (micro) batteries for electrochemical storage of energy, waveguides for integrated optical devices...). Thus, the survey of ionic transport in glasses is a topic of interest to the academic community as well to the glass industry.

Knowledge of mobile ion dynamics at both macroscopic and atomic levels is needed in order to answer the essential question: how can one link together structure, dynamics of ions and macroscopic properties of glasses? Only partial answers have been proposed to date.

The objective of this paper will be to summarise the state of our knowledge using the results that our group has obtained during the last years in the course of studying a family of fast ion conductive glasses, namely the silver chalcogenide glasses.

The following points will be emphasised:

- i) Variation of the conductivity with the mobile cation content ( $\sigma_{dc} \propto x_{(Ag)}$ , mechanisms of conduction).
- ii) Dynamic of ions ( $\sigma_{ac} \propto f$  (Hz) from few Hz to the IR frequencies).
- iii) The relationship between the glass structure (medium range order) and the conduction properties.

## 2. Experimental

Sample preparation and characterization, electrical conductivity and diffusion measurements, ion dynamic studies and structural investigations have been already described elsewhere (see for example publications 1-4).

## 3. Results and discussion

### 3.1. DC electrical conductivity

#### 3.1.1. Temperature dependence of conductivity dc ( $\sigma_{dc}$ )

Classically the electrical conductivity obeys the Arrhenius law  $\sigma_i = \sigma_0/T \exp(-E_{dc}/RT)$  where  $\sigma_0$  is the pre-exponential term,  $E_{dc}$  is the activation energy,  $R$  and  $T$  have their usual meaning. As an example, variations of the dc conductivity for 0.5 Ag<sub>2</sub>S-0.5 GeS<sub>2</sub> glass are shown in Fig. 1. Over the whole temperature range studied (350°C in this case, from 200°C to -150°C), a perfect linear variation is observed for  $\sigma_{dc}$  (at room temperature  $\sigma_{dc} = 10^{-4} \Omega^{-1}\text{cm}^{-1}$  et  $E_{dc} = 0.31 \text{ eV}$ ). For temperatures approaching  $T_g$  (near 300°C for this glass) a weak negative departure from the linearity has been observed for a number of fast ionic conductive glasses (5, 6). But this result remains controversial and requires further experimental confirmations (for the example chosen, the temperature dependence of the <sup>110</sup>Ag tracer coefficient shows a nearly perfect Arrhenius-type behaviour in the same temperature range (14)). It will not be discussed further in this paper.

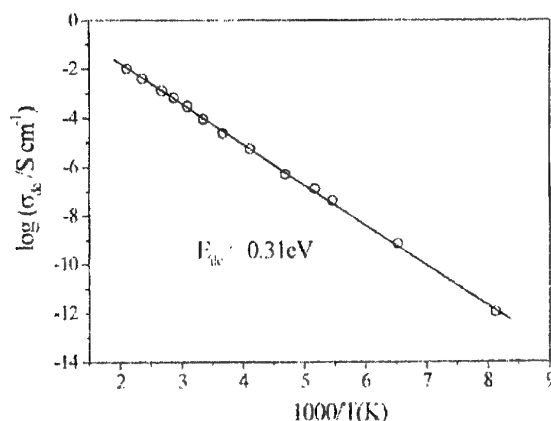


Fig. 1. Arrhenius variation of  $\sigma_{dc}$  for glass 0.5Ag<sub>2</sub>S-0.5GeS<sub>2</sub>. The lines are guides for the eyes.

As for many ionic solids conductors, ionic transport in glasses is a thermally activated process. For temperatures below the glass transition temperature  $T_g$ , structural relaxation times are much longer than the relaxation times for the mobile ions movements. Mobile cations move in a frozen network.

#### 3.1.2. Composition (mobile ion content) dependence of conductivity dc ( $\sigma_{dc}$ )

The ionic conductivity in glasses increases by many order of magnitude with increasing ion content (Fig. 2). For example for glasses belonging to the system  $x \text{ Ag}_2\text{S} - (1-x) \text{ GeS}_2$ , at room temperature  $\sigma_{dc}$  increases from  $6 \cdot 10^{-5} \Omega^{-1}\text{cm}^{-1}$  to  $10^{-3} \Omega^{-1}\text{cm}^{-1}$  when  $x$  varies from 0.3 to 0.55, ie conductivity is increased by a factor about 20 when the mobile ion content is increased by only a factor of 2. At the same time a decrease of activation energy is observed. In silver thiogermanate glasses  $E_{dc}$  varies from 0.36 to 0.32 eV. Different theories have been proposed to explain these drastic changes in the conductivity.



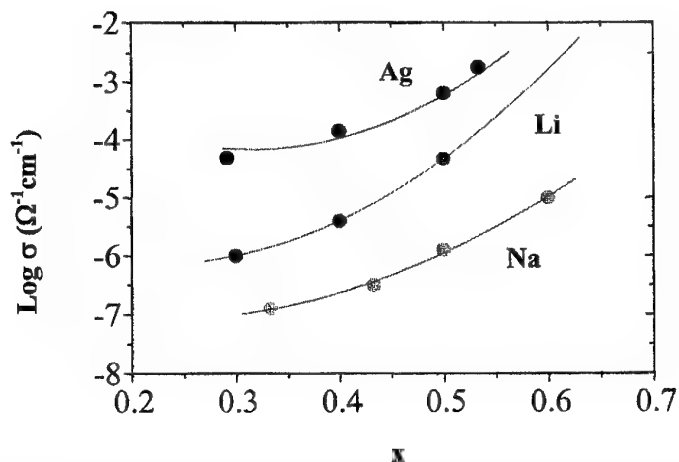


Fig. 2. Composition dependence of the conductivity for  $xM_2S-(1-x) GeS_2$  glasses ( $M = Ag, Li, Na$ ).

They can be divided into two categories:

- The strong electrolyte model, e.g. the Anderson and Stuart model (7) or others inspired by this model (8), in which the mobility of the ions varies according to their concentration and the temperature. All ions participate in the conduction.

- The weak electrolyte model, developed by Ravaine and Souquet (9) in which, on the contrary, the mobility is constant and independent of the concentration and the temperature. Only a fraction of the mobile ions in glass participate in the conduction.

Despite opposite assumptions similar predictions can be deduced from both models: an increase of the dielectric constant of the vitreous network induces an increase of the conductivity and a decrease of the activation energy. It was on the basis of this idea that the first sulfide glasses were synthesized in our group (10).

More recently dynamic structure (11) and jump relaxation (12) models have attempted to explain "quasi log-linear" composition dependence of the conductivity.

A simple ion transport regime operating over the entire composition range is usually proposed in these theories.

These approaches are supported by conductivity measurements covering only a narrow domain in composition, usually corresponding to the highest mobile cation content. This has been the natural focus of attention on obtaining the highest possible conductivity which was for many years the driving force for the research on conductive glasses.

Consequently experimental results covering a large range (several orders of magnitude) mobile ion concentration, which could be used to verify the theoretical predictions, are rather rare. This is especially true of data on tracer diffusion measurements which are essential to distinguish between the ionic or electronic transport at low or extremely low mobile ion contents. Moreover in a limited composition range, it is also difficult to distinguish between exponential or power-law isotherm composition dependence which play a key role in different theories.

Recently conductivity and  $^{110}Ag$  tracer diffusion measurements have been carried out for a number of silver chalcogenide glasses over a very wide composition range including  $Ag^+$  contents as small as few ppm [3, 13, 14]. As an example, glasses belonging to  $Ag-Ge-S$  systems have been studied from 0.008 to 25 % at.  $Ag$ . In such studies the conductivity increases by 9 orders of magnitude (from  $10^{-14}$  to  $10^{-5} \Omega^{-1}cm^{-1}$ ) with increasing mobile ion content. This enormous increase in the conductivity is accompanied by a dramatic decrease in the activation energy (from 1 to 0.4 eV). Figs. 3a and 3b show the conductivity isotherm variations at 298 K (Fig. 3a) and the same data plotted on a log-log scale at two temperatures 298 and 473 K (Fig. 3b). Figs. 4a and 4b show the  $^{110}Ag$  tracer diffusion measurements plotted on the same way for the same temperatures.

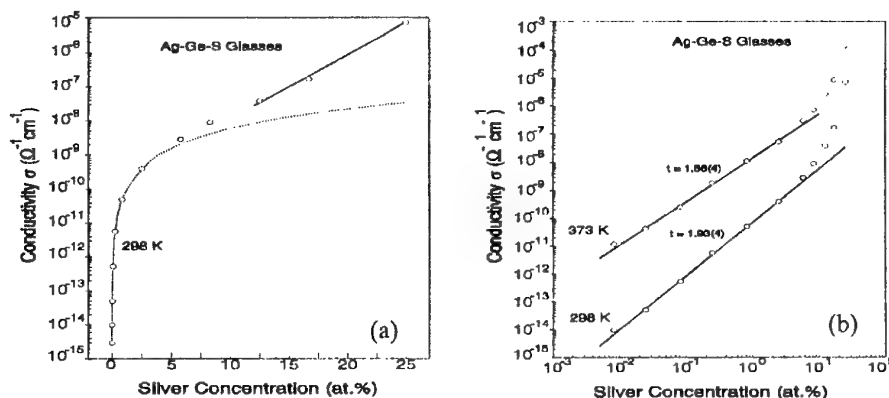


Fig. 3. Ionic conductivity  $\sigma_i(x)$  isotherms for Ag-Ge-S glasses plotted (a) on conventional way at 298 K and (b) on log-log scale at 298 and 373 K. Doted and solid lines represent the best fittings (Eq. 1 and 3). The percolation threshold is not sensibly different from 0% Ag hence a simple composition axis has been used in place of  $(x-x_c)$ .

In contrast to previous observations in which the phenomenon of percolation was unrecognized, in these glasses where the Ag ion content varies more than 3 order of magnitude (from 0.008 to 25 at %), at least three different ion transport regimes can be observed. i) Below the percolation threshold at  $x \approx 30$  ppm Ag, the glasses are ionic insulators. The silver ion transport number  $t_{Ag^+}$  is about 0,1 - 0,2. ii) Just above the percolation threshold for mobile ions the glass become predominantly ionic conducting ( $t_{Ag^+} > 0.6-0.8$  at  $x \geq 0.008$  at % and increases rapidly to 1 with  $x$ ). A characteristic feature of  $\sigma_i(x)$  and  $D_{Ag}(x)$  isotherms in the domain at  $x_c < x < 1-3$  at % Ag is a power-law composition dependence over  $\approx 2.5$  order of magnitude in silver concentration (Fig.3b and 4b).

$$\sigma_i(x, T) = \sigma_i(1, T) x^{t(T)} \quad (1)$$

$$D_{Ag}(x, T) = D_{Ag}(1, T) x^{t_D(T)} \quad (2)$$

where  $\sigma_i(1, T)$  and  $D_{Ag}(1, T)$  are the ionic conductivity and diffusion coefficient of a hypothetical phase at  $x = 1$ . The temperature dependent critical exponent  $t(T)$  and  $t_D(T)$  are related ( $t_D(T) = t(T) - 1$ ) according to the Nernst-Einstein equation ( $D_\sigma \propto \sigma_i x^{-1}$ ). The Haven ratio,  $H_R = D_{Ag}/D_\sigma$ , decreases in this composition range from  $\approx 1$  to  $\approx 0.7$  (Fig. 5). This transport regime is attributed to percolation in the critical region just above the percolation threshold. Theoretical considerations (the dynamic structure model (15) and statistical (occupation) effects (16) on percolative ionic conduction) are also in good agreement with experimental findings. iii) Far above the percolation threshold at  $x > 10$  at % Ag,  $\sigma_i(x)$  and  $D_{Ag}(x)$  both exhibit positive deviations from the expected percolation behaviour (Fig. 3b and 4b) with an exponential law dependence ( $\sigma_i(x) = \sigma_i(o) e^{ax}$  [3]). At the same time the Haven ration  $H_R$  becomes nearly constant  $H_r \approx 0.3$  (Fig. 5) indicating strongly correlated motion of the  $Ag^+$  ion. In this silver concentration domain, the ionic transport is not dependent any more on percolation pathway. Rather becomes network dependent with a strongly correlated motion of the  $Ag^+$  ions. This domain is called the modifier-controlled domain.

### 3.2. Ion dynamics - Complete conductivity spectra

Non-Debye relaxation is a characteristic of the ionic conductive glasses. It is often expressed by the Kohlraush-Williams-Watts (KWW) function in the time domain (17):

$$\phi(t) = \phi(o) \exp(-(t/\tau)^\beta) \text{ with } 0 < \beta < 1$$

Several earlier phenomenological expressions (Cole-Cole (18), Cole-Davidson (19) or Havriliak-Nagami (20)) also have been used to describe non-Debye relaxation in the frequency domain.

The frequency dependence of electrical conductivity in glassy is usually described by the so called "universal dynamic response" (UDR) first proposed by Jonscher (21).

$$\sigma(\omega) = \sigma_{dc} + A\omega^s \quad [4]$$

where  $0 < s \leq 1$  and  $\sigma_{dc}$  is the frequency independent conductivity.

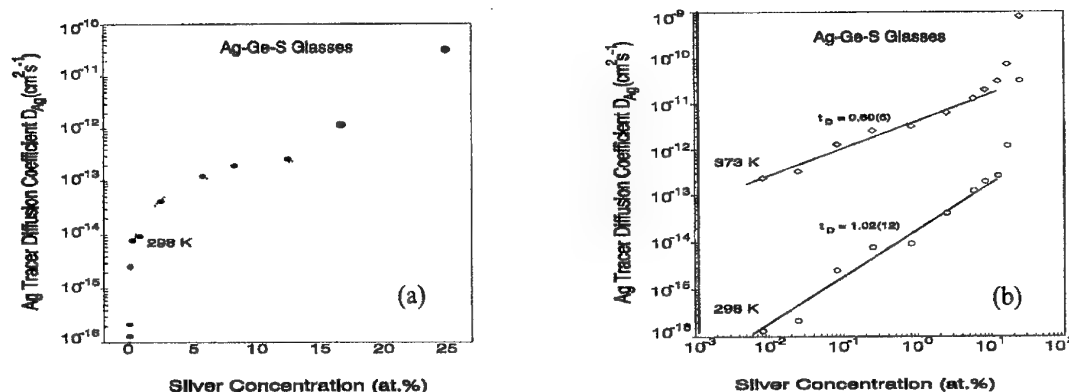


Fig. 4. Diffusion coefficient  $D_{Ag}(x)$  isotherms for Ag-Ge-S glasses plotted (a) on conventional way at 298 K and (b) on log-log scale at 298 and 373 K. Doted and solid lines represent the best fittings (Eq. 2). The percolation threshold is not sensibly different from 0% Ag hence a simple composition axis has been used in place of  $(x-x_c)$ .

Several models were developed to account for this behaviour. These models will be briefly discussed.

The coupling model proposed by Ngai (22) invokes the concept of correlated states between mobile species. In the case of ionic conductive glasses a correlation between mobile ions would take place after a critical time  $t_c$ . Consequently the relaxation rate would be a constant at very short time. For  $t > t_c$ , the relaxation would slow down and the time dependent relaxation rate would be expressed by  $w(t) = (1/\tau_0) (t/t_c)^{-p}$ ,  $\tau_0$  and  $t_c$  are thermally activated. The model predicts a power law behaviour for  $t > t_c$  and a plateau for  $t < t_c$ .

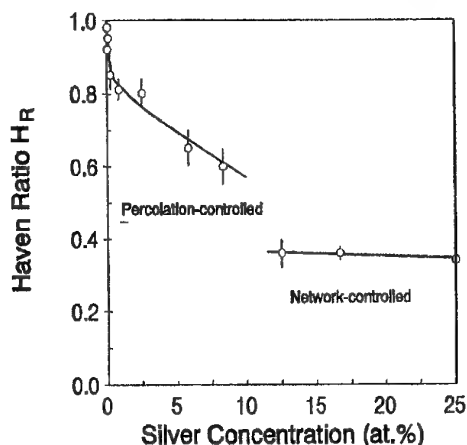


Fig. 5. Composition dependence of the Haven ratio  $H_R$  for Ag-Ge-S glasses. The lines are guides for the eyes.

The Jump Relaxation Model (JRM) developed by Funke (23) is based upon the existence of correlated forward-backward ion hops due to the retarded response of neighbouring species. The non-Debye character of the relaxation is due to the fact that the time constant of the back-hop process

increases as time progresses. This leads to a power-law dependence of the conductivity in the low frequency domain while a plateau should be observed in the high frequency region.

The Diffusion Controlled Relaxation Model (DCR) was proposed by Elliott (24). This model, based on interstitial mechanism, predicts a dispersive behaviour of conductivity with  $s = 0.5$  as a consequence of the  $t^{1/2}$  time dependence of the diffuse behaviour.

The "Counter Ion Model" (CIM) developed by Dieterich et al (25) and the "Diffusion Limited Percolation Model" (DLPM) proposed by Bunde et al (26) are based on lattice-gas model with inter-ion coulombic interactions. With such an assumption, Monte Carlo simulations of the diffusion of charged particles in disordered structures leads to a dispersive behaviour of conductivity with a sub-linear frequency exponent.

Recently conductivity measurements in the GHz region have shown a superlinear frequency dependence of the conductivity (1,27,28). The unified site relaxation model (USMR) (29) developed by combining the original JRM and some features of the dynamic structure model (DLPM) accounts for this apparent superlinear frequency dependence of the conductivity.

In addition all these models predict that  $A$  (eq. [4]) is thermally activated with an activation energy  $E_{ac}$  related to the dc activation energy  $E_{dc}$  by  $E_{ac} = E_{dc} (1 - s)$ . All of these models also predict the existence of high-frequency plateau

In summary the data indicate the presence of three conductivity regimes : the dc regime, a dispersive region where  $\sigma(\omega) = A\omega^s$  ( $s < 1$  and  $A$  is thermally activated with an activation energy  $E_{ac} = (1-s) E_{dc}$ ) and a third regime where  $\sigma(\omega) = B\omega^p$ . At high frequency and high temperature this regime shows a superlinear frequency dependence ( $p > 1$ ).

The characteristics of the third regime are still based upon very few experimental evidence. It is clear that systematic investigations of  $\sigma(\omega)$  as a function of frequency and temperature in very large temperature and/or frequency ranges are necessary to clarify this point. In a word to have a complete conductivity spectra become a necessity in order to support the models currently proposed.

What are the last data in this domain? Here again glasses belonging to Ag-Ge-S system and, more precisely, the glass with composition  $0.5 \text{ Ag}_2\text{S} - 0.5 \text{ GeS}_2$ , give us a good example (30).

Fig. (6) shows a log-log representation of the conductivity versus frequency in a very broad frequency range, from some Hz up to FIR frequencies (6 THz), and a large temperature domain (from 123 K to 473 K). When frequency was low enough, ie when the UDR (Jonscher law) applies,  $\sigma(\omega) \approx \sigma_{dc} + A\omega^s$ , to fit the experimental data led to an  $s$  value of 0.5. The parameter  $A$  was found thermally activated with an activation energy  $E_{ac} = 0.14 \text{ eV}$ . Within experimental error, it is in accordance with the value determined via  $E_{ac} = (1-s) E_{dc}$  ie 0.16 eV.

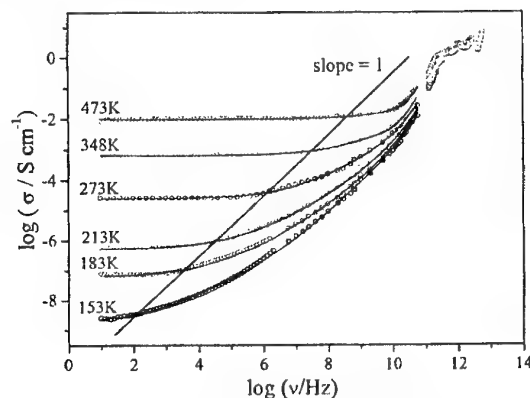


Fig. 6. Frequency dependent conductivity spectra for  $0.5\text{Ag}_2\text{S}-0.5\text{GeS}_2$  glass at various temperatures plotted on log-log scale. Straight line (slope 1) joins the crossover frequencies.

Solid lines represent the best fittings according to Eq. 5.

At higher frequencies, the power law from UDR was not adequate anymore to depict the spectra. It was necessary to add a second power law  $\sigma(\omega) \approx B\omega^p$ . The fit led to a value of the exponent  $p = 1$  (in agreement with Nowick results for the  $\text{Na}_2\text{O} - 3 \text{ SiO}_2$  glass for example) (31). The  $B$  term was very slightly temperature dependent. There was no need of an exponent greater than one to account for the data. This observation contrasts previous results for silver conduction oxide glasses

(27) or for alkali borate glasses (32) as even for the same glass but measured in narrow frequency range (1).

At far infrared frequencies, the conductivity showed a frequency dependence in  $\omega^2$ . It corresponds to the low frequency flank of the lowest vibrationnal mode. So it was easy to extrapolate such a contribution to lower frequencies and to subtract it. The obtained spectra could then be solely interpreted in terms of a hopping motion of the ions. But even in this case no high frequency plateau could be observed.

Consequently (30), the complete spectra could be perfectly fitted by:

$$\sigma(\omega) = \sigma_{dc} + A\omega^{0.5} + B\omega^1 + C\omega^2 \quad (5)$$

The temperature frequency diagram displayed in Fig. (7) allows the visualisation of the four conductivity regimes. One can observe a narrowing of regime III (exponent 1) to the benefit of regime II and IV (exponents 0.5 and 2 respectively) when the temperature is increased.

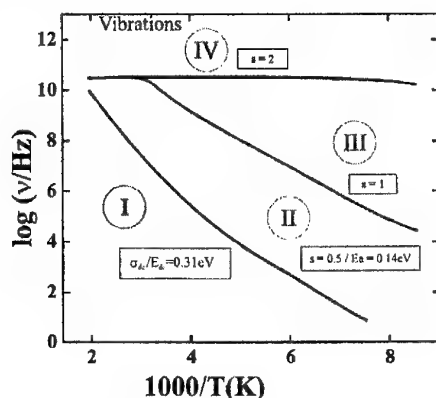


Fig. 7. Temperature-frequency diagram for 0.5Ag<sub>2</sub>S-0.5GeS<sub>2</sub> glass.

In conclusion these results show clearly the capital importance of reliable data measured in the widest temperature and frequency domains possible. Thus at high frequencies (GHz range) and high temperatures (in this case  $T > 150$  K) the superlinear frequency dependence of the conductivity recently evoked to describe the data can be discarded. Moreover from these data the existence of a high frequency plateau postulated by many models can be questioned.

### 3.3. Does the glass structure (intermediate-range order) play a role on conduction properties?

It is clear that in crystallized materials a relation exists between the structure of the material and its properties of ionic conduction. Beyond the type of conduction (vacancy (Schottky) interstitial (Frenkel) or interstitialcy mechanisms), one has a good idea of the structural characteristics that are leading to high ionic conductivity: i) a large number of empty equivalent sites should be available for the mobile ions to jump into, ii) the empty and occupied sites should have a similar potential energies with a low energy barrier between them iii) the structure should have in his framework open channels or preferential plane through which mobile ions may migrate.  $\alpha$ -AgI,  $\beta$ -alumina or material named NASICON are good illustrative examples of that.

In glass, because of the absence of long distance order, channel type arrangements or preferential planes favouring the diffusion of ions cannot exist. On the contrary, one can intuitively think that disorder should allow the existence of many vacant sites that are able to accept mobile ions and consequently to improve the conductivity. Finally, even if the structural units of the framework of glasses are well known (tetragonal Si, Ge, P..., trigonal As coordinations) the glass structure, ie the way of these units are linked, and even the coordination polyhedra for the mobile ions are still not very well known.

0.5 Ag<sub>2</sub>S - 0.5 GeS<sub>2</sub> glass: from silver isotopic-substitution neutron diffraction studies a structural model for the short and intermediate-range order has been proposed (4). Elongated tetrahedra are connected to two others through their apices, forming chain-like intermediate range ordering. The Ag<sup>+</sup> ions are presumed to sit between neighbouring chains, where they are coordinated by three S atoms (trigonal pyramids).

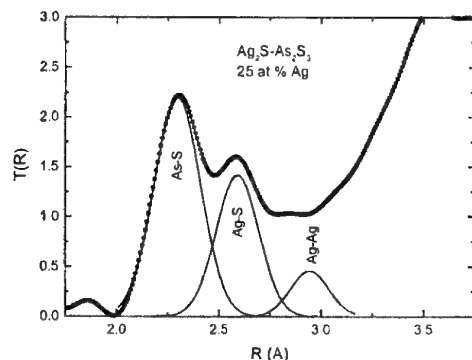


Fig. 8. Total pair correlation function  $T(R)$  for 0.5Ag<sub>2</sub>S-0.5As<sub>2</sub>S<sub>3</sub> glass. Fitting of peaks corresponding to coordination shells of As-S, Ag-S and Ag-Ag.

Ag<sub>2</sub>S - As<sub>2</sub>S<sub>3</sub> glasses: recent studies have been carried out using high-resolution neutron diffraction experiments at scattering vectors up to 40 Å<sup>-1</sup> (33) in order to find differences in the network structural organisation within the percolation and modifier controlled domains. In the percolation controlled domain ( $x \leq 1,2$  at % Ag) neither the short nor the intermediate-range order exhibits any significant transformations: the intensity of the first sharp diffraction peak (FSDP) at 1.25 - 1.35 Å exhibits relatively small changes as a function of the silver content, and the trigonal arsenic coordination and two-fold coordination of the sulphur species remain intact. In contrast, in the modifier-controlled domain, a nearly complete disappearance of As-As correlations at  $\approx 5$  Å, manifested by the strong decreases of the FSDP, has been observed indicating fragmentation of the host matrix. At the same time, the increase of the peak intensity near 3 Å (Ag-Ag correlation) reflects direct contacts of AgS<sub>3</sub> trigonal pyramids and formation of oligomeric silver-containing structural units. These structural units and their interconnections seem to be similar for many silver-rich chalcogenide glasses. As an example, total pair correlation functions  $T(R)$  for two chalcogenide glasses are shown. Fig. 8: 0.5 Ag<sub>2</sub>S-0.5 As<sub>2</sub>S<sub>3</sub> (25 at % Ag) glass (33); Fig. 9: 0.5 Ag<sub>2</sub>S-0.5 GeS<sub>2</sub> (33 at % Ag) glass (4).

We can use these structural data to examine the question of the relation between glass-structure and conductivity properties.

Let us consider first the percolation controlled domain. In this domain ( $x_c < x < 1-3$  at. % Ag) a power-law composition dependence characterises a variation of  $\sigma_i$  or  $D_{Ag}$  (eq. [1] and [2]) with Ag<sup>+</sup> content. Fig. 3b and 4b show that the slope of the log-log plot depends on the temperature. We have found that the slope of the plot, which define the power law exponent  $t(T)$  can be written as (14, 35).

$$t(T) = t_0 + T_0/T \cong T_0/T$$

consequently equations [1] and [2] can be re-written giving the following expressions.

$$\sigma_i(x, T) \cong \sigma_i(1, T) x^{T_0/T} = \sigma_0 \exp [-E_{dc}(x)/kT] \quad (6)$$

$$D_{Ag}(x, T) \cong D_{Ag}(1, T) x^{(T_0/T)-1} = D_0 x^{-1} \exp [E_D(x)/kT] \quad (7)$$

$$E_{dc}(x) = E_D(x) = E(x) = E_0 - k T_0 \ln(x/x_c) \quad (8)$$

where  $T_0$  is a critical temperature. This critical temperature which could be extracted either from the  $t(T)$  or from the  $E(x)$  values, is a primordial parameter to describe the percolation phenomena in glasses (14, 35). The percolative ion-transport depends on the numbers of "infinite" percolation clusters, on the one hand, and on their interconnectivity, on the other.

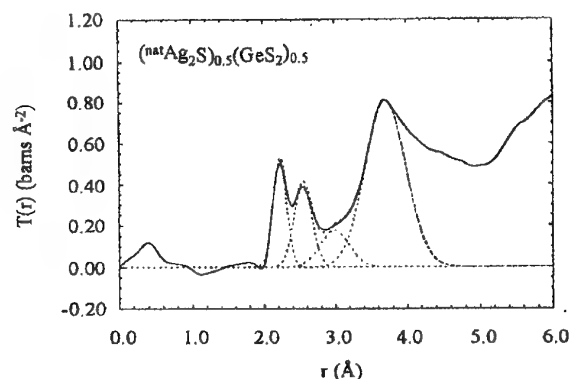


Fig. 9. Total pair correlation function  $T(R)$  for  $0.5\text{Ag}_2\text{S}-0.5\text{GeS}_2$  glass. Fitting of peaks corresponding to coordination shells of Ge-S, Ag-S and Ag-Ag and Ag-Ge and Ge-Ge combined.

The second term in equation [8] represents a configuration entropy term, where  $\ln(x/x_c)$  reflects the number and  $T_0$  to the interconnectivity of conduction pathways. Plotting the critical temperature  $T_0$  versus the average local coordination number of the host matrix  $\langle n \rangle$ , a nearly linear decrease of  $T_0$  with decreasing  $\langle n \rangle$  is observed (Fig.10).

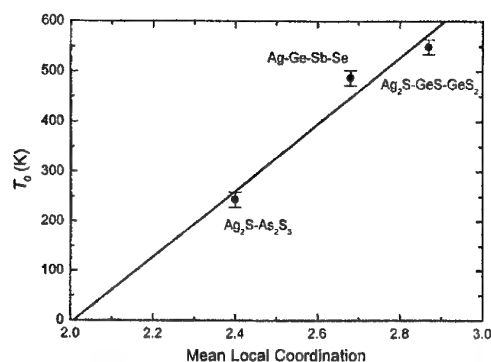


Fig. 10. Critical temperature  $T_0$ , characterising interconnectivity of percolation clusters, versus the average coordination number of the host matrix.

In conclusion, the ionic conductivity and tracer diffusion of silver chalcogenide glasses in the critical percolation domain ( $x_c \approx 30 \text{ ppm} < x < 1-3 \text{ at. \% Ag}$ ) are well described within the framework of modified geometrical percolation using a simple parameter  $T_0$  which reflects interconnectivity of "infinite" percolation clusters (macroscopic conduction pathways) embedded in the host matrix.

In the modifier-controlled domain far above the percolation threshold where i) Ag-Ag correlation can be observed in total pair correlation function  $T(R)$ , ii)  $\sigma_i(x)$  and  $D_{\text{Ag}}(x)$  exhibit positive deviations from percolation behaviour, the conductivity vs composition law is insensitive to the major changes in intermediate range order that occur when  $x_{\text{Ag}}$  is varied.

#### 4. Conclusions

The aim of this paper has been to summarise the state of our knowledge on ionic conductive chalcogenide glasses using silver chalcogenide glasses as an example.

Concerning the dc conductivity which expresses the long distance ionic diffusion,  $^{110}\text{Ag}$  tracer diffusion experiments ( $D_{\text{Ag}}$ ) and electrical measurements ( $\sigma_i$ ) carried out over an extremely large composition range show three distinctly different transport regimes i) below the percolation threshold at  $x_c \approx \text{few silver ppm}$  ( $\approx 30 \text{ ppm}$ ) the glasses are ionic insulators ii) just above the percolation



threshold ( $x_c < x < 1.3$  at % Ag)  $\sigma_i$  and  $D_{Ag}$  are very well described by a modified geometrical percolation model using a single parameter, the critical temperature  $T_o$ :  $\sigma_i(x) \propto x^{T_o/T}$ ,  $D_{Ag}(x) \propto x^{(T_o/T)-1}$ ,  $E(x) \propto k T_o \log(x/x_c)$ . This critical temperature, reflecting interconnectivity of "infinite" percolation clusters embedded in the glassy matrix depends on the structural organisation of the host matrix. iii) Far above the percolation threshold the  $Ag^+$  ion transport depends on the Ag content but not on the host matrix.

Accordingly only at low mobile ion content structure, or more precisely dimensionality of vitreous matrix seems to play an important role in ionic transport properties of glasses. For higher mobile cation content the conduction properties seem only governed by the amount of mobile species. In this concentration domain the structure of vitreous network does not seem to play any role.

Concerning the ac conductivity the complete conductivity spectra ( $\log \sigma(\omega)$  vs  $\log f$  (Hz)), obtained in a very broad temperature and frequency range, can be perfectly fitted by  $\sigma(\omega) = \sigma_{dc} + A\omega^{0.5} + B\omega^1 + C\omega^2$ . Thus at high frequencies (GHz range) and high temperatures the superlinear frequency dependence of the conductivity recently evoked to describe the data can be discarded. Moreover the existence of a high frequency plateau postulated by many models can be questioned.

## References

- [1] A. Pradel, G. Taillades, C. Cramer, M. Ribes, *Solid State Ionics* **105**, 139-148 (1998).
- [2] E. Robinel, B. Carette, M. Ribes, *J. Non-Cryst. Solids*, **57**, 49 (1983).
- [3] E. Bychkov, V. Tsegelnik, Yu. Vlasov, A. Pradel, M. Ribes, *J. Non-Cryst. Solids*, **208**, 1-20 (1996).
- [4] J. H. Lee, A. P. Owens, A. Pradel, A. C. Hannon, M. Ribes, S. R. Elliott, *Phys. Rev.*, **B54**, 3895-3909 (1996).
- [5] J. Kins, A. Martin, *Phys. Rev. Lett.*, **76**, 70 (1996).
- [6] M. Ribes, G. Taillades, A. Pradel, *Solid State Ionics*, **105**, 159-165 (1998).
- [7] O. Anderson, D. Stuart, *J. Am. Ceram. Soc.*, **37**, 573 (1954).
- [8] S. R. Elliott, *J. Non-Cryst. Solids*, **172-174**, 1343-1352 (1994).
- [9] D. Ravaine, J.L. Souquet, *Phys. Chem. Glasses*, **18**, 27 (1977).
- [10] B. Barrau, J.M. Latour, D. Ravaine, M. Ribes, *Silicates Industriels*, **A30**, 1 (1978).
- [11] P. Maass, A. Bunde, M. D. Ingram, *Phys. Rev. Lett.*, **68**, 3064 (1992).
- [12] K. Funke, B. Roling, M. Lange, *Solid State Ionics*, **105**, 195 (1998).
- [13] E. Bychkov, A. Bychkov, A. Pradel, M. Ribes, *Solid State Ionics*, **113-115**, 691 (1998).
- [14] E. Bychkov, *Solid State Ionics*, **136-137**, 1111-1118 (2000).
- [15] A. Bunde, M. D. Ingram, P. Maass, *J. Non-Cryst. Solids*, **172-174**, 1222 (1994).
- [16] A. Hunt, *J. Non-Cryst. Solids*, **175**, 59 (1994).
- [17] G. Williams, D. C. Watts, *Trans. Faraday Soc.*, **67**, 1323 (1971).
- [18] K. S. Cole, R. H. Cole, *J. Chem. Phys.*, **9**, 341 (1941).
- [19] D. W. Davidson, R. H. Cole, *J. Chem. Phys.*, **9**, 1489 (1951).
- [20] S. Havriliak, S. Negami *J. Polym. Sci.*, **14**, 99 (1966).
- [21] A. K. Jonscher, *Nature* **267**, 97 (1977).
- [22] K. L. Ngai, *J. Phys. Colloq.*, **C2**, 2, 61 (1992).
- [23] K. Funke, *Prog. Solid State Chem.*, **22**, 111 (1993).
- [24] S. R. Elliott, P. Owens, *Phil. Mag.*, **60**, 777 (1989).
- [25] J. Peterson, W. Dieterich, *Phil. Mag.*, **B65**, 231 (1992).
- [26] P. Maass, J. Peterson, A. Bunde, W. Dieterich, H. E. Roman, *Phys. Rev. Lett.*, **66**, 52 (1991).
- [27] C. Cramer, M. Buscher, *Solid State Ionics*, **105**, 109 (1998).
- [28] M. Cutroni, A. Mandanici, *Solid State Ionics*, **105**, 149 (1998).
- [29] A. Bunde, K. Funke, M. D. Ingram, *Solid State Ionics*, **86-88**, 1331 (1996).
- [30] R. Belin, G. Taillades, A. Pradel, M. Ribes, *Solid State Ionics*, **136-137**, 1025 (2000).
- [31] A. S. Nowick, A. V. Vaysleyb, Wu Liu, *Solid State Ionics*, **105**, 121 (1988).
- [32] C. Cramer, *Ber. Bunsenges Phys. Chem.*, **100**, 1497 (1996).
- [33] E. Bychkov, L. Price, *Solid State Ionics*, **136-137**, 1041 (2000).
- [34] E. Bychkov, A. Bolotov, L. Price, A. Pradel, M. Ribes, to be published.

## STRUCTURAL RAMAN STUDIES OF $\text{Ge}_x\text{S}_{1-x}$ CHALCOGENIDE GLASSES

I. P. Kotsalas, C. Raptis

Physics Department, National Technical University of Athens, 15780 Athens, Greece

The Raman spectra of binary  $\text{Ge}_x\text{S}_{1-x}$  chalcogenide glasses have been measured for various compositions and discussed in terms of the structural units present. High temperature Raman measurements in  $\text{Ge}_x\text{S}_{1-x}$  glasses have shown that, above the glass transition temperature  $T_g$ , irreversible two step crystallizations occur for the compound  $\text{GeS}_2$  ( $x=1/3$ ) and the moderately rich in Ge ( $x=0.35$ ) and S ( $x=0.30$ ) glasses, but in the case of the strongly enriched in S ( $x=0.20$ ) glass, a one step reversible crystallization takes place with the material returning to its starting glassy phase upon slow cooling to room temperature. The evolution of the  $A_1^c$  companion Raman band of  $\text{GeS}_2$  glass in the crystalline phases provides evidence (in support of predictions) that this controversial band is associated with *symmetric stretching of S atoms in bridges of edge-sharing  $\text{Ge}-(\text{S}_{1/2})_4$  tetrahedra*. Raman measurements above melting point have indicated the existence of tetrahedral units in the molten phase of these glasses. High pressure Raman measurements in  $\text{GeS}_2$  have shown that the bond lengths decrease substantially with pressure, while the material remains glassy throughout the pressure range of measurements (up to 10.8 GPa). It appears that all pressure induced effects are reversible after pressure relief.

(Received June 25, 2001; accepted september 3, 2001)

**Keywords:** Chalcogenide glasses, Raman spectroscopy, Temperature and pressure dependence, Phase transitions, Crystallization

### 1. Introduction

Chalcogenide glasses have drawn increasing attention over the past three decades because of their potential in photoresist [1,2], microelectronic [3-5], optoelectronic [6-9] and holographic [10,11] applications. In recent years, Ge-based chalcogenide glasses have been used for manufacturing optical waveguides of high transparency in the infrared window at  $1.3 \mu\text{m}$  and as host materials of rare earth ions for photonic applications [12-14]. Owing to all these applications, knowledge of their electronic and optical properties, as well as their microstructure (local and medium range structure) is very important over the entire glass forming range of compositions of the glass systems. It is generally known [15-19] that Ge-based chalcogenide glasses usually display a photobleaching effect upon illumination with band gap light, an effect which can be reversed after subsequent annealing [17-19] at an appropriate temperature below the glass transition temperature  $T_g$ . In fact, these photoinduced and thermally induced changes in their optical properties are often accompanied by structural changes which can be readily detected by Raman spectroscopy.

The structure of  $\text{Ge}_x\text{S}_{1-x}$  glasses at ambient conditions has been studied in the past by several groups [20-27] using Raman spectroscopy as the probing technique. It is generally accepted that a phase separation takes place in S-rich  $\text{Ge}_x\text{S}_{1-x}$  glasses ( $x < 1/3$ ), with the excess sulphur forming  $\text{S}_8$  ring clusters enclosed in the matrix of a, by large, *corner sharing  $\text{Ge}-(\text{S}_{1/2})_4$  tetrahedra network*. In contrast, two different models have been proposed for the compound  $\text{GeS}_2$  ( $x=1/3$ ) and the Ge-rich ( $x > 1/3$ ) glasses: According to the first [20,21], the structure of these glasses consists of an extended three dimensional and, more or less, chemically ordered network of  $\text{Ge-S}_n\text{Ge}_{4-n}$  ( $n=0,1,2,3,4$ ) tetrahedra centered about Ge atoms which are bonded to S and other Ge atoms, with the parameter  $n$  being largely determined by the S and Ge contents. In the second model, introduced [22,28] for the compound  $\text{GeS}_2$  and  $\text{GeSe}_2$  glasses, a layered structure is proposed similar to the two-dimensional (2D) crystalline phase [29-31] of the respective compound materials; in this model, the glass is built up by fragments of the 2D-phase, with each fragment consisting of *corner-sharing tetrahedra chains*

bridged by edge-sharing tetrahedra and being terminated by S-S (Se-Se) dimers which have directions perpendicular to the chains.

It is well known that  $\text{GeS}_2$  is a polymorphous material exhibiting, apart from the glassy phase, several crystalline phases having rather complicated low symmetry structures with a large number of molecules in the unit cell [29]. At ambient conditions,  $\text{GeS}_2$  can be found in two main crystalline modifications : (i) a three-dimensional structure (3D- $\text{GeS}_2$ ) in which the crystal lattice is made up by an extended array of *only corner sharing*  $\text{Ge}-(\text{S}_{1/2})_4$  tetrahedra, and (ii) a layered structure (2D- $\text{GeS}_2$ ) in which the lattice is built up by *both corner-sharing and edge-sharing tetrahedra*; in the latter structure, chains of corner-sharing tetrahedra are bridged via edge-sharing tetrahedra along a direction perpendicular to the chains. The two crystal phases can be distinguished in Raman experiments by the different frequency of the strongest (main)  $A_1$  mode which has been unambiguously assigned in both phases to symmetric stretching of S atoms in corner-sharing tetrahedra along the direction of chains. This mode was observed at  $339\text{ cm}^{-1}$  in the 3D-phase [30], while there is a disagreement for the 2D-phase with one report [30] claiming a frequency of  $356\text{ cm}^{-1}$  [30] and another at  $363\text{ cm}^{-1}$  [31].

A characteristic feature of the Raman spectrum of the glassy phase of  $\text{GeS}_2$  is a polarized band [20-27] for which, it was originally thought, there was no counterpart in the crystal phases. This so-called companion  $A_1^c$  mode, with a frequency ( $374\text{ cm}^{-1}$ ) about 10% greater than the normal  $A_1$  mode ( $342\text{ cm}^{-1}$ ) of the glassy phase, exhibits an anomalous dependence of intensity with composition in  $\text{Ge}_x\text{S}_{1-x}$  alloys [20,26]. The existence of this band in the Raman spectra of  $\text{GeS}_2$  and  $\text{GeSe}_2$  glasses prompted the proposition of the fragmented layered structure model [22,28] for these glasses and the band itself was assigned to symmetric vibrations of S-S dimers [22]. Elsewhere, the  $A_1^c$  band was associated with the medium range order (MRO) [23-25]. Finally, in another report [26], bearing in mind the higher frequency of this band compared to the  $A_1$  one, it was predicted that it should be related to *symmetric stretching of S atoms in bridges of edge-sharing tetrahedra*, by virtue of the higher force constant in the bridges in comparison to the chains.

There have not been any studies of structure of Ge-based chalcogenides glasses at high temperatures, although it is generally accepted that they crystallize above  $T_g$ . Most part of this work is concerned with the structural changes (as seen by Raman spectroscopy) occurring in glasses of the basic binary alloy system  $\text{Ge}_x\text{S}_{1-x}$  from room temperature, through  $T_g$  and  $T_m$  (melting point) and up to a temperature of about 130 K above  $T_m$ . The main objectives of the present work are : (i) to study the evolution of the Raman spectra with increasing temperature of the glasses and through the observed changes to draw conclusions about certain ambiguous spectral features, such as the controversial  $A_1^c$  companion Raman band, and the structure of these glasses as a whole, (ii) the systematic recording of structural changes taking place first with increasing and then with decreasing temperature and (iii) to obtain an idea about the structure of the  $\text{Ge}_x\text{S}_{1-x}$  melts and relate it to the structure of the respective glasses, in an attempt to get an insight on the mechanism of glass formation from the melt (quenching of the melt). In addition, Raman measurements at high hydrostatic pressures have been carried out in  $\text{GeS}_2$  glass in order to detect any changes of the structural units with pressure and to study the pressure dependence of the glassy network as a whole.

## 2. Experimental procedures

Glasses of the  $\text{Ge}_x\text{S}_{1-x}$  system covering a wide glass-forming region ( $0.17 \times 0.45$ ) were prepared using the melt quenching technique. Melts of predetermined atomic contents were kept inside a crucible at a temperature of about 100 K above  $T_m$  under rocking for about 24 hours, after which period the crucible was transferred quickly to water. The samples for the high temperature measurements were held inside small vacuum tight silica cells to avoid chemical changes of the materials, because  $\text{GeS}_2$ , and Ge-S alloys in general, decompose [32] and oxidize [33] in open space before they melt. The same samples and cells were used for the measurements of Raman spectra of molten  $\text{Ge}_x\text{S}_{1-x}$  alloys. A vacuum operated optical furnace [34] of low temperature gradients was used for the high temperature experiments. The high pressure experiments were performed using a diamond anvil cell (DAC) [35] which was loaded with a small size ( $\sim 50\text{ }\mu\text{m}$ ) glassy sample for the Raman measurements and ruby chips for monitoring (via the ruby luminescence) the pressure.

Two Raman set-ups were used for recording the spectra of glasses and their melts : One JOBIN YVON model T 64000 triple monochromator equipped with microscope and CCD detector for ambient conditions measurements, and a conventional SPEX model 1403 double monochromator for the high temperature and high pressure experiments. The 488 and 514.5 nm lines of an  $\text{Ar}^+$  laser were mainly used, but at very high temperatures (in molten state) the 647 nm line of a  $\text{Kr}^+$  laser was also used. The spectral slit width was between 3 and 4  $\text{cm}^{-1}$  for either double and triple monochromator set-up. Details regarding experimental procedures have been given elsewhere [36].

### 3. Results and discussion

#### 3.1. Raman spectra of $\text{Ge}_x\text{S}_{1-x}$ glasses at ambient conditions

In this section we present and discuss briefly our ambient conditions Raman data in connection with previous relevant studies, in order to provide the necessary background for discussing the high temperature and pressure data. Fig. 1 shows the polarized Raman spectra of  $\text{Ge}_x\text{S}_{1-x}$  glasses for four compositions: two S-rich glasses ( $x=0.20, 0.30$ ), the stoichiometric (compound)  $\text{GeS}_2$  glass ( $x=1/3$ ) and one Ge-rich glass ( $x=0.35$ ). There is good agreement between the Raman spectra of this work and those reported previously [20-27].

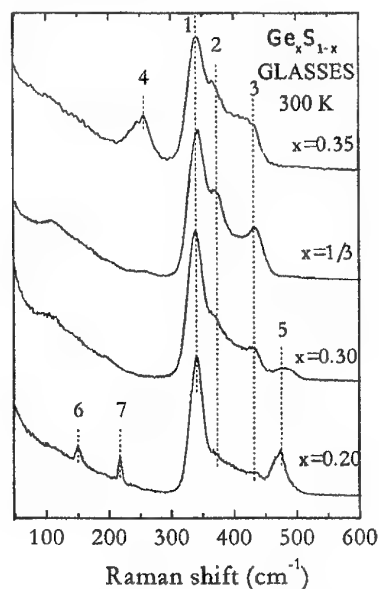


Fig. 1. Raman spectra of  $\text{Ge}_x\text{S}_{1-x}$  glasses for the compound ( $x=1/3$ ), one Ge-rich ( $x=0.35$ ) and two S-rich ( $x=0.20, 0.30$ ) compositions.

In the Raman spectrum of the compound  $\text{GeS}_2$  glass (Fig. 1), four bands are clearly observed at 110, 342, 374 and 434  $\text{cm}^{-1}$  and a fifth one is marginally observed at  $\sim 260 \text{ cm}^{-1}$ . The band at 110  $\text{cm}^{-1}$  has been attributed [27] to bond bending vibrations of S atoms in  $\text{Ge}(\text{S}_{1/2})_4$  tetrahedra, but judging from its low frequency and broad character we suggest that it may be due to intermolecular displacements of whole tetrahedral units. The bands at 342 and 374  $\text{cm}^{-1}$  are polarized and correspond to the  $A_1$  (main) and  $A_1^\circ$  (companion) modes mentioned in the introduction; it is generally accepted that the former is due to symmetric stretching of S atoms in the tetrahedra, while the latter has been a matter of controversy in the past and its origin is discussed in the next section 3.2 as is deduced from its temperature dependence. The band at 434  $\text{cm}^{-1}$  is relatively depolarized (compared to the  $A_1$  and  $A_1^\circ$  bands) and has been attributed to S-S bond stretching since a similar band has been observed in both fibrous [37] and liquid [38] sulphur which are known to contain sulphur chains. This implies the existence of either separate small sulphur chains in the network of  $\text{GeS}_2$  glass or interconnecting S-S units between tetrahedra. The appearance of homopolar (defective) S-S bonds in the compound glass indicates a deviation from the ideal network of only  $\text{Ge}(\text{S}_{1/2})_4$  tetrahedral units. In this situation

homopolar Ge-Ge bonds should, also, be present in the network of  $\text{GeS}_2$  glass and this is confirmed by the observation of the weak band at  $260\text{ cm}^{-1}$  which is attributed to such bonds as a similar band has been observed in amorphous Ge [39]. This argument is, also, supported by the big enhancement of intensity of this band in the Ge-rich  $\text{Ge}_x\text{S}_{1-x}$  glasses (Fig. 1). Further increase of the Ge-content ( $x > 0.35$ ) results in the appearance of other broad bands at lower frequencies ( $< 250\text{ cm}^{-1}$ ), an effect combined by a drop of intensity of the  $260\text{ cm}^{-1}$  as well the  $A_1$  and  $A_1^c$  bands, thus indicating a reduction of the  $\text{Ge}(\text{S}_{1/2})_4$  tetrahedral population.

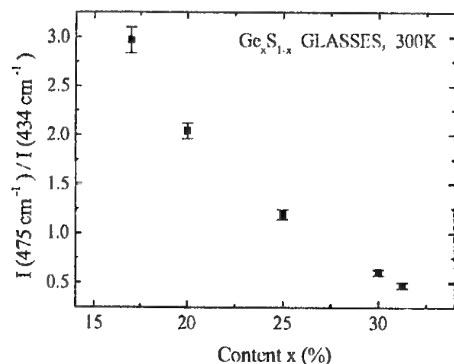


Fig. 2. Ratio of integrated intensities of the  $475\text{ cm}^{-1}$  to the  $434\text{ cm}^{-1}$  bands for  $\text{Ge}_x\text{S}_{1-x}$  glasses plotted against Ge content.

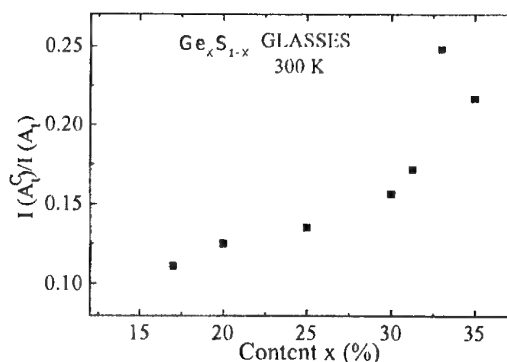


Fig. 3. Ratio of integrated intensities of the  $A_1(342\text{ cm}^{-1})$  to the  $A_1^c(374\text{ cm}^{-1})$  plotted against Ge content.

Another polarized band at  $475\text{ cm}^{-1}$  is observed in the spectra of the S-rich  $\text{Ge}_x\text{S}_{1-x}$  glasses (Fig. 1) for which there is general agreement [20-27] that is due to symmetric stretching in  $\text{S}_8$  rings. The intensity of this band increases with increasing S-concentration, while that of the  $434\text{ cm}^{-1}$  band decreases, showing a relative population increase of  $\text{S}_8$  rings against S-S chains. This effect is illustrated in Fig. 2 in which the integrated intensities ratio of the  $475$  to  $434\text{ cm}^{-1}$  bands is plotted against concentration. This ratio increases non-linearly with increasing S- (decreasing Ge-) content. The integrated intensities were deduced by fitting the bands to Gaussian functions.

### 3.2. High temperature phase transitions of $\text{Ge}_x\text{S}_{1-x}$ glasses

Figs. 4 - 7 show the Raman spectra of four  $\text{Ge}_x\text{S}_{1-x}$  glasses at various temperatures from room temperature up to a temperature close to melting point of the respective alloy. Also, in the same Figs. 4 - 7, the Raman spectra of the materials are shown after free (unforced) cooling to room temperature. Specifically, the four compositions include: the compound  $\text{GeS}_2$  glass ( $x = 1/3$ , Fig. 4), one moderately rich in Ge glass ( $x = 0.35$ , Fig. 5), one moderately rich in S glass ( $x = 0.30$ , Fig. 6) and a highly enriched in S one ( $x = 0.20$ , Fig. 7).

From the evolution of the Raman spectrum of  $\text{GeS}_2$  glass (Fig. 4), we conclude that two gradual phase transitions take place in this glass at high temperatures. First, at  $\sim 750\text{ K}$  the main  $A_1$  band becomes sharper, an effect which is accompanied by a simultaneous appearance of new sharp bands at low frequencies. At  $\sim 770\text{ K}$ , this band is quite narrow and looks similar (in terms of frequency, intensity and narrowness) to the characteristic  $A_1$  mode of the 3D-crystalline phase [30]. This sharp band is observed at  $\sim 337\text{ cm}^{-1}$ , that is slightly shifted (compared to the value of  $339\text{ cm}^{-1}$ , Ref.30) towards the lower frequencies because the material is at elevated temperature. All these observations indicate that the compound  $\text{GeS}_2$  glass undergoes a transition to the 3D-crystalline phase at  $\sim 750\text{ K}$ . Further increase of temperature to  $800\text{ K}$  results in the appearance of a new line at  $\sim 352\text{ cm}^{-1}$  which becomes stronger and sharper above this temperature at the expense of the rival  $A_1$  band of the 3D-phase. This new band is the dominant feature of the spectrum above  $900\text{ K}$  and up to melting point  $T_m$  ( $=1123\text{ K}$ ), and corresponds to the characteristic  $A_1$  mode of the 2D-crystalline phase [29,31]. This is confirmed by slow cooling of the material to room temperature (Fig. 4), with the 2D-phase being retained throughout the cooling process. This observation also shows that the

two step crystallization of  $\text{GeS}_2$  glass is irreversible. The first transition to the 3D-phase implies that the network of the  $\text{GeS}_2$  glass is, largely, three-dimensional, with the corner-sharing tetrahedra linkages being dominant over the edge-sharing ones. Finally, it should be noted that the  $434\text{ cm}^{-1}$  band of  $\text{GeS}_2$  diminishes with increasing temperature, well below the crystallization temperature.

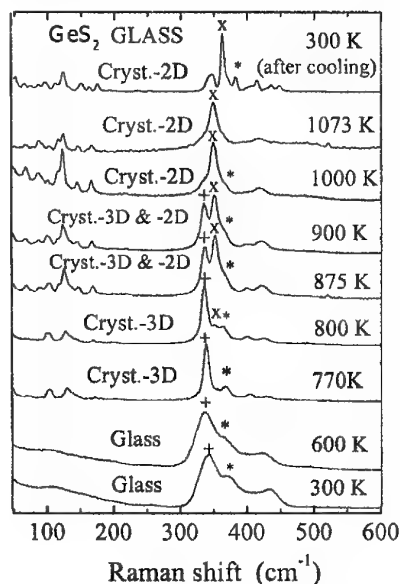


Fig. 4. Evolution of the Raman spectrum of  $\text{GeS}_2$  glass showing a two step irreversible crystallization. + main  $A_1$  band of glassy phase; \*  $A_1^c$  companion band of glassy phase; X main  $A_1$  band of the 2D-crystalline phase.

The evolution of the  $A_1^c$  band of  $\text{GeS}_2$  glass with temperature reveals that this band has, after all, a counterpart in the crystalline phases and this has been concluded after deconvoluting the high temperature Raman spectra. This band (and its successor in the 3D-phase) is well resolved up to 850 K, while above this temperature is seen (in the unconvoluted spectra) as a shoulder; however, it reappears upon cooling and is clearly resolved below 700 K, with a frequency of  $382\text{ cm}^{-1}$  in the room temperature spectrum of the 2D-phase. A similar band has been observed previously [29,31] in the Raman spectrum of the 2D-single crystal of  $\text{GeS}_2$  and assigned to symmetric stretching of S atoms in bridges of edge-sharing tetrahedra; hence, a similar assignment is implied for the  $A_1^c$  band of  $\text{GeS}_2$  glass, in agreement with previous predictions[26].

A similar two-step crystallization is observed at high temperatures in  $\text{Ge}_x\text{S}_{1-x}$  glasses having compositions close to that of the compound  $\text{GeS}_2$  glass, first to 3D- and then to the 2D-phase (Figs. 5 and 6). The 2D-phase is maintained up to melting point and following a subsequent cooling to room temperature, showing that crystallization of these moderately enriched in Ge and S glasses is also irreversible.

In the  $\text{Ge}_x\text{S}_{1-x}$  glass highly enriched in S, though, the structural changes observed at high temperatures are different (Fig. 7). It is reminded that a phase separation takes place in such glasses, with  $\text{S}_8$  ring clusters forming in the matrix of predominantly corner-sharing tetrahedra (three-dimensional glassy network, see also Fig. 3). Around 720 K, the  $A_1$  band becomes narrower, indicating that crystallization of the glassy matrix commences to the 3D-phase of  $\text{GeS}_2$ , a phase maintained up to melting point. (The exact value of the melting point for this glass is not known, but one can guess it should be around 870 K as the intensity of the spectrum drops substantially at this temperature, Fig. 7). It is significant that after cooling, the spectrum of the material is similar (both with regard to the lineshape and intensity) to that of the starting glass (Fig. 7), indicating that the one-step crystallization of highly enriched in S glasses is reversible. It has been observed in a previous work [40] that three-dimensional glassy networks of Ge-based chalcogenides favour the appearance of photo- and thermally-induced reversible structural changes because of their larger free volume. Here, the matrix of the highly rich in S glass has a largely three-dimensional structure which, it seems

facilitates successive reversible transitions from glass to crystal, but *always retaining its three dimensional character*. The latter should be attributed to the excess sulphur which fills the voids of the glassy matrix, thus preventing the network from becoming two-dimensional as is the case for glasses close to stoichiometry. A more detailed account of the high-temperature transitions is given elsewhere [36].

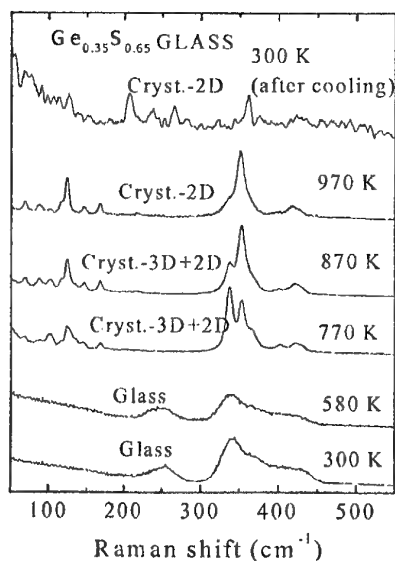


Fig. 5. Temperature dependence of Raman spectrum of  $\text{Ge}_{0.35}\text{S}_{0.65}$  glass (slightly rich in Ge) showing a two step irreversible crystallization to the 3D- and 2D-phases of  $\text{GeS}_2$ .

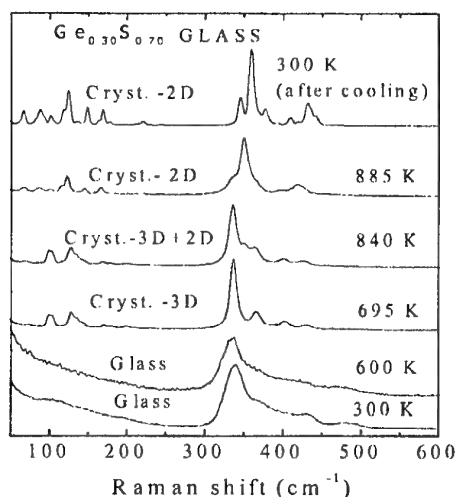


Fig. 6. Temperature dependence of Raman spectrum of  $\text{Ge}_{0.30}\text{S}_{0.70}$  glass (moderately rich in S) showing a two stage irreversible crystallization to the 3D- and 2D-phases of  $\text{GeS}_2$ .

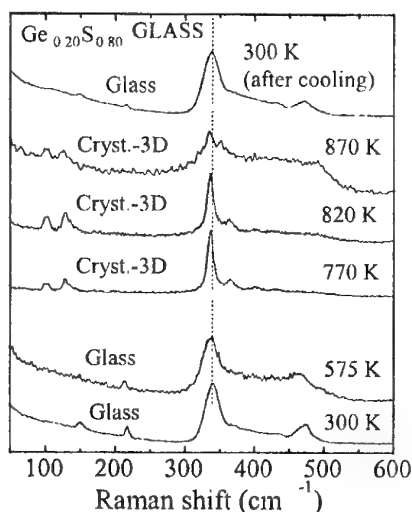


Fig. 7. Temperature dependence of Raman spectrum of the  $\text{Ge}_{0.20}\text{S}_{0.80}$  glass (highly rich in S) showing a one stage reversible crystallization to the 3D-phase of  $\text{GeS}_2$ .

### 3.3. Raman spectra of $\text{Ge}_x\text{S}_{1-x}$ melts

The Raman signal from all  $\text{Ge}_x\text{S}_{1-x}$  alloys drops abruptly above melting point as the molten samples become almost opaque to any laser line in the visible, that is, they acquire metallic behaviour. As a consequence, the Raman spectrum of the hot silica cell ( $\text{SiO}_2$  glass) appears in the



recorded spectrum as noise which exceeds the signal from the melt. However, we have succeeded to obtain the Raman spectrum of pure melts by subtracting, in each case, the Raman spectrum of the cell which has been recorded separately (without sample inside it) at a temperature coinciding or close to that of the melt

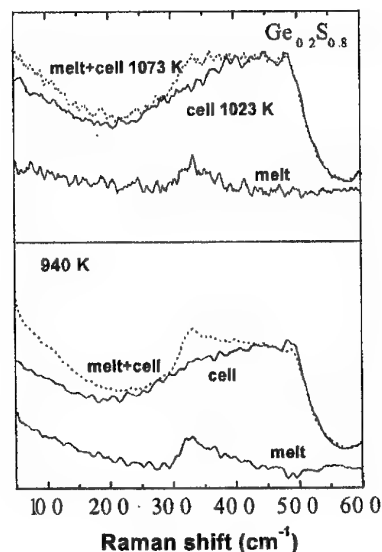


Fig. 8. Raman spectra of molten  $\text{Ge}_{0.20}\text{S}_{0.80}$  at two temperatures showing the characteristic band (at  $\sim 320 \text{ cm}^{-1}$ ) due to tetrahedral  $\text{Ge}-(\text{S}_{1/2})_4$  units. The Raman spectrum of the silica cell was recorded separately and subtracted from the overall spectrum of melt and cell.

As an example, we present in Fig. 8 the Raman spectrum of the  $\text{Ge}_{0.20}\text{S}_{0.80}$  melt at two temperatures as is deduced from the above described procedure. The detection of a weak band at  $\sim 330 \text{ cm}^{-1}$  in the spectrum of the pure melt provides evidence that the tetrahedral  $\text{Ge}-(\text{S}_{1/2})_4$  units exist in this molten alloy, at least at the lower temperature of 940 K. As the temperature is increased further (1073 K), this Raman band of the melt is only marginally observed (Fig. 8), which can be explained in terms of an increased melt opaqueness or of shorter life-times of the tetrahedral species with temperature. The latter interpretation is compatible with the suggestion that at high temperatures and particularly in the molten phase, the coordination number of Ge changes from 4 to 8 and the element becomes metallic [41,42]. This also explains the opaqueness of  $\text{Ge}_x\text{S}_{1-x}$  melts. Similar results have been obtained from other  $\text{Ge}_x\text{S}_{1-x}$  melts.

### 3.4. Raman spectrum of $\text{GeS}_2$ glass at high pressures

The pressure dependence of the Raman spectrum of  $\text{GeS}_2$  glass is shown in Fig. 9 for pressures up to 10.8 GPa. Also, in the same figure, the Raman spectrum of the glass is shown after pressure relief. A substantial shift towards the higher frequencies is observed of the whole packet of molecular bands, i.e. the main  $A_1$  band at  $342 \text{ cm}^{-1}$ , the companion  $A_1^c$  band at  $374 \text{ cm}^{-1}$  and the band due to S-S bonds at  $434 \text{ cm}^{-1}$ , although only the position of the  $A_1$  band is unambiguously detected at high pressures. These results indicate a substantial densification of the glass and a continuous decrease of the Ge-S and S-S bond lengths with pressure. The band at  $260 \text{ cm}^{-1}$  is not detected at high pressures.

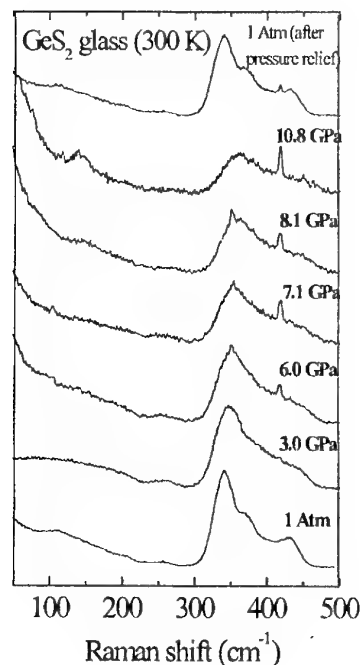


Fig. 9. Pressure dependence of the Raman spectrum of  $\text{GeS}_2$  glass showing a strong hardening of the Raman bands.

We have also observed a darkening of the glass at high pressures and a consequent continuous loss of transparency to all laser lines in the visible, which is in agreement with the strong red shift of the absorption edge observed in this glass with pressure [43]. This effect causes a big drop of the Raman intensity from the glass at high pressures and, most likely, results in the emergence of a sharp line at  $\sim 420 \text{ cm}^{-1}$  at a pressure of  $\sim 5 \text{ GPa}$  which is attributed [44] to Raman scattering from the sapphire ( $\text{Al}_2\text{O}_3$ ) window of the DAC or/and the ruby chips. This line emerges in the spectrum at high pressures when the Raman signal of the glass becomes very weak. Above  $10 \text{ GPa}$ , the glass became almost opaque to visible radiation. After releasing the pressure, the spectrum of  $\text{GeS}_2$  glass returns back, more or less, to its initial lineshape and intensity, thus implying no significant hysteresis effects in the glass.

#### 4. Conclusions

The study of the Raman spectra of  $\text{Ge}_x\text{S}_{1-x}$  glasses at high temperatures has shown that all glasses undergo a first-step transition to the 3D-crystalline phase of  $\text{GeS}_2$  which confirms that the network of these glasses is, by large, three-dimensional. At higher temperatures, the compound  $\text{GeS}_2$  and the moderately rich in Ge or S glasses sustain a second transition to the layered 2D-crystalline phase of  $\text{GeS}_2$  which is irreversible upon subsequent cooling to room temperature. In the highly rich in S glass, though, whose glassy matrix is made up almost exclusively of corner-sharing  $\text{Ge}(\text{S}_{1/2})_4$  tetrahedra, there is no second transition to the 2D-phase, with the material maintaining the 3D-crystal structure up to melting point and then reversing to its initial glassy state after cooling to room temperature; the reversibility and dimensionality preservation of the matrix of this glass is attributed to the presence of  $\text{S}_8$  ring clusters which "fill" the free volume of the three-dimensional matrix.

From the evolution of the  $A_1^\circ$  companion band of  $\text{GeS}_2$  glass in the crystalline phases, we have concluded that this band is due to symmetric stretching of S atoms in bridges of edge-sharing tetrahedra, in agreement with previous predictions.

All  $\text{Ge}_x\text{S}_{1-x}$  alloys become almost opaque above melting point and this is related to the metallic behaviour of Ge in the molten phase. However, there is evidence that the tetrahedral  $\text{Ge}(\text{S}_{1/2})_4$  units exist in the melts of these alloys, at least up to a certain temperature.

The application of pressure on the  $\text{GeS}_2$  glass results in a continuous densification of the glass which is manifested by the substantial hardening of the Raman bands with increasing pressure. The material darkens continuously with pressure because of a strong red shift of its absorption edge, but maintains its glassy phase throughout the pressure range (up to 10.8 GPa). It appears that all pressure induced effects (volume, bond lengths and optical transparency) are reversible after bringing the glass to ambient pressure.

### Acknowledgements

We would like to thank Professor G. Papatheodorou and his colleagues at the Institute of Chemical Engineering and High Temperature Chemical Processes of the Foundation of Research and Technology-Hellas, Patras, for providing the special silica cells, and Dr E.A. Pavlatou and Mr. A. Perakis for helping in some high temperature and high pressure experiments on  $\text{GeS}_2$  glass. We are also grateful to Professor M. Frumar and Dr M. Vlcek at the Department of General and Inorganic Chemistry, University of Pardubice, Czech Republic, for the facilities provided during the scientific visit of one of us (I.P.K) to the University of Pardubice.

### References

- [1] A. Yoshikawa, O. Ochi, H. Nagai, Y. Mizushima, *Appl. Phys. Lett.* **29**, 677 (1976).
- [2] M. J. Bowden, *Solid State Technology*, June 1981, p. 73.
- [3] D. Adler, *Scientific American* **236**, 36 (1977).
- [4] S. R. Ovshinsky, *J. Non-Cryst. Solids* **141**, 200 (1992).
- [5] V. M. Lyubin, V. K. Tikhomirov, *J. Non-Cryst. Solids* **164-166**, 1211 (1993).
- [6] M. Mitkova, T. Petkova, R. Markovski, V. Mateev, *J. Non-Cryst. Solids* **164-166**, 1247 (1993).
- [7] P. J. S. Ewen, A. Zekak, C. W. Slinger, G. Dale, D. A. Pain, A. E. Owen, *J. Non-Cryst. Solids* **164-166**, 1203 (1993).
- [8] H. Hisakuni, K. Tanaka, *Optics Lett.* **20**, 958 (1995).
- [9] B. G. Aitken, R. S. Quimby, *J. Non-Cryst. Solids* **213&214**, 281 (1997).
- [10] T. Ide, M. Suzuki, M. Okuda, *Japan. J. Appl. Phys, Part II* **34**, L529 (1995).
- [11] K. Tai, E. Ong, R. G. Vadimsky, *Proc. Electrochem. Society* **82-89**, 9 (1995).
- [12] V. Krasteva, D. Machewirth, G. H. Sigel Jr., *J. Non-Cryst. Solids* **213&214**, 304 (1997).
- [13] H. Harada, K. Tanaka, *J. Non-Cryst. Solids* **246**, 189 (1999).
- [14] D. A. Turnbull, B. G. Aitken, S. G. Bishop, *J. Non-Cryst. Solids* **244**, 260 (1999).
- [15] R. A. Street, R. J. Nemanich, G. A. N. Connel, *Phys. Rev.* **B 18**, 6915 (1978).
- [16] A. V. Kolobov, B. T. Kolomiets, V. M. Lyubin, N. Sebastian, M. A. Taguirdzanov, J. Hajto, *Soviet Phys. Solid State* **24**, 603 (1982).
- [17] K. Shimakawa, A. V. Kolobov, S. R. Elliott, *Adv. Phys.* **44**, 475 (1995).
- [18] C. Raptis, Z. G. Ivanova, *J. Appl. Phys.* **64**, 2617 (1988).
- [19] M. Vlcek, C. Raptis, T. Wagner, A. Vidourek, M. Frumar, I. P. Kotsalas, D. Papadimitriou, *J. Non-Cryst. Solids* **192&193**, 669 (1995).
- [20] G. Lucovsky, F. L. Galeener, R. C. Keezer, R. H. Geils, H. A. Six, *Phys. Rev.* **B 10**, 5134 (1974).
- [21] G. Lucovsky, R. J. Nemanich, F. L. Galeener, *Proc. of 7<sup>th</sup> Intern. Confer. on Amorphous and Liquid Semiconductors*, Edinburgh, 1977 (Ed. W.E. Spear), p. 130.
- [22] P. M. Bridenbaugh, G. P. Espinosa, J. E. Griffiths, J. C. Phillips, J. P. Remeika, *Phys. Rev.* **B 20**, 4140 (1979).

- [23] K. Murase, K. Yakushiji, T. Fukunaga, *J. Non-Cryst. Solids* **59&60**, 855 (1983).
- [24] K. Arai, *J. Non-Cryst. Solids* **59&60**, 1059 (1983).
- [25] P. Boolchand, J. Grothaus, M. Tenhover, M. A. Hazle, R. K. Grasselli, *Phys. Rev.* **B33**, 5421 (1986).
- [26] S. Sugai, *Phys. Rev.* **B 35**, 1345 (1987).
- [27] Ke. Tanaka, M. Yamaguchi, *J. Non-Cryst. Solids* **227-230**, 757 (1998).
- [28] J. A. Aronovitz, J. R. Banavar, M. A. Marcus, J. C. Phillips, *Phys. Rev.* **B 28**, 4454 (1983).
- [29] Z. V. Popovic, H. J. Stolz, *Phys. Status Solidi* **B 106**, 337 (1981).
- [30] K. Inoue, O. Matsuda, K. Murase, *Solid State Commun.* **79**, 905 (1991).
- [31] Z. V. Popovic, M. Holtz, K. Reiman, K. Syassen, *Phys. Status Solidi* **b 198**, 533 (1996).
- [32] G. J. Janz, *Molten Salts Handbook* (Academic Press, New York, 1967).
- [33] I. Tichy, A. Triska, M. Frumar, H. Ticha, *Philos. Mag.* **54**, 219 (1986).
- [34] C. Raptis, *J. Phys.* **E 16**, 749 (1983).
- [35] K. R. Hirsch, W. B. Holzapfel, *Rev. Sci. Instrum.* **52**, 149 (1981).
- [36] I. P. Kotsalas, C. Raptis, *Phys. Rev. B*, accepted for publication.
- [37] W. Dultz, H. D. Hochheimer, W. Muler-Lierheim, *Proc. of 5<sup>th</sup> Intern. Confer. on Amorphous and Liquid Semiconductors*, Vol. **II** (Taylor Francis, London, 1974).
- [38] K. Hattori, H. Kawamura, *J. Non-Cryst. Solids*, **59&60**, 1063 (1983).
- [39] J. C. Lannin, N. Malley, S. T. Kshirsagar, *Solid State Commun.* **53**, 939 (1985).
- [40] I. P. Kotsalas, D. Papadimitriou, C. Raptis, M. Vlcek, M. Frumar, *J. Non-Cryst. Solids* **226**, 85 (1998).
- [41] R. Zallen, *The Physics of amorphous Solids* (John Wiley & Sons, 1983), p. 254.
- [42] A. C. Wright, *NATO ASI Series 3*, Vol. **23**, Ed. M. F. Thorpe and M. I. Mitkova (Kluwer, 1997), p. 83.
- [43] B. A. Weinstein, R. Zallen, M. L. Slade, J. C. Mikkelsen Jr., *Phys. Rev.* **B 25**, 781 (1982).
- [44] S. P. S. Porto, R. S. Krishnan, *J. Chem. Phys.* **47**, 1009 (1967).

## PHYSICAL AGEING IN CHALCOGENIDE GLASSES

J. M. Saiter

LECAP, Faculté des Sciences, Université de Rouen, 76821 Mont Saint Aignan, Cedex, France

In this work, some relationships proposed in the literature in order to link the value of the glass transition temperature and the structure engaged in chalcogenide based alloys are discussed. We show that because of the bad knowledge of the real surrounding of the different atoms engaged in the material composition, these relationships must be used with some precautions. On the other hand, from the study of the physical ageing, general property for a glassy structure, we show that for specific values of the average coordination number ( $Z \approx 2.1$  and  $Z \approx 2.24$ ) calculated for system obeying to the 8-N rule, many properties as apparent activation energy for the relaxation, crystallisation ability, optical gap, viscosity, are modified. Finally, the physical ageing kinetic measurements are found dependent on the structures engaged in the glassy systems. In particular, we show that molecular species as  $\text{GeTe}_4$  can also move during ageing in spite of its massive character and strong connectivity.

(Received June 25, 2001; accepted September 3, 2001)

*Keywords:* Chalcogenide, Glass transition, Physical ageing

### 1. Introduction

Thirty years ago, the first sentence of a paper devoted to glassy chalcogenide based materials was, as an example:

"Chalcogenide glasses exhibit many useful electrical, opto-electrical threshold and memory switching properties and thus appear as good candidates for new technological applications".

Today, basically the same sentence is used and, in spite of all these useful properties, it seems that all these hopes have not been followed by concrete applications. Nevertheless these new properties and potential applications exist. Indeed, since the well-known xerography process using Se or SeAs, we may note lithography with  $\text{Ge}_{25}\text{Se}_{75}$  [1], CD compatible erasable disk with GeTe or GeTeSe [2], chemical sensors with AsS and AsSe based alloys [3], long lengths of low loss IR transmitting devices with  $\text{As}_{40}\text{S}_{60-x}\text{Se}_x$  [4] and also the use of switching and memory effects as observed in  $\text{Bi}_{26}\text{Te}_{135}\text{Se}_{36}$  [5] or photodarkening properties as in  $\text{As}_2\text{S}_3$ ,  $\text{As}_2\text{Se}_3$ ,  $\text{GeSe}_2$  or  $\text{GeS}_2$  [6,7].

In fact, one of the most important behaviour of a glassy structure is often omitted. By definition, a glass is characterised by a lack of thermodynamic equilibrium. As a consequence, all the physical properties are time dependent, generally refereed as physical ageing phenomenon [8]. As an example, Fig. 1 shows the variations with time of the current measured on a  $\text{Bi}_2\text{Se}_{98}$  thin film maintained at 293 K and submitted to a potential increment of 10 V. After more than 50 h, the current is not stabilised. The time constant (or distribution of time constant) characterising this behaviour cannot be obtained by electric charge transfers associated (or not) to defects recombination. This result implied that a relaxation process of large magnitude engaging the structure itself (atomic or molecular relaxation), must be taken into account. What are the consequences of molecular relaxation (physical ageing) on a given property? This key question must be associated with a second one: do correlation exists between the glass structure and its physical ageing kinetic? Today, it is not possible to propose a general model linking the glassy structure in a glass and its ability to relax. In this work, we present a set of results allowing the proposition of some interesting tendencies.

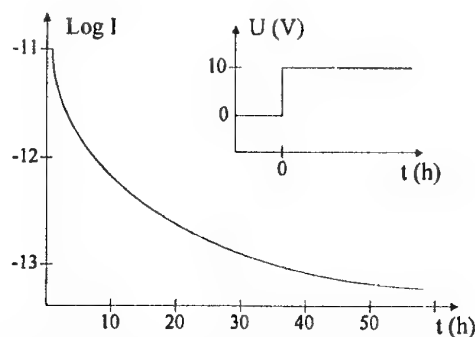


Fig. 1. Variations with time of the dark current measured on a  $\text{Bi}_2\text{Se}_{98}$  thin film.

Cooling a liquid with a rate high enough to avoid the crystallisation will lead it to the supercooled regime in which the viscosity will increase drastically as the temperature will decrease. For a given temperature ( $T_g$ ), or more precisely for a given domain of temperatures called the glass transition, the supercooled liquid is frozen in, the viscosity reaches values as large as  $10^{12}$  poises, and for  $T < T_g$  a glassy structure is obtained. As exemplified on Fig. 2, this glassy structure is characterised by an excess of free volume or, which is equivalent, by an excess of enthalpy, an excess of configurational entropy when comparison is made with the corresponding thermodynamic equilibrium state. Then, the disorder engaged into the glassy structure can be defined at different scales (short, medium or long range). As a second consequence, a glass kept at  $T < T_g$  will lose its excess of enthalpy by molecular relaxation to reach more favourable thermodynamic states. Thus, a glass kept during an infinite time at  $T < T_g$  must reach the thermodynamic equilibrium. This goal is obtained with the supercooled liquid state (extrapolated in the temperature domain  $T < T_g$ ) and not with the crystalline one (see Fig. 2). With other words, a glass cannot crystallise by physical ageing. To crystallise the material, it is necessary to heat the glass above its glass transition in order to reach a viscosity value low enough to authorise molecular rearrangements or atomic diffusions (Fig. 3). Many models are now available to analyse the relaxation kinetic [9-12] and it is now established that a good model must take into account the following characteristics. Molecular relaxations in the glass and for temperatures close to  $T_g$  are of cooperative natures. Relaxation kinetics cannot be described by a linear and an exponential time relaxation function and a distribution of relaxation time function must be taken into account. The phenomenon is reversible by a thermal cycle consisting of heating the glass above  $T_g$  and then cooling back to the annealing temperature, of course if no crystallisation occurs in the supercooled state.

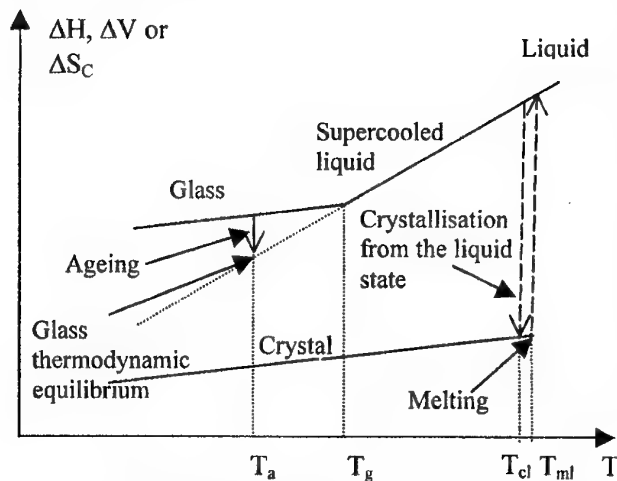


Fig. 2. Enthalpic diagram showing the glass transition and the crystallisation from the liquid state ( $T_{cl}$ ) and the melting  $T_{ml}$ .

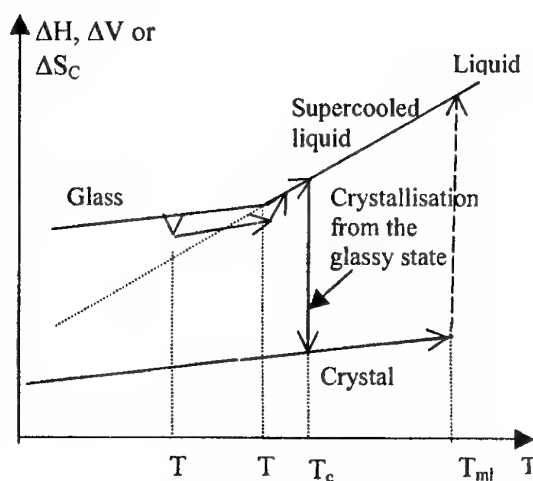


Fig. 3. Enthalpic diagram showing the crystallisation from the glassy state.

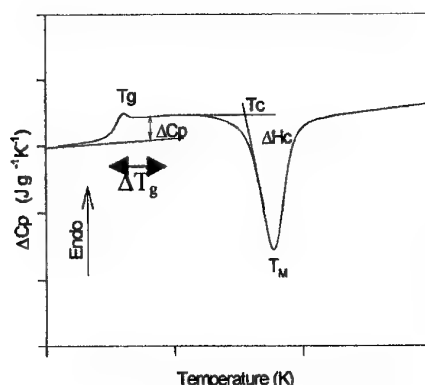


Fig. 4. Typical DSC trace obtained with a chalcogenide glass.

To analyse a glass, one of the easiest methods consists in performing calorimetric measurements. Fig. 4 shows a typical differential scanning calorimetric curves that could be obtained for instance on a Se glass. At low temperature, the glass transition is observed by only an endothermic  $\Delta C_p$  step if the sample is non-aged or an endothermic peak if the sample is aged. Then at higher temperature an exothermic peak of crystallisation also called cold crystallisation or devitrification to distinguish this transformation from the one obtained by slow cooling from the liquid state. Finally, the melting of the crystalline part occurs at higher temperatures (non-presented on Fig. 4) as an endothermic peak. Thus to characterise a glass, such measurements give us many facilities. We have: the glass transition temperature  $T_g$ , the value of  $\Delta C_p$  at  $T_g$ , the domain of temperature on which the glass transition occurs  $\Delta T_g = T_{gmax} - T_{gmin}$ , the area of the endothermic relaxation peak  $\delta H$ , the value of the crystallisation temperature ( $T_c$  or  $T_m$ ), the enthalpy of crystallisation  $\Delta H_c$  and finally the distance  $T_c - T_g$ . Each of these quantities can give us precious informations for the considered glass. For instance and for only the glass transition:

- 1) Greatest the  $T_g$ , greatest must be the rigidity of the medium [13,14].
- 2) Greatest  $\Delta T_g$ , greatest must be the width of the time relaxation distribution [15].
- 3) Greatest  $\Delta C_p$ , greatest must be the fragility (from the Angell strong fragile liquid glass former concept [16]).

Most of these quantities are not material constants but depend also on the measurement methods, on the constraints undergone and on the thermal history of the samples. For instance, the values of the cooling rate, the heating rate, the sample age, the value of the annealing temperature influence and modify the values of  $T_g$ ,  $\Delta T_g$ ,  $\delta H$ ,  $T_c$ ,  $\Delta H_c$  [17,21]. With other words, to compare data of different origins, many precautions must be taken but these dependencies can also give us many new opportunities to characterise a glassy structure. In this field, among all the different materials able to be studied, chalcogenide elements and alloys exhibit the great advantage to give a large variety of systems whose we may a priori control the structures. In the following, this opportunity will be analysed for different vitreous chalcogenide based alloys. In particular, the value of the glass transition temperature, and the relaxation kinetics will be investigated.

## 2. Glass transition temperature and structure

As previously mentioned, it is well established that  $T_g$  depends on the connectivity, and consequently on the rigidity of the vitreous network. This means that, using a linear polymeric structure as Se vitreous matrix, by adding an element with coordination number greater than 2, it will result an increase of the  $T_g$  values with the content of the added atom. The variations of  $T_g$  collected from the literature and obtained on the covalent systems  $Se_{1-x}Ge_x$ ,  $Se_{1-x}As_x$  and on the  $Se_{1-x}Bi_x$



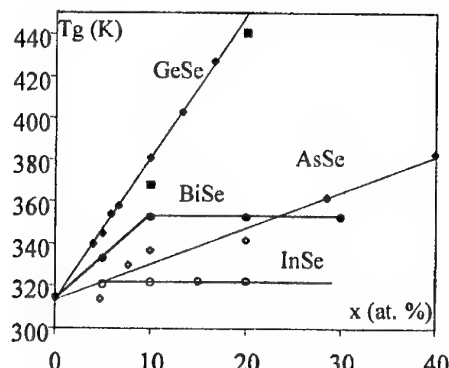


Fig. 5. Glass transition temperature of Se based binary glassy alloys as a function of concentration of added element.

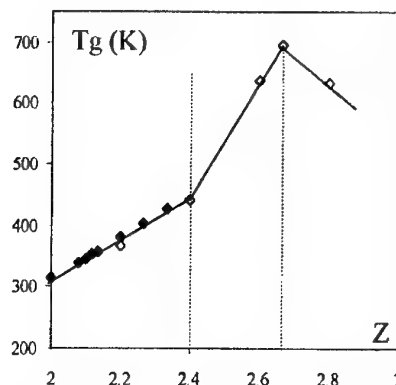


Fig. 6. Variations of T<sub>g</sub> versus Z for Se<sub>1-x</sub>Ge<sub>x</sub>. Lines are drawn as guides for the eyes.

and Se<sub>1-x</sub>In<sub>x</sub> [22-24] are presented on Fig. 5. It is clear that T<sub>g</sub> increases with x for the covalent systems (with Ge and As atoms). This is the expected behaviour, the threefold As atoms and the fourfold Ge atoms increasing the connectivity of the medium. For the Se-Bi system, T<sub>g</sub> increases at low Bi content and up to 10 at.%, while for Bi content greater than 10 at.%, T<sub>g</sub> remains a constant. For the Se-In system, T<sub>g</sub> remains a constant whatever the In content. The plateau is interpreted by the existence of demixed structures, respectively Bi<sub>2</sub>Se<sub>3</sub> and In<sub>2</sub>Se<sub>3</sub> micro-clusters. Since the works of J.C. Phillips [25] and K. Tanaka [26], it is established that glassy covalent networks exhibit two topological thresholds. Describing these glassy structures by means of virtual atoms bonded together with an average coordination number given by

$$Z = \sum_i x_i Z_i \quad (2.1)$$

(x<sub>i</sub> is the at.% content and Z<sub>i</sub> the coordination number of element i), the glass network must change from a floppy to a rigid type for Z = 2.4 (Phillips constraints theory) and changes from a two-dimensional layered structure to a three dimensional network arrangement for Z = 2.7 (Tanaka model). These two thresholds are well observed on the T<sub>g</sub> versus Z variations on many binary and ternary chalcogenide based glasses and is exemplified by the results concerning the Se<sub>1-x</sub>Ge<sub>x</sub> reported in Fig. 6. One neat way to describe the variations of T<sub>g</sub> with Z in chalcogenide glasses was proposed by Sreeram et al [23] according to the Gibbs DiMarzio modified relationship:

$$T_g = \frac{T_{g0}}{1 - \beta(Z - 2)} \quad (2.2)$$

where T<sub>g0</sub> is the glass transition temperature of the linear polymer and β a system parameter included between 0 < β < 1. The stochastic origin of the Gibbs DiMarzio modified equation, recently demonstrated by M. Micoulaut et al [27] allows to propose a topological origin, for the constant β according to the relationship:

$$\beta^{-1} = \sum_{i=1}^{M-1} (Z_i - 2) \ln \left[ \frac{Z_i}{2} \right] \quad (2.3)$$

where  $Z_i$  is the coordination number of element  $i$  added in the chalcogenide matrix. Many data have been successfully fitted with relationship 2, as for instance  $\text{Ge}_x\text{Sb}_y\text{Se}_{1-x-y}$ ,  $\text{Ge}_x\text{Sb}_y(\text{Se}_{60}\text{Te}_{40})_{1-x-y}$ ,  $\text{Ge}_x(\text{Sb}_{66}\text{As}_{34})_y(\text{Se}_{60}\text{Te}_{40})_{1-x-y}$  systems (compositions are per mole %). More recently, the problem of the role played by In atoms in the Ge-Se-In system was solved with the help of equation 2. As for the Se-In binary system, it was shown that In atoms do not participate to the variations of  $T_g$  in Ge-Se-In [24].

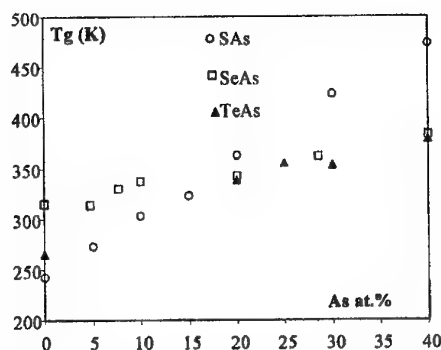


Fig. 7. Variations of  $T_g$  for As modified binary chalcogenide materials.

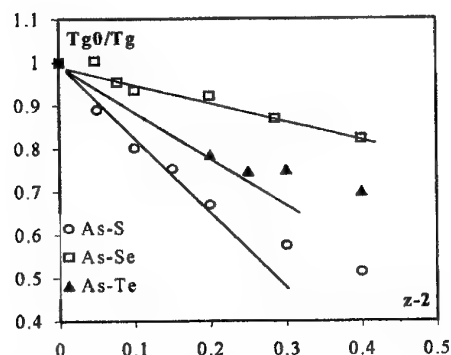


Fig. 8. Variations of  $T_{g0}/T_g$  with  $Z$  for chalcogenide-As alloys assuming  $Z_{\text{As}}=3$  and  $Z_{\text{chalcogene}}=2$ .

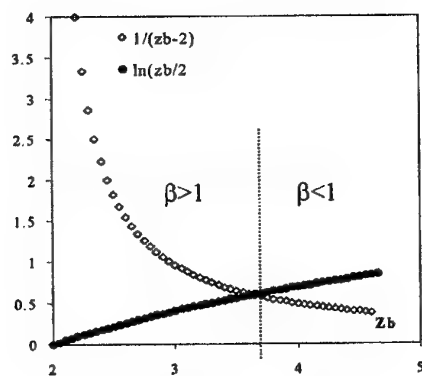


Fig. 9. Stochastic model limit.

Finally, it appears that until no heteropolar bonds are formed by the added element in the chalcogenide network and until it exists no ambiguity concerning the values of the coordination numbers of the different atoms constituting the investigated alloys, the variations of  $T_g$  with  $Z$  are well described by these formula and the topological thresholds are well observed. Nevertheless their universal characters must be proved yet. As an example, Fig. 7 shows the variations of  $T_g$  measured on  $\text{S}_{1-x}\text{As}_x$ ,  $\text{Se}_{1-x}\text{As}_x$  and  $\text{Te}_{1-x}\text{As}_x$  [22,23] as a function of  $x$ . For Se, and As atoms, it is clear that the 8-N rule is respected leading respectively to  $Z_{\text{Se}}=2$  and  $Z_{\text{As}}=3$ . If we assume that the 8-N rule is also respected by the other chalcogenide elements as it is often made in many works, the variations of  $T_{g0}/T_g$  with  $(Z-2)$  according to formula 2 must be linear and the slopes give directly the value of  $\beta$ . As evidenced by Fig. 8 no such linear variations are observed and moreover, the values of  $\beta$  found for  $\text{S}_{1-x}\text{As}_x$  and  $\text{Te}_{1-x}\text{As}_x$  are not conform to the model prediction (respectively 1.7 and 0.9). This non-universal character is also included in formula 2.3. Indeed, for a binary chalcogenide system  $\text{A}_x\text{B}_{1-x}$  for which B is the added element of coordinence  $Z_b$ , the condition  $0 < \beta < 1$  implies for formula (2.3) that:

$$\frac{1}{Z_b - 2} < \ln \frac{Z_b}{2} \quad (2.4)$$

It follows that the stochastic approach requires that the coordination number of the added atom  $Z_b$  must be greater than 3.6 (Fig. 9). Thus, it occurs that an universal relationship linking the glass transition temperature to a the value of the coordination number requires to find some more considerations about the nature of the added atom. Not so far of the stochastic model, it was shown for  $\approx 200$  different covalent chalcogenide alloys that a good correlation between the glass transition temperature and the overall mean bond energy exists according to Tichý et al. (2.5) [28] relationship:

$$T_g = T_{g0} + \frac{\delta(Z-2)E}{k_b \ln(\mu_{Tg}/\mu_0)} \quad (4)$$

where  $\delta$  is a material parameter,  $E$  the bond energy,  $\mu$  the viscosity and  $k_b$  the Boltzmann constant. Nevertheless, one more time, the use of relationship (2.5) requires to know the value of the coordination number of the added atom. To validate this relationship, the 8-N rule was used for elements as Te, In, Bi. As exemplified by the data reported in Table 1, if it is clear that the 8-N rule works well for Ge, As, Se elements, this is not clearly the case for the others. One way not yet investigated is the role of the steric constraints due to the size of the added element. Indeed, the glass transition can also be defined by means of free volume considerations. As shown on Fig. 10, even if the coordination number of Te atoms is supposed to be 2, when incorporated in a Se linear structure, its diameter is so large that its contribution to the disorder does not concern short range but medium range. As a consequence, twofold coordinated Te atoms can produce the same effects as that observed for an element having a smaller size and a greater coordination number.

Table 1. Values of the coordination number of some elements obtained by means of the 8-N rule compared with results obtained by EXAFS or other experimental methods.

Element	8-N rule	EXAFS/others	Ref
Se	2	2	
As	3	3	
Ge	4	4	
Te	2	2, 2.4, 3	29
Bi	3	3, 3.5, 4	30
In	4	3	31

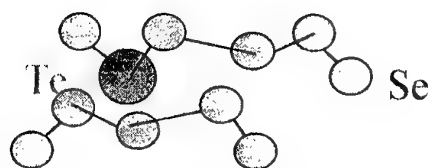


Fig. 10. The existence of Te atoms creates short and medium ranges disorder.

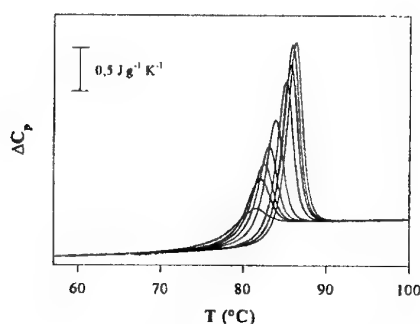


Fig. 11. Typical DSC trace obtained on a glass, kept at a constant temperature  $T < T_g$  aged with different durations. The endothermic peak of relaxation is shifted toward the highest temperatures and the enthalpy increases.

### 3. Relaxation kinetics & structure

As previously mentioned, a glass relaxes when it is kept at a temperature below  $T_g$ . On a DSC curve, this phenomenon is observed by an increase of the value of  $T_g$  with ageing time,

associated with an excess of enthalpy at  $T_g$  (Fig. 11). The variations with time of the configurational enthalpy can be written as:

$$\frac{d(\Delta H)}{dt} = \frac{\Delta H}{\tau} \quad (3.1)$$

where the relaxation time  $\tau$  must take into account the cooperative effects [32]. Different expressions for  $\tau$  have been proposed but all can be resumed by  $\ln(\tau) = F(T) + G(S)$ , where  $F(T)$  and  $G(S)$  are the contribution of the temperature and of the structure respectively. Assuming that  $\Delta H \approx \Delta C_p \Delta T$ , it was already shown that the variations of  $T_g$  with time can be written as [20]

$$\frac{dT_g}{dt} = - \frac{\Delta T_g \exp[(b - c\Delta C_p)\Delta T_g]}{a \exp\left(\frac{\Delta E_a}{RT}\right)} \quad (3.2)$$

where  $a$ ,  $\Delta E_a$ ,  $b$ ,  $c$ ,  $\Delta C_p$  (difference between  $C_p$  in the liquid and vitreous states) depends on the material. From a systematic study of the variations of  $T_g$  with the ageing time, the annealing temperature and using also the results obtained from the variations of  $T_g$  with the heating rate, all these quantities can be determined. In the following, only the results concerning  $\Delta E_a$  obtained on chalcogenide systems for which the 8-N rule is respected will be presented and discussed. Fig. 12 shows the variations of the apparent activation energy as a function of the average coordination number for GeSe and AsSe glassy systems. As we may note, in addition to Phillips and Tanaka thresholds, it appears for others values of  $Z$ , respectively  $Z \approx 2.1$  and  $Z \approx 2.24$ . These values of  $Z$  were also presented in the first paper of Phillips [25] from data concerning the viscosity [33] (Fig. 13), were also observed for crystallisation ability [34] (Fig. 14) and finally for the variations of the optical gap of AsSe [35] (Fig. 15). Assuming that the relaxation in pure Se takes places by molecular movements along the Se polymeric chain, it follows that the elementary cell for an elementary movement engages at least three adjacent Se atoms (Fig. 16). The development of the cross-linked structure by addition of Ge or As atoms decreases the number of Se cells. These Se cells vanish for  $Z \approx 2.24$  [20]. Thus Ge cells as As cells (Fig. 16) seem to not participate to the relaxation process and act only as blocking molecules. On the other hand, for  $Z \approx 2.1$  the number of blocking cells is large enough to erase the ability of the Se cells to move at large scale and thus to authorise for instance a crystallisation process [20]. As the steric volumes occupied by Ge, As, or Se atoms are not fundamentally different, basically the same phenomena occur, whatever the considered, property, when comparisons are done as a function of  $Z$ . Does it means that massive molecules as Ge cells or As cells cannot move? The answer is no. Indeed, as shown by the DSC traces reported on Fig. 17 and obtained on  $\text{Ge}_2\text{Se}_{98}$  aged more than 10 years at room temperature, two endothermic peaks of relaxation (each of large magnitude) are observed. This sample after rejuvenation exhibits the characteristic of non aged material. In fact the characteristic time constant for the relaxation process of Se cells is shorter (some months) than the characteristic time constant of the Ge cells (several years). To verify this observation, the relaxation kinetics of more complex systems ( $\text{Ge}_x\text{Te}_{1-x}$ ,  $0.15 < x < 0.20$ ) have been investigated. This system exhibits many advantages. It was extensively studied and if it is not established that the 8-N rule is respected by the Te atoms, it was clearly demonstrated that Ge atoms are fourfold coordinated to only Te atoms [36,37].

The relaxation kinetic were studied according to formula (2.4) and with the Tool Narayanaswamy Moynihan [32, 38, 39] relationship for the relaxation time

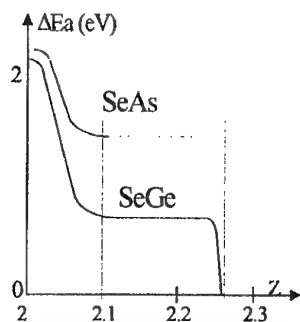


Fig. 12. Variations with  $Z$  of the apparent activation energy of the glass transition.

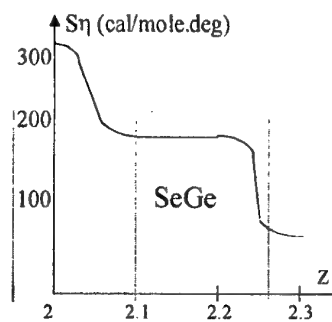


Fig. 13. Activation energy for the viscosity entropy.

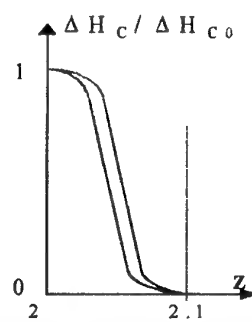


Fig. 14. Normalised crystallisation enthalpy for Ge-Se and As-Se glasses.

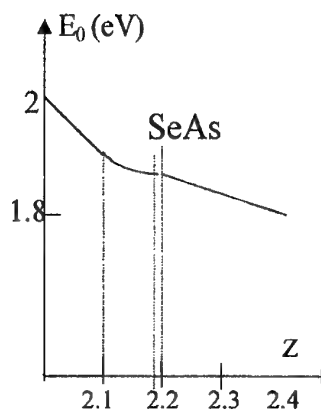


Fig. 15. Optical gap of As-Se.

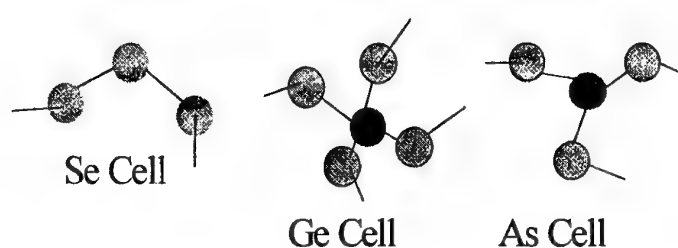


Fig. 16. Molecular structures in GeSe and AsSe glassy systems.

$$\tau = \tau_0 \exp\left(\frac{x\Delta h^*}{RT}\right) \exp\left(\frac{(1-x)\Delta h^*}{RT_f}\right) \quad (3.3)$$

where  $x$  ( $0 \leq x \leq 1$ ) is the nonlinearity parameter or Narayanaswamy parameter,  $\Delta h^*$  the apparent activation energy,  $T_f$  is the fictive temperature defined as the temperature at which the structure of the glass would be in equilibrium if instantaneously brought to it and the other symbols carry their usual meanings.

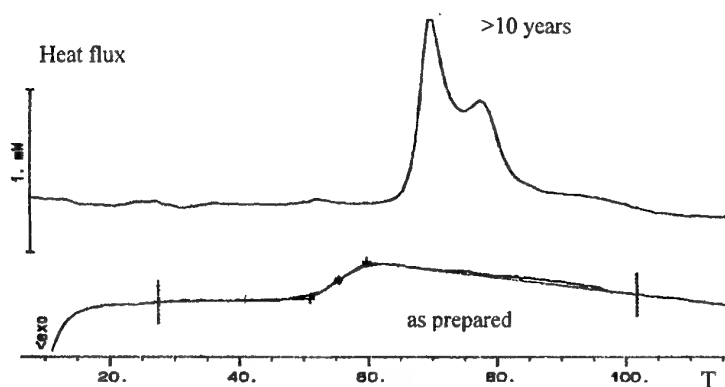


Fig. 17. DSC traces obtained on  $\text{Ge}_2\text{Se}_{98}$  aged more than 10 years at room temperature and for the same sample after rejuvenation.

The values of  $\Delta h^*$  and  $x$  have been determined by means of respectively the Moynihan [39] and the peak shift [40] methods. The values obtained for these parameters are reported in Table 2. In this table, in order to perform a comparison the results obtained for some glassy alloys of the Ge-Se system [41] are also reported.

Table 2. Values of the TNM parameters obtained for GeSe [41] and GeTe [42] glassy alloys.

Material	Se	Ge <sub>8</sub> Se <sub>92</sub>	Ge <sub>12</sub> Se <sub>88</sub>	Ge <sub>15</sub> Te <sub>85</sub>
X	0.57	0.60	0.50	0.67
$\Delta h^*$ (kJ/mole)	675	384	428	994
$T_g$ (°C)	36	74	105	128

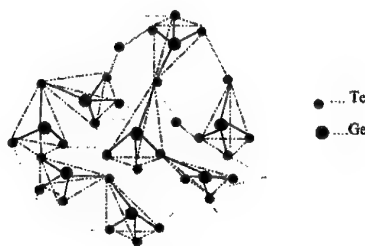


Fig. 18. Molecular species engaged in the relaxation process of Ge<sub>15</sub>Te<sub>85</sub>.

In regard with the Ge content in Ge<sub>15</sub>Te<sub>85</sub> and to the structure engaged in this class, the existence of Te chains is impossible. The high  $x$  value obtained for this system indicates that the structure effects (given by the second exponential in formula 7) is low when compared by the effect of the temperature (given by the first exponential in formula 7). This means that the cooperativity effects during the relaxation process are low or what is equivalent, the molecular species engaged in the relaxation process can practically move independently one from the other. This is totally at the opposite of what is observed for GeSe glasses. Thus, in spite that the surrounding of Te atoms in Ge<sub>15</sub>Te<sub>85</sub> is not well known, it is established that the structure of this glass results from the connection of tetrahedral GeTe<sub>4</sub> units sharing Te atoms at corners or edges (Fig. 18) and that the relaxation kinetic of this Ge<sub>15</sub>Te<sub>85</sub> exhibits all the characteristics of a linear polymeric structure but with very short time constant ( $\approx 100$  h at  $T_g - 10^\circ\text{C}$ ) [43]. This result confirms that massive molecular species more or less strongly connected together can relax.

#### 4. Conclusion

In this work we have shown that relationships proposed in the literature in order to link the value of the glass transition temperature and the structure engaged in chalcogenide based alloys must be used with some precautions until a good knowledge of the real surrounding of the different atoms engaged in the material composition is well demonstrated. On the other hand, from the study of the physical ageing, general property for a glassy structure, we show that for specific values of the average coordination number ( $Z \approx 2.1$  and  $Z \approx 2.24$ ) calculated for system obeying to the 8-N rule (As-Se, Ge-Se glassy systems), many properties as e.g. apparent activation energy for the relaxation, crystallisation ability, optical gap, viscosity, are modified. Finally, the physical ageing kinetic measurements are found dependent on the structures engaged in the glassy systems. In particular, we have shown that massive molecular species as GeSe<sub>4</sub> or GeTe<sub>4</sub> can also move during ageing but with very different time constants (several years for GeSe<sub>4</sub>, several weeks for GeTe<sub>4</sub>).

#### References

- [1] Hyun-Yong Lee, Hong Bay Chung, Jpn. J. Appl. Phys. **36**, 2409 (1997).
- [2] A. P. J. M. Jongenelis, J. H. Coombs, W. van Es-Spiekman, B. A. J. Jacobs, J. Appl. Phys. **79**, 8349 (1996).
- [3] Yu. G. Vlasov, E. A. Bychkov, A. V. Legin, Talanta, **41**, 1059 (1994).
- [4] J. S. Sanghera, V. Q. Nguyen, P. C. Pureza, R. E. Miklos, F. H. Kung, I. D. Aggarwal, J.

- Lightwave Techn. **14**, 743 (1996).
- [5] K. A. Sharaf Appl. Phys. **A53**, 218 (1991).
- [6] S. Ducharme, J. Hautala, P. C. Taylor, Phys. Rev. **41**, 12250 (1990).
- [7] Ke. Tanaka, A. Odajima, Solid State Commun. **12**, 961 (1980).
- [8] L. C. E. Struik, Physical ageing in amorphous polymers and other materials, Elsevier, Amsterdam, (1978).
- [9] I. M. Hodge, A. J. Berens, Macromolecules **15**, 762 (1982).
- [10] J. L. Gomez Ribelles, M. Monleon Pradas, A. Vidaurre Garayo, F. Romero Colomer, J. Mas Estelles and J. M. Meseguer Duenas, Macromolecules **28**, 5878 (1995).
- [11] A. J. Kovacs, J. J. Aklonis, J. M. Hutchinson, A. R. Ramos, J. Polym. Sci. B, Polym. Phys. Ed. **17**, 1097 (1979).
- [12] J. Grenet, J. P. Larmagnac, P. Michon, C. Vautier, Thin Solid Films **76**, 53 (1981).
- [13] E. A. Dimarzio, J. H. Gibbs, J. Polym. Sci. **60**, 121 (1959).
- [14] J. H. Gibbs, E. A. Dimarzio, J. Chem. Phys. **28**, 373 (1958).
- [15] A. Saiter, M. Hess, J. M. Saiter, European Polym. J. in press (2001).
- [16] C. A. Angell, 'Relaxation in complex systems', Ed. Ngai K. L. and Wright G. B., Naval Research Laboratory, Washington D. C., 1984, p.3.
- [17] J. M. Saiter, D. Langevin, P. Lebaudy, J. Grenet, J. Non-Cryst. Solids **172/174**, 640 (1994).
- [18] J. Grenet, J. P. Larmagnac, P. Michon, J. Therm. Anal. **25**, 539 (1982).
- [19] J. Grenet, J. M. Saiter, J. Bayard, C. Vautier, J. Thermal Anal. **38**, 557 (1992).
- [20] J. M. Saiter, A. Assou, J. Grenet, C. Vautier, Phil. Mag. B **64**, 33 (1991).
- [21] A. Hamou, J. M. Saiter, J. Bayard, J. Grenet, C. Vautier, Mat. Letters **12**, 442 (1992).
- [22] Z. U. Borisova, Glassy Semiconductors, Plenum Press, New York, 1981.
- [23] A. N. Sreeram, D. R. Swiler, A. K. Varshneya, J. Non-Cryst. Solids **127**, 287 (1991).
- [24] J. M. Saiter, J. Ledru, G. Saffarini, S. Benazeth, Mater. Lett. **28**, 451 (1994).
- [25] J. C. Phillips, J. Non-Cryst. Solids, **34**, 153 (1979).
- [26] Ke. Tanaka, Solid State Comm. **54**, 867 (1985).
- [27] M. Micoulaut, G. G. Naumis, Europhys. Letters **47**, 568 (1999).
- [28] L. Tichy, H. Ticha, Mater. Lett. **21**, 313 (1994).
- [29] A. Menelle, R. Bellissent, A. M. Flank, Europhys. Lett. **4**, 705 (1987).
- [30] C. Vautier, Sol. State Phenomena **71**, 249 (2000).
- [31] J. Ledru, J. M. Saiter, G. Saffarini, S. Benazeth, J. Non-Cryst. Solids **232-234**, 634 (1998).
- [32] A. Q. Tool, J. Am. Ceram. Soc. **29**, 240 (1946).
- [33] S. U. Nemolov, Soviet J. Phys. Chem. **37**, 1026 (1964).
- [34] J. M. Saiter, J. Ledru, A. Hamou, G. Saffarini, Physica B, **245**, 256 (1998).
- [35] V. I. Mikla, J. Phys. Condens. Matter **9**, 9209 (1997).
- [36] J. M. Saiter, Qing Ma, S. Benazeth, M. Belhadji, C. Vautier, Mater. Lett. **19**, 287 (1994).
- [37] J. M. Saiter, S. Benazeth, Qing Ma, M. Belhadji, C. Vautier, J. Non-Crystalline Solids **192-193**, 369 (1995).
- [38] O. S. Narayanaswamy, J. Am. Ceram. Soc. **54**, 491 (1971).
- [39] C. T. Moynihan, A. J. Easteal M. A. deBolt, J. Tucker, J. Am. Ceram. Soc. **59**, 12 (1976).
- [40] A. J. Kovacs, J. J. Aklonis, J. M. Hutchinson, A. R. Ramos, J. Polym. Sci. B Polym. Phys. **17**, 1097 (1979).
- [41] P. Cortes, S. Montserrat, J. Ledru, J. M. Saiter, J. Non-Cryst. Solids **235-237**, 522 (1998).
- [42] J. M. Saiter, K. Chebli, A. Hamou, Physica B **293**, 98, (2000).
- [43] K. Chebli, J. M. Saiter, J. Grenet, A. Hamou, G. Saffarini, Physica B (2001) in press.

## EFFECT OF OXYGEN ON THE PHOTOINDUCED CHANGES IN THE ELECTRONIC STRUCTURE OF $\text{As}_{50}\text{Se}_{50}$ GLASS FILMS

S. Krishnaswami, H. Jain, A. C. Miller<sup>a</sup>

Department of Materials Science and Engineering, Lehigh University, Bethlehem, PA 18015, USA

<sup>a</sup>Zettlemoyer Center for Surface Studies, Lehigh University, Bethlehem, PA 18015, USA

The effect of ambient on photoinduced changes in the electronic structure of  $\text{As}_{50}\text{Se}_{50}$  chalcogenide glass was investigated using high resolution X-ray photoelectron spectroscopy (XPS).  $\text{As}_{50}\text{Se}_{50}$  films were deposited on Si substrate in the vacuum of the spectrometer, and then irradiated under bandgap laser light *in situ* as well as *ex situ* in air. Very little difference was observed in the XPS spectra of the as deposited film before and after *in situ* irradiation. However, *ex situ* irradiation of the film in air showed changes in the chemical environment of both elements, and an enrichment of the surface with oxygen and Se, but depletion of As. The depth profile of these changes, as obtained by angle resolved XPS, describes the light-induced reaction with oxygen. The new results point to a crucial role of oxygen in photoinduced structural changes.

(Received July 12, 2001; accepted September 3, 2001)

**Keywords:** AsSe amorphous film, Photoinduced changes, Oxygen effect.

### 1. Introduction

Chalcogenide glasses are known for being sensitive to near-bandgap light, which produces several types of photoinduced changes in structure and properties [1,2]. These changes can be permanent, metastable or temporary with regard to light exposure. Numerous interesting applications have been conceived and designed based on the light sensitive properties of chalcogenide glasses, especially in amorphous thin film form [3-6].

In general, the photoinduced effects are believed to arise from the excitation of electrons across the bandgap (e.g. photodarkening [7,8]) and consequent atom displacements (e.g. in photocrystallization [9], photoexpansion [10], and opto-mechanical effect [6]). Recent studies on photoinduced effects such as photoexpansion of chalcogenide films suggest a uniform expansion of the material from photorelaxation, but other investigations indicate photoinduced oxidation as an underlying change [11-13]. Therefore, it is important to realize the role of the ambient in these observed photoinduced phenomena. In this paper, we report initial results of the angle-resolved X-ray photoelectron spectroscopy (ARXPS) experiments for characterizing the effect of ambient atmosphere on the electronic structure of  $\text{As}_{50}\text{Se}_{50}$  glass film when exposed to *in situ* and *ex situ* bandgap laser light irradiation.

### 2. Experimental

$\text{As}_{50}\text{Se}_{50}$  glass films were deposited on (100) silicon crystal wafer as substrate, by heating bulk  $\text{As}_{50}\text{Se}_{50}$  in a quartz crucible placed within the sample preparation chamber connected to the analysis chamber of the spectrometer. The material was heated under the vacuum of  $10^{-7}$  Torr or better using a tungsten filament with the evaporation time of about 10 minutes to yield approximately 700-950 Å thick films. The specimens were stored in vacuum, and in the dark to prevent any inadvertent light-induced changes. For controlled irradiation, the sample was exposed at ambient temperature to laser light ( $\lambda = 660$  nm) of  $150 \text{ mW/cm}^2$  intensity from a laser diode source. For the *in situ* irradiation of the film inside the spectrometer in a vacuum of better than  $\sim 10^{-8}$  Torr, the laser-diode was placed next to one of the quartz windows, through which light could pass and strike the sample surface. The beam



position was varied with the help of an optical translation stage such that the laser-illuminated area coincided with the region analyzed by the spectrometer. The duration of laser irradiation, both in vacuum and in air, was typically up to ~12 h. The *ex situ* irradiation was conducted in the air at room temperature.

The XPS spectra were obtained using a Scienta spectrometer (ESCA-300) with monochromatic Al  $K_{\alpha}$  X-rays (1486.6 eV). The instrument was operated in a mode that yielded a Fermi-level width of 0.4 eV for Ag metal. At this level of resolution, the instrumental contribution to the line width was small (< 10%). The ARXPS data consisted of survey scans over the entire binding energy range and selected scans over the valence band or core-level photoelectron peaks of interest at varying angles of X-ray incidence. An energy increment of 1 eV was used to record survey scans and 0.05 eV for valence band and core-level spectra. The spectra were recorded for 15°, 30°, 45° and 90° of X-ray incidence, with the analysis depth of photoelectrons estimated to be  $30\text{\AA} \cdot \sin(\theta)$ , where  $\theta$  is the angle between the surface and the detector, and 30 Å is the estimated attenuation length for the electrons from As and Se. Data analysis was conducted with the ESCA-300 software package using a Voigt function and Shirley background subtraction.

### 3. Results

The valence band (VB) spectra of  $\text{As}_{50}\text{Se}_{50}$  film for 90° X-ray incidence are compared in Fig. 1 for four cases of film conditions: {1} as prepared film which is unirradiated and unexposed to air, {2} film which is laser irradiated in vacuum for ~12 h and unexposed to air, {3} film which is exposed to air but unirradiated, and {4} film that is laser irradiated in air for ~12 h. In conditions {3} and {4}, the exposure of the film to air was for the same duration, so that any differences observed between them is due to the photoinduced effects in air. In general, the conductivity of silicon substrate was high enough that the samples exhibited little charging from photoelectron emission. Nonetheless, for accurate comparison of spectra from different samples, the four spectra in Fig. 1 are shifted in energy such that the steep rise of top edge of the valence band coincides with the zero of the binding energy (BE).

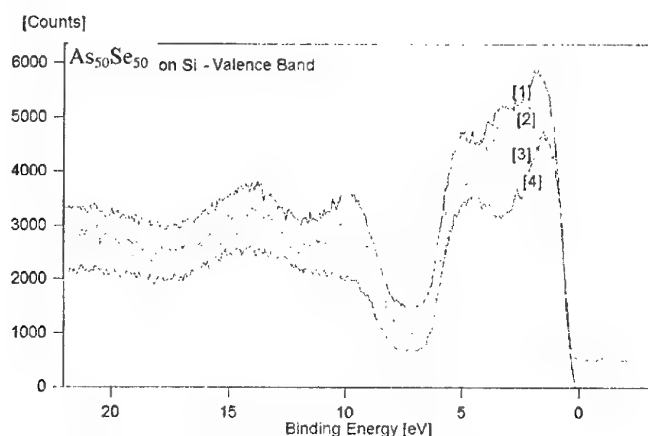
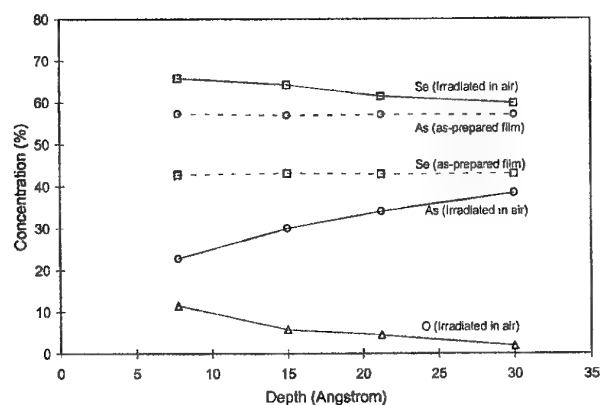


Fig. 1. Comparison of valence band of  $\text{As}_{50}\text{Se}_{50}$  film at 90° incidence for: {1} As deposited, unirradiated and unexposed to air; {2} Laser irradiated in vacuum for ~12 h and unexposed to air; {3} Unirradiated but exposed to air, and {4} Irradiated in air for ~12 h and exposed to air.

The scaled spectra {1}, {3} and {4} show differences throughout the VB down to ~15 eV, but the largest differences are found in the upper band that extends down to a BE of ~6 eV, which is the band that arises from the 4p bonding states of As and Se and the 4p lone pair of Se. The VB spectra of {1} and {2} do not show significant difference. In other words, there are no obvious structural changes occurring in the glass film due to *in situ* irradiation alone. However, after the film is exposed to air, we find that the peak around ~3 eV gradually diminishes in intensity, and finally disappears for the film irradiated in air. Secondly, there is a decrease also in the intensity of the peak at ~9 eV.

Table 1. Composition of elements for four different conditions of  $\text{As}_{50}\text{Se}_{50}$  film on Si at various angles of x-ray incidence.

$\text{As}_{50}\text{Se}_{50}$ film condition	Angle (deg)	Depth (Å)	As (at.%)	Se (at.%)	O (at.%)	As/Se
{1} – as prepared film : unirradiated and unexposed	15	7.8	57.3	42.8	--	1.34
	30	15.0	56.9	43.1	--	1.32
	45	21.2	57.1	42.9	--	1.32
	90	30	57.0	43.0	--	1.33
{2} – In-situ: irradiated in vacuum and unexposed to air	15	7.8	57.5	42.5	--	1.35
	30	15.0	57.4	42.6	--	1.34
	45	21.2	57.1	42.9	--	1.33
	90	30	56.9	43.1	--	1.32
{3} – unirradiated and exposed to air	15	7.8	34.9	59.2	5.9	0.59
	30	15.0	39.3	55.7	5.0	0.71
	45	21.2	44.6	53.2	2.2	0.84
	90	30	48.4	51.7	–	0.94
{4} – Ex-situ: irradiated in air and exposed to air	15	7.8	22.8	65.7	11.5	0.35
	30	15.0	30.1	64.1	5.8	0.47
	45	21.2	34.1	61.5	4.5	0.55
	90	30	38.4	59.8	1.8	0.64

Fig. 2. Concentration of As, Se and O as a function of depth for as-prepared  $\text{As}_{50}\text{Se}_{50}$  film (broken line) and, for film laser irradiated in air for ~12 h (solid line). Lines are drawn to guide the eye.

The core-level X-ray photoelectron spectra show oxygen in the film under conditions {3} and {4} as listed in Table 1. Initially, the as prepared film (condition {1}) shows no oxygen in the surface region. The As/Se ratio ~1.33, and is independent of angle. It is higher than the value anticipated from the bulk value but apparently consistent with our preparation method showing a preferential deposition of arsenic rich units. Even after the film is irradiated with laser in vacuum for ~12 h, within the experimental scatter we see no change in the As, Se and oxygen concentration in the surface region (condition {2} vs. {1}). The As/Se ratio remains constant at ~1.33. Similarly, no significant changes were detected in the As and Se 3d core levels and valence band (Fig. 1) spectra for these two film conditions. Therefore, laser irradiation of the oxygen-free film under vacuum has caused no detectable changes in the electronic structure of the chalcogenide glass film. However, as the film is exposed to atmosphere, we detect oxygen in the film (film condition {3}). The concentration of

oxygen decreases from  $\sim 5.87$  at.% to  $\sim 0.0$  at.% as we investigate deeper into the film surface. This can be seen from the composition at shallow angles, which shows more oxygen content compared to the results at  $45^\circ$  or  $90^\circ$ . The As/Se ratio has significantly reduced from the previous value of  $\sim 1.33$  (see Table 1). However, it increases from 0.59 to 0.94 as we explore deeper into the surface, showing a strong correlation with the amount of oxygen that has diffused from the surface into the film. Another striking feature is that oxygen content on film surface increases further due to the laser irradiation in air (film condition {4}), with a corresponding decrease in As/Se, which is consistent with our previous observations [14]. In this film, we observe about  $\sim 2$  at.% oxygen at  $90^\circ$ , which was below the detectable concentration in condition {3} for the same angle. Since the films in {3} and {4} were exposed to air for the same duration, the above observation represents a light enhanced diffusion of oxygen into the film. The change in the concentration of As, Se and O is seen in the corresponding changes in the core levels as well as in the valence band spectra. The concentration of As, Se and O at various depths of the  $\text{As}_{50}\text{Se}_{50}$  film is shown in Fig. 2 for the as-prepared sample held in vacuum, and the film irradiated in air with laser. We have observed an increase in oxygen concentration with corresponding changes in As and/or Se concentration, both when the sample was exposed to air or *ex situ* irradiated in air (see Table 1 and Fig. 2). Therefore, oxygen must be bonded to As or Se, and not be simply as part of some organic or non-bonded impurity layer as previously thought [14].

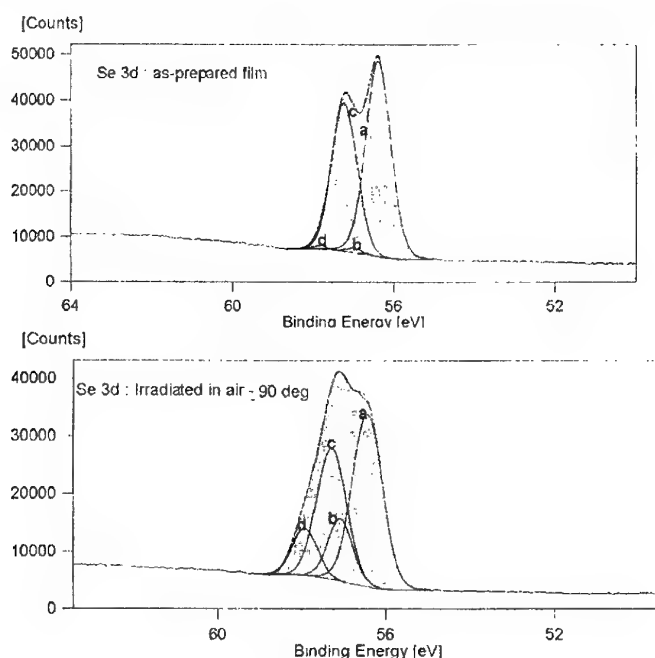


Fig. 3. Effect of laser irradiation on Se 3d core level of  $\text{As}_{50}\text{Se}_{50}$  film on Si substrate at  $90^\circ$  incidence. Peaks 'a' and 'c' represent the  $3d_{5/2}$  and  $3d_{3/2}$  doublets of Se bonded to As, while peaks 'b' and 'd' represent  $3d_{5/2}$  and  $3d_{3/2}$  doublets of Se bonded to Se.

Fig. 3 shows core-level 3d doublets for Se in the as prepared and *ex situ* laser irradiated ( $\sim 12$  hrs)  $\text{As}_{50}\text{Se}_{50}$  thin film on silicon for  $90^\circ$  incidence. The change in Se-3d core level due to irradiation to light is quite dramatic. Initially, in the as prepared film, the 3d peak is well resolved into the  $3d_{5/2}$  and  $3d_{3/2}$  doublet. The curve fitting suggests a small contribution from an energy shifted second doublet. The two pairs of the  $3d_{5/2} - 3d_{3/2}$  doublets indicate two different bonding environments for Se, viz., homopolar (Se-Se) and heteropolar (Se-As) bonds. This identification of two types of Se bonds is more subtle than between bridging and non-bridging Se reported by Sanghera et al. [15]. The peaks 'a' and 'c' represent the  $3d_{5/2}$  and  $3d_{3/2}$  doublet for heteropolar Se-As, while 'b' and 'd' represent the  $3d_{5/2}$  and  $3d_{3/2}$  doublet for homopolar Se-Se respectively. The lower binding energies for the Se-As components is because of the net positive charge on As. The curve fitting parameters for the two doublet pairs are listed in Table 2. For a given doublet, the same intensity ratio and BE separation were used as experimentally obtained on pure Se. Further, the full width at half maximum (FWHM), asymmetry, and mix in the Voigt function were assumed to be the same for the two components. With

these constraints the uncertainty in peak position and area of each component is expected to be ~0.05 eV and ~2%, respectively, although the relative error is smaller.

Table 2. Summary of fitting results for Se 3d core level peak for As<sub>50</sub>Se<sub>50</sub> film on Si.

Sample	Peak name	Position (eV)	FWHM (eV)	Asymmetry	% Se-Se
As-prepared	a (3d <sub>5/2</sub> in Se-As)	56.38	0.74	0.00	1.4
	c (3d <sub>3/2</sub> in Se-As)	57.23	0.74	0.00	
	b (3d <sub>5/2</sub> in Se-Se)	56.98	0.42	0.00	
	d (3d <sub>3/2</sub> in Se-Se)	57.83	0.42	0.00	
Irradiated in air – 90°	a (3d <sub>5/2</sub> in Se-As)	56.44	0.84	0.00	23.2
	c (3d <sub>3/2</sub> in Se-As)	57.29	0.84	0.00	
	b (3d <sub>5/2</sub> in Se-Se)	57.08	0.71	0.00	
	d (3d <sub>3/2</sub> in Se-Se)	57.93	0.71	0.00	
Irradiated in air – 45°	a (3d <sub>5/2</sub> in Se-As)	56.48	0.95	0.08	18.6
	c (3d <sub>3/2</sub> in Se-As)	57.33	0.95	0.08	
	b (3d <sub>5/2</sub> in Se-Se)	57.13	0.67	0.04	
	d (3d <sub>3/2</sub> in Se-Se)	57.98	0.67	0.04	
Irradiated in air – 30°	a (3d <sub>5/2</sub> in Se-As)	56.67	1.08	0.03	11.0
	c (3d <sub>3/2</sub> in Se-As)	57.52	1.08	0.03	
	b (3d <sub>5/2</sub> in Se-Se)	57.25	0.64	0.00	
	d (3d <sub>3/2</sub> in Se-Se)	58.10	0.64	0.00	
Irradiated in air – 15°	a (3d <sub>5/2</sub> in Se-As)	56.73	1.15	0.00	7.1
	c (3d <sub>3/2</sub> in Se-As)	57.58	1.15	0.00	
	b (3d <sub>5/2</sub> in Se-Se)	57.09	0.60	0.04	
	d (3d <sub>3/2</sub> in Se-Se)	57.94	0.60	0.04	

From Table 2, we note that the FWHM for the Se-As and Se-Se doublet pairs in the as-prepared film is 0.74 and 0.42 eV respectively. The % of Se in Se-Se bonds relative to total Se, as calculated from area under the respective doublets is listed in the last column of Table 2. Initially, for the as-prepared film, the % of Se-Se bonds at a depth of 30 Å is very small, about ~1.4%. After irradiation to light in air, the doublet structure transforms such that the 3d components of Se-As ('a' and 'c') have broadened (FWHM increases from 0.74 eV to 0.84 eV) with a simultaneous reduction in intensity, while the components of Se-Se ('b' and 'd') have increased in intensity (Fig. 3). The % of Se-Se bonds is ~23.2% at a depth of ~30 Å (90° incidence). In other words, the number of Se-Se bonds has increased due to irradiation. Evidently the light causes a broadening of Se-As components and an increase in the fraction of Se-Se bonds as well, as described quantitatively by the values in Table 2. The symmetric broadening of a Se peak indicates creation of environments with higher and lower charge density (such as in a valence alternation pair) than in the as prepared state. Further, the fraction of Se-Se bonds decreases as we move to the surface of the film, such that at a depth of 7.7 Å (15° incidence) it reduces to a value of 7.1%. The effect of light on As-3d core level is opposite to that of Se, as also noted previously [14]. The 3d components become narrower due to irradiation, suggesting homogenization of the As environment.

A comparison of As and Se 3d peak shapes at different angles of X-ray incidence for the film irradiated in air with laser is shown in Fig. 4. One can see that there are variations in the peak shapes as well as changes in intensity in both As and Se 3d core levels, suggesting different bonding environments. In As spectra, the main peak at ~45.5 eV is present at all angles of incidence. However, the broad band seen as a shoulder around ~46.2 eV in the 15° spectrum transforms into a distinct peak as we observe deeper into the film. Another striking feature is the small broad hump around ~49 eV present only in the

15° spectrum, as indicated by the arrow. The separation in BE of this hump from the As-3d<sub>5/2</sub> peak is ~3.5 eV. Since the As-3d<sub>5/2</sub> level for As<sub>2</sub>O<sub>3</sub> and As<sub>2</sub>O<sub>5</sub> is expected to be at ~3.6 and 4.4 eV higher BE than that for As element, this hump appears to be due to oxygen associated with As in the form of As<sub>2</sub>O<sub>3</sub>. As we investigate deeper into the film surface, the broad band smears out and is no longer present at higher angles. This suggests that As<sub>2</sub>O<sub>3</sub> is present only at the top few monolayers of the film surface. The Se-3d level at 15° shows an asymmetric peak at ~58.2 eV. As we increase the angle of incidence, the peak increases in intensity. At 45°, we begin to observe a small shoulder to the right of the main peak at ~57.6 eV. Finally, at normal incidence, the original peak can be resolved into two doublet components, as shown in Fig. 3. Unlike As, we do not observe any effects of oxide formation in Se core level spectra. Thus the oxygen present on the film surface is associated with As only.

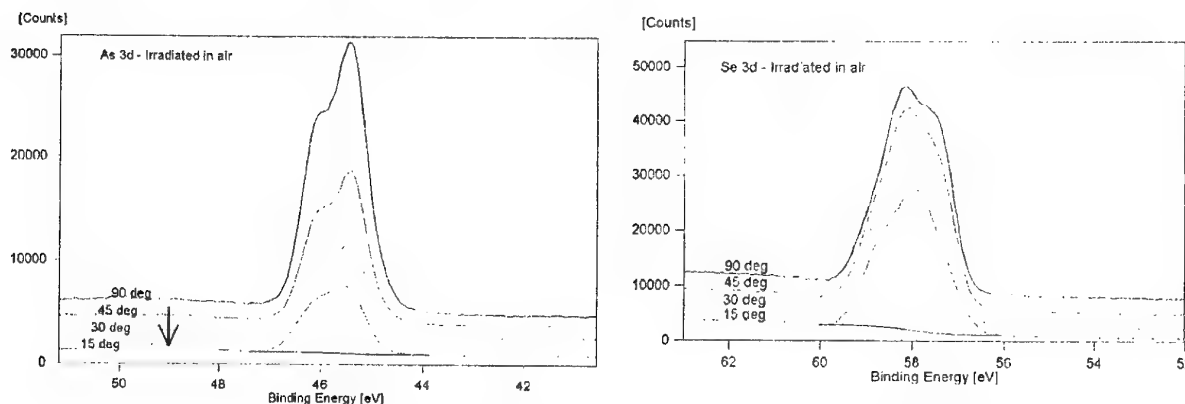


Fig. 4. Comparison of As and Se 3d peak shapes at different angles of x-ray incidence for As<sub>50</sub>Se<sub>50</sub> film on Si, laser irradiated in air for ~12 h.

#### 4. Discussion

According to theoretical calculations [16,17], the VB of As-Se glasses consists of two major bands (see Fig. 1). The upper band at ~0–6.0 eV arises from the 4p states of As and Se. Within this band the leading peak at ~1 eV represents the 4p electron lone pair on Se atoms, and rest of the band arises from the 4p bonding electrons. The VBs of elemental As and Se consist of broad peaks (not shown), from As-As and Se-Se bonding of the 4p electrons at ~2 and ~4 eV, respectively. Of course, in As-Se alloys the As-Se bonding states would distort the VB spectrum and hence the bands at ~2 eV and ~4 eV should represent some mixing of As and Se states. The lower band of AsSe at ~6.5–16.5 eV is separated from the upper band by a minimum. It represents 4s states of As and Se, which can be distinguished by overlapping broad humps centered at ~9.3–9.8 and 14.0–14.5 eV, respectively.

Irradiation of the film under vacuum does not cause any obvious changes in the VB (see Fig. 1) and/or in As and Se concentration (see Table 1). There seems to be very weak, if at all, a compositional or structural change on the film surface when irradiated under vacuum. On the other hand, a decrease in density of states (DOS) at ~2.5–3.5 eV is consistently observed, as shown in Fig. 1 (film conditions {1}, {3} and {4}) when the film is exposed to and/or irradiated in air with laser. The magnitude of the reduction in intensity increases with the duration of irradiation. Since the DOS in this energy range arises from the bonding of As atoms, we conclude that the observed irreversible changes in structure result from the loss of As. The concurrent decrease in the intensity of ~9 eV peak, which arises from As-4s electrons, confirms this conclusion that has been also obtained from Raman spectroscopy [18]. Our recent observations of the *in situ* changes in local structure around As and Se by extended X-ray absorption fine structure (EXAFS) further confirm that arsenic atoms play lead role in producing the irreversible changes in the structure [19]. However, the absence of structural and compositional changes under *in situ* irradiation in vacuum raises questions about the importance of ambient atmosphere, mainly oxygen, on photoinduced effects in chalcogenide glasses. A similar concern was raised from the observation of similar kinetics of the growth of arsenic oxide and irreversible photoinduced effects on such films [20]. On the other hand, there are several observations of temporary photoinduced effects, such as the opto-mechanical effect [6], which are not likely to be due to a reversible diffusion of oxygen. Therefore, we believe that although oxygen itself is not at the center of structural changes in arsenic selenide glasses, it strongly enhances their magnitude in a catalytic fashion.

The effect of laser irradiation on the structure of amorphous  $\text{As}_{50}\text{Se}_{50}$  film, which is observed in XPS spectra, can be considered as a reversible or a metastable change depending on whether or not it disappears with illumination at room temperature. Any difference in the spectra for the as-prepared and *ex situ* irradiated specimens would be from metastable or permanent structural changes. These changes may be summarized from the core-level data as:

(a) The As-3d peaks become narrower, which indicates that the irradiation helps reorganize the As atoms such that their chemical environment becomes more homogenous. The FWHM for the film approaches that of crystalline As, suggesting considerable uniformity in its bonding.

(b) The Se-3d peaks become broader and at the same time there is an increase in the fraction of Se-Se bonds in the film. Thus the effect of irradiation on Se is just the opposite, indicating an increased variation of its environment.

(c) A very striking observation is that the ratio of As/Se at the surface decreases significantly as a result of *ex situ* irradiation. Previously, Kolobov et al. [21], Jain et al. [14] and Kitahara and Arai [22] noted similar changes. The observed changes of surface composition could be due to the light-induced preferential segregation of Se from the bulk to the surface, or evaporation of relatively more volatile arsenic oxide [23]. Interestingly, the decrease of the As/Se ratio was recovered on annealing at a higher temperature, and reinstated on irradiation again. The process could be repeated many times with the As/Se ratio cycling, in a reversible manner, between the irradiation and annealing treatments [21,22]. Therefore, it seems unlikely that the volatilization of arsenic oxide is the primary cause of this composition change.

We suggest that the variation of As/Se ratio is simply a consequence of different energy of formation of Se and As 'lattice' defects. The concept of point defects such as vacancies or interstitial in a glassy structure is inherently vague and we know little about them in the present material. Nonetheless, there is evidence that the Se atoms move much more readily than the As atoms in an As-Se glass [24], as one would expect from their 2 and 3 fold coordination, respectively. So it should be energetically easier to create a defect on Se sites (sub-lattice) than on As sites (sub-lattice) by moving the respective atoms from the interior to the surface. The situation is analogous to alkali halides in which it is easier to create an alkali defect (vacancy) than a halogen defect (vacancy). Then following the classical treatment of Kliewer and Koehler [25], there should be segregation of Se on the surface accompanied by a Se deficient (or equivalently an As rich) space charge under the surface. Here, this process is facilitated by exposure to light. Of course, in practice a space charge (and consequent segregation) would be observable only if the sample resistivity is high enough to prevent its decay by the moving electrons and holes. Apparently, the presence of oxygen in the surface layer serves this purpose; without it the surface region has too high conductivity to create a space charge. In principle, the effect of temperature on segregation and/or space charge is determined by the presence of impurities [25]. However, the inhomogeneous distribution of oxygen and exposure to light makes the situation very complex, which we will expound in a future publication. If the predominant effect of temperature is simply to enhance the conductivity, then one can understand how the As/Se ratio is recovered on heating in the experiments in [21, 2222].

Recent AFM studies have shown the formation of pyramid-like structures on the surface of  $\text{As}_{50}\text{Se}_{50}$  film when irradiated in air with laser. These features were not observed when film was irradiated in vacuum [20]. Apparently, the pyramids represent the product of a reaction between the  $\text{As}_{50}\text{Se}_{50}$  film and ambient atmosphere. The change in surface composition and oxygen content of similar arsenic selenide films in our previous study [14] and the work of Berkes et al. [11], Márquez et al. [12] and Dikova et al. [13] support this suggestion. The similarity of morphology in the recent and previous studies strongly suggests that the pyramids are particles of  $\text{As}_2\text{O}_3$ . Furthermore, the present results show that oxygen is associated with As (in the form of  $\text{As}_2\text{O}_3$ ) rather than Se. This is exhibited in the form of a broad hump in As-3d spectra at  $\sim 49$  eV (see Fig. 4), which indicated that oxygen is bonded to As only at the top few monolayers of film surface. Since such a bump is absent in the Se-3d core level, we conclude that there is no detectable oxygen associated with Se.

The changes in the peak shapes of As and Se 3d core levels at different depths from the surface of the film indicate that there exist different chemical environments around these atoms. From Fig. 4, we see more dramatic changes in the shape of Se-3d peaks than those of the As-3d levels. Thus Se exists in relatively distinct, more than one bonding states. On the basis of electronegativity of As and Se, we assign these two chemical environments of Se, as seen in Fig. 3, to Se-As and Se-Se bonds. We do not consider any formation of Se-O bonds since Se in such a bond will have much higher BE than observed.

Finally, we note that with increasing depth from the surface of film, the fraction of Se-Se bonds increases. This is a very surprising observation because presumably such bonds are formed from the initially present Se-As bonds on exposure to laser light. Since the intensity of light should be decreasing with increasing depth, one would have expected the highest fraction of Se-Se bonds in the very top layer.

A simple explanation of this counter-intuitive trend is as follows. The change in the intensity of light across the film should be quite small considering that the maximum thickness detected by the XPS is  $\sim 30$  Å. So the permanent changes in the structure, which most easily occur around Se atoms, are in fact facilitated by the presence of As that has the lowest concentration in the top surface layer (refer Fig. 2). Our study of *in situ* EXAFS in air supports this reasoning [19].

## 5. Conclusion

The present work has demonstrated that the presence of oxygen is catalytic, if not a requirement, for creating photoinduced changes in the electronic structure of arsenic selenide glasses. When illuminated with a laser under vacuum, no significant compositional or structural changes occur on the surface of the  $\text{As}_{50}\text{Se}_{50}$  film. On the other hand, when irradiation takes place in ambient atmosphere, the surface is depleted of As and enriched with Se, which can be understood in terms of the difference in the energy of formation of As and Se point defects. Besides, prolonged illumination in air causes conversion of Se-As bonds to Se-Se bonds. Results confirm that oxygen from the ambient diffuses into the surface, with a concurrent depletion of As at the surface.

## Acknowledgement

The authors thank Professors M. Vlcek and D.A. Drabold for helpful discussions. They also thank the National Science Foundation for supporting this work under a Focused Research Group grant (DMR-0074624).

## References

- [1] K. Shimakawa, A. Kolobov, S. R. Elliott, *Adv. Phys.* **44**, 475 (1995).
- [2] K. Tanaka, *Rev. Solid. St. Sci.* **4**, 641 (1990).
- [3] N. P. Eisenberg, M. Manevich, M. Klebanov, S. Shutina, V. Lyubin, *Proc. SPIE-Int. Soc. Opt. Eng.* **2426**, 235 (1995).
- [4] M. Klebanov, S. Shutina, I. Bar, V. Lyubin, S. Rosenwaks, V. Volterra, *Proc. SPIE-Int. Soc. Opt. Eng.* **2426**, 198 (1995).
- [5] H. M. Kim, J. W. Jeong, C. H. Kwak, S. S. Lee, *Appl. Opt.* **34**(26), 6008 (1995).
- [6] P. Krecmer, A. M. Moulin, R. J. Stephenson, T. Rayment, M. E. Welland, S. R. Elliott, *Science* **277**, 1799 (1997).
- [7] V. L. Averyanov, A. V. Kolobov, B. T. Kolomiets, V. M. Lyubin, *J. of Non-Cryst. Solids* **45**, 343 (1981).
- [8] V. M. Lyubin, V. K. Tikhomirov, *J. Non-Cryst. Solids* **114**, 133 (1989).
- [9] K. Tanaka, K. Ishida, *J. Non-Cryst. Solids* **227-230**, 673 (1998).
- [10] H. Hamanaka, K. Tanaka, A. Matsuda, S. Iizima, *Solid St. Commun.* **19**(6), 499 (1976).
- [11] J. S. Berkes, S. W. Ing, W. J. Hillegas, *J. Appl. Phys.* **42**, 4908 (1971).
- [12] E. Márquez, J. M. González-Leal, R. Prieto-Alcón, R. Jiménez-Garay, M. Vlcek, *J. Phys. D: Appl. Phys.* **32**, 3128 (1999).
- [13] J. Dikova, N. Starbov, K. Starbova, *J. Non-Cryst. Solids* **167**, 50 (1994).
- [14] H. Jain, S. Krishnaswami, A. C. Miller, P. Krecmer, S. R. Elliott, M. Vlcek, *J. Non-Cryst. Solids* **274**, 115 (2000).
- [15] J. S. Sanghera, J. Heo, J. D. Mackenzie, R. M. Almeida, *J. Non-Cryst. Solids* **101**, 18 (1988).
- [16] S. G. Bishop, N. J. Shevchik, *Phys. Rev.* **B12**, 1567 (1975).
- [17] I. Chen, *Phys. Rev.* **B7** 3672 (1973), **B8** 1440 (1973).
- [18] A. Sklenar, M. Vlcek, P. Bezduška, *Proc. 5th ESG Conf.*, Eds. A. Helebrant, M. Maryska, S. Kasa, , Prague, Czech Republic p. C1-99, June 1999.
- [19] G. Chen, H. Jain, M. Vlcek, S. Khalid, Poster presented at the first Amorphous and Nanostructural Chalcogenides Workshop, Bucharest, June 25-28, 2001.
- [20] J. T. Bloking, S. Krishnaswami, H. Jain, M. Vlcek, R. P. Vinci, *J. Opt. Mater.*, in press (2001).
- [21] A. V. Kolobov, Y. P. Kostikov, S. S. Lantratova, V. M. Lyubin, *Sov. Phys. Solid St.* **33**, 444 (1991).
- [22] T. Kitahara, T. Arai, *Jpn. J. Appl. Phys.* **18**, 1635 (1979).
- [23] M. Janai, P. S. Rudman, *Photogr. Sci. Tech.* **20**, 234 (1976).
- [24] G. Chen, H. Jain, S. Khalid, J. Li, D. A. Drabold, S. R. Elliott, submitted to *Solid St. Commun.*
- [25] K. L. Kliewer, J. S. Koehler, *Phys. Rev.* **140**, A1226 (1965).



## DISCOVERY OF THE INTERMEDIATE PHASE IN CHALCOGENIDE GLASSES

P. Boolchand, D. G. Georgiev, B. Goodman<sup>a</sup>

Department of Electrical and Computer Engineering and Computer Science,  
University of Cincinnati, Cincinnati, Ohio 45221-0030

<sup>a</sup>Department of Physics, University of Cincinnati, Cincinnati, Ohio  
45221-0011

We review Raman scattering, Mössbauer spectroscopy and T-modulated Differential Scanning Calorimetry experiments on several families of chalcogenide glasses. Mean-field constraint theory, and numerical simulations of the vibrational density of state (floppy modes) in random and self-organized networks are used to analyze the measurements. Our results provide evidence for *three* distinct phases of network glasses: *floppy*, *intermediate* and *rigid*, as a function of progressive cross-linking or mean coordination number ( $\bar{r}$ ). These phases are characterized by distinct elastic power-laws. The *intermediate* phase is characterized by a vanishing non-reversing heat-flow,  $\Delta H_{nr}(\bar{r}) \rightarrow 0$ , suggesting that glass compositions in this phase are configurationally close to their liquid counterparts, i.e. *self-organized*. The compositional width (and centroid) of the *intermediate phase* is found to be determined by glass structure. In *random* networks, the width of the *intermediate phase* almost *vanishes*, and a *solitary floppy* to *rigid* phase transition is observed, in excellent accord with extended constraint theory. In the chalcogenides, some degree of self-organization invariably occurs and opens an *intermediate phase* between the *floppy* and *rigid* phases, signaling the breakdown of mean-field constraint theory, but in harmony with recent numerical results on self-organized networks.

(Received August 23, 2001; accepted September 11, 2001)

**Keywords:** Intermediate phase, Non-reversing heat flow, Self-organization

### 1. Introduction

The microscopic origin of glass formation has been debated for over 50 years. It is generally believed that glass formation is a kinetic phenomenon [1], although the aspects of liquid structure that lead to a glass rather than a crystal upon cooling are not obvious at present. Even basic issues on liquid dynamics, such as the propensity of a non-Arrhenius T-variation of viscosity ( $\eta$ ), with only a *select few* liquids displaying an exception to that behavior, remains largely a mystery. The challenges to understand glass structures and liquid structures by diffraction methods [2] alone are enormous and have met with limited success. In spite of these challenges, important new ground has been broken particularly in understanding glass structures by using local probes [3] of structures and thermal analysis methods [4]. The latter developments are now beginning to impact our views on liquid structures and dynamics, as we shall see in the present review.

In this review we highlight the elastic (Raman mode frequencies) and thermal response of chalcogenide glasses examined as a function of cross-linking or mean-coordination number,  $\bar{r}$ . We describe how these experimental results lead in a natural fashion to the existence of three distinct glass phases: *floppy*, *intermediate* and *rigid* that are characterized by distinct elastic power-laws as a function of  $\bar{r}$ . An important result to emerge from the thermal measurements (Temperature Modulated DSC) is the existence of *compositional windows* [3] across which the non-reversing heat flow,  $\Delta H_{nr}$ , nearly vanishes. These *windows* are characteristic of glasses in the intermediate phase and are associated with the absence of network stress [5]. Glass transitions become almost completely *thermally reversing* for glass compositions in the intermediate phase. The *intermediate phase* thus becomes synonymous with existence of "*thermally reversing glass compositional windows*", henceforth denoted simply as *windows*. Experiments also reveal that the thresholds in thermal and



elastic behavior coincide [6] and that both are manifestations of glass structure changes as the global connectivity of a network is progressively increased.

For a glass system in which the evolution of network structure with global connectivity is *random*, the window width is found [7] to nearly *vanish* and, correspondingly, an abrupt floppy to rigid transition manifests. The more usual circumstance encountered in glasses is one in where the evolution of cross-linked atomic-scale structures displays some "*self-organization*", leading to the opening of the window. We shall illustrate this with specific examples.

The discovery of thermally reversing windows has fundamental implications in understanding soft matter. The absence of network stress in the intermediate phase is associated with *facile photomelting* of that phase under optical illumination. This could relate to the observation of photomelting [8] in  $\text{As}_2\text{S}_3$  glass and the giant photocollapse [9] of obliquely deposited porous  $\text{GeSe}_2$  films [9]. Both glass systems are intrinsically phase separated on a molecular scale. In both cases the chalcogen-rich phase is thought to undergo a photomelt.

There are also early indications that glass compositions in the *intermediate phase* heated past  $T_g$ , display an Arrhenius T-variation of viscosity. Such a variation is characteristic of *strong* liquids, in the strong-fragile classification [10].

In *section 2*, we comment on overview of the theoretical tools employed to analyze the elastic response of glasses. In *section 3*, we provide experimental results on four families of chalcogenide glasses where intermediate phases are documented, in some cases by both Raman scattering and MDSC measurements. The special case of the chalcogenide Ge-S-I with dangling-bond structure is discussed in *section 4*. In *section 5*, we provide evidence of photomelting in the intermediate phase of the  $\text{Ge}_x\text{Se}_{1-x}$  binary glass system. We conclude in *section 6* with a summary of the principal results.

## 2. Rigidity transition in random networks – theory

### 2.1 Basic ideas

An important step to understand glasses at a basic structural level emerged in 1979 when J. C. Phillips introduced ideas based on mechanical-constraint counting [11] algorithms to explain glass forming tendencies in network forming systems. He reasoned that for a liquid to form a glass composed of a network possessing well-defined local structures, interatomic forces must form a hierarchical order. The strongest covalent forces between nearest neighbors serve as Lagrangian (mechanical) constraints defining the elements of local structure (building blocks). Constraints associated with the weaker forces of more distant neighbors must be intrinsically broken leading to the absence of long-range order. He speculated that the glass forming tendency is optimized when the number of Lagrangian local-bonding constraints per atom,  $n_c$ , just equals the number of degrees of freedom. For a 3d network,

$$n_c = 3 \quad (1)$$

In covalent solids, there are two types of near-neighbor bonding forces; bond-stretching ( $\alpha$ -forces) and bond-bending ( $\beta$ -forces). The number of Lagrangian bond-stretching constraints per atom is  $n_\alpha = r/2$ , and of bond-bending constraints is  $n_\beta = 2r-3$ . For the case when all  $\alpha$ - and  $\beta$ -constraints are intact and no dangling ends (one-fold coordinated atoms,  $n_1/N = 0$ ) exist in the network, equation (1) implies that the optimum mean coordination number is  $\bar{r} = 2.40$ . Highly overcoordinated or undercoordinated structures are not conducive to glass formation and, upon cooling, lead to crystalline solids. Phillips' speculation is in excellent accord with the general experience on glass formation in inorganic solids.

In 1983, M. F. Thorpe pointed [12] out that undercoordinated networks would possess, in the absence of the weaker longer range forces, a finite fraction of zero-frequency normal vibrational modes, the *floppy modes*. In fact, he found from simulations on random networks that the number of floppy modes per atom,  $f$ , is rather accurately described by the mean-field constraint count according to the relation,

$$f = 3 - n_c \quad (2)$$

This led to the realization that a glass network will become spontaneously rigid when  $f \rightarrow 0$ , defining a *floppy* to *rigid phase transition*. Fig. 1 shows a plot of  $f$  against  $\bar{r}$  for the cases of two random networks, one generated by scission of an amorphous Si network and the other by scission of an amorphous (C) diamond network. In both instances, the second derivative of  $f$  with respect to  $\bar{r}$  shows [13] a fairly sharp *cusp* at  $\bar{r}_c$  (C) = 2.375(3) and  $\bar{r}_c$  (Si) = 2.385(3), respectively, quite close to the mean-field value of  $\bar{r}_c = 2.40$ . The numerical simulations also reveal an exponential tail to  $f(\bar{r})$  at  $\bar{r} > \bar{r}_c$ . In contrast the mean-field calculations give a linear variation of  $f(\bar{r})$  till zero at  $\bar{r}_c = 2.40$ , and  $f = 0$  for  $\bar{r} > \bar{r}_c$ .

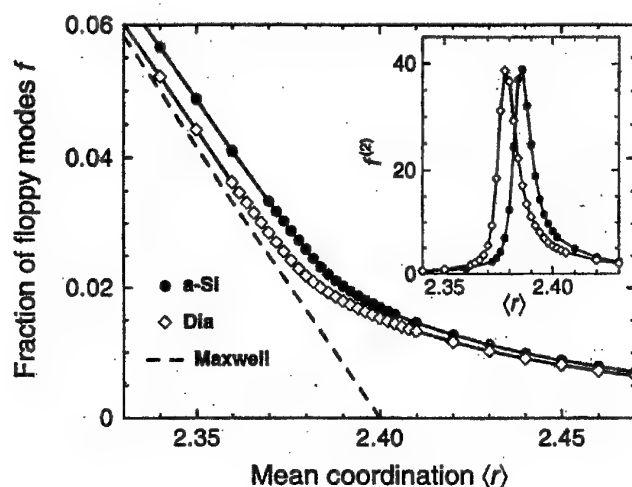


Fig. 1. The number of floppy modes per degree of freedom,  $f$ , for two bond-diluted models, based on the diamond lattice and on amorphous Si. The inset shows the second derivative of  $f$  with respect to  $\langle r \rangle$  for the same models (Ref. 13). The broken line gives the predicted linear variation for mean-field constraint counting (Maxwell).

A significant result of these numerical simulations on random networks is the prediction of a rather robust *power-law variation* of elastic constants [14, 15]  $C$  (longitudinal, transverse and shear) as a function of  $\bar{r}$ ,

$$C = A(\bar{r} - \bar{r}_c)^p \quad (2)$$

in the *rigid regime* with  $p = 1.4 - 1.50$ . We shall return to this prediction later.

## 2.2 Broken bond-bending ( $\beta$ ) constraints

In glasses one rarely observes [4] the solitary rigidity transition  $\bar{r}_c = 2.40$  as discussed above. In part, this is because glasses soften at a finite temperature  $T_g$ , in contrast to the constraint and harmonic elasticity theory predictions which are based on  $T = 0$  K calculations. Since  $\alpha$ -forces exceed  $\beta$ -forces by a factor of 3 or more, in glass systems possessing a high  $T_g$  and/or weak  $\beta$ -forces, constraints associated with  $\beta$ -forces may be intrinsically *broken* [16, 17]. For a network with a finite fraction ( $m_r/N$ ) of  $r$ -fold ( $r \geq 2$ ) coordinated atoms that have their  $\beta$ -constraints broken, the mean-field rigidity transition will be upshifted [4] in  $\bar{r}$  according to

$$\bar{r}_c = 2.40 + \frac{2}{5} \left( \frac{m_2}{N} \right) + \frac{6}{4} \left( \frac{m_3}{N} \right) + 2 \left( \frac{m_4}{N} \right) \quad (3)$$

$\text{SiO}_2$  glass is a celebrated example of a network where the  $\beta$ -constraint associated with the bridging O atoms is intrinsically broken. This is due to the rather high  $T_g = 1200^\circ\text{C}$ , of  $\text{SiO}_2$  which leads thermal energies at  $T_g$  to completely overwhelm the strain energy barrier associated with a sharply defined O-bridging angle. The result is a wide distribution of the bridging O-bonding angle as inferred from diffraction experiments [18]. In this case,  $m_2/N = 2/3$ , the fraction of oxygen atoms per formula unit and according to Eq. (3), the condition  $n_c = 3$  now occurs at  $\bar{r} = 2.67$  since  $m_3/N = m_4/N = 0$ . The propensity toward glass formation in this prototypical oxide derives from the fact that the stoichiometric  $\text{SiO}_2$  glass composition is optimally constrained [17] even though  $\bar{r} = 2.67$ !

A second example is the case of the  $\text{Ge}_{1-x}\text{Sn}_x\text{Se}_2$  ternary in which the  $\beta$ -forces associated with the lighter Ge group IV atom are much *stronger* than those associated with the heavier and more metallic group IV atom Sn. The result is that the  $\beta$ -constraints associated with all Sn-atoms at  $T_g \approx 200^\circ\text{C}$  are broken, and a rigidity transition is predicted by (3) to be at

$$\begin{aligned} 1/3[4(1-x) + 4(x) + 4] &= 2.40 + 2x/3 \\ \text{or } x_c &= 2/5 \end{aligned} \quad (4)$$

Here  $m_2/N = m_3/N = 0$  and  $m_4/N = x$ . The predicted threshold [19] is quite close to the observed threshold ( $x_c = 0.35$ ) in  $^{119}\text{Sn}$  Mössbauer spectroscopy measurements [20] on these ternary glasses.

### 2.3 Networks with dangling ends

Halogens in covalently bonded systems and hydrogen in Si are some familiar examples of networks with dangling ends, i.e., atoms that are one-fold coordinated (OFC). The mean-field constraint counting is modified as follows: for an atom with  $r > 1$

$$n_\alpha = r/2 \quad (5a)$$

$$n_\beta = 2r - 3 \quad (5b)$$

For an OFC atom there is no  $\beta$  constraint and the rigidity transition condition ( $n_c = 3$ ) now occurs when

$$\bar{r}_c = 2.40 - 0.4(n_1/N) \quad (6)$$

leading in general to a downshift [21] of the threshold from the magic value of 2.40. In general, OFC-atoms play no role if the base glass network (without one-fold coordinated atoms) is optimally coordinated [22]. On the other hand, these atoms will soften [23] an overconstrained base network and conversely stiffen [22] an underconstrained base glass network.

### 2.4 Rigidity transitions in self-organized networks

In our discussion so far, we have not distinguished between onset of *rigidity* from onset of *stress*. A network can be *isostatically rigid*, that is, with no stress present. Stresses are said to exist when already present bond lengths and/or angles must change on the addition of more atoms to the structure. Thus, the imposition of additional cross links or constraints can lead to *redundant constraints* and to the accumulation of *stress*. An example can serve to illustrate the idea. Consider 4 elastic bars hinged at their ends to form a square. A square is not a rigid structure because it can be sheared into a rhombus. A crossbar attached to opposite vertices of the square will result in an isostatically (barely) rigid structure. A second crossbar attached across the remaining two vertices provides a redundant constraint and will result in accumulation of stress in the structure. Isostatically rigid and stressed rigid random structures are expected to be physically different in behavior, as we now discuss.

Let us consider a cross-linked random network with  $\bar{r} = 2.2$  so that it consists of floppy regions and sparsely populated isostatically rigid inclusions. Next we insert additional cross-links in a *selective* fashion; we allow a cross-link in the floppy segment of the network, but not in an isostatically rigid region to avoid redundant constraints and stress. The process is a form of self-organized growth. The question remains, how far can we proceed before stressed rigidity manifests itself. The issue was recently addressed in a numerical simulation of self-organized growth by M.F. Thorpe et al. who found [23] that, in a scissored amorphous Si Network, isostatic rigidity manifests at  $\bar{r} = \bar{r}_c(1) = 2.375(15)$  while stressed rigidity onsets at  $\bar{r} = \bar{r}_c(2) = 2.392(15)$  as shown in Fig. 2. In a real system, self-organization process may be driven by free energy of a glassy melt. These simulations [23] suggest that there are *two transitions*, a floppy to an isostatically rigid state followed by an isostatically rigid to a stressed rigid state. Glass compositions residing between the floppy and stressed rigid phase define the *intermediate phase*. These simulations are in sharp contrast to those on random networks that predict [13] the stress and rigidity transition to coincide and occur at a unique value of  $\bar{r}$ .

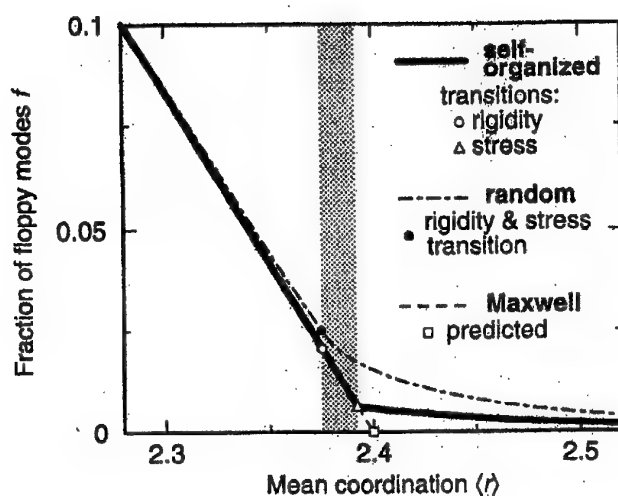


Fig. 2. The fractions of floppy modes per degree of freedom for the diluted diamond lattice for the random case (broken line) and the self-organized case (solid line). For the self-organized case the rigidity transition (o) and the stress transition (D) rise to the intermediate phase shown as the shaded region. Fig. taken from Ref. 13.

Raman and MDSC experiments on chalcogenide glasses provide evidence of two rigidity transitions, as we shall describe next in *section 3*. There is at present a significant difference with respect to the values of  $r_c(1)$  and  $r_c(2)$  between the numerical model and experiments. Still these new numerical simulations represent a significant advance and provide a physical basis for characterizing the nature of the two transitions and some insights into the *self-organized* intermediate state.

### 3. Experimental probes of rigidity transitions

Different types of experimental methods have given evidence on the nature of rigidity transitions in glasses. These include T-modulated Differential Scanning Calorimetry [4], Raman [4, 24] and Brillouin scattering [25], Neutron scattering [29], and Mössbauer spectroscopy [26], viscosity [27], thermal expansion [28], and Molar volume measurements. Anomalies in compositional trends of electronic behavior of glasses near the rigidity transition have also been observed, such as the semiconductor to metal transition pressures [30] and electric fields for electronic switching [31]. The connection between electronic behavior and glass structure remains to be understood in this context, however.

### 3.1 Thermally reversing windows and the intermediate phase

Differential Scanning Calorimetry (DSC) has been used to establish glass transition temperatures,  $T_g$ , for the past 50 years. Although the glass transition itself is quite wide ( $> 20^\circ\text{C}$ ), one can usually localize the inflexion point of the heat flow endotherm to within  $\pm 2^\circ\text{C}$ , and thus define  $T_g$ . However, it is well known that not only does the shape of the heat flow endotherm depend on the baseline of the instrument, but also on the thermal history of the sample and the scan rate employed. Several of these limitations have been overcome in a recent variant of DSC known as MDSC. In the latter, the programmed heating rate [32] includes a sinusoidal T-modulation superimposed on a linear T ramp used to scan through the glass transition. Because of increased sensitivity, an order of magnitude reduction in scan rates ( $1\text{--}3^\circ\text{C}/\text{min}$ ) can be used in MDSC in relation to those ( $10\text{--}20^\circ\text{C}/\text{min}$ ) used in DSC. Furthermore, in MDSC it is possible to deconvolute the total heat-flow rate into a part that tracks the T-modulation and is known as the *reversing heat flow rate*, leaving a part that does not track the T-modulation, which is known as the *non-reversing heat-flow rate*.

Experience on a wide variety of glass systems shows that the non-reversing heat-flow rate displays a Gaussian-like peak as a *precursor* [2] to the glass transition. The latter is observed as a smooth step-like shift of the reversing heat-flow rate as illustrated in Fig. 3.

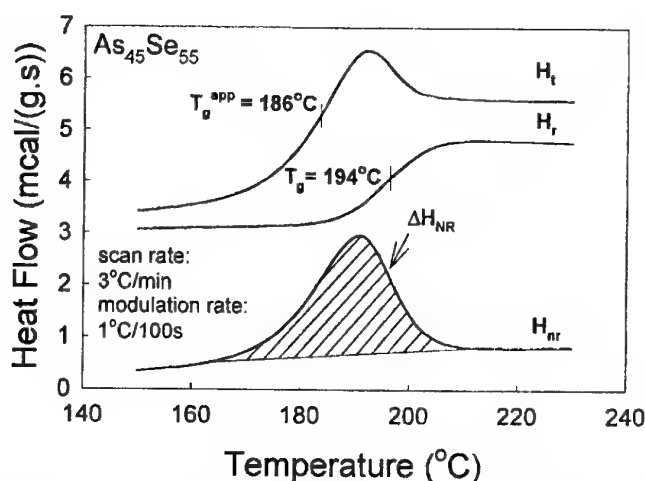


Fig. 3. MDSC scan of  $\text{As}_{45}\text{Se}_{55}$  glass showing deconvolution of the total heat flow  $H_t$  into reversing,  $H_r$ , and non-reversing,  $H_{nr}$ , components. Fig. is taken from Ref. 34.

The area under the non-reversing heat flow rate will be denoted henceforth as  $\Delta H_{nr}$ , the *non-reversing heat-flow*.  $\Delta H_{nr}$  is thermal history sensitive. It is found to saturate in time typically after 100 hours to a fully relaxed glass. In this work,  $\Delta H_{nr}$  is used to denote the *saturated* value, and it measures the latent heat between the relaxed solid glass and its melt. The sigmoidal jump in the reversing heat flow observed in these experiments is *independent of the baseline of the instrument*. It establishes the thermodynamic jump  $\Delta C_p$  in the specific heat between the glass and its melt and its inflection point can be taken to define  $T_g$ . Furthermore, by scanning up and then down in T across  $T_g$ , one can correct for the small but finite scan-rate-dependent shift of  $T_g$  and thus obtain *scan-rate independent*  $T_g$  and  $\Delta H_{nr}$ . Such  $T_g$ 's, independent of scan rates and sample thermal history, are closely correlated with glass compositions [5, 33, 34]. Compositional trends in  $T_g$  provide a measure of global connectivity of the network, an idea that has been made quantitative in the past few years by stochastic agglomeration theory [35]. The  $\Delta H_{nr}$  term provides a measure of how different a glass is from the liquid in a configurational sense. For glass compositions in the *intermediate phase*,  $\Delta H_{nr}$  term is found to nearly *vanish*. This unequivocally suggests that glass- and liquid-structures in the window compositions are *closely similar* to each other and that both are *stress free* in a global sense.

In Fig. 4, we provide examples of thermally reversing windows observed in chalcogenide glasses. In the  $\text{Ge}_x\text{Se}_{1-x}$  binary, the  $\Delta H_{nr}$  term is found [16] to *decrease* by almost an order of

magnitude in the  $0.20 < x < 0.26$  (or  $2.40 < \bar{r} < 2.52$ ) composition region (indicated by a pair of arrows). This composition range serves to define the thermally reversing window in this binary. We will revisit these results in conjunction with Raman results later.

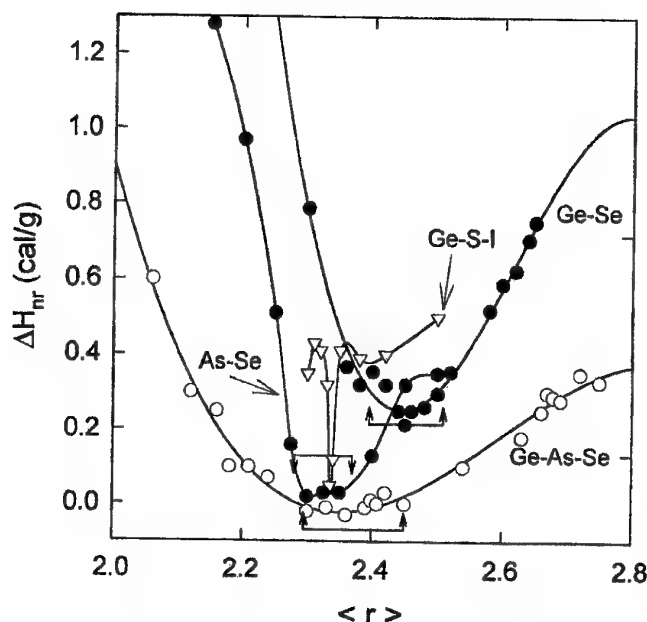


Fig. 4. Non-reversing heat,  $\Delta H_{nr}$ , as a function of mean coordination number  $\langle r \rangle$  for four different glass systems. The Ge-As-Se ternary shows the widest window (Ref. 5) while the Ge-S-I the narrowest (Ref. 7).

In the  $\text{As}_x\text{Se}_{1-x}$  binary the window centroid is somewhat shifted [34] to lower  $\bar{r}$ ,  $2.29 < \bar{r} < 2.37$ . This is a surprising result, given the fact that the stoichiometric glass  $\text{As}_2\text{Se}_3$  corresponds to  $\bar{r} = 2.40$  and is widely viewed to be an optimally coordinated, chemically ordered, and continuous random network of  $\text{As}(\text{Se}_{1/2})_3$  pyramids. This, along with the non-Arrhenius  $T$ -variation [1] of viscosity of liquid  $\text{As}_2\text{Se}_3$ , suggests that the traditional view cannot be the complete picture and that the stoichiometric glass is neither *completely chemically ordered* nor is it optimally coordinated. The difference appears to be associated with an intrinsic nanoscale phase separation into As-rich and Se-rich clusters, as is suggested by local-probe results and by the  $T_g$  maximum near  $x = 2/5$ . The fact (Fig. 4) that  $\text{As}_x\text{Se}_{1-x}$  glasses in the  $0.29 < x < 0.37$  composition range appear to be *optimally coordinated* is incompatible with *presence of* pyramidal  $\text{As}(\text{Se}_{1/2})_3$  units being the only As-centered local units in the Se-rich glasses ( $x < 0.40$ ). The shift of the window to  $x < 0.40$  suggests that quasi-tetrahedral units of the type  $\text{Se} = \text{As}(\text{Se}_{1/2})_3$  in which the valence of As is formally  $5+$ , are probably also present. The attractive feature of these quasi-tetrahedral units is that the number of constraints per atom for such a unit is *exactly* 3, even though the unit is undercoordinated ( $\bar{r} = 2.285$ ). This special circumstance arises because of the terminal (non-bridging) Se atom. In the  $\text{P}_x\text{Se}_{1-x}$  binary, one also observes a thermally reversing window [33] in the same cation concentration range. In this binary, there is evidence for 4-fold coordinated P from NMR measurements [36].

The thermally reversing window in the  $\text{Ge}_x\text{As}_x\text{Se}_{1-2x}$  ternary is widest [5] of the four chalcogenide glass systems presented in Fig. 4. Here one can expect the ternary to be made up of several types of optimally coordinated building ( $n_c = 3$ ) blocks,  $\text{As}(\text{Se}_{1/2})_3$  pyramids,  $\text{Se} = (\text{As})(\text{Se}_{1/2})_3$  quasi-tetrahedra,  $\text{Se}_n$  chain segments with corner-sharing  $\text{Ge}(\text{Se}_{1/2})_4$  tetrahedra. The increased number of optimally coordinated units in this ternary opens new possibilities to form the elements of medium-range structure in a self-organized backbone. It is for this reason, we believe, that the window is rather wide in the ternary.

The spectacularly narrow window found [7] in the  $\text{Ge}_{0.25}\text{S}_{0.75-y}\text{I}_y$  ternary puts in perspective the large width of windows seen in the binary and ternary chalcogenides. We shall discuss the special case of this chalcogenide in section 5. It appears to be a model example of a *random network* and the

collapse of the thermally reversing window is due to absence of self-organization in this "random" network.

In summary, thermally reversing windows deduced from MDSC measurements serve to define the extent of the *intermediate phase* present in ternary As-Ge-Se glasses as sketched in the phase diagram of Fig. 5. The *intermediate phase* opens up in between the *floppy* and *rigid* phases and near glass compositions corresponding to  $\bar{r} = 2.40$ . The results of Fig. 5 showcase the central *new result* of this work. These thermal thresholds are found to coincide with elastic thresholds deduced from Raman optical elasticities on these glasses, as we shall discuss next.

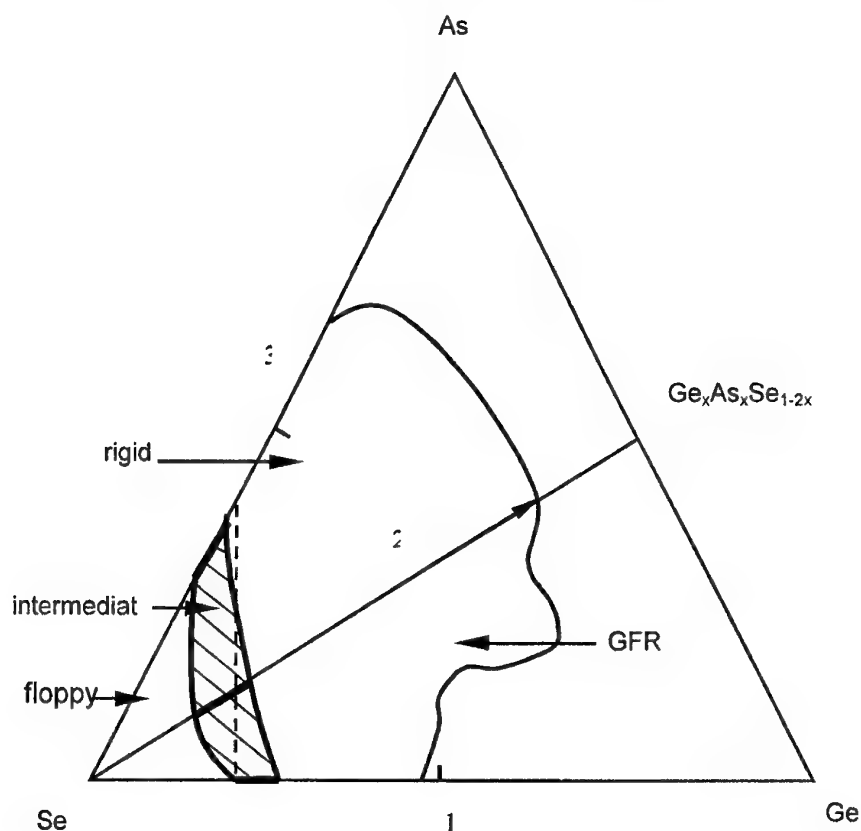


Fig. 5. The glass-forming region in the Ge-As-Se ternary glass system. The broken line corresponds to  $\langle r \rangle = 2.40$ . The shaded region gives the opening of the intermediate phase between the floppy and the rigid phases, and it straddles the  $\langle r \rangle = 2.40$  line.

### 3.2 Raman scattering, elastic thresholds and the intermediate phase

Although Raman scattering has been widely used as a probe [37-40] of glass structure for the past three decades, its application as a probe of the *rigidity transitions* in network glasses is a *recent* [4, 6, 16] development. In many cases, when vibrational bands associated with a specific network building block can be resolved in the Raman lineshapes, it is possible to quantitatively follow mode frequency changes with glass composition. And although the scale of mode frequencies are set by the strength of  $\alpha$ - and  $\beta$ -forces, shifts in mode frequencies with glass compositions result from inter-building-block couplings. Raman scattering experiments on several IV-VI glass systems have now been performed [6, 16]. These comprehensive results provide supporting evidence for two rigidity ( $r_c(1)$ ,  $r_c(2)$ ) transitions in these chalcogenide glasses, in that elastic thresholds correlate well with thermal thresholds deduced from MDSC measurements.

A plot of the CS mode frequency ( $\nu_{CS}$ ) in  $\text{Ge}_x\text{Se}_{1-x}$  glasses as a function of Ge concentration yields kinks [41] near  $x_c(1) = 0.20$  and  $x_c(2) = 0.26$  as shown in Fig. 6. For glass compositions at  $x > x_c(2) = 0.26$ , we have fit to an underlying elastic power-law by plotting  $\nu_{CS}^2$  against  $\bar{r} - \bar{r}_c(2)$  on a

loglog plot, and obtain a power-law of  $p = 1.54(10)$  as shown in Fig. 7. The result is reminiscent of the numerical simulations [23] of elastic constants in random networks constrained by  $\alpha$ - and  $\beta$ -forces for which  $p$  in the rigid regime is predicted to be 1.40 - 1.50. These results provide unambiguous evidence for the onset of a new rigidity at  $x_c > 0.26$ .

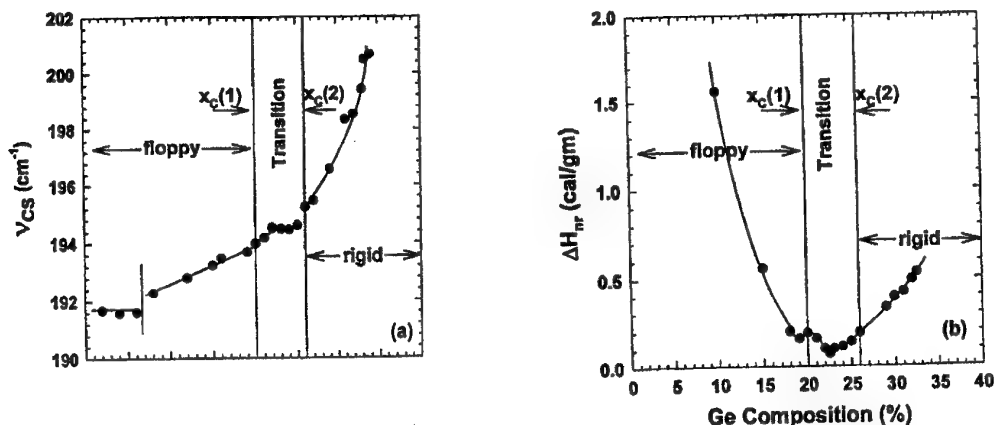


Fig. 6a). Raman mode frequency variation of corner-sharing ( $n_{CS}$ ) tetrahedra in  $Ge_xSe_{1-x}$  plotted as a function of  $x$ ; b) Non-reversing heat variation,  $\Delta H_{nr}(x)$ , in  $Ge_xSe_{1-x}$  glasses. Fig. is taken from Ref. 41.

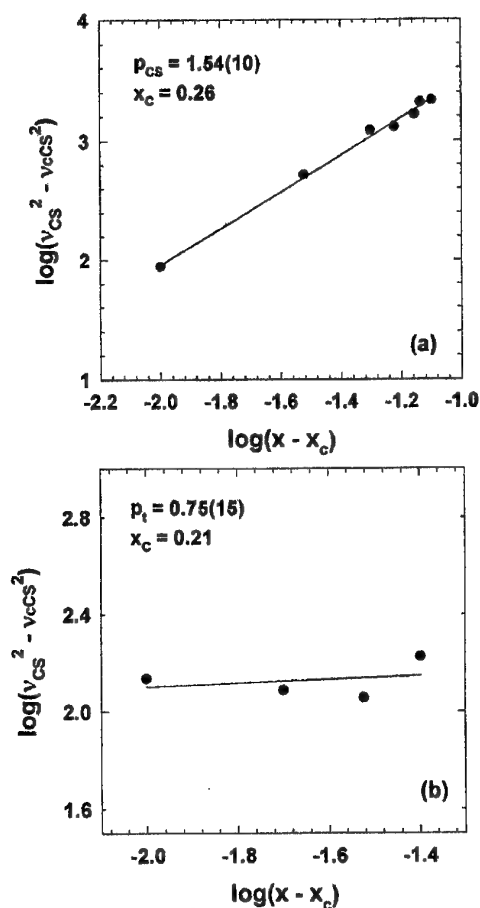


Fig. 7. Plots of  $\log_{10}(n^2 - n_c^2(x))$  against  $\log_{10}(x - x_c)$  for the CS mode frequency in  $Ge_xSe_{1-x}$  glasses. The plots give respective power laws for CS - mode - based optical elasticity in the rigid region,  $p_{CS}$ , and in the transition region,  $p_t$ . Fig. taken from Ref. 41.



In the  $0.20 < x < 0.26$  composition range, a similar fit of the CS mode frequency squared against  $\bar{r} - \bar{r}_c(1)$  on a loglog plot, yields a much lower value of  $p = 0.75(15)$ . Such a sub-linear power-law may be compared to the finite scaling result [42] which is  $2/d = 2/3$  for  $d = 3$  (3d network). To obtain a power-law  $p < 1$ , one must invoke large-scale or long-range fluctuations as are discussed in equilibrium-scaling theory.

A distinctly different elastic behavior is suggested in the  $0.10 < x < 0.20$  composition range from the Raman measurements, namely a linear  $\nu_{CS}(x)$  variation. Furthermore, at  $x < 0.07$ , Raman measurements show  $\nu_{CS}(x)$  to become independent of  $x$ , a regime in which the  $T_g(x)$  variation is found to be linear [41, 43] with a slope  $(dT_g/dx = T_0/\ln 2)$ . In the lowest  $x (< 0.07)$  regime, the  $T_g(x)$  trends,  $\nu_{CS}(x)$  trends, and Mössbauer site-intensity ratios in  $^{129}\text{I}$  spectroscopy [44], all point to a *stochastic regime* of agglomeration in which CS  $\text{Ge}(\text{Se}_{1/2})_4$  units *randomly* cross-link  $\text{Se}_n$ -chain segments to define a floppy phase of these binary glasses. In the  $0.10 < x < 0.20$ , ES tetrahedral units may appear in addition to CS ones and precipitate nuclei of isostatically rigid inclusions in which more extended-range structural correlations evolve. In this particular regime the challenges are more formidable and our current understanding of  $T_g(x)$  trends,  $\nu(x)$  trends continues to be qualitative. More work is needed to understand the underlying behavior.

The compositional trends in  $\nu_{CS}(x)$  and  $\Delta H_{nr}(x)$  as seen in Raman and MDSC measurements are shown in Fig. 6. There are clear correlations between these trends, which are driven by aspects of glass structure. In particular, the  $\nu_{CS}(x)$  variation of Fig. 6 shows that the rigidity transition near  $x_c(1) = 0.20$  appears to be continuous, i.e., second order, while the stress transition near  $x_c(2) = 0.26$  discontinuous or first order. Thorpe et al. [45] have suggested that the network rigidity nucleates at small rings,  $n < 6$ . Numerical simulations in networks that possess no rings, such as *random bond networks* [45] and *Bethe lattices*, [46] show a *first order* transition to a stressed backbone structure. Stressed rigidity is believed to nucleate in  $n$ -membered rings with  $n < 6$  in general. These results suggest that in the binary  $\text{Ge}_x\text{Se}_{1-x}$  glasses the concentration of small rings,  $n = 5, 4$ , must be quite small at  $x < 0.26$  for the transition to be first order.

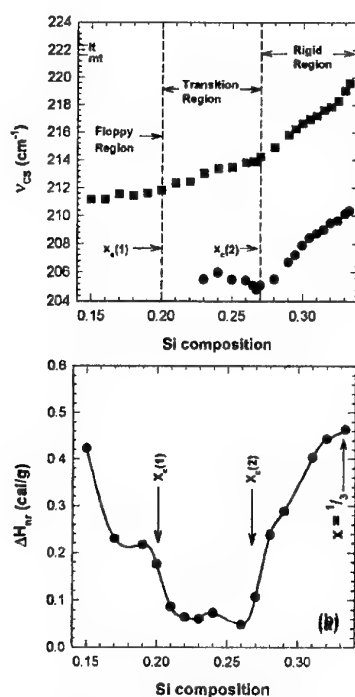


Fig. 8a). Raman mode frequency variation of corner-sharing ( $n_{CS}$ ) tetrahedra in  $\text{Si}_x\text{Se}_{1-x}$  plotted as a function of  $x$ ; b) Non-reversing heat variation,  $\Delta H_{nr}(x)$ , in  $\text{Si}_x\text{Se}_{1-x}$  glasses. Both observables show the opening of the intermediate phase in the  $x_c(1) < x < x_c(2)$  region. Fig. is taken from Ref. 6.

Fig. 8 shows parallel Raman and MDSC results to Fig. 6 for the  $\text{Si}_x\text{Se}_{1-x}$  binary glass system taken from ref. 6. The correlation between the elastic and the thermal-thresholds is rather *compelling* in this system, probably because the glass structure is dominated by chains of ES tetrahedra. The *intermediate phase* extends from  $x_c(1) = 0.20$  to  $x_c(2) = 0.26$ , quite similar to the one seen [41] in the  $\text{Ge}_x\text{Se}_{1-x}$  binary.

### 3.3 Lamb-Mössbauer factors and rigidity transition in glasses

Mössbauer spectroscopy has served as a powerful, local probe [47] of glass structure. The Mössbauer hyperfine structure observed in glasses provides means to probe the local environment of the resonant nucleus/atom. Furthermore, the T-dependence of the integrated area under a nuclear resonance through measurements of the Lamb-Mössbauer factor, has proved to be a useful probe [26] of *low-frequency vibrational excitations* in glasses. Thus, both the static and dynamic structures about a resonant atom in a network glass can be elegantly probed. This subject has been reviewed elsewhere, the interested reader is referred to those publications [47].

### 3.4 T-dependence of viscosity and the intermediate phase

The T-dependence of viscosity of glass forming liquids has been studied [48] for the past 30 years. Liquids are classified as *strong* [49] if an Arrhenius T-dependence of viscosity is observed, and are *fragile* if a strongly non-Arrhenius T-dependence of viscosity is observed. An elegant means of presenting these results is on a plot of  $\log \eta$  against  $1/T$  normalized to  $T_g$ , as illustrated in Fig. 9a for melts of the As-Se binary glass system. These results are taken from the work of Nemilov and Petrovckii [50]. In Fig. 9b, the dark circles are the activation energy for viscosity,  $E_\eta^A(x)$  at  $T_g$ . In this figure we have also superposed (open circles) the compositional trend in  $\Delta H_{nr}(x)$  taken from our work.

Fig. 9 demonstrates that compositional trends in  $E_\eta^A(x)$  track those in  $\Delta H_{nr}(x)$ , a pattern observed in two other glass systems where the results are available. Glass compositions in the intermediate phase, upon melting, display an Arrhenius T-variation of viscosity, i.e., give rise to *strong liquids*. On the other hand, both floppy and rigid glasses give rise to *fragile liquids* with a strongly non-Arrhenius T-variation of viscosity.

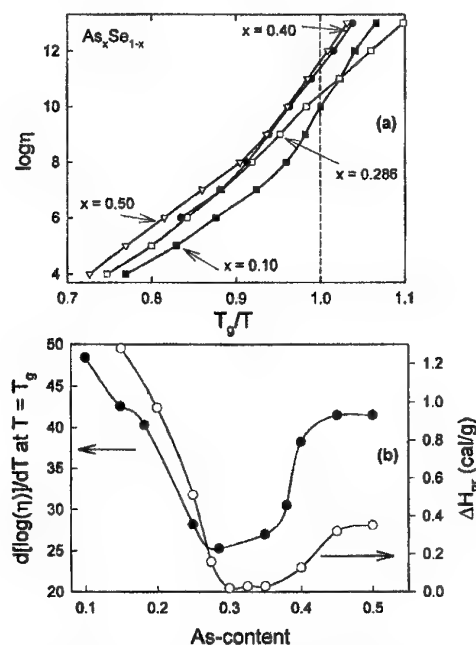


Fig. 9a). Plot of  $\log \eta$  against  $1/T$  normalized at  $T_g$  taken from ref. 50. (b) Non-reversing heat,  $\Delta H_{nr}$ , and the activation energy for viscosity  $d(\log \eta)/dT$  at  $T_g$ , in  $\text{As}_x\text{Se}_{1-x}$  glasses as a function of As content. Note both observables track each other suggesting that the glass softening behavior carries the memory of liquid dynamics.

The central message underlying the correlation of Fig. 9 may be summarized. The viscosity  $\eta$  of a liquid provides a measure of the shear relaxation time ( $\tau_s$ ) through the Maxwell relation,

$$\eta = \tau_s G_\infty \quad (7)$$

where  $G_\infty$  is the high-frequency shear modulus. Since  $G_\infty$  is known to be largely  $T$ -independent,  $E_\eta^A$  thus also serves as an activation energy for shear relaxation time in a liquid. The correlation observed in Fig. 9 shows a connection between the glass structure and *liquid dynamics*. It is becoming increasingly clear that concepts of global connectivity developed to describe glass networks extend well into the liquid state, conversely, that the underlying dynamics of structural arrest of a liquid on solidification is related to the global connectivity of the liquid structure. The discovery of the intermediate phase thus allows us for the first time to correlate the *strong-fragile* classification [49] of liquids with the *floppy-intermediate-rigid* classification of glasses. Glasses in the *intermediate phase* give rise to *strong* liquids. Glasses in both the *floppy* and *rigid* phases give rise to *fragile* liquids. *Fragility* is thus a multivalued concept and needs to be refined. Since both floppy and rigid glasses give rise to fragile liquids, it remains to be understood in what manner does the  $T$ -dependence of viscosity of floppy liquids differ from that of rigid liquids.

We conclude this section with two remarks. First,  $\text{As}_2\text{Se}_3$  glass is often regarded as an optimally coordinated ( $\bar{r} = 2.40$ ,  $\bar{n}_c = 3$ ) glass network. Surprisingly, neither the  $T$ -dependence of melt viscosity nor the measured  $\Delta H_{tr}$  puts this composition in the thermally reversing window, although it is not far away (Fig. 9b). The small deviation of this glass composition away from the edge of the thermally reversing window suggests that the glass is slightly overconstrained relative to its putative composition. Such a result can arise if the glass network is intrinsically *phase separated* into Se-rich and As-rich regions with the latter phase comprising the rigid backbone.

Second, systematic studies of the  $T$ -dependence of viscosities of chalcogenide liquids as a function of composition are likely to provide important insights into aspects of nanoscale phase separation in the liquid state that apparently not only control the dynamics in the liquid state but also the nature of the structurally arrested state in the glass.

#### 4. A very narrow thermally reversing window in $\text{Ge}_{0.25}\text{S}_{0.75-y}\text{I}_y$ glasses

Additional insights into the molecular origin of thermally reversing windows in network glasses have recently emerged from studies on the chalcogenides [51] Ge-S(or Se)-I. Here we start with a marginally rigid base glass of  $\text{Ge}_{0.25}\text{S}_{0.75}$  composition and systematically replace S by I, to get ternary  $\text{Ge}_{0.25}\text{S}_{0.75-y}\text{I}_y$  glasses in the  $0 < y < 0.30$  concentration range. The global glass forming tendency in this ternary was recognized by Dembovsky [52], and the present compositions reside in that part of the phase diagram where the glass forming tendency is actually rather high [21]. One expects I to chemically bond with Ge because of Pauling charge transfer effects and to replace bridging S with terminal I in the backbone. The replacement converts tetrahedrally coordinated CS  $\text{Ge}(\text{S}_{1/2})_4$  units ( $m = 0$  units) into mixed tetrahedral units of the type  $\text{Ge}(\text{S}_{1/2})_{4-m}\text{I}_m$  with  $m = 1, 2, 3$  and eventually 4, as  $y$  is systematically increased. The  $m = 4$  units form monomers,  $\text{GeI}_4$  molecules, that are decoupled from the backbone.

MDSC experiments on this system show  $T_g(y)$  to systematically decrease with  $y$  at first slowly in the  $0 < y < 0.15$  range and then sharply in the  $0.15 < y < 0.17$  range as shown in Fig. 10. In the  $0 < y < 0.15$  concentration range stochastic agglomeration theory permits a quantitative analysis of the  $T_g(y)$  trends through the ways in which the various  $m$ -units combine or agglomerate to form the backbone. But the central result to emerge from these MDSC measurements is the compositional dependence of  $\Delta H_{tr}(y)$  which has a *sharply* defined *global minimum* centered at  $y = y_c = 0.162(4)$  (corresponding to  $\bar{r} = 2.34$  of the ternary). In the estimate of  $\bar{r}$ , we take the  $r$  of Ge, S, and I to be 4, 2 and 1, respectively.

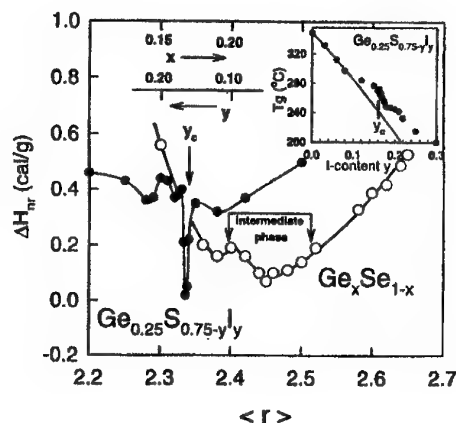


Fig. 10. Variation of the non-reversing heat flow,  $\Delta H_{nr}$ , as a function of  $\langle r \rangle$  in the ternary  $\text{Ge}_{0.25}\text{S}_{0.75-y}\text{I}_y$  and in the binary  $\text{Ge}_x\text{Se}_{1-x}$ . The inset shows the  $T_g(y)$  variation in the ternary and the smooth line is the prediction of the agglomeration theory. Fig is taken from Ref. 7.

According to equation 6, mean-field constraint counting for the  $\text{Ge}_{0.25}\text{S}_{0.75-y}\text{I}_y$  ternary is

$$\bar{r}_c = 2.40 - 0.4y_c \quad (8a)$$

or

$$4(1/4) + 2(3/4 - y_c) + 1(y_c) = 2.40 - 0.4y_c$$

$$y_c = 1/6 = 16.6 \quad (8b)$$

in excellent accord with the value of  $y_c = 0.162(4)$  observed for the minimum in  $\Delta H_{nr}(y)$ .

The physical picture emerging from these MDSC measurements is that iodine alloying in the marginally rigid base glass,  $\text{Ge}_{0.25}\text{S}_{0.75}$  steadily de-polymerizes the backbone thereby leading to a reduction in  $T_g$ . Near  $y_c = 0.162$ , there is a precipitous reduction in  $T_g$ , and  $\Delta H_{nr}$  shows a global minimum corresponding to a sharply defined rigid to floppy transition that is in excellent accord with extended mean-field constraint theory.

Obvious questions arise: why is the rigid to floppy transition so *sharp* in this chalcogenide glass system? Why is the threshold in perfect agreement with constraint theory? Raman scattering results on these glasses provide important clues [7] to address these issues. Through them one can quantitatively decode the concentrations  $N_m(y)/N$  of the various  $m$ -units from the relative strengths of the Raman peaks identified [53] with the symmetric stretching modes of the  $m = 0, 1, 2, 3$  and 4 quasi-tetrahedra. Fig. 11 provides a plot of trends in  $N_m/N(y)$  deduced from the Raman results. On this plot we have also included the predicted variation of the  $N_m/N$  concentrations (smooth lines) if the iodine alloying were to proceed *randomly* according to combinatorial calculations. Here one cannot overemphasize that the smooth lines are *not a fit to the data* but merely the prediction of the combinatorial calculations. The excellent agreement between theory and experiment up to  $y = 0.17$  carries a central message: evolution of the Ge-S backbone upon progressive alloying with I for S proceeds in a truly *random* fashion up to the phase transition. In glass science it is popular to invoke continuous random networks. Our experiments here show that it is actually rare ( $\text{Ge}_{0.25}\text{S}_{0.75-y}\text{I}_y$  being one of the exceptions) that glass networks are random and continuous.

Returning back to the rigidity transition, one can now unambiguously relate the *sharpness* of the phase transition to the *stochastic evolution* of the backbone that precludes self-organization and formation of extended range structures composed of rings. In turn these results suggest that the large width of the intermediate phase encountered in the  $\text{Ge}_x\text{Se}_{1-x}$  binary (see Fig. 11) and other glasses (Fig. 4), is probably the result of substantial structural reorganization of the backbone when the latter is optimally constrained. Some of the structural reorganization taking place may consist of optimally constrained filamentary structures that pack well and globally lower molar volumes of these glass compositions [29]. The decoupling of these filamentary structures may intrinsically contribute to a lowering of the  $\Delta H_{nr}$  term by avoiding cross-linking. And it remains to be seen if the pronounced

scattering at the first sharp diffraction peak reported by S. Hosokawa [54] in anomalous x-ray absorption studies on Ge-Se glasses in the thermally reversing window compositions is actually a manifestation of the filamentary structures.

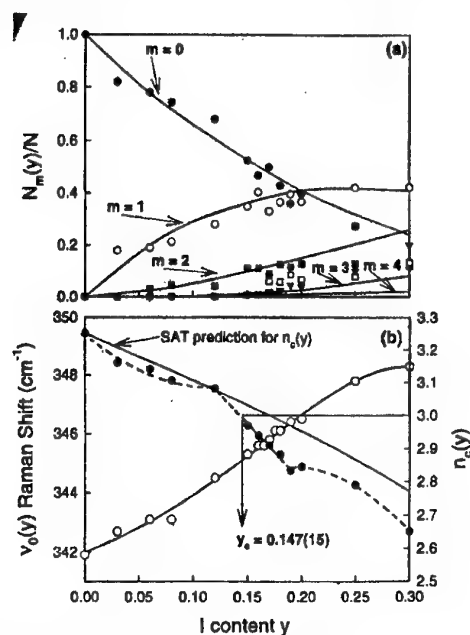


Fig. 11a). Concentration  $N_m(y)/N$  of the mixed tetrahedra,  $m = 0, 1, 2, 3, 4$ , plotted as a function of  $y$  in the  $\text{Ge}_{0.25}\text{S}_{0.75-y}\text{I}_y$  ternary. The smooth curves are the prediction of simple combinatorial calculation (Ref. 7) and are not a fit to the data points. (b) Raman mode frequency variation  $\nu_0(y)$  of  $m = 0$  units and the Raman count of mean-field constraints per atom  $n_c(y)$  (Ref. 7), plotted as a function of I content. The smooth line is the stochastic agglomeration theory prediction for  $n_c(y)$ .

## 5. Photomelting of the intermediate phase

Semiconducting glasses when illuminated by near band-gap radiation can alter the molecular structure of the intermediate phase. We have carried forward detailed micro- as well as macro-Raman scattering measurements on the same batch of  $\text{Ge}_x\text{Se}_{1-x}$  glasses. In both sets of experiments [41], the back-scattering was excited with the weakly absorbing red light of 647.1 nm radiation from a Kr-ion laser, and the power levels kept in the 500  $\mu\text{W}$  range for the micro-Raman and 5 mW range for the macro-Raman measurements. In the micro-Raman measurements the exciting light is brought to a sharp focus of less than 5  $\mu\text{m}$  spot size using a microscope with 80x objective in a model T64000 triple monochromator Raman scattering facility from Instruments, S.A., Inc. On the other hand, in the macro-Raman measurements, the exciting light is brought to a loose focus of about 1 mm spot size using a macrochamber in the same scattering facility. The spot-size reduction by at least two orders of magnitude translates into an approximately four orders of magnitude reduction in the photon flux (number of photons/ $\text{cm}^2/\text{sec}$ ) used to excite the Raman scattering in the macro-configuration ( $10^{18}$  photons/ $\text{cm}^2/\text{s}$ ) in relation to the micro-configuration ( $10^{22}$  photons/ $\text{cm}^2/\text{sec}$ ).

Figs 12a (Fig. 6 repeated) and 12b show the compositional dependence  $\nu_{\text{CS}}(x)$  of the CS  $\text{Ge}(\text{Se}_{1/2})_4$  mode frequency observed in  $\text{Ge}_x\text{Se}_{1-x}$  glasses obtained under low and high flux density radiation configurations, respectively, to excite the Raman scattering. The striking difference between Figs. 12a and 12b is the collapse of the intermediate phase which originally extended from  $x_c(1) = 0.20$  to  $x_c(2) = x = 0.26$  down to a single transition point at  $x_c = 0.23$ . At both  $x_c(2)$  and  $x_c$ ,  $\nu_{\text{CS}}(x)$  shows an apparent jump or discontinuity, after which it increases as a power-law that is characteristic of increasing structural stress. Correspondingly, the floppy-phase region is extended from  $x_c(1)$  up to  $x_c$ .

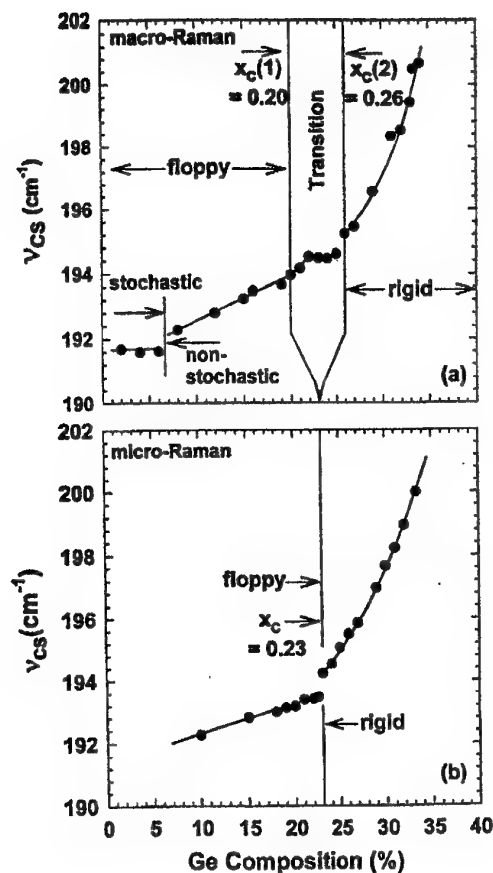


Fig. 12. Corner-sharing mode frequency variation,  $\nu_{CS}(x)$ , in  $\text{Ge}_x\text{Se}_{1-x}$  glasses from low intensity (macro-) (a) and high intensity (micro-) Raman (b) measurements. In the latter the intermediate phase collapses to a single point.

The high-flux density illumination clearly has induced changes in chemical bonding, resulting in a *photo-melt*. In either the floppy phase or the rigid phase in the photo-melted state, the overall variation of  $\nu_{CS}$  is seen to differ little from the behavior in the original glass. We argue that this indicates that chemical bonding of fourfold coordinated Ge and twofold coordinated Se atoms is originally random enough in these phases so that further randomization by the exciting light only produces statistically similar structures. (It is also possible that melting does not occur at all in the floppy and rigid phases at the flux densities of our experiments because  $\Delta H_{nr}$  is too large but occurs selectively in the intermediate phase where  $\Delta H_{nr}$  is very small.

The intermediate-phase structure is destroyed presumably by randomization of the bond-distribution. This is suggested by our earlier interpretation of the intermediate phase (following the calculations [23] of Thorpe et al.) as being an *isostatic* structure with no redundant bonding, i.e., no bonding over that required to produce rigidity. This means that an *isostatic* bond configuration is highly *non-random*, since bonds that would be redundant are "repelled". This repulsion can be maintained as we increase the bond density  $\bar{r}$  up to the point where the local chemistry can no longer be satisfied without any redundancy. Then a first order transition to a stressed backbone occurs.

In contrast, the randomly bonded structure in the photo-melted state will be floppy up to the concentration  $x_c$  where the first rigid (and stressed) backbone develops – in accordance with the original floppy-to-rigid-transition picture proposed by Phillips and Thorpe in the early 1980's. (We note, however, that  $x_c = 0.23$  here corresponds to  $r_c = 2.46$ , a value somewhat larger than the mean-field constraint counting value,  $\bar{r}_c = 2.40$  because some of the constraints are intrinsically broken [16]).

Let us engage the notion of *isostacy* to further understand the differences between Fig. 12a and Fig. 12b. Note first that, because of bond repulsion, isostatic structures are more efficiently

packed than randomly bonded structures in achieving a percolating backbone, that is, they require fewer Ge cross-linking atoms; so that  $x_c(1)$ , the lowest bond density to reach rigidity, will be less than  $x_c$ , the lowest value for redundant structures. Under photo-melting, these more efficient structures disappear and rigidity only reappears at the higher value  $x_c$ . Between  $x_c$  and  $x_c(2)$ , the corner-sharing  $\text{Ge}(\text{Se}_{1/2})_4$  tetrahedra in the *isostatic* phase will reside mostly in unstressed local environments so that  $v_{\text{CS}}(x)$  will remain constant. At this point we recall that the calculations of Thorpe et al. [23] show that a majority of the atoms are in the backbone as soon as it is formed and that only a small number of added redundant bonds are required for converting the backbone structure to a stressed phase. Thus the change in  $v_{\text{CS}}$  at either  $x_c$  or  $x_c(2)$  is essentially discontinuous and, between these two concentrations, the photo-melted state will have redundant bonds with attendant stressed rigidity.

We conclude this section with two remarks. The present observations suggest that the microscopic origin of the giant photocontraction effects observed by K. L. Chopra et al. [9, 55] in thin-films of  $\text{GeSe}_2$  may actually represent photomelting of the columnar structure peculiar to the films deposited at high obliqueness angles. The films at high obliqueness angles are intrinsically phase separated on a molecular scale into Se-rich columns and Ge-rich intercolumnar material and the role of illumination is to cause an irreversible photomelting of the stress-free, optimally coordinated columns, as will be shown in a forthcoming publication [56].

The observation of photomelting of  $\text{As}_2\text{S}_3$  fibers by sub-bandgap (green) radiation reported by K. Tanaka appears to represent photomelting of the intermediate phase in As-S binary glasses. Compositional windows defining the *intermediate phase* in the group V chalcogenides shown that although the stoichiometric glass compositions  $\text{As}_2\text{Se}_3$  and  $\text{As}_2\text{S}_3$ , are not part of the intermediate phase, these are not sufficiently far removed from that phase, not to show photomelting effects completely.

## 6. Concluding remarks

The physical behavior of prototypical network glasses, examined systematically as a function of chemical composition, or mean coordination number  $\bar{r}$ , shows the existence of two compositions ( $\bar{r}_c(1)$ ,  $\bar{r}_c(2)$ ) across which the *elastic*, *thermal*, and *structural* behavior appears to display a threshold behavior. Raman scattering measurements show existence of elastic thresholds at  $\bar{r}_c(1)$  and  $\bar{r}_c(2)$  with distinct power-laws, which when analyzed in terms of numerical simulations in random- and self-organized network, reveal that glasses at low  $\bar{r}$  ( $\bar{r} < r_c(1)$ ), are *floppy*, in the *intermediate* composition interval ( $\bar{r}_c(1) < \bar{r} < \bar{r}_c(2)$ ) are *isostatically rigid*, and at high  $\bar{r}$  ( $\bar{r} > r_c(2)$ ) *stressed rigid*. T-modulated DSC measurements of the non-reversing heat flow term,  $\Delta H_{\text{nr}}(\bar{r})$ , show a global minimum in the  $\bar{r}_c(1) < \bar{r} < \bar{r}_c(2)$  interval with the heat flow term increasing by almost *an order of magnitude* in the *floppy-phase* ( $\bar{r} < \bar{r}_c(1)$ ) and in the *stressed rigid phase* ( $\bar{r} > \bar{r}_c(2)$ ). The activation energy of viscosity  $E_{\eta}^A(\bar{r})$  for corresponding liquids mimics compositional trends in  $\Delta H_{\text{nr}}(\bar{r})$  and shows a *global minimum* in the intermediate phase. Furthermore, T-dependence of viscosity for glass (liquid) compositions in the intermediate phase display an *Arrhenius behavior*, in sharp contrast to the non-Arrhenius behavior encountered in both the floppy- and stressed-rigid phases. Compositional trends in molar volumes,  $V_M(\bar{r})$  of glasses also reveal a global minimum [29] in the intermediate phase, suggesting that the underlying network structure are rather efficiently packed.

These experimental findings suggest that glasses in the intermediate phase consist of networks that are optimally constrained and self-organized, those in the floppy phase are underconstrained and entropically stressed while those in the stressed rigid-phase are mechanically overconstrained and enthalpically stressed.

The width ( $r_c(2) - r_c(1)$ ) and centroid ( $(r_c(1) + r_c(2))/2$ ) of the intermediate phase in  $\bar{r}$  space, observed in several chalcogenide and chalcogen halide glasses shows that these  $\bar{r}$  values are manifestations of structure at a *short-range* and at a *medium-range* distances. For the case of the chalcogen halide glass system,  $\text{Ge}_{0.25}\text{S}_{0.75-y}\text{I}_y$ , where the evolution of glass structure as a function of iodine content is found to be truly *stochastic*, the *width* of the intermediate phase *vanishes* and a *solitary* rigid to floppy transition is documented at a composition ( $y = y_c = 1/6$ ). The result is in excellent

agreement with mean-field constraint counting algorithms extended to include networks with dangling ends. In the case of this chalcogenide glass system, the stochastic evolution of glass structure precludes self-organization and opening of an intermediate phase. In return, the existence of intermediate phases with significant width  $r_c(2) - r_c(1)$  in binary and ternary chalcogenide glasses shows that the optimally constrained backbone displays substantial self-organization. And it is possible that the latter may consist of filamentary structural elements that are qualitatively decoupled from each other.

### Acknowledgements

One of us (PB) would like to thank M. Popescu for the invitation to participate in the 1st Amorphous and Nanocrystalline Chalcogenide Workshop held in Bucharest. Y. Wang, D. Selvanathan, W. J. Bresser and J. Wells assisted in the experiments described in this review. We have benefited with on-going discussions with J. C. Phillips, M. F. Thorpe, M. Micoulaut and K. A. Jackson in the course of this work. This work is supported by National Science Foundation grant DMR-01-01808.

### References

- [1] A. C. Angell in *Insulating and Semiconducting Glasses*, Ed. P. Boolchand, World Scientific Press, Inc., Singapore, 2000.
- [2] E. C. Weeks, J. R. Croker, A. C. Levitt, A. Schofield, D. A. Weitz, *Science* **287**, 627 (2000). Also see A.C. Wright in *Insulating and Semiconducting Glasses*, Ed. P. Boolchand, World Scientific Press, Inc., Singapore, p. 147, 2000.
- [3] P. Boolchand in *Insulating and Semiconducting Glasses*, Ed. P. Boolchand, World Scientific Press, Inc., Singapore, p. 191, 2000.
- [4] P. Boolchand, D. Selvanathan, Y. Wang, D. G. Georgiev, W. J. Bresser in *Properties and Applications of Amorphous Materials*, Ed. M. F. Thorpe, L. Tichy, Kluwer Academic Publishers, Dordrecht, p. 97, 2001.
- [5] Y. Wang, P. Boolchand, M. Micoulaut, *Europhysics Letters* **52**, 633 (2000).
- [6] D. Selvanathan, W. J. Bresser, P. Boolchand, *Phys. Rev.* **B61**, 15061 (2000). Also see *Solid State Commun.* **111**, 619 (1999).
- [7] Y. Wang, J. Wells, D. G. Georgiev, P. Boolchand, K. A. Jackson, M. Micoulaut, *Phys. Rev. Lett.* (in press).
- [8] H. Hisakuni, K. Tanaka, *Science* **270**, 974 (1995).
- [9] K. L. Chopra, K. S. Harshavardhan, S. Rajgopalan, L. K. Malhotra, *Solid State Commun.* **40**, 387 (1981).
- [10] C. A. Angell, K. L. Ngai, G. B. McKenna, P. F. McMillan, S. W. Marti, *Appl. Phys. Rev.* **88**, 3113 (2000).
- [11] J. C. Phillips, *J. Non Cryst. Solids* **34**, 153 (1979).
- [12] M. F. Thorpe, *J. Non Cryst. Solids* **57**, 355 (1983).
- [13] M. F. Thorpe, M. V. Chubynsky in *Properties and Applications of Amorphous Materials*, Ed. M. F. Thorpe, L. Tichy, Kluwer Academic Press, Dordrecht, p. 61, 2001.
- [14] H. He, M. F. Thorpe, *Phys. Rev. Lett.* **54**, 2107 (1985).
- [15] D. S. Franzblau, J. Tersoff, *Phys. Rev. Lett.* **68**, 2172 (1992).
- [16] X. W. Feng, W. J. Bresser, P. Boolchand, *Phys. Rev. Lett.* **78**, 4422 (1997).
- [17] M. Zhang, P. Boolchand, *Science* **266**, 1355 (1994).
- [18] R. L. Mozzi, B. E. Warren, *J. Appl. Crystallogr.*, **2**, 164 (1969).
- [19] J. C. Phillips, *Solid State Commun.*, **47**, 203 (1983).
- [20] M. Stevens, J. Grothaus, P. Boolchand, *Solid State Commun.*, **47**, 199 (1983).
- [21] P. Boolchand, M. F. Thorpe, *Phys. Rev.*, **B50**, 10366 (1994).
- [22] P. Boolchand, M. Zhang, B. Goodman, *Phys. Rev.*, **B53**, 11488 (1996).
- [23] M. F. Thorpe, D. J. Jacobs, M. V. Chubynsky, J. C. Phillips, *J. Non Cryst. Solids*, **266-269**, 872 (2000).



- [24] Y. Wang, M. Nakaravra, O. Matsuda, K. Murase, *J. Non Cryst. Solids*, **266-269**, 872 (2000).
- [25] Y. Vaills, Y. Luspain, G. Hauret, *Mat. Sci. Eng.*, **B40**, 199 (1996).
- [26] For Mössbauer Lamb-Mössbauer factors see: P. Boolchand, W. Bresser, M. Zhang, Y. Wu, J. Wells, R.N.ENZWEILER, *J. Non Cryst. Solids*, **182**, 143 (1995). For neutron scattering work see: W. A. Kamitakahara, R. L. Cappelletti, P. Boolchand et al. *Phys. Rev.*, **B44**, 94 (1991).
- [27] R. Bohmer, C. A. Angell, *Phys. Rev.*, **B45**, 1091 (1992).
- [28] U. Senapati, A. K. Varsheneya, *J. Non Cryst. Solids*, **185**, 289 (1995).
- [29] A. Feltz, H. Aust, A. Blayer, *J. Non Cryst. Solids*, **55**, 179 (1983). For work on other chalcogenides also see: S. Mahadevan, A. Giridhar, *J. Non Cryst. Solids*, **152**, 42 (1993).
- [30] S. Asokan, M. Y. N. Prasad, G. Parathasarthi et al. *Phys. Rev. Lett.*, **62**, 808 (1989).
- [31] R. A. Narayan, S. Asokan, A. Kumar, *Phys. Rev.*, **B63**, 092203.
- [32] T. Wagner, S. O. Kasap, K. Maeda, *J. Mat. Research*, **12**, 1892 (1997); also see Reprint #TA-210, T.A. Instruments, Inc., New Castle, Delaware.
- [33] D. G. Georgiev, M. Mitkova, P. Boolchand, H. Brunklaus, H. Eckert, M. Micoulaut, *Phys. Rev. B* (in press).
- [34] D. G. Georgiev, P. Boolchand, M. Micoulaut, *Phys. Rev.*, **B62**, R9228 (2000).
- [35] R. Kerner, M. Micoulaut, *J. Non Cryst. Solids*, **176**, 271 (1994).
- [36] D. Lathrop, H. Eckert, *J. Phys. Chem.*, **93**, 7895 (1989).
- [37] F. L. Galeener, *J. Non Cryst. Solids* **123**, 182 (1990).
- [38] G. Lucovsky, *Solid State Commun.*, **29** 571 (1979).
- [39] J. E. Griffiths, G. P. Espinosa, J. P. Remeika et al. *Phys. Rev.*, **B25**, 1272 (1982).
- [40] K. Murase, *Insulating and Semiconducting Glasses*, Ed. P. Boolchand, World Scientific Press, Inc., Singapore, 2000, p. 415.
- [41] P. Boolchand, X. W. Feng, W. J. Bresser, *J. Non Cryst. Solids* (in press).
- [42] J. T. Chayes, L. Chayes, D. S. Fisher et al. *Phys. Rev. Lett.* **57**, 2999 (1986).
- [43] M. Micoulaut, *Eur. Phys. J.*, **B1**, 277 (1998).
- [44] W. J. Bresser, P. Boolchand, P. Suranyi, *Phys. Rev. Lett.* **56**, 2493 (1986).
- [45] M. F. Thorpe, D. J. Jacobs, N. V. Chubynsky, A. J. Rader in *Rigidity Theory and Applications*, Ed. M. F. Thorpe and P. M. Duxbury, Kluwer Academic/Plenum Publishers, p. 39, 1999.
- [46] C. F. Mourkazel, P. M. Duxbury in *Rigidity Theory and Applications*, Ed. M. F. Thorpe and P. M. Duxbury, Kluwer Academic/Plenum Publishers, p. 69, 1999.
- [47] P. Boolchand in *Insulating and Semiconducting Glasses*, Ed. P. Boolchand, World Scientific Press, Inc., Singapore, p. 369, 2000.
- [48] For a recent review of the subject see, P.G. Debenedetti and F.H. Stillinger in *Nature*, **410**, 259 (2001).
- [49] C. A. Angell, *Science*, **267**, 1924 (1995).
- [50] S. V. Nemilov, G. T. Petrovckii, *Zh. Prikl. Khim.*, **36**, 977 (1963).
- [51] M. Mitkova, P. Boolchand, *J. Non Cryst. Solids*, **240**, 1 (1998).
- [52] S. A. Dembovsky, V. V. Kirilenko, Y. A. Buslaev, *Neorg. Mater.*, **7**, 328 (1971).
- [53] K. A. Jackson, A. Briley, S. Grossman, D. V. Porezag, M.R. Penderson, *Phys. Rev.*, **B60**, R14985 (1999).
- [54] S. Hosokawa, *J. Optoelectronics and Advanced Mat.*, **3**, 199 (2001) and references therein.
- [55] See S. Rajgopalan, B. Singh, P. K. Bhat, D. K. Pandya, K. L. Chopra, *J. Appl. Phys.*, **50**, 489 (1979).
- [56] P. Boolchand, W. J. Bresser, T. Rajgopalan, K. L. Chopra (unpublished).

## DYNAMICS OF Ge-Se GLASSES AT STIFFNESS TRANSITION

Y. Wang, T. Nakaokay<sup>a</sup>, K. Murase

Department of Physics, Graduate School of Science, Osaka University,  
1-1 Machikaneyama, Toyonaka, Osaka 560-0043, Japan

Present address:

<sup>a</sup>Institute of Industrial Science, University of Tokyo, 4-6-1 Komaba Meguro-ku, Tokyo  
153-8505, Japan

Using the Raman scattering technique, we have investigated the thermal relaxation processes at various ranges of temperature in  $\text{Ge}_x\text{Se}_{1-x}$  glasses. Below 100 K, the reason why the peak position of the  $A_1$  mode of  $\text{GeSe}_{4/2}$  tetrahedra shows a positive shift with temperature is that the network relaxes, caused by a thermal excitation of soft bending modes related to  $\text{Se}_n$  ( $n > 2$ ) chain structures. This strengthens the remaining stretching modes. For rigid glasses (of average coordination number,  $\langle r \rangle > 2.4$ , or  $x > 0.20$ ), few  $\text{Se}_n$  ( $n > 2$ ) units contained in the structure result in well mixed local vibrational modes. At the stiffness transition, the changes in peak positions with temperature in 100-300 K are the same, although the local modes differ markedly in frequency. In the temperature range 300-750 K including the glass transition temperatures ( $T_g$ ), relaxational modes, quasi-elastic contributions in the low-frequency region of 10-80  $\text{cm}^{-1}$ , appear around the  $T_g$  only in the floppy ( $x \leq 0.20$ ) glasses, but it is undetectable in the rigid glasses ( $x \geq 0.23$ ). We confirm that the quasielastic contribution originates from the fast ( $\beta$ ) process of relaxation. The compositional dependence of the quasielastic intensity is well explained by the constraint counting theory under the assumption that the origin of the relaxational modes is from the floppy modes. We attribute the relaxation modes mainly to the damping or jumping motions of the rotating  $\text{Se}_n$  segments, which could be regarded as the microscopic picture of the floppy modes in the Se-contained network glasses.

(Received July 16, 2001; accepted September 11, 2001)

**Keywords:** Chalcogenide glass, Dynamics, Raman scattering, Stiffness transition

### 1. Introduction

The covalent network glass system Ge-Se has been well studied and analyzed in terms of structural theories [1-13]. The mean-field constraint theory [1-4] for network glasses is proving to be useful in explaining many anomalous behavior around the critical composition of the rigidity transition threshold at an average coordination number,  $\langle r \rangle = 2.4$ , corresponding to  $x = 0.20$  for  $\text{Ge}_x\text{Se}_{1-x}$  [5-13]. Short- and medium-range order in  $\text{Ge}_x\text{Se}_{1-x}$  glasses can be varied continuously to form both the floppy and rigid glass structures in the sense of the constraint theory, since, in the composition range  $0.00 \leq x \leq 0.40$ , the coordination numbers of Ge and Se are 4 and 2, respectively. According to the theory, the character of the network glass undergoes a qualitative change from being easily deformable at  $\langle r \rangle < 2.4$  to being rigid at  $\langle r \rangle > 2.4$ .

Kamitakahara et al. [7] reported the dynamic density of state around 5 meV and showed the existence of the floppy mode ("zero-frequency" mode in floppy glass) by studying the inelastic neutron spectra of chalcogenide glasses. Recently, Boolchand et al. [11] demonstrated that the results from Raman scattering, modulated differential scanning calorimetry, molar volumes and Mössbauer spectroscopy work provide evidence of a multiplicity of stiffness transitions, an onset point near  $\langle r \rangle_{(1)} = 2.40$  and a completion point near  $\langle r \rangle_{(2)} = 2.46$ . We discuss the properties of bond-stretching, -bending and -rotating modes by studying the temperature dependence of optical bands, since the structural units relative to the bands are individually influenced by the nearby connectivity of the network. A microscopic structural explanation of the floppy mode is proposed as the damping or jumping motions of the rotating  $\text{Se}_n$  ( $n > 2$ ) segments. The criticality of the stiffness transition

observed by Raman scattering is discussed from the point of view of a structural admixture of  $\text{Se}_n$  and  $\text{GeSe}_{4/2}$  units.

The Dynamics of the glasses at the stiffness transitions is this review's subject that also contains the structural relaxations at glass transition temperature,  $T_g$ . The physical origin of a fast  $\beta$  process in glass material and its possible connection to the  $\alpha$  relaxation are questions that are at present completely unclear. The structural relaxations around  $T_g$  are subjects of increasing interest in connection with the poorly understood glass transition phenomenon. It has been probed by infrared hole burning at cryogenic temperatures that topological effects rather than chemical ones must be considered to explain the energetic relaxations among glassy configurations in Ge-As-Se chalcogenides [14]. The relevance of the concept of  $\langle r \rangle$  has also been explored in the liquid state [15 - 17]. These studies of ternary chalcogenide alloys have provided evidence for a correlation between the rigidity percolation and the departure from Arrhenius behavior, i.e., the fragility. However, it remains unclear whether another key aspect of the glass transition, viz., the structural relaxation also shows a systematic composition dependence. We discuss the structural relaxations at  $T_g$  through the investigation of temperature dependence of quasielastic contribution appearing in  $10\text{-}80\text{ cm}^{-1}$  in terms of network connectivity. A sharpness of the transition, a first-order-like transition, of the relaxational dynamics from floppy to rigid is understood in terms of self-organization concept.

## 2. Experimental

The constraints per atom of Ge-Se glasses are varied by changing the Ge composition, because few dangling bonds are formed in samples obtained by conventional quenching method.  $\text{Ge}_x\text{Se}_{1-x}$  glasses were prepared from high purity Ge (99.9999%) and Se (99.999%) elements which were etched in CP4 (a solution of  $\text{HNO}_3$ , HF, and  $\text{CH}_3\text{COOH}$  in a volume ratio 8:10:5) and a KOH water solution, respectively. The etched elements were sealed in an evacuated ( $\sim 10^{-6}$  Torr) silica ampoule in a desired molar ratio. The ampoule was slowly heated up to  $960^\circ\text{C}$  (for Se glass up to  $400^\circ\text{C}$ ) in a rocking furnace and the melts were homogenized for at least 24 hours. Then, they were equilibrated at about  $150^\circ\text{C}$  above the liquidus for an additional 24 hours before quenching in iced water. All the measured samples, with  $\langle r \rangle = 2.00\text{-}2.70$  ( $x = 0\text{-}0.35$ ), are picked from the as-prepared broken pieces with a typical dimension of  $5 \times 5 \times 1\text{ mm}$ .

In noncrystalline materials, Raman scattering processes are allowed to occur from essentially all the vibrational modes of the material. Usually the intensity  $I(\omega)$  of scattered light is proportional to the vibrational density of states (VDOS),  $g(\omega)$ . The experimental setup for Raman scattering is shown in Fig. 1. Raman scattering was measured in a backscattering configuration, excited by a DCM dye laser (1.83 eV) pumped by an  $\text{Ar}^+$  ion laser (Spectra-Physics Stabilite 2017). At the excitation energy or lower, resonant Raman effect is negligible. For avoiding light-induced events and restricting the sample temperature difference from the environment to less than  $3^\circ\text{C}$ , excitation light was focused onto a rectangular region of about  $2 \times 0.2\text{ mm}^2$  (line-focusing) with a low-power density less than  $3\text{ W/cm}^2$ .

The back-scattered light is collected and analyzed with a triple grating polychromator (JOBIN YVON T64000) and CCD detector in polarized and depolarized configurations. The samples were sealed in a silica tube in an argon gas atmosphere ( $\sim 360$  Torr) to avoid oxidation, and they were heated stepwise in an electric furnace. The temperature during the accumulation for each spectrum was fixed within  $\pm 1^\circ\text{C}$ . The heating rate between the successive measured temperatures was about  $3^\circ\text{C/min}$ . During the accumulation, 10 minutes or less for each spectrum, no change was observed in the spectra below  $T_g$ , and the changes were very small even above  $T_g$  except at the crystallization temperature. A temperature-programmed cryostat (Oxford optistat) is employed for the low-temperature measurements. The glass transition temperature was measured by using a Perkin-Elmer model DSC-7 differential scanning calorimeter at a heating rate of  $10^\circ\text{C/min}$ .

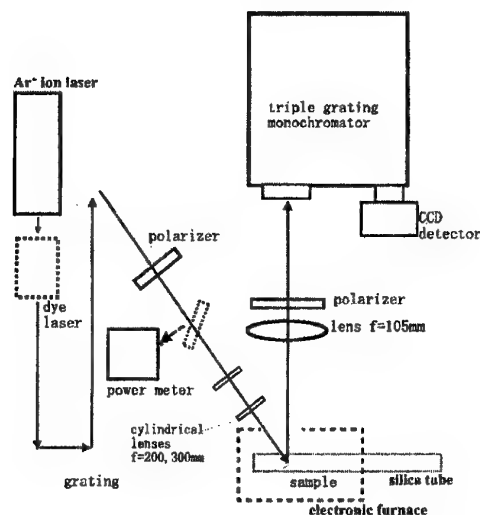


Fig. 1. Experimental setup for the high temperature Raman scattering measurement.

### 3. Results and discussion

#### 3.1 Temperature dependence of Raman spectra

Stokes Raman spectra of  $\text{Ge}_x\text{Se}_{1-x}$  glasses for various composition at 80 K are shown in Fig. 2. In this paper, Raman spectra are reduced by  $[n(\omega) + 1]$  and normalized to the maximum intensity, which for low Ge concentration is the peak at  $255 \text{ cm}^{-1}$  or at  $200 \text{ cm}^{-1}$  for high Ge concentration. In g-Se, the dominant peak at  $255 \text{ cm}^{-1}$  and a shoulder at the lower frequency side are relevant to the bond-stretching modes of  $\text{Se}_n$  chains [18]. The weight of Se-chains related intensity decreases with increasing Ge concentration, which qualitatively reflects the changes in the vibrational density of states. It follows that the number of  $\text{GeSe}_{4/2}$  tetrahedra increases with increasing Ge content. A strong peak at lower or a weak one at higher energy side in the vicinity of  $200 \text{ cm}^{-1}$  is associated with the breathing mode of  $\text{GeSe}_{4/2}$  tetrahedra which are connected by sharing corners or edges, respectively [19]. It should be noted that even in the glass of Ge content of 8 percents a small amount of tetrahedra shares edges. For  $\text{GeSe}_2$  and  $\text{Ge}_{35}\text{Se}_{65}$ , the Ge-Ge bond related band at  $180 \text{ cm}^{-1}$  increases with Ge content. In  $\text{GeSe}_2$  glass, the Ge-Ge and Se-Se "wrong bonds" are assumed to release the exceeding tension or stress in the highly distorted network, since its mean coordination number  $\langle r \rangle$  is 2.67. And the Se-Se vibrational bands are observed at  $260 \text{ cm}^{-1}$  with the resonant Raman condition. Further discussion on the Ge-Ge and Se-Se "wrong" bonds in  $\text{GeSe}_2$  glass will be done elsewhere [20].

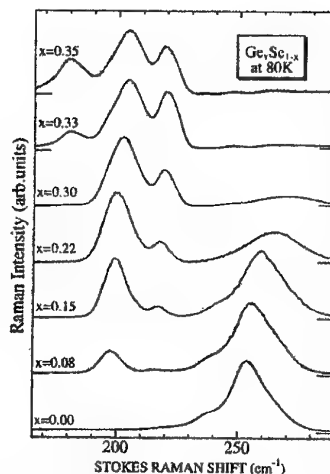


Fig. 2. Polarized Raman spectra for  $\text{Ge}_x\text{Se}_{1-x}$  at 80 K. The resolution of the spectra is better than  $1 \text{ cm}^{-1}$ .

In  $\text{Ge}_x\text{Se}_{1-x}$  glasses, the basic structural units are  $\text{Se}_n$  chains and  $\text{GeSe}_{4/2}$  tetrahedra. The former are floppy units that build floppy regions in the network; the latter are rigid units that construct rigid ones. Studying the temperature dependence of vibrational properties of Se-Se or Ge-Se bond for each unit will supply crucial information on the microstructure of the network. Fig. 3 shows Raman spectra for  $\text{Ge}_8\text{Se}_{92}$  glass from 20 K to room temperature. The spectrum at the successive higher temperature is plotted with the base line raised by the same value. To take systematic analyses, the line shape of the spectra in the range of 160–300  $\text{cm}^{-1}$  is fitted by one straight line and four Gaussian curves, corresponding to two breathing modes of  $\text{GeSe}_{4/2}$  tetrahedra and two Se-chain related modes.

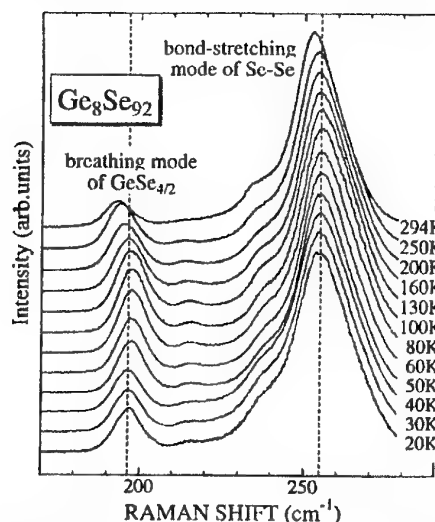


Fig. 3. Raman spectra for  $\text{Ge}_8\text{Se}_{92}$  glass at various temperatures. The spectra are obtained in a T-increasing sequence.

Here, we focus on temperature dependence of peak positions of  $\text{GeSe}_{4/2}$  breathing mode,  $A_1$ , at 200  $\text{cm}^{-1}$  and Se-Se bond-stretching mode at 255  $\text{cm}^{-1}$ , as shown in Figs. 4 (a) and (b). In the floppy glass of  $\text{Ge}_8\text{Se}_{92}$ , an anomalous peak shift of the  $A_1$  mode, a positive shift with temperature, is observed below 100 K. This anomalous feature is hard understood without introducing a structural change at very low temperature.

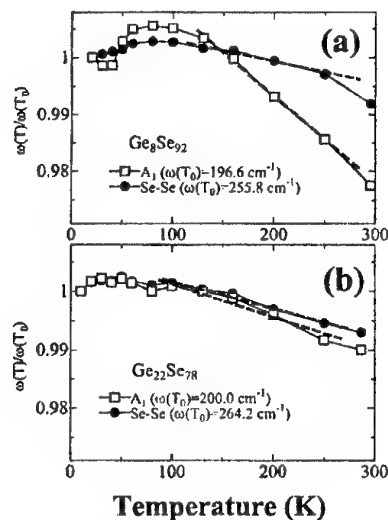


Fig. 4. The temperature dependence of the  $A_1$  breathing mode of tetrahedra and the Se-Se bond-stretching mode. Both are scaled by the frequency of each mode at the lowest temperature we measured. (a) displays the typical case in floppy glasses and (b) the rigid glasses.

As we cool the glass down to 20 K (well below the  $T_g$ 's), each structural unit freezes at either critical temperature below which the unit is forbidden to change its topology in the network. In Ge-Se network, first the  $\text{GeSe}_{4/2}$ -unit rich region freezes, and at this time they might not be constraint or stressed. If all the atoms vibrate in limited spaces caused by the constraction of volume with decreasing temperature, a large number of stress or tension then should be induced since the glassy sample is not an ideal glass. Appending such stress or tension on the local structural units of  $\text{GeSe}_{4/2}$  tetrahedra and  $\text{Se}_n$  chains, the structure of each unit must be distorted more or less (we can not expect an isotropic force in the microscopic region, though it is in a glass). The decrease in frequency of the  $A_1$  mode during the cooling process suggests that the tetrahedra should depart from their regular structure under the anisotropic stress or tension. The similar stress or tension should influence the Se-chain structure too. The reason why the Se-Se bond-stretching mode shows less temperature dependence than the  $A_1$  mode does is probably because of the bending force of Se-Se bond much weaker than its stretching one. Most of the distortion in the  $\text{Se}_n$  ( $n > 2$ ) chains can cause a wide distribution of Se-Se-Se bond angle that makes the Se-Se bending mode broad as well. At present, however, it is unfortunate that we can only measure the "rest" stretching mode of Se-Se bond. In  $\text{Ge}_8\text{Se}_{92}$  glass,  $\text{Se}_n$  chains are the dominant structural units and  $\text{GeSe}_{4/2}$  tetrahedra are probably isolated from each other. The structural units of  $\text{Se}_n$  ( $n > 2$ ) chains, as shown in Fig. 5, are assumed as the key units for the heavily distorted tetrahedra "relaxing" to the regular structure. We suppose that the rotating motion of Se(2) atom on the axis through the Se(1) and Se(3) atoms will completely freeze at 20 K. For the Se(3) atom, if there is a Se(4) atom next to it, the same discussion as for the Se(2) atom holds. With increasing temperature, the rotating mode of Se(2) atom could be thermally excited, since the relative force determined by the structure, consisting of two priori free dihedral angles, is fairly weak. Such thermally excited rotating motion supplies channels to leak the stress or tension by the way of changing the topology of network. The heavily distorted network then relaxes and make the "remaining" (or observed)  $A_1$  mode strengthened. When temperature is approaching to 100 K, the rotating modes is totally excited, and thereafter the vibrational peaks start to shift in negative behavior due to anharmonic effects.

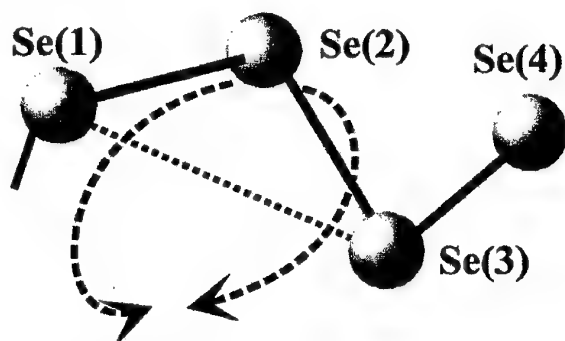


Fig. 5. Schematic diagram for atom arrangements of  $\text{Se}_n$  chains. The Se(2) atom rotates on the axis through the Se(1) and Se(3) atoms. The rotating motion is constrained by two prior free dihedral angles consisting of the next nearest neighbor forces. The same rotating mode for the Se(3) exists with the Se(4) bonding to it.

In our measured samples, the most remarkable positive shift of the  $A_1$  mode occurs in the  $\text{Ge}_8\text{Se}_{92}$ . For  $x < 0.08$ , although the positive shift (with the same origin) is expected, it might be difficult to figure them up strictly because of a smaller population of tetrahedra to form the vibrational density of states, which brings big errors in fitting the line shape of  $A_1$  mode. The network could settle the stress or tension through the large floppy region consisting of  $\text{Se}_n$  chains surrounding the  $\text{GeSe}_{4/2}$ -rich region. While for  $\text{Ge}_{15}\text{Se}_{85}$ , the floppy region that surrounds the rigid region of  $\text{GeSe}_{4/2}$  units is not large enough to provide space for the distorted tetrahedra "relaxing". Nevertheless, we consider the rotating mode in Fig. 5 to be a probable microstructural explanation for the floppy modes in Se-contained covalent network glasses. The same kind of rotating modes has been discussed in the computing analysis for modeling the flexible and rigid regions in proteins [12]. The easy excited dihedral angles that free the rotating motion of Se(2) and Se(3) in Fig. 5 is assumed as the bananas graphs proposed by Thrope et al. [4]. The soft constraint rotating modes (anyway glass is solid) could be regarded as the floppy modes in a realistic floppy glasses. Most of properties of covalent glasses

are discussed at room temperature or higher, at which such "constraint" (at low temperature) floppy modes are totally free. That is why the elegant constraint theory works so well [5-13], although the theory settles the problem of networks at 0 K.

With increasing  $x$ , the floppy glass is approaching to the rigidity percolation threshold of  $\langle r \rangle = 2.4$  ( $x = 0.20$ ). The stiffness transition behavior clearly appears in the temperature dependence of the vibrational modes between 100 K and room temperature where the anharmonic effects determine the essential rules. As shown in Fig. 4, large drops of the shifts for both the  $A_1$  mode and the Se-Se mode at room temperature are observed in the floppy glasses. The room temperature is the temperature to which the samples were quenched (it should be 0 °C for an accurate discussion), and at which they rested for a long time. Between 100 K and 250 K, we can draw straight lines through the data for both of the two modes and get well linear fits. The slopes of lines as a function of  $x$  and mean coordination number  $\langle r \rangle$  for both the  $A_1$  mode and the Se-Se mode are plotted in Fig. 6. A nice convergence of the slopes, like the shifts themselves, comes to a common value at  $x = 0.22$ . This is the stiffness transition at which the number of degrees of freedom is equal to the number of constraints [11]. Apparently, all the observed modes shift together at this transition, because the network becomes almost ideally random to realize a maximum mixing of the different local modes.

For the rigid glasses, the fact that few  $\text{Se}_n$  ( $n > 2$ ) units are included in the structure is the reason of admixture of all the local modes. Probably the same mixing of Se-Se bending motion goes into both the  $A_1$  and Se-Se stretching modes. So although the local modes of the  $A_1$  breathing and the Se-Se stretching have different frequencies, 200  $\text{cm}^{-1}$  and 255  $\text{cm}^{-1}$ , respectively, the changes in those frequencies (scaled by their frequency at the lowest measured temperature) become the same. This kind of mixing should occur in a long-range scale and well detected by the light-probe technique.

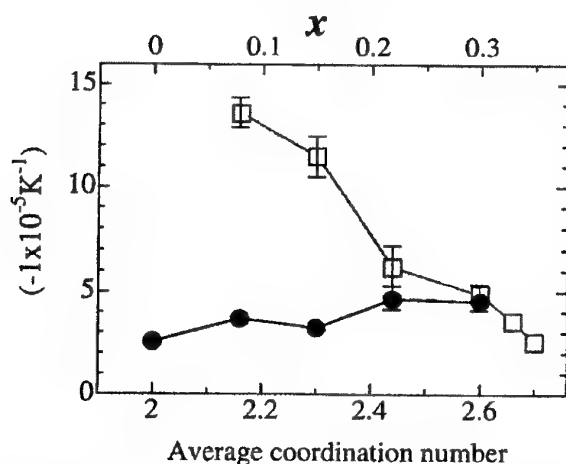


Fig. 6. The slope of straight line obtained from the data of each modes in the temperature range of 100-250 K. The  $A_1$  mode ( $\square$ ) has a fourth time large of the volume obtained from the Se-Se stretching mode ( $\bullet$ ) for  $\langle r \rangle < 2.4$ . While for  $\langle r \rangle > 2.4$ , they are similar. The lines are guide to the eye.

For the floppy glasses, the  $A_1$  mode shifts much more than the Se-Se bond-stretching mode does. The probable reason is that the mixing of Se-Se bending motion into the bending of Se-Ge-Se permits all the bending modes mixing in the floppy glasses. In other words, the  $A_1$  band is not a pure breathing mode because of the admixture of bending modes. Thus, the Se-Se stretching mode shows less temperature dependence than the  $A_1$  one in which the soft bending modes are mixed.

### 3.2 Low-frequency spectra

Generally, low-frequency Raman spectra of glasses and supercooled liquids usually contain two contributions: relaxational (overdamped) and vibrational ones. Below  $T_g$ , the spectra are dominated by vibrational contributions termed the boson peak (BP). The Raman intensity  $I(\omega)$  of the vibrational part varies according to the Bose factor  $n(\omega)$ , i.e.,  $I(\omega) \propto n(\omega) + 1$  in many glasses [21,22].

The relaxational part of the dynamical structure factor varies with temperature more strongly than the Bose factor, and it becomes virtually dominating at temperatures higher than  $T_g$  [23-25]. As an example, we show the Stokes Raman spectra of  $\text{Ge}_{10}\text{Se}_{90}$  in Fig. 7. The Raman spectra are normalized, for convenience, by the integrated intensity of optical modes between  $170\text{ cm}^{-1}$  and  $330\text{ cm}^{-1}$ , including the  $A_1$  mode of CST around  $195\text{ cm}^{-1}$ , the breathing mode of EST around  $211\text{ cm}^{-1}$ , and the stretching mode of Se-Se bonds around  $255\text{ cm}^{-1}$  [6,19]. The following discussion does not significantly effected by the normalization way; we focus on only the line-shape of the low-frequency spectra. At  $30^\circ\text{C}$  (the room temperature), the low-frequency spectra are dominated by a strong BP around  $20\text{ cm}^{-1}$ . Since the Raman spectra are reduced by the temperature factor  $[n(\omega, T)+1]/\omega$ , the BP intensity should be independent of temperature. At  $150^\circ\text{C}$  a quasielastic contribution arising from relaxational modes is superposed on the BP. The inset in Fig. 7 shows the depolarization ratio, defined as a ratio of the scattered intensity with propagation of the electric field parallel to the scattering plane ( $I_{\text{VH}}$ ) to the corresponding vertical one ( $I_{\text{VV}}$ ). No sudden drop with decreasing the frequency to zero both at room temperature and above  $T_g$  confirms no Rayleigh line contribution in the low-frequency spectra.

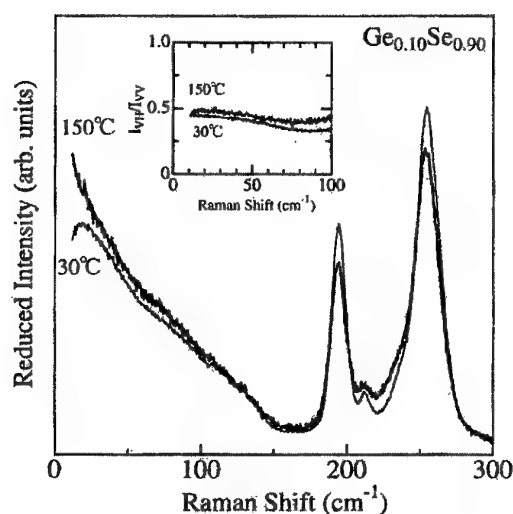


Fig. 7. Raman spectra of  $\text{Ge}_{0.10}\text{Se}_{0.90}$  glass at room temperature and above the glass transition temperature ( $T_g = 100^\circ\text{C}$ ) in VV polarization configuration. The inset shows the depolarization ratio ( $I_{\text{VH}}/I_{\text{VV}}$ ).

We inquire the composition dependence of the relaxational mode. Fig. 8 shows the normalized and reduced low-frequency Raman spectra of  $\text{Ge}_x\text{Se}_{1-x}$  glasses in the composition range ( $0.07 \leq x \leq 0.35$ ) covering the rigidity transition ( $x = 0.20$ ). At room temperature, the low-frequency spectra are dominated by the BP around  $20\text{ cm}^{-1}$  in all the glasses. Around  $T_g$  quasielastic contribution resulting from relaxational modes appears in the "floppy" glasses ( $x \leq 0.20$ ), and it grows with temperature. The appearance of the relaxational modes in the threshold composition ( $x = 0.20$ ) is due to breaking parts of the bond-bending constraint from Se atoms [9]. We regard the  $\text{Ge}_{20}\text{Se}_{80}$  glass as floppy ones in the following discussion as well. On the other hand, the strong quasielastic contribution is not detected in the rigid glasses ( $x \geq 0.23$ ) even above  $T_g$ . On the contrary to the floppy glasses, the intensity around the BP decreases with temperature. Such a decrease is related to structural changes occurring in rigid glasses, as we will discuss elsewhere [26]. Thus, it is found that the dynamics around  $T_g$  is distinctly different between the floppy glasses and rigid ones.

### 3.3 Relaxational modes

Mainly, two approaches to fit the low-frequency Raman data have been suggested, where the quasielastic (QE) and BP contributions are represented either as a convolution or as a superposition.



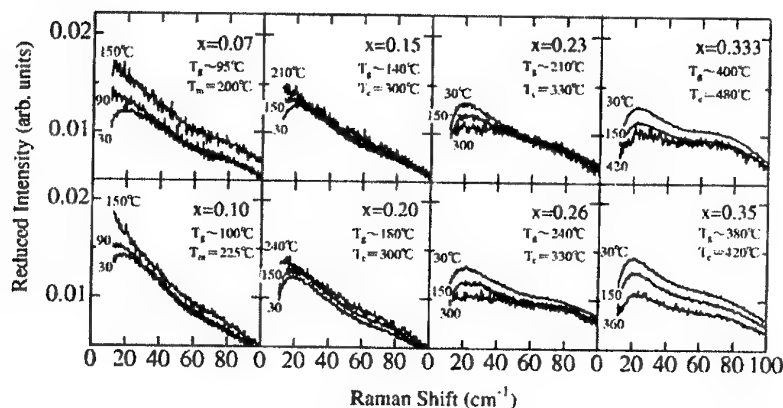


Fig. 8. Temperature dependences of the low-frequency Raman spectra of  $\text{Ge}_x\text{Se}_{1-x}$  in VV configuration. The spectra are reduced by the temperature factor  $[n(\omega, T) + 1]/\omega$ , and normalized to the integrated intensity of the optic modes ( $170\text{--}330\text{ cm}^{-1}$ ).

The first approach, or the convolution model, relies on ideas originated from the “in-direct” scattering mechanism of Winterling [27], where it is assumed that the QE line represents a low-frequency relaxation like part of the one phonon response function. In other words, the vibrational excitations are coupled to some relaxing variable that induces broadening to each frequency of the BP [28]. This way of interpretation of low-frequency Raman spectra has been essentially based on the following three putative similarities between the QE and the BP contributions. (i) The depolarization ratio is strictly constant, e.g., independent of the frequency in the whole region of both the QE line and the BP since the QE line is caused by the BP vibration. This constancy is not hold good in some glasses [29]. The  $\text{Ge}_x\text{Se}_{1-x}$  system is one of them. The depolarization ratio in that frequency region is not constant as shown in Fig. 9. (ii) There is a correlation between the strength of the fast dynamics described by the relative strength of the QE scattering and the BP [25] and the fragility (a dynamic character of an amorphous material). However, it has recently been shown that the correlation is not completely systematic [29]. (iii) The phonon-photon coupling coefficient  $C(\omega)$  is constant in the frequency range from the QE line ( $\sim 0\text{ cm}^{-1}$ ) up to the BP maximum frequency ( $\sim 20\text{ cm}^{-1}$ ). Recent experimental determinations of the phonon-photon coupling coefficient, through the comparison of neutron and Raman-scattering data, have shown that the statement (iii) does not definitely hold [30]. Thus, the aforementioned statements, which are used as the stronger evidence in favor of the convolution model, are based on incomplete informations. From the above argumentation we will employ the second approach, or the superposition model, in the subsequent analysis.

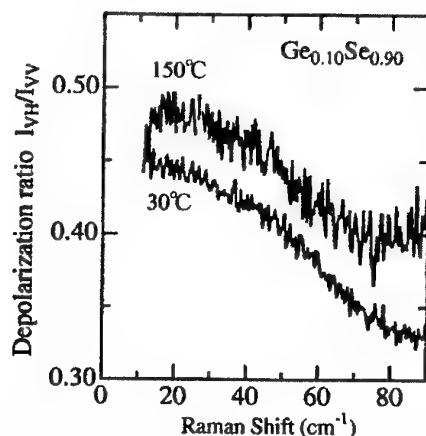


Fig. 9. xpanded view of depolarization ratio of  $\text{Ge}_{0.10}\text{Se}_{0.90}$  glass.

In the superposition model, the spectrum is modeled [31] as a sum of two separate contributions: QE contribution described by a Lorentzian line and the BP contribution. We assume a very small QE contribution at room temperature and a temperature-independence of the BP intensity

in floppy glasses. These assumptions enable us to extract QE contribution by subtracting the spectrum at room temperature from those at high temperatures:  $I^{qe}(T) = I^{exp}(T) - I_{BP}(30^\circ\text{C})$ , where  $I^{exp}(T)$  and  $I_{BP}(30^\circ\text{C})$  are the experimentally measured intensities reduced by the Bose factor at  $T(^{\circ}\text{C})$  and  $30^\circ\text{C}$ , respectively. Although the extraction from the lower temperature spectrum ( $< 30^\circ\text{C}$ ) might be better, photoexcited carriers having the longer decay times at lower temperatures affect the spectrum more effectively in the Ge-Se system.

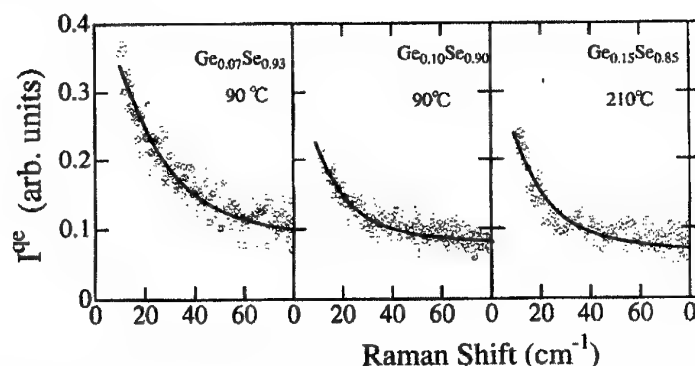


Fig. 10. Representative sets of extracted quasielastic spectra of  $\text{Ge}_x\text{Se}_{1-x}$  glasses, subtracted by BP. Each spectrum is well fitted by a single Lorentzian function (solid line).

Fig. 10 shows the extracted QE contribution ( $10\text{--}80\text{ cm}^{-1}$ ) being well fitted by a Lorentzian function:

$$I^{qe} = I_0^{qe}(\Gamma/2\pi)/[\omega^2 + (\Gamma/2)^2], \quad (1)$$

where  $I_0^{qe}$  is the QE intensity and  $\Gamma$  is the damping rate. The resulting fit-parameters,  $I_0^{qe}$  and  $\Gamma$  are presented in Fig. 11. In all the floppy glasses, the QE intensity  $I_0^{qe}$  increases with temperature. At  $T_g$ , the QE intensity progressively increases with increasing Se content. The structural units involving Se atoms should play an important role on the relaxational motions. The damping rate  $\Gamma$  is nearly independent of both temperature and composition. The temperature independence supports that the QE contribution originates from the fast ( $\beta$ ) process of relaxation. From the inverse of the average damping rate, we can estimate the corresponding relaxation time in a first approximation. The estimated time of about 0.8 psec is consistent with the result of neutron spin echo measurement for amorphous Se. The fast relaxation time obtained by the measurement has been much shorter than 2 psec [32]. The composition independence of the relaxation time demonstrates that the relaxation mechanism itself does not change significantly with composition. Now we explore a quantity that corresponds to the QE intensity,  $I^{qe}$ , in the dynamical glass transition theory. One of the essential quantities to discuss the glass transition is the density-density correlation function  $F(t)$ . The function has been calculated by the mode coupling theory (MCT) [33] and molecular dynamics simulation [34] in some glasses.  $F(t)$  can be experimentally obtained by neutron spin-echo experiments [32,35] and inelastic neutron scattering [36-39] as well.

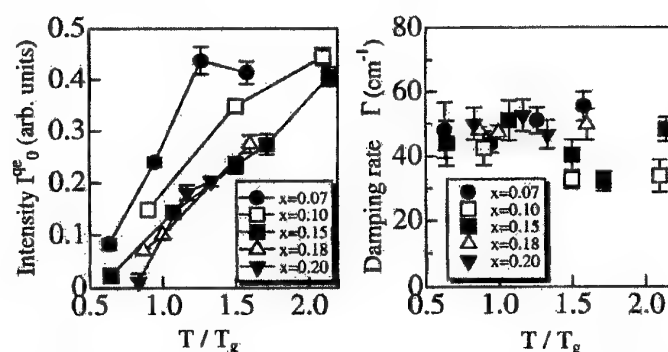


Fig. 11. Quasielastic intensity  $I_0^{qe}$  and damping rate  $\Gamma$  obtained by a Lorentzian fit to the low-frequency spectra ( $10\text{--}80\text{ cm}^{-1}$ ) of floppy  $\text{Ge}_x\text{Se}_{1-x}$  glasses. Temperature is normalized to  $T_g$ .

Fig. 12 shows the schematic view of a typical shape of  $F(t)$  curves at various temperatures. Each curve consists of a slow relaxation component ( $\alpha$  relaxation) and a fast relaxation component ( $\beta$  relaxation). Historically, the slow component has been described by the empirical Kohlrausch-Williams-Watts formula [40]:

$$F(t) = f_0 \exp(-t / \tau_{\text{slow}})^\beta, \quad (2)$$

where  $\tau_{\text{slow}}$  is the characteristic slow relaxation time,  $\beta$  is the Kohlrausch stretch exponent typically ranging between 0.3 and 0.9 for structural glasses, and  $f_0$  is the extrapolation to  $t = 0$  of the slow relaxation component. The complement of  $f_0$ , namely,  $1 - f_0$ , is the relative "weight" of the fast relaxing part of the correlation function. The weight increases from a finite value at  $T_g$  to 1 far above  $T_g$  without a large change of the fast relaxation time. One notices that the quantity  $1 - f_0$  behaves like  $I_0^{qe}$ . The density fluctuations can induce susceptibility fluctuations. Since the Fourier transformation of the space-time correlation function of the susceptibility fluctuations is generally proportional to the Raman scattering intensity, the fast relaxing weight of  $1 - f_0$  should qualitatively reflect in the QE intensity  $I_0^{qe}$ . The weights of the fast and slow components correspond to the number of the degrees of freedom of atomic motions relaxing fast and slow, respectively. The QE intensity increasing with temperature will be due to the increase of the fast relaxing degrees of freedom.

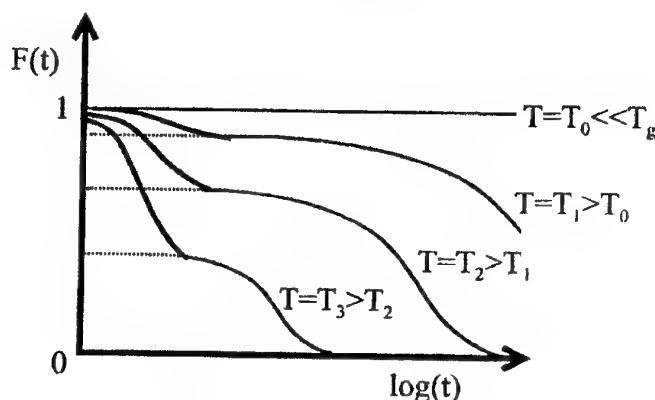


Fig. 12. Schematic view of the time-dependent density-density correlation function  $F(t)$  shown in a semilogarithmic plot.  $F(t)$  is normalized to  $F(0) = 1$ . Each curve consists of a fast relaxation (thick solid line) and a slow relaxation component (thin solid line).

We now identify the structural units mainly responsible to the relaxational motions. The QE intensity at  $T_g$  decreases with increasing Ge content  $x$ . The relaxational modes do not appear at and above  $x = 0.23$ . The threshold composition is close to the rigidity transition threshold of  $\langle r_c \rangle = 2.4$ .

By considering a Kirkwood-Keating type of potential [41,42], the floppy networks, in which the number of degrees of freedom per atom (that is 3 in a three dimensional space) is larger than the number of constraint per atom, have low-frequency (ideally, zero-frequency) floppy modes [3, 43]. The fraction of floppy modes available in a network is  $f = 2 - (5 \langle r \rangle / 6)$ ; the fraction decreases to zero at  $\langle r_c \rangle$  with increasing  $\langle r \rangle$ . The composition dependence of the floppy modes is very similar to that of the QE intensity. Thus, one arrives at the following picture; a part of the motions in the floppy modes causes relaxational (damping or jumping) motions around and above  $T_g$ , which couple with light to result in the QE scattering. In other words, the number of relaxing degrees of freedom in the floppy modes corresponds to the weight of the fast relaxing component.

In Ge-Se system, the rotating motion of the  $\text{Se}_n$  ( $n > 2$ ) segments, as shown in Fig. 13, has been proposed as the probable microstructural explanation for the floppy modes [44,45]. The segments have locally larger degrees of freedom than the number of constraints. This kind of rotating modes has been discussed in computer simulations for modeling the flexible and rigid regions in the Se-containing network glasses and proteins [4,12]. We propose that the  $\text{Se}_n$  segments cause the

relaxational motions involving damping or jumping motions around and above  $T_g$ . Such motions of the  $\text{Se}_n$  segments should play an essential role on the relaxational modes.

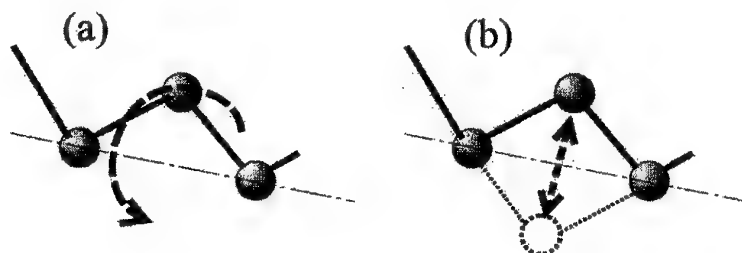


Fig. 13. Schematic view for atomic arrangements of  $\text{Se}_n$  segments ( $n = 3$ ) having rotational degrees of freedom. The damping (a) and / or the jumping (b) motions of the segments are proposed for the dominant motions contributing to the QE scattering.

Next we discuss an interesting connection of the increase of the QE intensity with the free volume model [46]. The free volume model is one of the conventional theoretical approaches for the liquid-glass transition, which can successfully describe the change of viscosity as well as the thermodynamic quantities, specific heat and thermal expansion at the liquid-glass transition. According to the theory, a glass-forming system consists of solid-like and liquid-like cells. When the temperature increases, the fraction of the liquid-like cells  $p$  increases. When  $p$  is larger than a percolation threshold  $p_c$ , there is an infinite, connected, liquid-like cluster and the material turns into the liquid state. When  $p$  is less than  $p_c$ , it lies in the glass state. Thus, the liquid-glass transition is treated as the percolation of the liquid-like cells. On the other hand, the rigidity transition is also treated as a percolation problem [3]; in floppy networks, floppy units percolate while rigid units do not, as shown in Fig. 14. We assume that, with increasing temperature, the floppy units become the liquid-like cells in which the atomic motions relax or damp. Since the floppy units percolate in floppy glasses, it follows that the liquid-like cells percolate around  $T_g$ . The percolation of the liquid units arising from the floppy units should achieve the strong QE line in our spectral range. We suppose that both of the increases of fast relaxing degrees of freedom and the number of the liquid-like units with temperature lead to the increase of the QE intensity. On the other hand, in our spectral range, the QE contribution is hardly observed in rigid glasses. This will be due to no "remaining" degrees of freedom in rigid units according to constraint counting theory; the number of constraints is larger than that of degrees of freedom. Then, even though the rigid units can become liquid-like cells, the relaxational motions of the liquid-like rigid units will be quite different with floppy ones; the characteristic time may be beyond our spectral range.

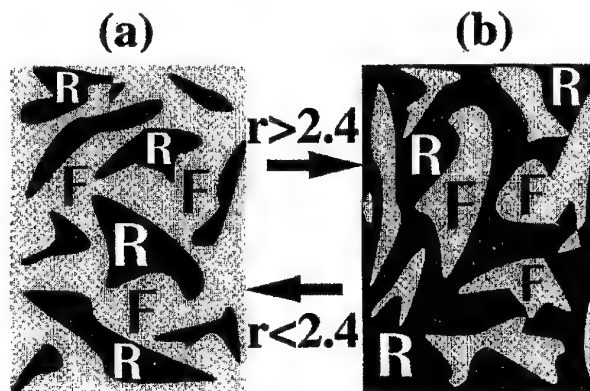


Fig. 14. Schematic illustration of floppy and rigid regions. In floppy network (a) the floppy regions percolate while in rigid one (b) the rigid regions percolate. There is an intermediate phase between the floppy and rigid networks, in which the network is a well admixture of floppy regions and rigid ones.

### 3.4 Self-organization

We emphasize again that the relaxational modes observed in Se-rich glasses ( $x \leq 0.20$ ) become hardly observed when the Ge content is slightly increased from  $x = 0.20$  to 0.23. We feel that the transition for the appearance of the relaxational modes is surprisingly sharp beyond the expectation from the mean-field constraint theory.

Boolchand et al. [11] have suggested that the rigidity transition is richer in nature than that predicted by the previous mean-field constraint theory [1-3], based on the measurements of Raman scattering, Mössbauer spectroscopy, modulated differential scanning calorimetry, and molar volumes. They have proposed the existence of an intermediate phase that starts near  $\langle r_{(1)} \rangle = 2.40$  ( $x = 0.20$ ) and is completed near  $\langle r_{(2)} \rangle = 2.46$  ( $x = 0.23$ ). Recent numerical simulations [47] have shown that the glasses in the intermediate phase are "self-organized" at some level. The network in the intermediate phase is rigid, but is formed with less (or no) overstressed region with the help of self-organization. With the self-organization processing, some constraints are removed from the overstressed region to apply on some floppy units. This process decreases the global constraints on the overconstrained region through sacrificing the degrees of freedom of the floppy region locally.

As displayed in Fig. 8, when the relaxational modes do not appear, the BP intensity decreases with temperature. The decrease of the BP intensity is caused by structural changes, as we will discuss elsewhere [26]. The structural changes occurring in the intermediate phase ( $x = 0.23$ ) should have a tendency to self-organize the network. The self-organization process moving the constraint on the overconstrained units to floppy ones should decrease the local degrees of freedom of some floppy units. By this process, the number of responsible units for the relaxational modes, which may still be slightly remained in the  $x = 0.23$  glass, is reduced to an undetectable number in our system. Thus, the self-organization process can sharpen the transition from floppy to rigid in the relaxational dynamics.

### References

- [1] J. C. Phillips, *J. Non-Cryst. Solids* **34** (1979) 153 and *J. Non-Cryst. Solids* **43** (1981), 37 and *Phys., Today* **35**, 27 (1982).
- [2] J.C. Phillips, in *Rigidity Theory and Applications*, ed. by M.F. Thorpe and P.M. Duxbury, (Kluwer Academic Publishers, New York), (1999) p. 155.
- [3] M. F. Thorpe, *J. Non-Cryst. Solids*, **57** (1983) 355 and H. He and M. F. Thorpe, *Phys. Rev. Lett.*, **54**, 2107 (1985).
- [4] M. F. Thorpe, D. J. Jacobs, B. R. Djordjević, in *Insulating and Semiconducting Glasses*, ed. by P. Boolchand, (World Scientific Publishers, Singapore), (2000) p. 95.
- [5] K. Murase, T. Fukunaga, in *Defects in Glasses*, Mater. Res. Soc. Symp. Proc., **61**, (1986) 101.
- [6] K. Murase, in Ref. [4], p. 415.
- [7] W. A. Kamitakahara, R. L. Cappelletti, P. Boolchand, B. Halpap, F. Gompf, D. A. Neumann and H. Mutka, *Phys. Rev.*, **B44**, 94 (1991).
- [8] Y. Wang, O. Matsuda, K. Inoue, O. Yamamuro, T. Matsuo, K. Murase, *J. Non-Cryst. Solids*, **232-234**, 702 (1998).
- [9] X. Feng, W. J. Bresser, P. Boolchand, *Phys. Rev. Lett.*, **78**, 4422 (1997).
- [10] P. Boolchand, in Ref. [4], p. 415 and p. 369.
- [11] P. Boolchand, X. Feng, D. Selvanathan, W. J. Bresser, in Ref. [2] p. 279.
- [12] D. J. Jacobs, L. A. Kuhn, M. F. Thorpe, in Ref. [2] p. 357.
- [13] Y. Wang, M. Nakamura, O. Matsuda, K. Murase, *J. Non-Cryst. Solids*, **266-269**, 872 (2000).
- [14] S. P. Love, A. J. Sievers, B. L. Halpap, S. M. Lindsay, *Phys. Rev. Lett.*, **65**, 1792 (1990).
- [15] M. Tatsumisago, B. L. Halpap, J. L. Green, S. M. Lindsay, C. A. Angell, *Phys. Rev. Lett.*, **64**, 1549 (1990).
- [16] Y. Tsuchiya, *J. Non Cryst. Solids*, **122**, 205 (1990).
- [17] R. Bohmer, C. A. Angell, *Phys. Rev.*, **B 45**, 10091 (1992).
- [18] G. Lucovsky, F. L. Galeener, *J. Non-Cryst. Solids*, **35& 36**, (1980) 1209 and G. Lucovsky, *J. Non-Cryst. Solids*, **97& 98**, 155 (1987).

- [19] K. Murase, K. Inoue, O. Matsuda, in *Current Topics in Amorphous Materials: Physics and technology*, ed. by Y. Sakurai, Y. Hamakawa, T. Masumoto, K. Shirae and K. Suzuki, (Elsevier, Amsterdam), p. 47 (1993).
- [20] Y. Wang, K. H. Tanaka, T. Nakaoka, K. Murase, submitted to *Phys. Rev. B*.
- [21] E. Rössler, A. P. Sokolov, A. Kisliuk, D. Quitmann *Phys. Rev.*, **B 49**, 14967 (1994).
- [22] A. Brodin, L. M. Torell, *J. Raman Spectrosc.*, **27**, 723 (1996).
- [23] M. Kruumlger, M. Soltwisch, I. Petscherizin, D. Quitmann, *J. Chem. Phys.*, **96**, 7352 (1992).
- [24] A. P. Sokolov, E. Roumlssler, A. Kisliuk, D. Quitmann, *Physica*, **A201**, 67 (1993).
- [25] A. P. Sokolov, E. Roumlssler, A. Kisliuk, D. Quitmann, *Phys. Rev. Lett.*, **71**, 2062 (1993).
- [26] T. Nakaoka, Doctoral Thesis, Osaka Univ. (2001) T. Nakaoka, Y. Wang, K. Murase, submitted to *Phys. Rev. B*.
- [27] G. Winterling, *Phys. Rev.*, **B 12**, 2432 (1975).
- [28] V. Z. Gochiyaev, V. K. Malinovskiy, V. N. Novikov, A. P. Sokolov, *Philos. Mag.*, **B 63**, 777 (1991).
- [29] S. N. Yannopoulos, G. N. Papatheodorou, *Phys. Rev.*, **B 62**, 3728 (2000).
- [30] L. Saviot, E. Duval, N. Surovstev, J. F. Jal, A. J. Dianoux, *Phys. Rev.*, **B 60**, 18 (1999); A. Fontana, R. Dell'Anna, M. Montagna, F. Rossi, G. Viliani, G. Ruocco, M. Sampoli, U. Buchenau, and A. Wischnewski, *Europhys. Lett.*, **47**, 56 (1999).
- [31] N. Theodorakopoulos, J. Jackle, *Phys. Rev. B* **14** (1976) 2637; J. Jackle, in *Amorphous Solids: Low Temperature Properties*, edited by W. A. Phillips (Springer, Berlin, 1981), p. 151.
- [32] Ch. Simon, G. Faivre, R. Zorn, F. Batallan, J. F. Legrand, *J. Phys.*, I (France) **2**, 307 (1992).
- [33] W. Gotze, in *Liquids, Freezing and the Glass Transition*, edited by J. P. Hansen, D. Levesque, J. Zinn Justin (North Holland, Amsterdam, 1990); W. Gotze and L. Sjogren, *Rep. Prog. Phys.*, **55**, 241 (1992).
- [34] D. Caprion, H. R. Schober, *Phys. Rev.*, **B 62**, 3709 (2000).
- [35] F. Mezei, W. Knaak, B. Farrago, *Phys. Rev. Lett.*, **58**, 571 (1987).
- [36] F. Fujara, W. Petry, *Europhys. Lett.*, **4**, 571 (1987); M. Kiebel, E. Bartsch, O. Debus, F. Fujara, W. Petry, and H. Sillescu, *Phys. Rev.*, **B 45**, 10 301 (1992).
- [37] B. Frick, D. Richter, W. Petry, and U. Buchenau, *Z. Phys.*, **B 70**, 73 (1988); B. Frick and D. Richter, *Phys. Rev.*, **B 47**, 14 795 (1993).
- [38] T. Kanaya, T. Kawaguchi, K. Kaji, *J. Chem. Phys.*, **98**, 8262 (1993).
- [39] J. Colmenero, A. Arbe, A. Alegria, *Phys. Rev. Lett.*, **71**, 2603 (1993).
- [40] R. Kohlrausch, *Pogg. Ann. Phys.*, **91**, 198 (1854); G. Williams and D. C. Watts, *Trans. Faraday Soc.* **66**, 80 (1970); G. Williams, D. C. Watts, S. B. Dev, and A. M. North, *ibid.* **67**, 1323 (1971).
- [41] J.G. Kirkwood, *J. Chem. Phys.*, **7**, 505 (1939).
- [42] P.N. Keating, *Phys. Rev.*, **145**, 637 (1966).
- [43] Y. Cai, M.F. Thorpe, *Phys. Rev.*, **B 40**, 10535 (1989).
- [44] Y. Wang, T. Nakaoka, K. Murase, in *Phase Transition and Self-organization in Electronic and Molecular Network*, edited by J. C. Phillips and M. F. Thorpe (Kluwer Academic/ Plenum Publishers, 2001) p. 85.
- [45] Y. Wang, M. Nakamura, T. Nakaoka, O. Matsuda, K. Murase, *J. Non-Cryst. Solids*, in press.
- [46] M. H. Cohen, G. S. Grest, *Phys. Rev.*, **B 20**, 1077 (1979).
- [47] M. F. Thorpe, D. J. Jacobs, M. V. Chubynsky, J. C. Phillips, *J. Non-Cryst. Solids*, **266-269**, 859 (2000).

## THE ROLE OF DEFECTS IN CARRIER TYPE REVERSAL IN BISMUTH DOPED Ge-Se GLASSES BY PHOTOLUMINESCENCE SPECTROSCOPY

N. Asha Bhat, K. S. Sangunni, K. S. R. K. Rao

Department of Physics, Indian Institute of Science, Bangalore -560 012, India

The role played by defects in bringing out n-type conduction in  $\text{Ge}_{20}\text{Se}_{80-x}\text{Bi}_x$  and  $\text{Ge}_{20}\text{Se}_{70-x}\text{Bi}_x\text{Te}_{10}$  glasses is using investigated photoluminescence (PL) spectroscopy. It was found that for both the systems, the compositions at lower Bi content exhibit luminescence with fine features associated while the compositions that show n-type conduction do not exhibit luminescence. The identification of the associated fine features, carried out by deconvoluting the experimental spectra, reveals that Bi addition brings out a relative diminishing in  $\text{D}^+$  defects as compared to  $\text{D}^-$  ones. The study gives an overall indication for the role played by native defects in bringing out n-type conduction in Bi-doped glasses.

(Received June 25, 2001; accepted September 3, 2001)

**Keywords:** Ge-Se glass, Photoluminescence, Defects, Bi doped

### 1. Introduction

The physical properties of semiconducting chalcogenide glasses, that are promising materials in various applications, are profoundly influenced by the presence of inherent defects. One such property is the appearance of n-type conduction in Bi doped glasses ( $\text{Ge}_{20}\text{Se}_{80-x}\text{Bi}_x$  and  $\text{Ge}_{20}\text{Se}_{70-x}\text{Bi}_x\text{Te}_{10}$ ) above  $x \geq 8$  [1,2]. In the past two decades, the extensive studies carried out to understand the mechanism of n-type conduction in these Bi doped glasses have lead to two different explanations. The first one among them is based on the evidences for phase separation at microscopic level, the conclusions drawn from which claim the presence of  $\text{Bi}_6^-$  atoms [1-3]. On the other hand, the second one based, on structural studies, asserts the presence of positively charged  $\text{Bi}_3^+$  or  $\text{Bi}_4^+$  atoms [4-6]. The n-type conduction according to the former description is due to the microcrystallites of n-type conducting  $\text{c-Bi}_2\text{Se}_3$  embedded in the rest of the glassy matrix while on the contrary, according to the later, it is due to the relative decrease in inherent  $\text{D}^+$  defects. Though the two contradictory ideas are addressed recently in a consistent way [7], studies on the role played by defects in bringing out n-type conduction in Bi doped glasses are very rare [8].

The inherent defects in chalcogenide glasses originate mainly from the rearrangements taking place at the prevalent chain ends and are denoted either as  $\text{D}^+$  and  $\text{D}^-$  charged dangling bonds or equivalently as  $\text{C}_3^+$  and  $\text{C}_1^-$  valence alternation pairs (VAP)[9,10]. Also, the VAPs that form very close to each other are called intimate valence-alternation pairs (IVAP). These defects give rise to states in the gap and are conjectured to be the luminescence centers in chalcogenide glasses[11]. In the present paper we address the role played by these defects in bringing out n-type conduction in glassy  $\text{Ge}_{20}\text{Se}_{80-x}\text{Bi}_x$  and  $\text{Ge}_{20}\text{Se}_{70-x}\text{Bi}_x\text{Te}_{10}$  systems using photoluminescence spectroscopy.

### 2. Experimental details

Bulk glassy samples of interest were prepared by conventional melt-quenching technique from 5N pure elemental materials. The samples prepared in this way were confirmed to be x-ray amorphous. Differential scanning calorimetry scans were done on the samples to determine their glassy nature.

Samples having surface dimensions of  $2 \times 2 \text{ mm}^2$  were selected for PL studies. No grinding or polishing was done because samples already had shiny surfaces in their as-prepared form.

To carry out photoluminescence studies a Fourier Transform Photoluminescence Spectrometer (MIDAC corp. USA) was used. Samples to be studied were mounted on a sample holder and then were suspended in a liquid helium cryostat and excited with an  $\text{Ar}^+$  laser ( $\lambda = 514.5 \text{ nm}$  or  $E \sim 2.41 \text{ eV}$ ) with 2 mm beam diameter. The experiment was carried out at 4.2 K with  $150 \text{ mW/cm}^2$  excitation power density. PL signals coming from the samples were analyzed using a Michelson interferometer and detected by a liquid-nitrogen cooled Ge-photodiode. The interferograms with a resolution of 2 meV were recorded by averaging out 0 coadded scans using a personal computer attached to the spectrometer. The excitation was turned on just before recording each spectrum.

### 3. Results and discussion

The PL spectra recorded for the two systems  $\text{Ge}_{20}\text{Se}_{80-x}\text{Bi}_x$  and  $\text{Ge}_{20}\text{Se}_{70-x}\text{Bi}_x\text{Te}_{10}$  with varying Bi concentration are given in Figs. 1 and 2. For lower concentration of Bi, the range of luminescence spectra falls in a broad range 0.7 to 1.2 eV like in a-Se [12]. Again like a-Se, these compositions exhibit luminescence with fine features indicating transitions at three separate energies. However, no luminescence is observed for n-type compositions having higher Bi content.

On the whole, addition of Bi in both Ge-Se and Ge-Se-Te systems reduces the overall PL intensity with an exception of an initial increase in Ge-Se system. The initial increase in Ge-Se system resembles the trends observed when Ge and Te are added to Se, probably because the initial addition of Bi to Ge-Se can facilitate in further breaking of long Se chains. This can give rise to an increase in the concentration of under and overcoordinated inherent defects which are conjectured to be the luminescence centers in chalcogenide glasses. However, as can be seen from the figures, when the concentration of Bi is further increased beyond 4 at%, the intensity goes down to the disappearance of luminescence for compositions that show n-type conduction. Reduction in inherent defects that act as radiative recombination centers can be one of the reasons for the decrease and subsequent disappearance of luminescence intensity.

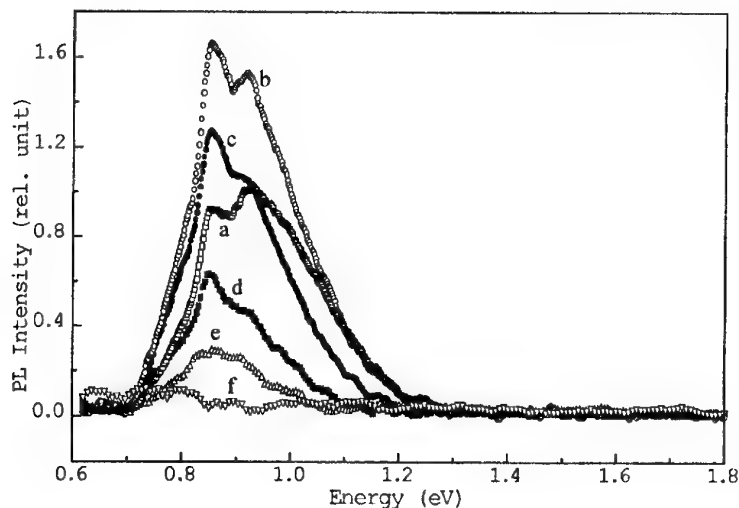


Fig. 1. Photoluminescence spectra for  $\text{Ge}_{20}\text{Se}_{80-x}\text{Bi}_x$  semiconducting glasses at 4.2 K and  $150 \text{ mW cm}^{-2}$  incident power for a.  $x = 0$ , b.  $x = 2$ , c.  $x = 4$ , d.  $x = 6$ , e.  $x = 8$  and f.  $x = 10$ . No luminescence was observed for composition for  $x = 12$  as well as in  $x = 10$ .



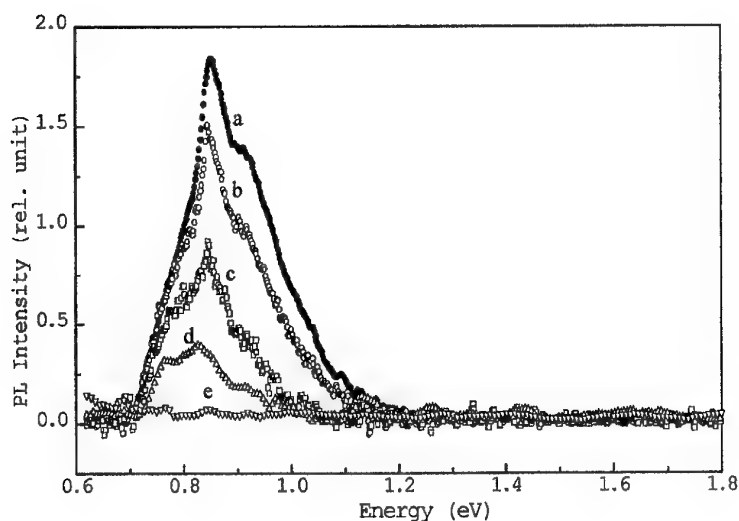


Fig. 2. Photoluminescence spectra for  $\text{Ge}_{20}\text{Se}_{80-x}\text{Bi}_x\text{Te}_{10}$  semiconducting glasses at 4.2 K and  $150 \text{ mW cm}^{-2}$  incident power for a.  $x = 0$ , b.  $x = 2.5$ , c.  $x = 5$ , d.  $x = 7.5$  and e.  $x = 9$ . No luminescence was observed for the compositions  $x = 10$  and  $x = 11$  as well as in  $x = 9$ .

Apart from a decrease in inherent defects, there can be a host of nonradiative processes which can play a significant role in reducing PL efficiency in n-type conducting samples. One such process which mostly the chalcogenide glasses is photoconduction since the quantum efficiency curves for photoluminescence and photoconductivity are complementary to each other and can be written as

$$\eta_0 + \eta_p = 1 \quad (3.1)$$

where  $\eta_0$  and  $\eta_p$  are the quantum efficiencies for photoluminescence and photoconduction, respectively. The relation strongly holds when the excess photon energy required to quench photoluminescence is smaller than that required to ionize excitons. Hence, more the exciting photon energy greater will be the kinetic energy of the exciton created. This in turn will enhance the quantum efficiency for photoconduction with a corresponding drop in the same for photoluminescence. Earlier experimental studies have shown that addition of Bi in  $\text{Ge}_{20}\text{Se}_{80-x}\text{Bi}_x$  brings down the optical band gap from 2.0 eV at  $x=0$  to nearly 1.2 eV for n-type conducting samples [1,2]. The excitation energy in the present investigations is 2.41 eV for all the samples as a result of which the excess excitation energy for n-type conducting glasses amount to nearly 1 eV and can enhance photoconduction with a simultaneous reduction in PL efficiency. The experimental reports on photoconduction in Ge-Se-Bi glasses indeed give evidences for such an increase in photoconductivity with Bi addition [13]. Besides photoconduction, there is a second possibility for absence of PL in n-type conducting glasses. Extrinsic as they are, the n-type glasses will have a significant amount of extended states occupied even at 0K. As a result, the probability of absorption near band edges will be diminished, Lesser the absorption, poorer will be the PL efficiency.

Similarities observed in the PL energy range for samples with lower Bi content and for a-Se confirms the more general nature of luminescent centers in chalcogenides vis-à-vis the inherent defects. These inherent defects include VAPs and IVAPs and are also denoted as random  $\text{D}^+$  and  $\text{D}^-$  and nonrandom  $\text{D}^+$  and  $\text{D}^-$ , respectively. In principle both VAPs and IVAPs can act as PL centers and luminescence energy range can be explained on the basis of these defects as luminescence centers [12]. The similarities in the three features observed in Bi-doped glasses and a-Se suggest that addition of Bi does not create any extra luminescence centers though it can give rise to some sort of defect centers which are non-radiative.

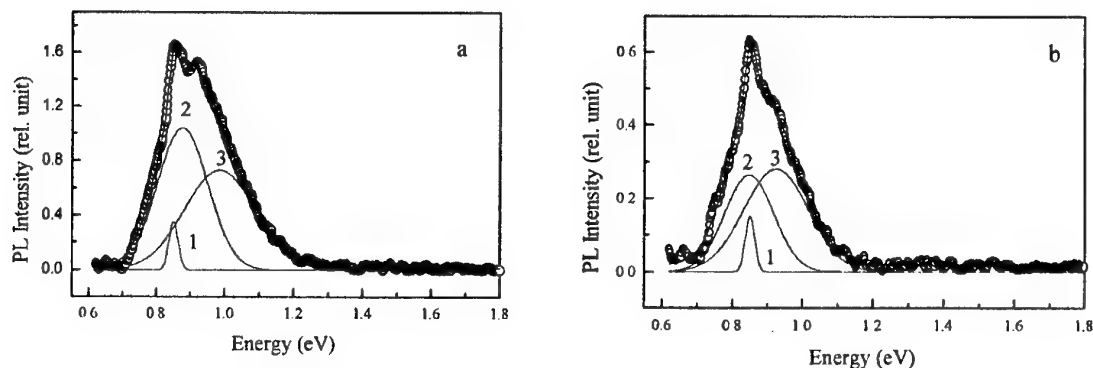


Fig. 3. Deconvoluted experimental spectra for a.  $x = 2$  and b.  $x = 6$  in  $\text{Ge}_{20}\text{Se}_{80-x}\text{Bi}_x$  glasses.

Conventionally, luminescent transitions at low temperatures are described by Gaussian line broadening mechanism and similar is the case proposed for chalcogenide glasses too [8]. Therefore to deconvolute the three distinct luminescence transitions embedded in the experimental PL spectra is considered a linear combination of three Gaussians (amplitude version) given by

$$y = y_0 + \sum_{i=1}^3 A_i \exp\left(-0.5\left(\frac{x - x_{c_i}}{w_i}\right)^2\right) \quad (3.2)$$

with  $y_0$  representing offset and  $A_i$ ,  $x_{c_i}$  and  $2.355w_i$  representing the amplitude, peak position and full width at half maxima (FWHM) of  $i$ th transition. The deconvoluted experimental spectra in Ge-Se-Bi and Ge-Se-Te-Bi systems for some samples that showed PL are given in figures 3 and 4. In Table 1 are listed the best fitting parameters along with the area under each deconvoluted spectra ( $\sqrt{2\pi} A_i w_i$ ). The resultant of the three deconvoluted spectra fits very well with the experimental spectra. Identification of the three deconvoluted spectra with radiative transitions at different inherent defects is done according to the following arguments.

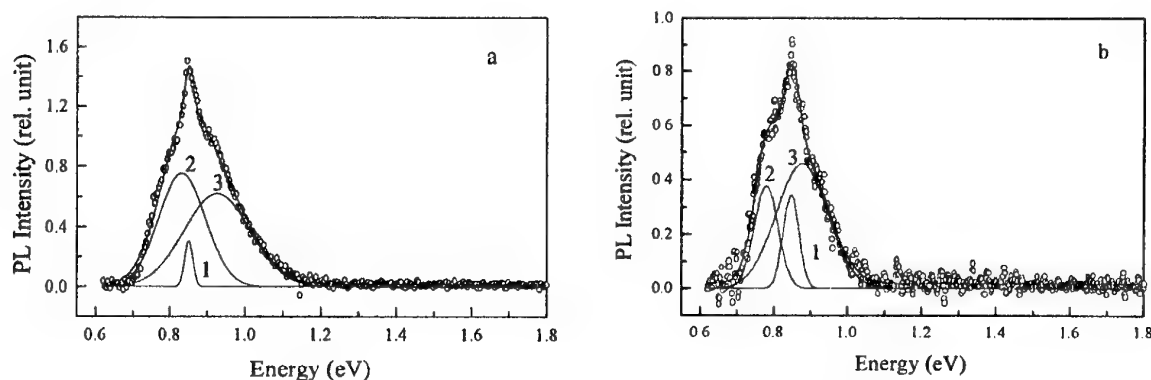


Fig. 4. Deconvoluted experimental spectra for a.  $x = 2.5$  and b.  $x = 5$  in  $\text{Ge}_{20}\text{Se}_{70-x}\text{Bi}_x\text{Te}_{10}$  glasses.

PL in semiconductors is generally due to electron-hole recombination and its origin can be traced to six different transition [14]. They are the transition between a) a free electron and a free hole ( $fe \rightarrow fh$ ), b) an electron trapped in a shallow or deep level and a free hole ( $etsh \rightarrow fh$  or  $etdl \rightarrow fh$ ), c) a free electron and a hole trapped in shallow or deep level ( $fe \rightarrow htsh$  or  $fe \rightarrow htsh$ ) and d) electron-hole pairs trapped at defect pairs in the gap ( $etdl \rightarrow htsh$ ). The energy level scheme for gap states in semiconducting chalcogenide glasses is sketched in Fig. 5(a) in which the energy levels arising due to random and non-random  $D^-$  and  $D^+$  defect centers are positioned according to the phenomenological

defect models[15]. The shallow donor and acceptor levels represent the random  $D^+$  and  $D^-$  defects and the deep donor and acceptor levels represent non-random  $D^+$  and  $D^-$  defects. The donor levels act as trap levels for electrons whereas the acceptor levels act as trap levels for holes.

Coming to the present results, the deconvoluted spectra in Figs. 3 and 4 are significantly Stokes-shifted from the excitation energy (2.41eV) as well as the respective optical bandgap energies. Such a large shift of half the band gap magnitude is not feasible if at all there are any band-to-band radiative transitions[16]. Interestingly, energy and width of one of the three deconvoluted spectra appears insensitive to compositional variation. According to the defect models, IVAP defect centers forming neutral defect pairs are known to be insensitive to dopant atoms[15]. The insensitive deconvoluted spectra can therefore be identified with the recombination transition at IVAPs. At the same time, according to charged defect models, there is a larger distortion associated with random  $D^+$  than for random  $D^-$  and, therefore, the radiative transition involving  $D^+$  will occur at lesser energy than that involving  $D^-$ . Utilizing these ideas, we identify the second deconvoluted spectra with transition occurring at  $D^+$ (etsl  $\rightarrow$  fh) and the third one with the transition at  $D^-$ (fe  $\rightarrow$  htsl). The multiple transitions discussed above can be illustrated with the help of a configurational coordinate diagram as shown in Fig. 5(b).

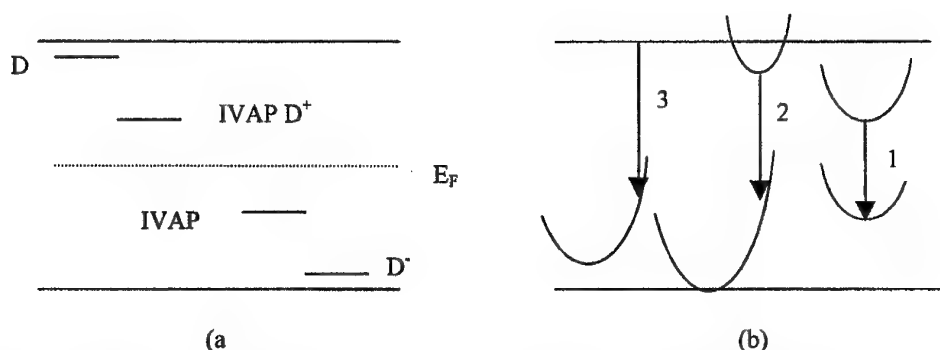


Fig. 5. (a)Energy level scheme for VAP and IVAP defects in chalcogenide glasses and (b) Configurational coordinate diagram illustration of multiple PL transitions involving gap levels denoted by 1- the IVAP pair recombination. 2 - etsl  $\rightarrow$  fh and 3- fe  $\rightarrow$  htsl.

With this identification we can now discuss the consequences of Bi addition to Ge-Se and Ge-Se-Te glasses. In both these systems addition of Bi gives rise to a reduction in the width of the two broader transitions along with a shift in their peak position to lower energy side. This is natural if we recall that the broader transitions are assigned to random VAPs which are more likely to get influenced by external dopants unlike IVAPs. The lowering of energy of transitions associated with random VAPs is probably due the higher atomic radii of Bi atoms added that can push the corresponding energy levels away from the band edges, towards the Fermi level.

From Table 1 and also from the deconvoluted spectra in Figs. 3 and 4, we can see that at 6 and 5 at% of Bi in Ge-Se and Ge-Se-Te systems, respectively, the relative area under the second deconvoluted spectra is less than that under the third. As the area under the curve depends on the density of defect centers giving rise to the corresponding PL, it can be said that the concentration of  $D^+$  defects decreases more rapidly than the concentration of  $D^-$  as Bi replaces Se. This is possible if Bi atoms added enter the glassy matrix as positive defects. For Bi to go as positive defect it has to have a coordination number of less than its valence i.e. five. Most of the structural studies carried out in the past like EXAFS, Raman and IR have all pointed out a coordination of three for Bi with a positive charge on it. Though a recent EXAFS study has claimed the coordination of Bi to be four[6] as against all the earlier structural studies, it is interesting to note that it has in fact envisaged Bi atoms to be positively charged. The relative reduction in  $D^+$  defects as compared to  $D^-$  defects indeed gives a clear evidence for Bi atoms entering as positively charged defects into the glassy matrix. Some earlier studies pointing out a reduction in hole drift mobility as compared to electron drift mobility with the addition of Bi[17] substantiate our findings as it is known that  $D^+$  and  $D^-$  defects act as electron and hole traps, respectively. With this in mind a discussion on the mechanism of appearance of n-type conduction in Bi doped glasses is presented here.

Table 1 The extracted features from the experimental spectra for different compositions and the area under the respective deconvoluted spectra.

Sample	$xc_1$ (eV)	$w_1$ (eV)	Area	$xc_2$ (eV)	$w_2$ (eV)	Area	$xc_3$ (eV)	$w_3$ (eV)	Area
$\alpha$ -Se	0.849	0.030	0.017	0.859	0.148	0.379	0.954	0.206	0.229
Ge <sub>20</sub> Se <sub>80</sub>	0.850	0.034	0.088	0.903	0.160	1.127	1.01	0.202	1.00
Ge <sub>20</sub> Se <sub>78</sub> Bi <sub>2</sub>	0.851	0.028	0.122	0.877	0.148	1.944	0.986	0.204	1.852
Ge <sub>20</sub> Se <sub>76</sub> Bi <sub>4</sub>	0.851	0.026	0.084	0.863	0.140	1.358	0.963	0.190	1.238
Ge <sub>20</sub> Se <sub>74</sub> Bi <sub>6</sub>	0.851	0.026	0.087	0.848	0.138	0.458	0.925	0.184	0.644
Ge <sub>20</sub> Se <sub>70</sub> Te <sub>10</sub>	0.851	0.024	0.129	0.859	0.144	1.989	0.956	0.192	1.414
Ge <sub>20</sub> Se <sub>67.5</sub> Bi <sub>12.5</sub> Te <sub>10</sub>	0.851	0.022	0.085	0.832	0.127	1.198	0.926	0.176	1.371
Ge <sub>20</sub> Se <sub>65</sub> Bi <sub>5</sub> Te <sub>10</sub>	0.847	0.028	0.090	0.784	0.072	0.220	0.873	0.140	0.628

From a thorough review of all the earlier studies, a coordination of three for Bi appears more convincing as it can be made consistent even with the phase separation evidences [7]. Accordingly, we envisage Bi atoms to exist as positively charged defects with three nearest Se neighbours in Ge-Se glassy matrix to bring out an imbalance in  $D^+$  -  $D^-$  defect pairs. An additional consequence of Bi atoms entering as  $Bi_3^+$  defects in the glassy matrix is the availability of extra electrons in the conduction band extended states, evidence for which also is available in the literature[18]. These two changes combined with the setting in of microscopic inhomogeneities in the form of  $\alpha$ -  $Bi_2Se_3$ [7] can lead to a condition wherein the Fermi level can no longer be pinned. A shifts in  $E_F$  towards the conduction band is the natural consequence of these effects, eventually bring out n-type conduction at higher Bi content in both Ge-Se and Ge-Se-Te glasses.

#### 4. Conclusions

Compositional dependence of photoluminescence in  $Ge_{20}Se_{80-x}Bi_x$  and  $Ge_{20}Se_{70-x}Bi_xTe_{10}$  glasses is studied. It is observed that addition of Bi brings out a reduction in the relative concentration of  $D^+$  as compared to  $D^-$  defects. The imbalance accompanied by the contribution of extra electrons brings out n-type conduction in Bi doped glasses. The observation is in good agreement with the earlier structural studies.

#### References

- [1] N. Tohge, T. Minami, Y. Yamamoto, M. Tanaka, J. Appl. Phys. **51**, 1048 (1980).
- [2] N. Tohge, T. Minami, M. Tanaka, J. Non-Cryst. Solids **37**, 23 (1980).
- [3] J. C. Phillips, Phys. Rev. **B36**, 4265 (1987).
- [4] S. R. Elliott, A. T. Steel, J. Phys. C: Solid State Phys. **20**, 4335 (1987).
- [5] T. Ikari, T. Tanaka, K. Ura, K. Maeda, K. Futagami, S. Shigetomi, Phys. Rev. **B47**, 4984 (1993).
- [6] G. Saffarini, J. M. Saiter, A. Zmailan, J. Optoelectronics and Advanced Materials **3**, 485 (2001).
- [7] N. Asha Bhat, K. S. Sangunni, Solid State Commun. **116**, 297 (2000).
- [8] E. Mytilineou, Zhaohui Lin, P. C. Taylor, Solid State Commun. **84**, 617 (1992).
- [9] R. A. Street, N. F. Mott, Phys. Rev. Lett. **35**, 1293 (1975).
- [10] M. Kastner, D. Adler, H. Fritzche, Phys. Rev. Lett. **37**, 1504 (1976).
- [11] R. A. Street, Adv. Phys., **25**, 395 (1976) and references therein.
- [12] N. Asha Bhat, K. S. Sangunni, K. S. R. K. Rao, to be published.
- [13] N. Tohge, T. Takahiro, Y. Yonesakim, T. Minami, J. Appl. Phys. **58**, 4225 (1985).
- [14] G. Blasse, B. C. Grabmaier, Luminescent Materials, (Springer Verlag, 1994).
- [15] E. A. Davis, Topics in applied Phys: Amorphous Semiconductors, (Springer Verlag, Berlin, 1979) p. 41.
- [16] S. R. Elliott, Physics of Amorphous Materials, Longman Group UK Limited, London, (chapter 6), 1983.
- [17] T. Takahashi, J. Non-Cryst. Solids **44**, 239 (1981).
- [18] O. Matsuda, T. Ohba, M. Taniguchi, J. Non-Cryst. Solids, **198-200** p2, 688 (1996).

## EFFECT OF PHOTO AND THERMAL DISSOLUTION OF SILVER ON THE ELECTRICAL PROPERTIES OF a-As<sub>2</sub>S<sub>3</sub>

N. Goyal, A. Zolanvari, S. K. Tripathi

Department of Physics, Center of Advanced Study in Physics, Panjab University, Chandigarh, 160014, India

The paper reports the effect of dissolution of silver in arsenic sulphide. The conductivity of As<sub>2</sub>S<sub>3</sub> decreases with doping. The a.c conductivity is proportional to  $\omega^s$  for undoped as well as doped samples. The value of frequency exponent "s" increases with doping. A new structural model along with Correlated Barrier Hopping model has been used to explain these results.

(Received June 30, 2001; accepted September 3, 2001)

**Keywords:** Amorphous As<sub>2</sub>S<sub>3</sub>, Silver photo and thermal dissolution, ac conductivity

### 1. Introduction

The photo - dissolution of Ag into chalcogenide glasses is a promising phenomenon for ultrahigh resolution photolithographic process and for fabrication of optical components [1,2,3]. The investigations have shown the possibility to use Ag photo doped chalcogenide glasses (Ge-Te, As-Ge-Te) for temperature and voltage sensors [4,5]. The results of the measurements indicate that the conductivity of chalcogenide glasses decreases with photo/thermal dissolution of Ag into these glasses. The conductivity of glasses for given voltage/temperature, parameters increases tremendously after dissolution of Ag.

Structural studies using Raman spectra have indicated that the silver photo-doped films of As<sub>30</sub>S<sub>70</sub> are homogeneous and have a structure similar to that of bulk glass Ag<sub>30</sub>As<sub>22</sub>S<sub>48</sub> [6, 7].

However, it has been observed that (by alloying Ag with As<sub>2</sub>S<sub>3</sub> (bulk doping) the conductivity of As<sub>2</sub>S<sub>3</sub> increases [8,9] and the large increase in the conductivity has been explained on the basis of the increase in the number of charged dangling bands. We report here measurements of electrical properties of As<sub>2</sub>S<sub>3</sub> before and after dissolution of Ag into it. They show how the electrical properties of As<sub>2</sub>S<sub>3</sub> change after the dissolution of silver. The interesting results (different than bulk doping of Ag) have been explained on the basis of the structural changes occurring in the material as a consequence of dissolution of Ag. A new model has been proposed. The modified Correlated Barrier Hopping model (CBH model) [10-12] has been used to explain the effect of doping.

### 2. Experimental

The samples in the form of pellets (diameter: 0.687 cm; thickness: 1 + 2 mm) were prepared by compressing the finely ground powder of a-As<sub>2</sub>S<sub>3</sub> to maximum compaction at 10<sup>7</sup> Pa, using a hydraulic press. All pellets were annealed at 398 K for 24 hours in order to minimize the effect of grain boundaries. X-ray diffraction pattern of the material and pellets confirmed the amorphous nature of the samples. The undoped sample was an amorphous As<sub>2</sub>S<sub>3</sub> pellet, coated with aquadag on both faces for obtaining electrical contacts. The dissolution of silver into As<sub>2</sub>S<sub>3</sub> was carried out separately on pellets by coating their faces with a thick layer of conducting silver paste and thereafter subjecting them to two different treatments i.e. (i) *optical*, and (ii) *thermal*. In first case, both faces of silver-coated pellets were exposed to intense UV radiations for two hours on each face. In the second case, the silver coated pellet was given a heat treatment by transferring it immediately into oven at different temperatures (below T<sub>g</sub>) varying between 363 K to 393 K for 24 hours.

A General Radio Bridge (model 1620-A) was used for measurements of frequency dependence a.c conductance and capacitance of the samples over a frequency range of 1 kHz to 100

kHz in the temperature range 273 - 373 K. A three terminal sample holder was used for these measurements.

### 3. Results

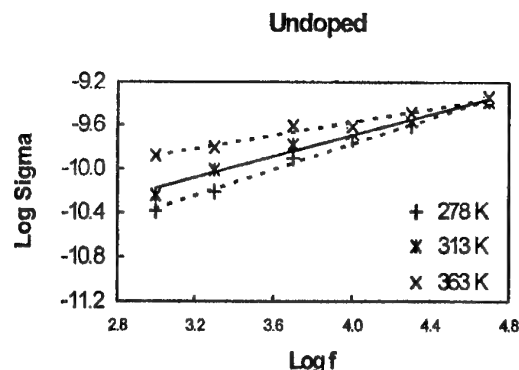


Fig. 1. Conductivity vs. frequency for different temperatures of undoped arsenic sulphide.

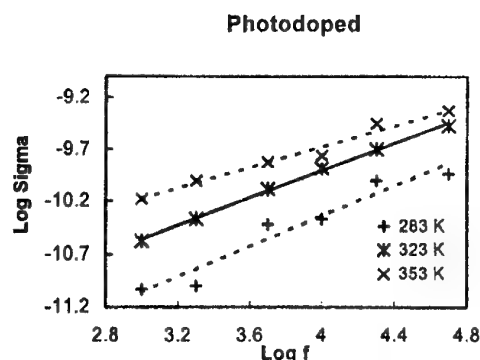


Fig. 2. Conductivity vs. frequency for different temperatures of photo-doped arsenic sulphide.

Figs. 1,2 show the frequency dependence of the measured conductivity for undoped, photo-doped and thermal-doped samples.

The following law is valid:

$$\sigma_{ac} = A \omega^s \quad (3.1)$$

The figures show that the slope of the decreases with increasing temperature for all samples. This clearly indicates that the value of "s" decreases with increasing temperature.

Fig. 3 shows the temperature dependence of frequency exponent "s" for all the samples. Figure indicates that the value of "s" decreases with increasing temperature, but increases with doping at same temperature.

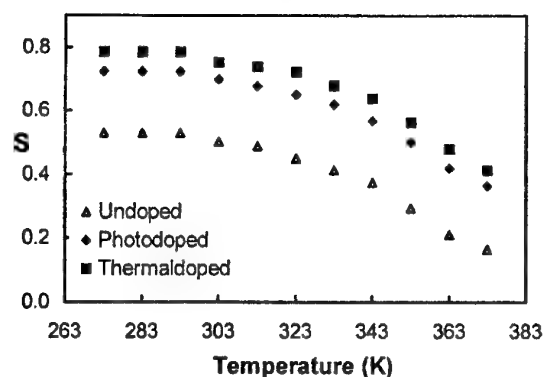


Fig. 3. Frequency exponent "s" temperature vs. for undoped, photo doped & thermal-doped samples.

However it has been observed that in case of thermal doping, if the doping temperature is increased, the value of "s" also increases (Fig. 4).

Fig. 5(a, b, c and d) shows the frequency dependence of dielectric constant k at the four different temperatures for undoped, photo-doped, and thermal-doped  $As_2S_3$ .

Figures clearly indicate that at lower temperatures, the dielectric constant is same for photo-doped and undoped  $As_2S_3$  whereas it is higher for thermal-doped  $As_2S_3$ .

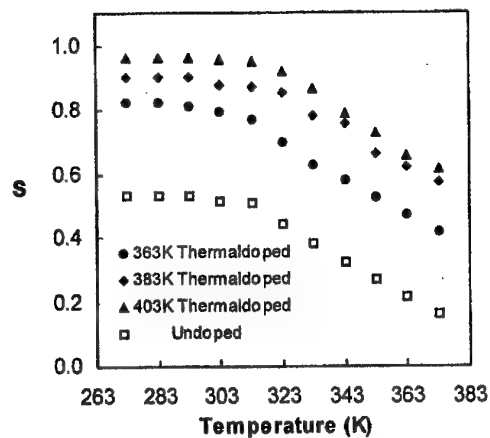


Fig. 4. Frequency exponent "s" vs. temperature for thermal - doped  $\text{Ag-As}_2\text{S}_3$  (doping temperature being different).

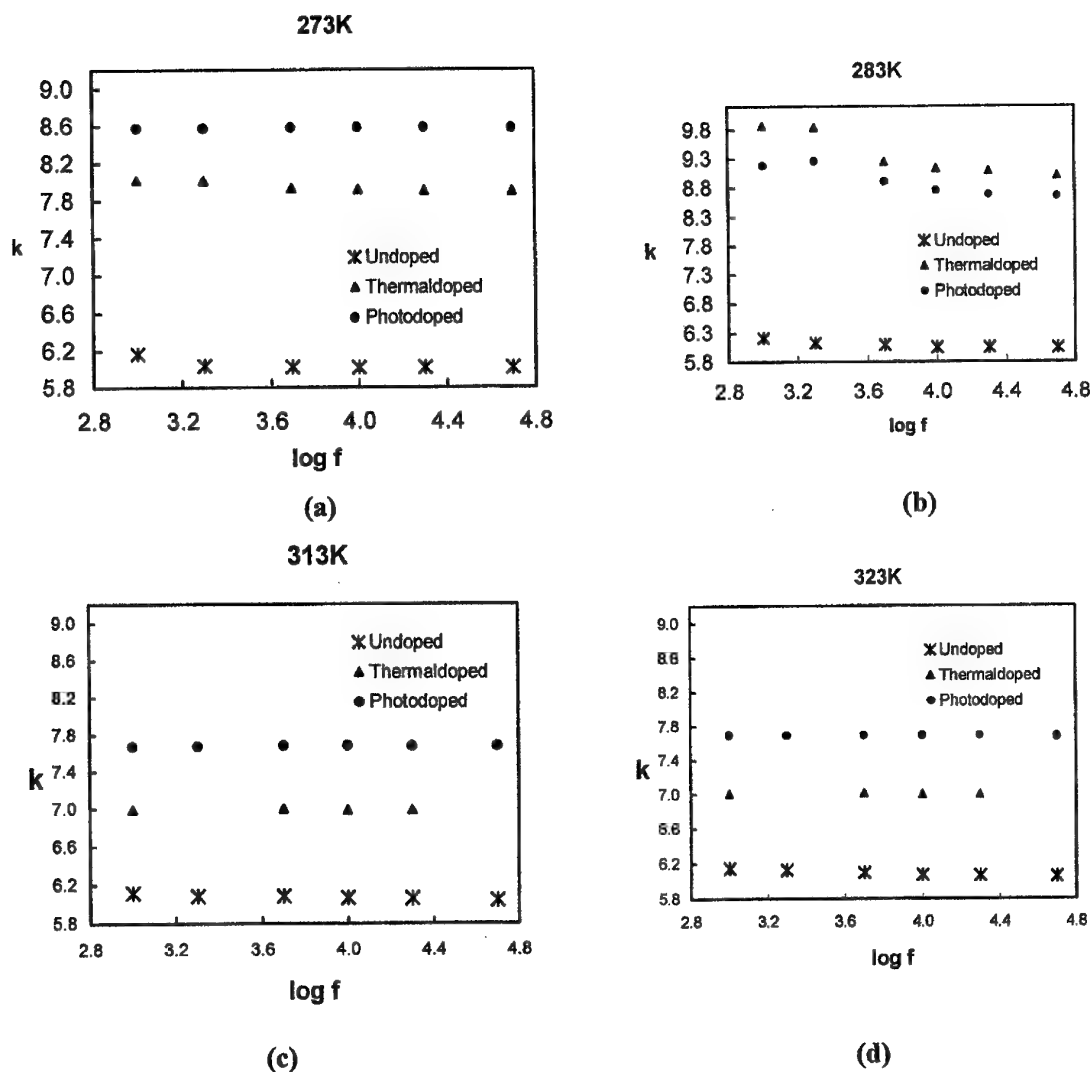


Fig. 5. Dielectric constant vs. log of frequency for undoped, photo doped and thermal doped  $\text{Ag-As}_2\text{S}_3$  samples at (a) 273K, (b) 283K, (c) 313K and (d) 323K.

However, at higher temperatures the value of the dielectric constant,  $k$ , is maximum for photo-doped  $\text{As}_2\text{S}_3$ , whereas the value of  $k$  for undoped  $\text{As}_2\text{S}_3$  does not vary much with temperature.

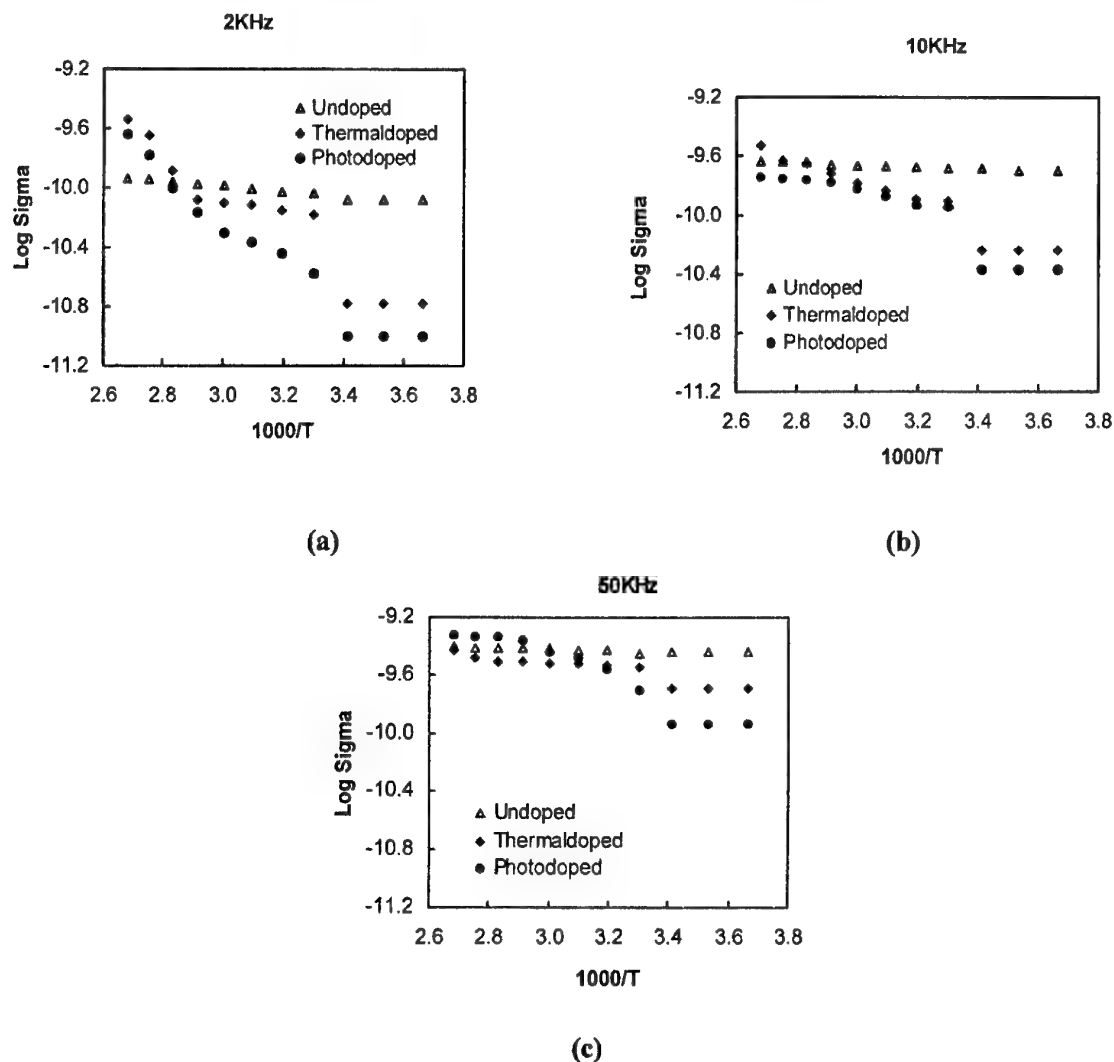


Fig. 6. Arrhenius plot for conductivity for undoped, photo doped and thermal doped samples at (a) 2 kHz, (b) 10 kHz and (c) 50 kHz.

Fig. 6(a, b & c) shows the temperature dependence of all samples of  $\text{As}_2\text{S}_3$  at 2 kHz, 10 kHz and 50 kHz. Figures indicate that for undoped sample conductivity does not change much with temperature. However, in the case of Ag-doped samples, the conductivity shows a sharp jump in the conductivity at around 283K. It is also clear from figures that the conductivity of  $\text{As}_2\text{S}_3$  decreases on doping, particularly in the lower temperature range. The figures show that the fall in conductivity, because of doping is maximum for photo-doped  $\text{As}_2\text{S}_3$  at lower temperatures.

Fig. 7(a, b) shows the temperature dependence of dielectric constant  $k$  at two different frequencies (2 kHz & 50 kHz). The figures indicate that at lower temperatures the value of  $k$  for undoped and photo-doped samples is nearly constant, whereas it is slightly more for thermal-doped sample. However, at about 283K, the value of  $k$  suddenly increases for thermal - doped sample and at about 293 K there is a jump in the value of  $k$  for photo-doped sample. This jump in the value of  $k$  is higher for photo-doped samples than for thermal-doped samples.



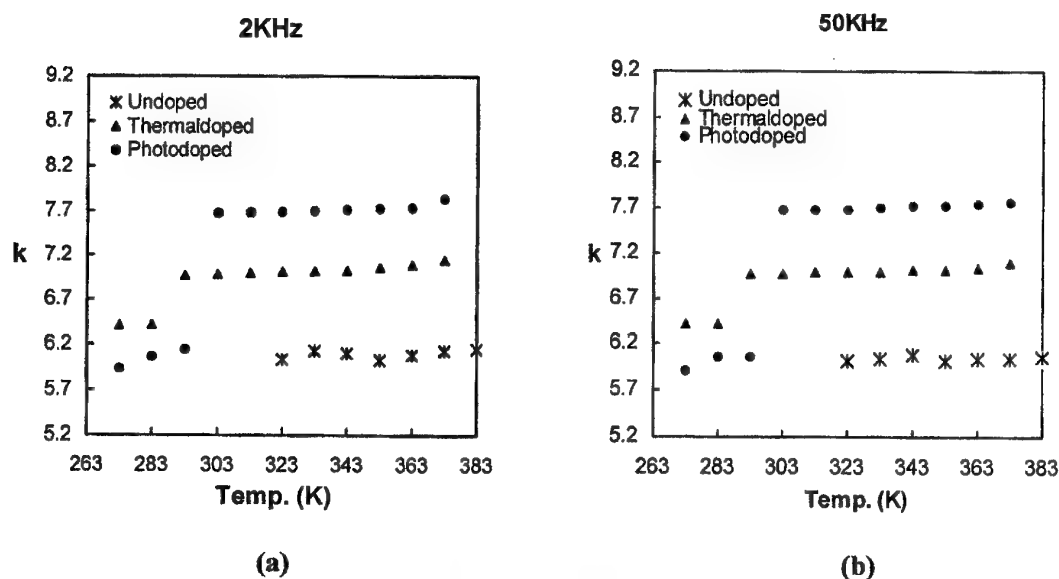
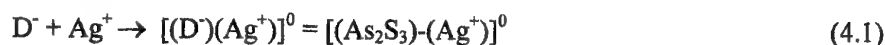


Fig. 7. Dielectric constant vs. temperature for undoped, photo doped and thermal - doped samples at (a) 2 kHz and (b) 50 kHz.

#### 4. Discussion

The above results can be easily explained using a modified Correlated Barrier Hopping Model (CBH). It has been established that the dissolution of silver into chalcogenide involves the migration of Ag<sup>+</sup> ions and electrons. We have large number of D<sup>+</sup>, D<sup>-</sup> and unsaturated D<sup>0</sup> defect sites in chalcogenides [11, 12].

A new equilibrium is expected after the migration of Ag<sup>+</sup> and electrons, i.e.



and



These reactions suggest that, on doping, the concentration of D<sup>0</sup> centres decreases.

According to Correlated Barrier Hopping model [10]:

$$\sigma_{ac} = \frac{n}{24} \pi^2 N N_P \epsilon' \omega R_\omega^6 \quad (4.3)$$

Where  $n$  is the number of polarons involved in the hopping process  $R_\omega$  is the hopping distance for the condition  $\omega\tau = 1$  and is given by [10, 11]:

$$R_\omega = \frac{4ne^2}{\epsilon' \{ \omega + kT \ln(\omega\tau_0) \}} \quad (4.4)$$

The value of frequency exponent  $s$  is calculated from equations (4.3) and (4.4) and is equal to:

$$s = \frac{d(\ln \sigma_{ac})}{d(\ln \omega)} = 1 - \frac{6kT}{W - kT \ln \left( \frac{1}{\omega\tau_0} \right)} \quad (4.5)$$

$NN_p$  is given by [11]:

$$NN_p = N_T^2 \quad (\text{for bipolaron hopping}) \quad (4.6)$$

Where  $N_T$  is the number of density of states.

$$NN_p = N_T^2 \exp\left(\frac{-U_{\text{eff}}}{2kT}\right) \quad (\text{For single polaron hopping}) \quad (4.7)$$

Total conductivity is the combined mechanism of these hopping processes.

These processes are bipolaron hopping between  $D^+$  and  $D^-$  centres, single polaron hopping between  $D^0$  and  $D^-$  centres, and  $D^0$  and  $D^+$  centres. Also  $W$  is equal to  $W_M$ , which is slightly less than band-gap for bipolaron hopping, whereas, it is equal to  $W_1$  and  $W_2$  for two types of single-polaron hopping, which are substantially less than  $W_M$  for bipolaron hopping. The smaller values of  $W_1$  and  $W_2$  for single polaron hopping means, that value of  $R_W$  is much more for single polaron hopping as compared to bipolaron hopping as per equation (5), which in turn means that the contribution of each  $D^0$  centre to conductivity is much more than  $D^+$  or  $D^-$  centre (equation 4.3). Therefore, the diminishing in  $D^0$  centres causes a decrease in the value of conductivity at lower temperatures as has been observed in Fig. 6a,b,c.

The neutral dipolar states  $[D^+Ag^+]^0$  are expected to interact with each other, thereby forming long dipolar chains. These dipolar chains do not contribute to conductivity at lower temperatures. Fig. 6 shows that at lower temperature the dielectric constant is almost the same for pure  $As_2S_3$ , and optically doped  $Ag-As_2S_3$ , thereby indicating that the dipolar states  $Ag^+-D^-$  do not contribute to dielectric constant. However, a higher value of dielectric constant at lower temperatures for thermal-doped  $Ag-As_2S_3$  indicates that some of these dipolar states  $[Ag^+-D^-]$  may be non-interacting (not being part of long dipolar chains) and, thereby, contributing to dielectric constant. However, at higher temperatures, the dielectric constant is higher than in undoped  $As_2S_3$  for both thermal-doped  $Ag-As_2S_3$  and optically doped  $Ag-As_2S_3$ . This indicates that at higher temperatures these dipolar chains break down and start contributing to increased capacitance/dielectric constant.

A jump in the value of conductivity and dielectric constant for doped  $As_2S_3$  at higher temperatures as per Figs. 6 and 7 can be also attributed to breakage of dipolar chains. A jump in the dielectric constant of optically doped  $Ag-As_2S_3$ , which has been observed at higher temperature than that of thermal-doped  $Ag-As_2S_3$  is also indicative of the fact that interaction of dipolar states is stronger for optically doped  $Ag-As_2S_3$  and, therefore, requires higher energy for breaking-down the dipolar chains.

## References

- [1] S. Shtutina, M. Khebanov, V. Lyubin, S. Rosenwaks, V. Voltena, *Thin Solid Films*, **261**, 263 (1995).
- [2] S. A. Dumford, J. M. Lavine, *J. Vac. Sci. Tech.*, **B12**, 44 (1994).
- [3] Tl. Koba, T. Wagner, P. J. S. Ewen, A. E. Owen, *Phil. Mag.*, **B71**, 311 (1995).
- [4] K. K. Srivastava, A. Vohra, *Phil. Mag.*, **B61**, 201 (1990).
- [5] P. Khurana, A. Vohra, K. K. Srivastava, *Journal of Material Science Materials in electronics*, **1**, 175 (1990).
- [6] A. P. Firth, P. J. S. Ewen, A. E. Owen, C. M. Huntley, *Adv. in Resist Technol. and Process*, **II**, *SPIE*, **539**, 160 (1985).
- [7] A. E. Owen, A. P. Firth, P. J. S. Ewen, *Phil. Mag. (GB)*, **52**, 347 (1985).
- [8] N. Goyal, M. Lal, A. Vohra, *phys. state sol.* **B171**, 477 (1992).
- [9] N. F. Mott, *Phil. Mag.*, **34**, 1101 (1976).
- [10] S.R. Elliott, *Phil. Mag.*, **36**, 1291 (1977).
- [11] K. Shimakawa, *Phil. Mag.*, **B46**, 123 (1982).
- [12] K. Shimakawa, *Phil. Mag.*, **B48**, 77746 (1983).

## MICROSTRUCTURE OF GLASSES AND GLASS-CRYSTALLINE MATERIALS IN THE SYSTEM $\text{TeO}_2\text{-V}_2\text{O}_5\text{-Ag}_2\text{O-AgI}$

E. Kashchieva, Y. Ivanova, V. Ivanova, S. Nedev, Y. Dimitriev, E. Lefterova<sup>a</sup>

University of Chemical Technology and Metallurgy, 1756 Sofia, Bulgaria

<sup>a</sup>Central Laboratory for Electrochemical Power Sources - BAS, 1113 Sofia, Bulgaria

The aim of this paper was to investigate the formation of nano- and microheterogeneities in glasses and glass-ceramics in the system  $\text{Ag}_2\text{O-TeO}_2\text{-V}_2\text{O}_5\text{-AgI}$ . The phase formation is studied by XRD analysis and the microstructure by TEM and SAED analysis. The particle size distribution of silver was obtained by computer analysis of TEM micrographs. Various types nano- and micro-scale heterogeneities were found: background nanostructure, nano- and microcrystals, droplet-like immiscibility formations as heterogeneous targets for crystal development and separated metal silver particles.

(Received June 6, 2001; accepted September 3, 2001)

**Keywords:** Oxide glass, Microstructure, Ion conducting material, Solid electrolyte

### 1. Introduction

The ionic conducting silver containing glasses hold an important place between the amorphous solid electrolytes [1-5]. They are respective materials with promising properties especially when their compositions are based on combination of several glass formers, glass modifiers, Ag-oxide and Ag-chalcogenide.

The clustering tendency in silver containing materials involves makes necessary a detailed microstructure investigation because the phases with high ionic conductivity could be concentrated in the microaggregate structures. The appearance and development of nano- and micro-scale heterogeneities, their interaction with the homogeneous glassy matrix and further evolution towards metastable immiscibility formations determines the conducting behaviour of the materials.

The present work is dedicated to glasses and glass-ceramics in the four component system  $\text{Ag}_2\text{O-TeO}_2\text{-V}_2\text{O}_5\text{-AgI}$ . Our interest towards this system is stimulated by the combination of both non-conventional glass-forming oxides  $\text{TeO}_2$  and  $\text{V}_2\text{O}_5$ , coupled with  $\text{Ag}_2\text{O}$  and  $\text{AgI}$ . Recently, in several publications there was discussed the synthesis of ionic conductive glasses containing the above noted glass-formers [6-14]. The aim of the work is to study the formation of nano- and microheterogeneities in glasses and glass-ceramics in the system  $\text{Ag}_2\text{O-TeO}_2\text{-V}_2\text{O}_5\text{-AgI}$ . This work is a continuation of some previous investigations concerning the phase formation and crystallisation in this system [15-18].

### 2. Experimental

As precursors for synthesis of glasses and glass-crystalline materials in the system  $\text{TeO}_2\text{-V}_2\text{O}_5\text{-Ag}_2\text{O-AgI}$  grade reagents  $\text{TeO}_2$ ,  $\text{V}_2\text{O}_5$ ,  $\text{Ag}_2\text{O}$  and  $\text{AgI}$  are used. The batches are melted in porcelain crucibles at 600 - 800°C temperature range. In order to trace the evolution of various types microaggregation processes in the glassy and crystalline materials convenient compositions with different thermal history are chosen. Two kinds of cooling were applied: slowly cooling of the melts in the crucibles and fast cooling between copper plates. Cross sections containing 50 mol. % and 60 mol. %  $\text{AgI}$  are studied for the  $\text{Ag}_2\text{O}$  content from 10 to 30 mol. %. For comparison, compositions without  $\text{Ag}_2\text{O}$  or  $\text{TeO}_2$  were investigated.

The phase formation was studied by X-ray diffraction (XRD) analysis using DRON UM 1 with  $\text{Cu K}_\alpha$  radiation. The microstructure of the samples was studied by transmission electron microscopy (TEM) by means of EM-400, Philips electron microscope. TEM was applied on C+Pt replicas from fresh fractured surfaces of the bulk materials. TEM and SAED analysis of silver particles were made on replicas

with single or double stage extraction. The particle size distribution was determined by computer analysis of TEM micrographs.

### 3. Results and discussion

In some samples of the three component system  $\text{TeO}_2\text{-V}_2\text{O}_5\text{-AgI}$  the process of stable liquid phase separation leads to formation of two visually separated layers with different macro- and microstructure. A composition 50%  $2\text{TeO}_2\cdot\text{V}_2\text{O}_5$ , 50% AgI is shown as an example. At micro-scale level the glassy layer is homogeneous. Very rarely in some regions nano- and microheterogeneities with technological origin we are observed (Fig. 1a). Clearly developed crystalline formations situated in the range 10 - 15  $\mu\text{m}$  are typical for the second layer (Fig. 1b). The XRD analysis (Fig. 2) shows that the main crystalline phase is  $\beta\text{-AgI}$  which is stable at low temperatures in relation to the cooling rates applied. For both layers these data are in good agreement with the microstructure of the sample.

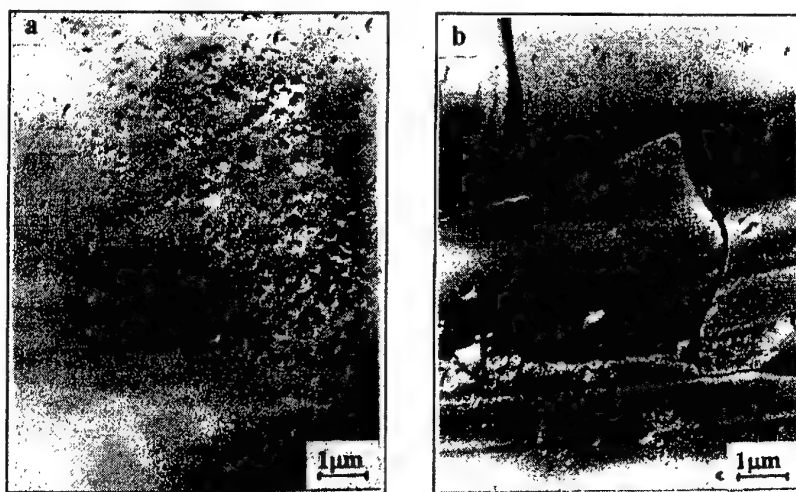


Fig. 1. TEM micrographs of the sample with composition 50% $2\text{TeO}_2\cdot\text{V}_2\text{O}_5$ , 50% AgI: a) glassy layer; b) crystalline layer.

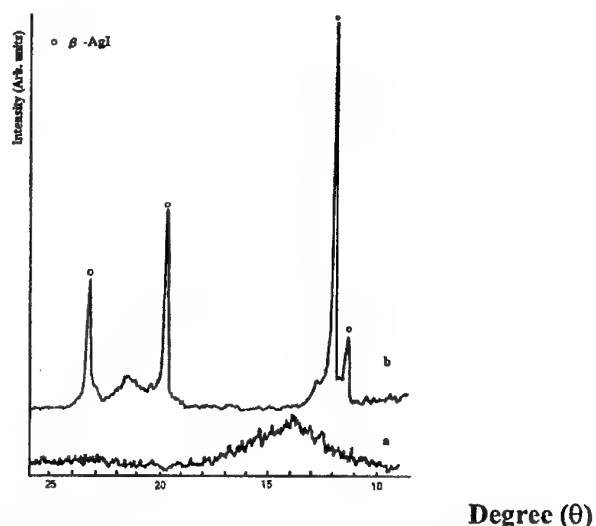


Fig. 2. XRD spectra of sample with composition 50% $2\text{TeO}_2\cdot\text{V}_2\text{O}_5$ , 50% AgI: a) glassy layer; b) crystalline layer.

In the samples from the four component system, containing a constant amount of 50 mol. % AgI, for  $\text{Ag}_2\text{O}$  content from 10 to 15 mol. %, visually homogeneous glasses were obtained. According to the XRD analysis these samples are amorphous. By TEM observation it is found that different kinds of

microaggregation processes take place (Fig. 3a): i) background nanostructure ranged in size between 20 and 50 nm; ii) crystals with sizes about 200-300 nm; iii) droplet-like immiscibility formations as heterogeneous targets for crystal development; iii) silver particles between 10 nm and 200 nm, that are extracted on the replica surface. These particles are presented in Fig. 3b for sample with composition  $20\text{TeO}_2, 15\text{V}_2\text{O}_5, 15\text{Ag}_2\text{O}, 50\text{AgI}$ . According to the histogram (Fig. 4) the size of metal silver particles is situated mainly at two intervals between 5-10 nm and 20-25 nm. They are observed in all samples studied, only in some separated regions and their appearance could be result of reduction processes.

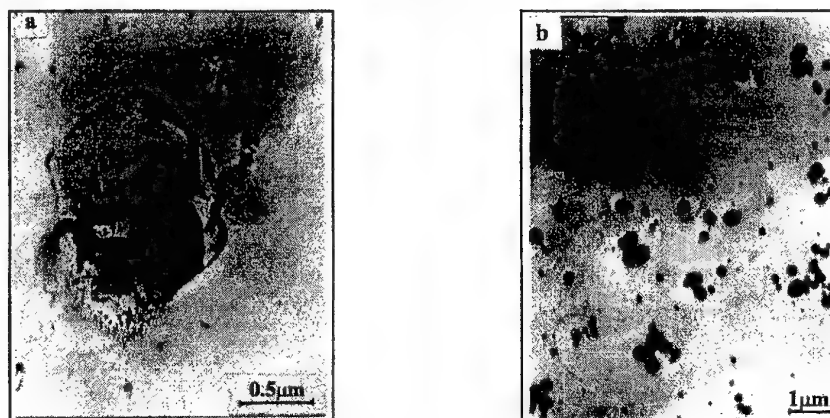


Fig. 3. Microstructure of samples with composition:  
a)  $10\text{TeO}_2, 30\text{V}_2\text{O}_5, 10\text{Ag}_2\text{O}, 50\text{AgI}$ ; b)  $20\text{TeO}_2, 15\text{V}_2\text{O}_5, 15\text{Ag}_2\text{O}, 50\text{AgI}$ .

Their concentration is higher when  $\text{Ag}_2\text{O}$  content increases as it can be seen in (Fig. 5) for one composition of the three component system  $\text{V}_2\text{O}_5\text{-Ag}_2\text{O-AgI}$  containing 30 mol. %  $\text{Ag}_2\text{O}$ . The obtained SAED patterns correspond to pure metal silver (Fig. 5).

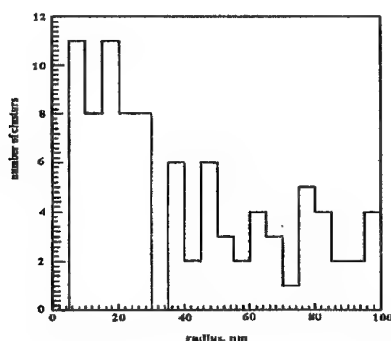


Fig. 4. Histogram showing the distribution of silver particles in sample with composition  $20\text{TeO}_2, 15\text{V}_2\text{O}_5, 15\text{Ag}_2\text{O}, 50\text{AgI}$ .

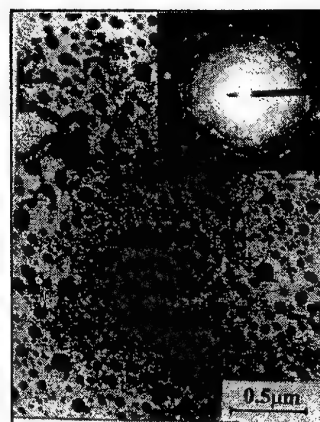


Fig. 5. TEM micrograph and SAED of the sample with composition.

Its presence simultaneously with the main crystalline phase  $\beta\text{-AgI}$ , is confirmed by XRD analysis of glass-crystalline sample of the four component system containing 60 mol. %  $\text{AgI}$  (Fig. 6). The microstructure of these visually glass-crystalline samples depends on the cooling rate applied. By fast cooling in the samples remains an amorphous matrix in which are dispersed droplet-like immiscibility formations and crystals (Fig. 7a). At slow cooling the aggregation trend is better pronounced and allows the crystallisation development in all bulk samples (Fig. 7b).

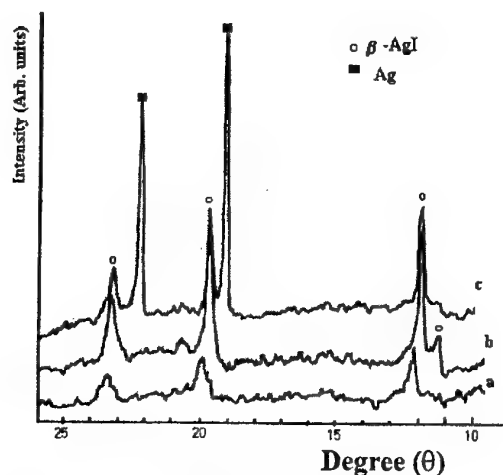


Fig. 6. XRD spectra of:

- a) glass-crystalline sample with composition:  $5\text{TeO}_2, 17.5\text{V}_2\text{O}_5, 17.5\text{Ag}_2\text{O}, 60\text{AgI}$ ;  
 b) glass-crystalline sample with composition:  $10\text{TeO}_2, 15\text{V}_2\text{O}_5, 15\text{Ag}_2\text{O}, 60\text{AgI}$ ;  
 c) crystalline sample with composition:  $10\text{TeO}_2, 15\text{V}_2\text{O}_5, 15\text{Ag}_2\text{O}, 60\text{AgI}$ .

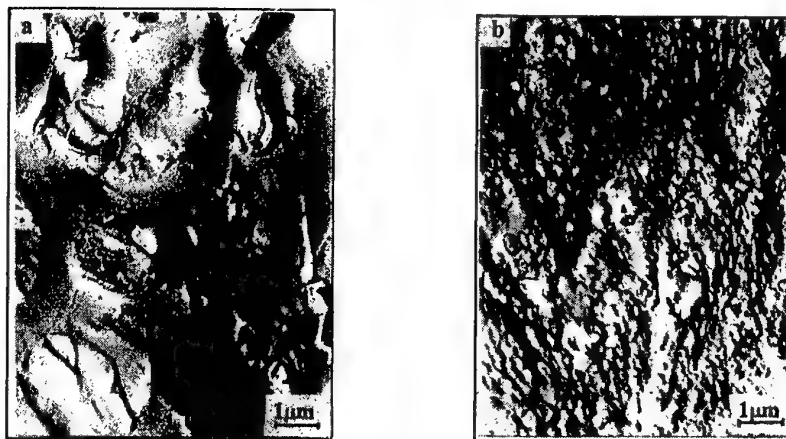


Fig. 7. Microstructure of the samples with the compositions:

- a)  $10\text{TeO}_2, 15\text{V}_2\text{O}_5, 15\text{Ag}_2\text{O}, 60\text{AgI}$ ; b)  $5\text{TeO}_2, 17.5\text{V}_2\text{O}_5, 17.5\text{Ag}_2\text{O}, 60\text{AgI}$ .

#### 4. Conclusions

Depending on the composition and thermal history of the samples various types of nano- and micro-scale heterogeneities were found in the glasses and glass-crystalline materials obtained in the system  $\text{TeO}_2\text{-V}_2\text{O}_5\text{-Ag}_2\text{O-AgI}$ : background nanostructure, nano- and microcrystals, droplet-like immiscibility formations as heterogeneous targets for crystal development and dispersed metal silver particles. The possibility for the appearance of these structures should be taken into account at the synthesis of ionic conductive silver containing solid electrolytes.

#### Acknowledgement

This work was supported by the Bulgarian National Foundation for Science, under Contract No. X-527/2001.

#### References

- [1] C. A. Angel, *Solid State Ionics* **18/19** 72 (1986); *Annu. Rev. Phys. Chem.* **43**, 693 (1992).
- [2] T. Minami, M. Tatsumisago, N. Mashida, *Chim. Chronica, New Ser.* **23**, 227 (1994).
- [3] T. Minami, *Bull. Inst. Chem. Res. Kyoto Univ.* **72**, 305 (1994).
- [4] P. Znasic, *Silikaty* **33**, 169 (1989).
- [5] E. D. Lefterova, P. V. Angelov, Z. B. Stoyanov, Y. B. Dimitriev, *Analytical Laboratory* **6**(3) 1 (1997).

- [6] A. Zahra, C. Zahra, M. Ganteaume, S. Rossignol, B. Tanguy, J. Videau, J. Portier, J. Therm. Anal. **38**, 749 (1992).
- [7] S. Rossignol, J. M. Reau, B. Tanguy, J. J. Videau, J. Portier, J. Non-Cryst. Solids **155**, 77 (1993).
- [8] S. Rossignol, J. Reau, B. Tanguy, J. Videau, J. Portier, J. Dexpert-Ghys, B. Piriou, *ibid.* **162**, 244 (1993).
- [9] J. Dexpert- Ghys, B. Piriou, S. Rossignol, J. M. Reau, B. Tanguy, J. J. Videau, J. Portier, *ibid.* **170**, 167 (1994).
- [10] T. Minami, K. Imazawa, M. Tanaka, *ibid.* **42**, 469 (1980).
- [11] C. D. Yin, T. Osuka, H. Morikawa, F. Marumo, H. Oyanagi, *ibid.* **74**, 237 (1985).
- [12] A. Rajalakshmi, M. Seshasayee, T. Yamaguchi, M. Nomura, H. Ohtaki, *ibid.* **113**, 260 (1989).
- [13] S. Patnaik, A. Rajalakshmi, M. Seshasayee, H. Ohtaki, Solid State Ionics **59**, 229 (1993).
- [14] T. Nishida, H. Ide, Y. Takashima, T. Yagi, S. Tomariguchi, T. Ishizuka, A. Sakai, J. Mat. Sci. **24**, 1687 (1989).
- [15] E. D. Lefterova, P. V. Angelov, N. Nikolova, Y. Y. Ivanova, Y. B. Dimitriev, Proc. XII-th Conf. on Glass and Ceramics, Varna, 24-26 Sept. 1996, Ed. B. Samuneva, Y. Dimitriev, «Science Invest», Sofia, 1997, p. 240.
- [16] E. D. Lefterova, P. V. Angelov, Y. B. Dimitriev, Proc. XIII-th Conf. on Glass and Ceramics, Varna, 29 Sept. - 1 Oct. 1999, Eds. B. Samuneva, S. Bachvarov, I. Gutzov, Y. Dimitriev, «Science Invest », Sofia, 1999, Vol.1 Glass, p.124.
- [17] Y. Dimitriev, Y. Ivanova, M. Dimitrova, E. D. Lefterova, P. V. Angelov, J. Mater. Sci. Lett. **19**, 1513 (2000).
- [18] Y. Dimitriev, M. Mariniv, Y. Ivanova, Compt. Rend. Acad. Bulg. Sci. **25**, 1205 (1972).

## ELECTRICAL SWITCHING IN CHALCOGENIDE GLASSES- SOME NEWER INSIGHTS

S. Asokan

Department of Instrumentation, Indian Institute of Science, Bangalore 560012, India

The recent studies on the switching behavior of several chalcogenide semiconductors indicate that there exists a close relation between the electrical switching and structural effects in these materials; the two network topological Thresholds, namely the Rigidity Percolation and the Chemical Threshold are found to influence considerably the composition dependence of the switching voltages/fields of many memory and threshold switching glasses. Further, changes in the coordination of constituent atoms are found to effect a change in the switching behavior (memory to threshold). Also, an interesting relation has been established between the type of switching exhibited and the thermal diffusivity of the material.

(Received June 25, 2001; accepted September 3, 2001)

**Keywords:** Electrical switching, Chalcogenide glasses, Amorphous semiconductors, Photo-acoustic spectroscopy

### 1. Introduction

Electrical switching in chalcogenide glasses has been discovered by Ovshinsky nearly about three decades ago [1]. Though the promised applications in information storage or power control have not been fully realized, electrical switching has remained to be one of the fascinating properties of these materials.

The relation between switching parameters and other properties of chalcogenide glasses has been a topic of intense investigations for long time. Several investigations have been directed towards understanding the relation between the switching voltages and glass transition temperature [2,3], crystallization temperature [4], electrical resistivity [5], ambient temperature and conductivity activation energy [6], etc., of glassy chalcogenides. In the recent times, considerable attention has been given to understand the influence of the two network topological thresholds, namely the Rigidity Percolation Threshold (RPT) and Chemical Threshold (CT) respectively, on the switching behavior of chalcogenide glasses [7-9]. Rigidity Percolation deals with network connectivity and at the rigidity percolation threshold an equilibrium is established in a chalcogenide network glass, between the degrees of freedom per atom and the number of constraints acting on it [10-13]. For a network with purely covalent bonding, the rigidity percolation occurs at a mean coordination number  $\langle r_c \rangle = 2.4$  [10-13]. If medium range order is taken into account in the constraint balance equation, the percolation threshold may shift to higher  $\langle r_c \rangle$  values [14]. It has also been recently pointed out that in certain glassy systems, the Rigidity Percolation may be spread over a range of composition around the mean-field threshold of  $\langle r_c \rangle = 2.4$  [15,16]. The Chemical Threshold (CT) is usually taken to be the critical composition at which the chemical ordering is maximized in a chalcogenide network glass, with the bonding being fully heteropolar [17]. The stoichiometric glass, which is energetically closest to the crystalline state, is also considered to be a Chemical Threshold in a glassy system.

In this paper, an effort is made to summarize the effect of RPT and CT in the composition dependence of switching fields of a variety of chalcogenide glasses. Further, the role played by the coordination of the constituents, thermal diffusivity, etc. in determining the type of switching exhibited by the sample is discussed.

### 2. Experimental

Bulk, semiconducting chalcogenide glasses have been prepared by vacuum-sealed melt quenching method. Appropriate quantities of high purity constituent elements were sealed in an evacuated quartz ampoule (at  $10^{-5}$  Torr) and slowly heated in a horizontal rotary furnace. The ampoules were maintained at 1000 °C and rotated continuously for about 24 hours at 10 RPM to ensure the homogeneity of the melt. The ampoules are subsequently quenched in a bath of ice water and NaOH mixture to get bulk glassy samples. The amorphous nature of the quenched samples was confirmed by X-ray diffraction. The electrical switching studies are undertaken in an IBM PC controlled system developed in the



laboratory [18]. Samples polished to the required thickness are mounted in a holder made of brass, in between a flat plate top electrode and a point contact electrode using a spring loading mechanism. A constant current is passed through the sample and the voltage developed across the sample is measured.

### 3. Results and discussion

#### i) Effect of topological thresholds on switching voltages

Fig. 1(a) shows the I-V characteristics of  $\text{Ge}_{20}\text{Te}_{80}$  and  $\text{Ge}_{23}\text{Te}_{77}$  glasses from the series  $\text{Ge}_x\text{Te}_{100-x}$  ( $15 \leq x < 25$ ). They indicate that these samples exhibit memory switching. The switching voltages of  $\text{Ge}_x\text{Te}_{100-x}$  glasses lie in the range 4-11 kV/cm.

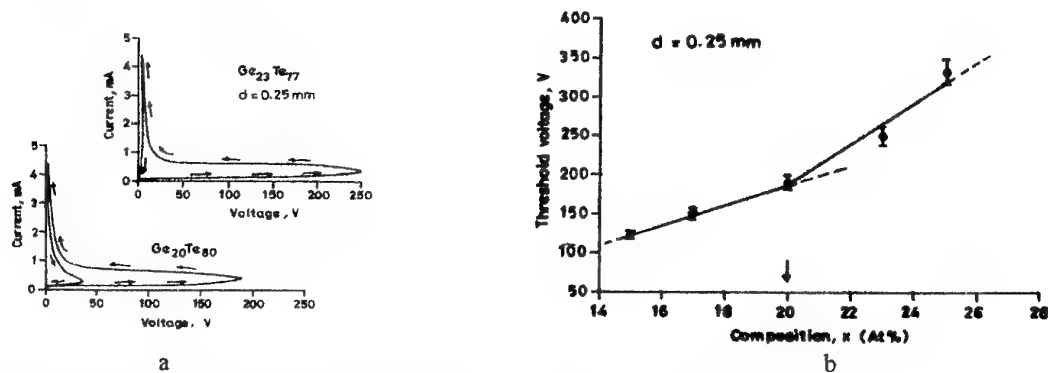


Fig. 1. a) I-V characteristics of  $\text{Ge}_{20}\text{Te}_{80}$  and  $\text{Ge}_{23}\text{Te}_{77}$  glasses, b) Composition dependence of switching voltages of  $\text{Ge}_x\text{Te}_{100-x}$  glasses.

The variation of switching voltages with the composition of  $\text{Ge}_x\text{Te}_{100-x}$  glasses is presented in Fig. 1(b), which shows that the switching voltages of  $\text{Ge}_x\text{Te}_{100-x}$  samples increase with Ge content (x) in the composition range  $15 \leq x < 20$ . At the composition  $x = 20$ , there is a sharp change in slope (lower to higher) in the composition dependence of switching voltage. It has been identified long back that the composition  $x = 20$  in the  $\text{Ge}_x\text{Te}_{100-x}$  system corresponds to its percolation threshold [19] and the average coordination for this composition ( $\langle r \rangle$ ) is 2.4, the mean field estimate of the RPT according to a Phillips theory [10-13]. Hence the sharp slope change in the switching voltages of  $\text{Ge}_x\text{Te}_{100-x}$  glasses observed at  $x = 20$  can be associated with the Rigidity Percolation. In this system, it has not been possible to see the influence of Chemical Threshold on the switching voltages, as the composition range of bulk glass formation is below the CT. Fig. 2 (a) shows the I-V characteristics of  $\text{Ge}_{7.5}\text{As}_x\text{Te}_{92.5-x}$  glass, representing the series  $\text{Ge}_{7.5}\text{As}_x\text{Te}_{92.5-x}$  ( $15 \leq x \leq 60$ ). It can be seen from this figure that Ge-As-Te samples exhibit memory type electrical switching at fields around 7 kV/cm. The composition dependence of threshold fields ( $E_t$ ) of  $\text{Ge}_{7.5}\text{As}_x\text{Te}_{92.5-x}$  glasses, is shown in Fig. 2 (b), which indicates that  $E_t$  increases linearly with x in the composition range  $15 \leq x \leq 25$ . At  $x = 25$ , a distinct change in slope is observed. It is interesting to note that the composition  $x = 25$  corresponds  $\langle r \rangle = 2.4$ , the RPT of the  $\text{Ge}_{7.5}\text{As}_x\text{Te}_{92.5-x}$  glassy system, and the slope change seen in  $E_t$  of Ge-As-Te glasses, can therefore be clearly associated with rigidity percolation. Above the RPT, the switching fields of  $\text{Ge}_{7.5}\text{As}_{50}\text{Te}_{42.5}$  increase again with composition, but with a higher slope. Further, a reversal in trend is observed at the composition  $x = 50$ , which leads to a minimum in  $E_t$  at  $x = 52.5$ . The composition at which a minimum is seen in  $E_t$  of  $\text{Ge}_{7.5}\text{As}_x\text{Te}_{92.5-x}$  glasses, is likely to correspond to the chemical threshold of the system. The memory switching in chalcogenide glasses is known to involve crystallization of the sample, which in turn requires structural reorganization [20]. With increasing rigidity, the network becomes less flexible and structural reorganization becomes more difficult. Hence, memory-switching fields is likely to progressively increase with increasing network rigidity and one could expect a slope change (from a lower to a higher value) in the composition dependence of switching voltages/fields across the percolation threshold [7].

Further, in a glassy system, the chemically ordered glass can be considered to be energetically closest to the crystalline phase [7,8]. Therefore, the driving force required for the crystallization is the least for this sample. Based on this, one could expect the memory-switching voltages to exhibit a minimum at the chemical threshold of a glassy system. Thus the observed anomalies in the composition dependence of switching voltages/fields of Ge-Te and Ge-As-Te glasses at the RPT and CT, are consistent with the expectations.

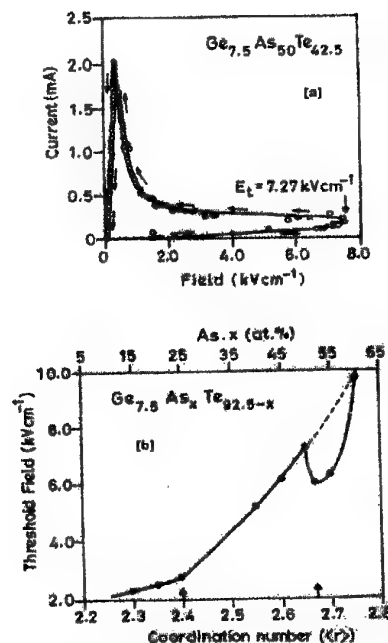


Fig. 2. a) I-V characteristics of a representative Ge<sub>7.5</sub>As<sub>50</sub>Te<sub>42.5</sub> Glass, b) The composition dependence of threshold fields of Ge<sub>7.5</sub>As<sub>x</sub>Te<sub>92.5-x</sub> Glasses.

## ii) Role of coordination of constituents in switching behavior

Fig. 3 shows the I-V characteristics and switching behavior of Al<sub>20</sub>As<sub>x</sub>Te<sub>80-x</sub> glasses, which indicates that there is a change in the switching behavior of the sample with composition. Al-As-Te samples with lower arsenic concentrations (<5 at. %) exhibit memory switching and those with higher Al concentrations (> 5 at. %) show threshold behavior. Magic Angle Spinning Nuclear Magnetic Resonance (MASS NMR) studies show that in Al<sub>20</sub>As<sub>x</sub>Te<sub>80-x</sub> glasses [21], aluminum has two different coordination environments, namely 4-fold and 6-fold respectively. At lower arsenic concentrations, the ratio between 4-fold and 6-fold coordinated Al atoms is around 50 %. With increasing x, the fraction of 4-fold coordinated Al atoms decreases and it becomes zero around 25-atom % of arsenic. It is clear from the MASS NMR studies that in glasses, which exhibit threshold behavior, Al is predominantly 6-fold coordinated. The 6-fold coordinated aluminum atoms lead to increased structural cross-linking. In these samples with higher network connectivity, structural reorganization required for memory switching becomes difficult and threshold behavior is favored. On the other hand, in samples with lower arsenic content, the 4-fold coordinated Al atoms provide the structural flexibility and promote memory switching.

It is also interesting to note here that the As-As bond length is much smaller than that of Te-Te. Therefore, the free rotation of molecules becomes difficult at higher arsenic proportions, because of the higher energy barrier for rotation. The formation of arsenic pair-locks also contributes for the change in the switching type observed at higher arsenic content.

## iii) Thermal diffusivity and switching behavior

The variation of thermal diffusivity of Al<sub>20</sub>As<sub>x</sub>Te<sub>80-x</sub> glasses with x, has been obtained using Photo-Acoustic Spectroscopy (PAS) [22]. The thermal diffusivity ( $\alpha_s$ ) of Al<sub>20</sub>As<sub>x</sub>Te<sub>80-x</sub> glasses has been found to increase progressively with arsenic content and culminates in a peak around x = 20. Further, the PAS measurements reveal that the thermal diffusivity of the Al-As-Te samples that show memory behavior, is lower than that of samples exhibiting threshold switching [22]. Also, the electrical conductivity of samples with lower arsenic content is higher than that at higher arsenic content. Under the influence of electric field, the glass specimens with lower arsenic content will experience a higher Joule heating due to the higher conductance. The lower  $\alpha_s$  in these samples also implies a higher resistivity to the flow of diffusing thermal waves. This means that the rate at which the heat is removed from the regions carrying the current (filament region), is lower in samples with lower arsenic content. As a consequence, there will be a rise in temperature, which can trigger phase transformation and memory switching. On the other hand, in samples with higher arsenic percentages, the lower electrical conductivity in conjunction

with higher thermal diffusivity may preclude high enough temperature rise in their conducting region to cause any structural phase transformation. In such a case, the threshold behavior is seen.

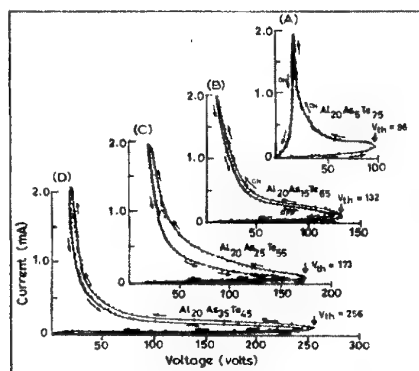


Fig. 3. Composition dependent switching behavior of  $\text{Al}_{20}\text{As}_x\text{Te}_{80-x}$  glasses.

#### 4. Conclusion

Electrical switching studies on a variety of chalcogenide glasses indicate that the network topological effects such as Rigidity Percolation and the Chemical Threshold influence considerably the composition dependence of the switching voltages of these materials. Further, factors like coordination of the constituent atoms, thermal diffusivity, etc., are found to determine type of switching exhibited (memory or threshold) by chalcogenide glasses.

#### Acknowledgements

The author expresses his thanks to his co-workers Dr. R.Chatterjee, Dr. S.S.K.Titus, Dr. S.Prakash, Dr. S.Murugavel, Dr. R.Aravinda Narayanan and Dr. Srirang Manohar.

#### References

- [1] S. R. Ovshinsky, Phys. Rev. Letts. **21**, 1450 (1968).
- [2] A. Alegria, A. Arrabarrena, F. Sanz, J. Non-Cryst. Solids **58**, 17 (1983).
- [3] S. Prakash, S. Asokan, D. B. Ghare, Semicond. Sci. Tech. **9**, 1484 (1994).
- [4] S. S. K. Titus, R. Chatterjee, S. Asokan, A. Kumar, Phys. Rev. B **48**, 14650 (1993).
- [5] N. A. Hegab, M. Fadel, K. A. Sharaf, Vacuum **46**, 1351 (1995).
- [6] M. F. Kotkata, M. A. Afifi, H. H. Habib, N. A. Hegab, M. M. Abdel-Aziz, Thin Solid Films **240**, 143 (1994).
- [7] R. Aravinda Narayanan, S. Asokan, A. Kumar, Phys. Rev. **B54**, 4413 (1996).
- [8] R. Aravinda Narayanan, S. Asokan, A. Kumar, Phys. Rev. **B63**, 092203-1 (2001).
- [9] J. T. Devaraju, B. H. Sharmila, S. Asokan, K. V. Acharya, Philos. Mag. B (2001) (in press).
- [10] J. C. Phillips, J. Non-Cryst. Solids **34**, 153 (1979).
- [11] J. C. Phillips, M. F. Thorpe, Solid State Commun. **53**, 699 (1985).
- [12] P. Boolchand, M. F. Thorpe, Phys. Rev. **B50**, 10366 (1994).
- [13] A. K. Varshneya, A. N. Sreeram, D. R. Swiler, Phys. Chem. Glasses **34**, 179 (1993).
- [14] K. Tanaka, J. Non-Cryst. Solids, **103**, 149 (1988).
- [15] X. Feng, W. J. Bresse, P. Boolchand, Phys. Rev. Letts. **78**, 4422 (1997).
- [16] D. Selvanathan, W. J. Bresser, P. Boolchand, B. Goodman, Sol. State Commun. **111**, 619 (1999).
- [17] G. Lucovsky, T. M. Hayes in Amorphous Semiconductors Ed. M. H. Brodsky, Springer-Berlin, 197a, p.215.
- [18] R. Chatterjee, K. V. Acharya, S. Asokan, S. S. K. Titus, Rev. Sci. Instrum. **65**, 2382 (1994).
- [19] S. Asokan, G. Parthasarathy, E. S. R. Gopal, Philos. Mag. **57**, 49 (1987).
- [20] D. Adler, Sci. American **236**, 3 (1977).
- [21] S. Murugavel, S. Asokan, Phys. Rev. **B58**, 3022 (1998).
- [22] Srirang Manohar, S. Murugavel, S. Asokan, Phys. Rev. B (submitted).

## NON-DESTRUCTIVE EVALUATION OF PURIFIED $\text{HgI}_2$ STARTING MATERIALS

M. Schieber, A. Zuck, M. Lukach

Graduate School of Applied Science, The Hebrew University of Jerusalem, Jerusalem 91904, Israel

In order to prepare high purity starting materials it is necessary to make thorough impurity analyses. The chemical analytical methods which were used during 25 years at EG&G, EM, Inc. and at Sandia National Laboratories-Livermore Ca. to identify these impurities were ICP or SSGMS. However despite the many impurities identified in the ppm and even in the ppb level no direct correlation could be obtained between the impurity content and the performance of the nuclear radiation detectors investigated. The present paper will review results obtained on various purified  $\text{HgI}_2$ , using a non-destructive method like photoluminescence that correlates with detector performance. In fact, it is possible to correlate the presence and the intensity ratio of specific bands in the photoluminescence spectrum of a  $\text{HgI}_2$  crystal to its impurity content and stoichiometry.

(Received July 12, 2001; accepted September 3, 2001)

*Keywords:* Mercuric iodide, Photoluminescence, Purification methods

### 1. Introduction

Mercuric iodide, due to high atomic numbers of the elements (80-53), large band gap (2.15 eV) and the low energy needed to generate one electron-hole pair, is one of the most interesting materials for  $\gamma$  and X-rays detectors at room temperature [1]. The potential for manufacturing spectrometer from  $\text{HgI}_2$  has been demonstrated [2], but the role of defects and impurities in the as-grown crystals is not well understood. What is well known is the fact that by improving the purification and/or by adding new purification steps the quality of the nuclear detector response was improved. Which is the bad impurity, which can be accused to be the major culprit for carrier recombination and trapping is not known very accurately. Correlation between detector quality and stoichiometry, structural imperfections in the crystal and impurity contamination have been, extensively studied [3-7]

Mercuric iodide having an adequate purity for successful crystal growth and device preparation can be prepared with a certain sequence of well established purification steps [1]. However, the optimization of the purification process is limited by the lack of reliable analytical methods for measuring impurities in this material. As shown by Merz and al. [8] Bao et al. [9], Schieber et al., [10], the  $\text{HgI}_2$  ability to produce high-quality detectors [11] may be tested by a non-destructive method like photoluminescence (PL). In particular, it is possible to correlate the presence and the intensity ratio of specific bands in the PL spectrum of  $\text{HgI}_2$  crystal to the detector grade that may be correlated by using that starting material. Examples will be given to show the PL Merz-Bao procedure is used to characterize  $\text{HgI}_2$  crystal growth starting materials.

### 2. Photoluminescence studies

The classical paper by Merz [8] showed that the PL bands change with purification sequence as given in Fig. 1 One could clearly see that band # 2 increases with each step of sublimation of a commercial starting material, by which every x represents one cycle of sublimation and 4x means four cycles of sublimation. Band #3 decreases while band #1 is also changed.

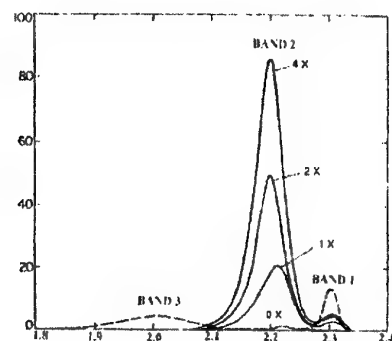


Fig. 1. Photoluminescence at 90K of  $\text{HgI}_2$  powders, commercially purchased (0x) and after several cycles of sublimation, 1x, 2x, 3x and 4x meaning the number of sublimation cycles that the material underwent. (reprinted from Ref. 14).

The PL spectrum of  $\text{HgI}_2$  is usually divided in two main regions. The near band gap region, or band-1, dominated by excitonic transitions, and the long wavelength region, which includes several broad emissions labeled band-2, band-3 and band-4. The excitonic region consist of at least 26 narrow emission lines [13], attributed to free excitons, bound excitons and excitonic phonon replicas [14]. The band-2, centered at about 560 nm, is the main spectral component of the PL spectra of  $\text{HgI}_2$ . It is attributed to iodine deficiency [8]. A third and a fourth band (band-3 and band-4), attributed to impurities present in the material [14], have been observed in the spectra at 620 and 775 nm, respectively.

The defects and impurities responsible of these PL bands play a major role determining the detector performance [8,9]. Good crystallinity is testified by a relatively strong and narrow band-1, and is therefore advisable for high quality detectors. The correlation of band-2 to detector performance is still not clear [9], but certainly the presence of this band is related to iodine deficiency and therefore must be kept as low as possible to avoid stoichiometric defects. The third band, which is induced by contamination impurities, must be avoided for high quality detector preparation.

### 3. Examples of $\text{HgI}_2$ samples analyzed

In order to explain better the correlation between various purification steps and the PL results we are reproducing some of the published results [10] (produced by one of the co-authors A. Zuck for his M.Sc Thesis Hebrew University of Jerusalem). The PL studies were performed at 10 K on various polycrystalline-starting materials of  $\text{HgI}_2$  and compared with a high quality single crystal from which spectrometric grade nuclear radiation detectors were prepared. The materials investigated were: 1. Commercial purchased powder of  $\text{HgI}_2$  which has a poor purity and which cannot be used to produce nuclear radiation detectors, 2. Aqueous synthesized materials from  $\text{HgCl}_2$  and KI, 3. Same as #2 synthesized powders but using a different stirring rate, 4. Conventional  $\text{HgI}_2$  4XMSI purification method, which means, four repeated open tube sublimations (4X), melting (M) and followed by an additional close tube sublimation (S) in presence of iodine (I) [1,11], 5. Re-crystallized by Physical Vapor Deposition from 4XMSI source material, 6. Re-crystallized material from commercial  $\text{HgI}_2$  precursor in presence of polyethylene. In this case the source material is mixed with 2% in weight of polyethylene powder and then heated to 250 °C. The  $\text{HgI}_2$  condenses at the cold end of the ampoule. This purification method is called PE treatment [1,10,11] and is known in the literature as platelet growth 7. Same preparation procedure as for #6, but where the polyethylene is in form of a sheet, 8. Same preparation as #7 followed by another PE treatment (2xPE), 9. Single crystal grown from starting materials as #4, from which good detectors were prepared, and which was milled and then re-crystallized as #6. The samples were characterized by low temperature (10 K) photoluminescence. The spectra were obtained using the 488 nm line of an  $\text{Ar}^+$  laser, with 0.1  $\text{Wcm}^{-2}$  power density and 1 mm laser spot diameter. The spectral resolution was 3 nm.

### 4. Results and discussion

The PL spectra of the nine samples are reported in Fig. 2. The PL spectrum of the commercial powder is the most structured one. On one side it is characterized by a very sharp and intense excitonic band and a relatively low band-2, meaning that the powder grains have good stoichiometry and crystalline

perfection, on the other side a strong impurity band-3 appears at 620 nm. This confirms the importance of purifying the commercial powder before using it as a starting material for  $\text{HgI}_2$  crystal growth. Better results can be obtained by controlled aqueous solution synthesis. Here, while maintaining a good stoichiometry, the impurity content is much less (shown by a reduction of a factor five of the band-3 intensity) than in the commercial powder and the inclusion seems to be influenced by stirring speed (see differences between samples 2 and 3). As expected, the standard 4XMS procedure [1] depletes the iodine content of the powder (see the strong reduction of band-1 respect to band-2). On the other side the impurity band is completely disappeared, in agreement with previous studies [8]. Re-crystallization of 4XMSI powders (sample 5), worsens the stoichiometry ratio of precursors, while leaving the impurity band-3 fairly low. Much better results can be obtained by PE treatment of the commercial Baker  $\text{HgI}_2$  powders (samples #6-#8). Here, as in the 4XMSI sample before re-crystallization (sample 4) we have a strong predominance of stoichiometry defect related band-2 and no impurity related band-3. The same considerations may be done for sample 7 and 8, where in the latter, however, we do not observe any improvement repeating two times the PE treatment. Impurity related band reappears in the control sample 9, probably due to the additional processing steps as milling, etc. Even in this sample the iodine deficiency related band -2 is strongly predominant.

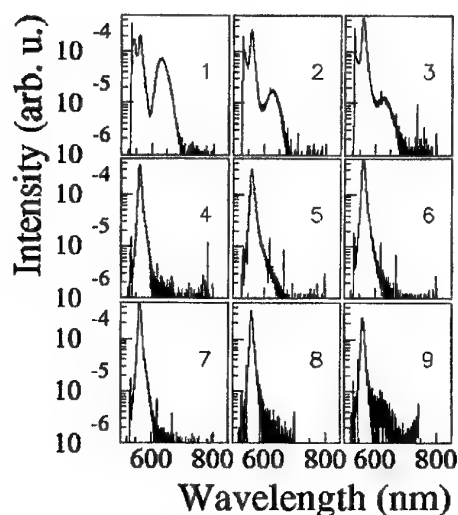


Fig. 2. Photoluminescence spectra of different  $\text{HgI}_2$  precursor samples. The scale intensity scale is the same for each spectra. The sample number is reported in each panel.

In the search of highly purified  $\text{HgI}_2$  precursors with the correct stoichiometry, the same approach was used to determine the detector performance by PL measurement. This assures a precursor quality as near as possible to the need for high quality detector fabrication.

A strict relation of band-3 intensity and the detector quality is reported in the literature [9]. Fig. 3 shows the relative intensity of the impurity related band in our samples. We recorded several spectra for each sample to overcome possible in-homogeneities in these powder samples. Obviously, preparing the  $\text{HgI}_2$  precursors in a controlled environment and choosing the correct stirring speed can obtain a strong reduction of the impurity band. The best aqueous solution sample shows an impurity content that is only slightly higher than the standard 4XMSI treated samples (#4, #5 and #9). A strong improvement in reduction of the impurity content is achieved via PE treatment of the precursors. PE treatment reduces the band-3 relative intensity more than one order of magnitude. The change of polyethylene form from powder to foil is not affecting its purifying ability. Second PE treatment does not improve the impurity reduction. As a matter of fact, all the PE treated samples have impurity content less than the detector grade  $\text{HgI}_2$  crystal (sample #9).

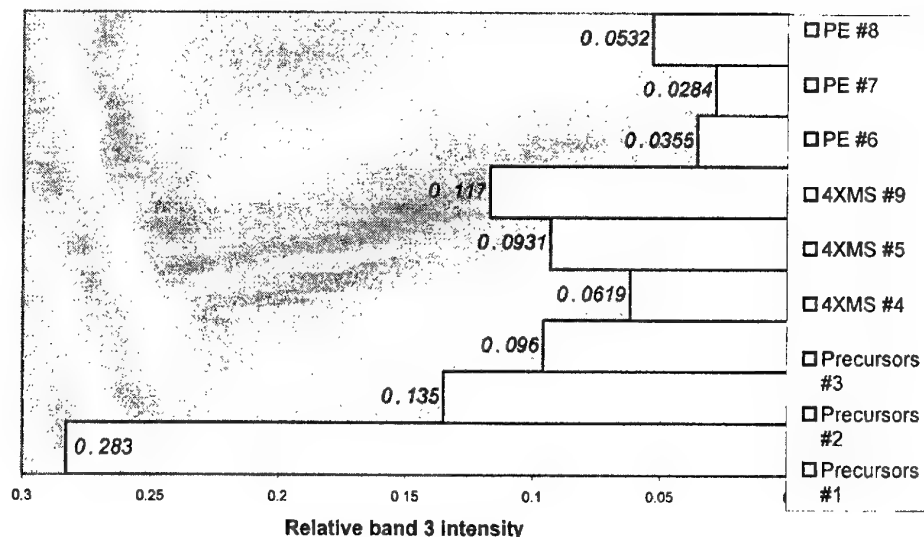


Fig. 3. Relative intensity of band-3, normalised to the total spectrum integrated intensity.

No KI-etching was applied to the powder samples before PL measurements. Our spectra are therefore affected by aging effect. As shown by Bao et al. [15,16], it mainly affects the relative importance of the excitonic lines inside band-1. However, the detector grade is influenced by the ratio between band-2 and a specific line in band-1 (line P2) which is unaffected by aging and dominates the band-1 of an aged sample [9]. We therefore simply reported in Fig. 4 the ratio between band-2 and band-1 integrated intensities. As previously observed [8], the sublimation treatments depletes the iodine content of  $\text{HgI}_2$ , which gives a band-2 to band-1 ratio of treated powders at least 1 order of magnitude higher than in aqueous solution grown precursors. However, the sample which has undergone to standard PE treatment (poly-ethylene in form of powder), shows a strong reduction of the ratio, which is only a factor three higher than in the aqueous solution samples, therefore displaying a relatively good stoichiometry.

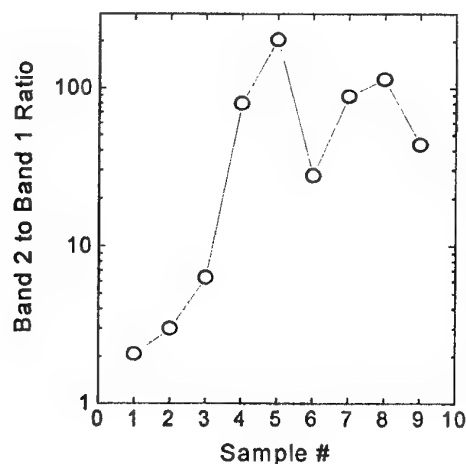


Fig. 4. Band-2 to band-1 ratio of the PL spectrum of  $\text{HgI}_2$  at 10k shown in Fig. 2.

## 5. Conclusions

The PL characterization of  $\text{HgI}_2$  precursors presented in this work suggests the PE treatment as the optimum both for the impurity content and for the relatively good stoichiometry of the resulting powders. Over the standard 4XMSI has the advantage of a lower iodine deficiency that makes it preferable for detector quality fabrication. The mechanism involved in this purification treatment is still under study. It was speculated that polyethylene influences the vapor transport and the mechanism of  $\text{HgI}_2$  formation by reacting with impurities or mercuric iodide at the crystal growth surface [11]. We have also demonstrated the ability of PL to provide that analytical method for measuring impurities in this material so important for a real optimization of the growth process.

## References

- [1] M. Schieber, H. Hermon, M. Roth, MRS proceedings (1993).
- [2] J. P. Ponpon, M. Sieskind, Nucl. Instr. and Meth. **A380**, 173 (1996). See also many papers published on this subject.
- [3] M. Schieber, I. Beinglass, C. Dishon, A. Holzer, G. Yaron, IEEE Trans. Nucl. Sci. **NS-25**, 644 (1978).
- [4] I. Beinglass, C. Dishon, A. Holzer, M. Schieber, J. Cryst. Growth **42**, 166 (1977); I. Beinglass, C. Dishon, A. Holzer, S. Ofer, M. Schieber, Appl. Phys. Lett. **30**, 611 (1977).
- [5] A. Tadjine, D. Gosselin, J. M. Koebel, P. Siffert, Nucl. Instr. and Meth. **213**, 77 (1983).
- [6] Y. F. Nicolau, Nucl. Instr. and Meth. **213**, 13 (1983).
- [7] E. S. Cross, G. Buffleben, E. Soria, R. James, M. Schieber, R. Natarajan, V. Gerrish, Nucl. Instr. and Meth. **A380**, 23 (1996).
- [8] J. L. Merz, Z. L. Wu, L. Van Den Berg, W. F. Schneppe, Nucl. Instr. and Meth. **213**, 51 (1983).
- [9] X. J. Bao, T. E. Schlesinger, R. B. James, S. J. Harvey, A. Y. Cheng, V. Gerrish, C. Ortale, Nucl. Instr. and Meth. **A317**, 194 (1992).
- [10] M. Schieber, A. Zuck, S. Sanguinetti, M. Montalti, L. Melekhov, J. Nissenbaum, E. Grilli, M. Guzzi, R. Turchetta, W. Dulinski, D. Husson, J. L. Riester, Nucl. Instr. and Meth. **428**, 25 (1999).
- [11] P. Faile, A. J. Dabrowski, G. C. Huth, J. S. Iwanczyk, J. Cryst. Growth **50**, 752 (1980).
- [12] A. Burger, D. Nason, L. Van Der Berg, M. Schieber, "Growth of Mercuric Iodide", in Semiconductors for Room temperature Nuclear detector Applications, edited by T. E. Schlesinger and R. B. James, Semiconductors and Semimetals Vol. **43**, p.86, (Academic Press, San Diego, 1995).
- [13] X. J. Bao, T. E. Schlesinger, R. B. James, C. Ortale, L. Van Der Berg, J. Appl. Phys. **69**, 2951 (1990).
- [14] I. Akopyan, B. Novikov, S. Permogorov, A. Selkim, V. Travnikov, Phys. Status Solidi **B70**, 353 (1975).
- [15] X. J. Bao, R. B. James, T. E. Schlesinger, "Growth of Mercuric Iodide", in Semiconductors for Room temperature Nuclear detector Applications, edited by T. E. Schlesinger and R. B. James, Semiconductors and Semimetals Vol. **43**, p.169, (Academic Press, San Diego, 1995).
- [16] X. J. Bao, R. B. James, C. Y. Hung, T. E. Schlesinger, A. Y. Cheng, C. Ortale, L. Van Der Berg, SPIE Proc. **1736**, 60 (1992).



## MnS AND CdS CLUSTERS ENCAPSULATED IN NATURAL ZEOLITES

F. Iacomi

Department of Physics, "Al. I. Cuza" University, R-6600, Iasi, Romania

MnS and CdS clusters were synthesized inside some natural zeolite frameworks by treating the  $\text{Mn}^{2+}$ ,  $\text{Cd}^{2+}$  ion exchanged forms with 1 molar aqueous solution  $\text{Na}_2\text{S}$ . The optical and EPR spectra suggest that semiconductor clusters are formed into the zeolite channels. The absorption edge changes as a function of cluster-cluster contact distance in the zeolite (from 475 nm, for clinoptilolite-CdS, to 350 nm, for laumontite-CdS). The crystalline fields of exchange sites determines the manganese species and the nature of MnS clusters ( $E_g = 3.1 - 4.66$  eV). The formation of semiconductor clusters into zeolites modifies the zeolite electrical properties.

(Received June 25, 2001; accepted September 3, 2001)

*Keywords:* Zeolite, MnS clusters, CdS clusters, Size effects.

### 1. Introduction

Recent advances in semiconductor cluster synthesis have opened the door towards systematic studies of small clusters in the condensed phase. Clusters with diameters ranging from 10 to 150 Å can be synthesized in a variety of media such as polymers, glasses, zeolites [1,2]. Size dependence of their optical, electronic and possibly other properties dictates that the clusters exhibit a narrow distribution of their average diameters.

The zeolite structures allow to vary the cluster concentration, and the intercluster geometry in a controlled manner over the periodicity defined by the host zeolite lattice [3,4]. Host matrices like zeolites reduce the interchain and interlayer perturbation often encountered in other low dimensional solids [5].

In this work we report our observations of small MnS and CdS clusters formed inside the channels of two natural zeolite frameworks: microcrystalline clinoptilolite and laumontite single crystal. Clinoptilolite is one of the most abundant natural zeolite and has a broad spectrum of industrial applications. The clinoptilolite structure exhibits three types of structural channels confined by tetrahedral ring systems. A and B channels run parallel to  $c$ -axis and are confined by ten- and eight-membered rings of tetrahedra with a highly disordered Si, Al distribution ( $7.05 \times 4.25$  Å respectively  $4.60 \times 3.95$  Å). C channels which are determined by another set of eight-membered rings run parallel to  $a$  axis and the [102] direction. The channel system is two-dimensional parallel to (010). Exchange cations (Na, K, Ca, Mg) exhibit a coordination to framework oxygens and water molecules in the channels [6,7]. Laumontite, a less common zeolite, is a monoclinic mineral characterized by single 4 - ring tetrahedral chains as secondary building units and large channels of ten - membered tetrahedral rings ( $4.6 \times 6.4$  Å) which are parallel to  $c$ -axis. The channels are occupied by Ca and  $\text{H}_2\text{O}$  and minor Na and K [8,9].

The optical and electrical properties of semiconductor clusters in zeolites were investigated.

### 2. Experimental

The semiconductor clusters were prepared in water media, according to the procedure of Barnakov et al. [10], who noted that the stability of the samples obtained by this method is very high. In order to remove the impurities, the powdered clinoptilolite, from Mărsid-Romania, was first submitted to an acid treatment, using 1N HCl solutions [11]. The zeolites in their sodium cation form were first thermally treated at 673K during 4 h and then ion-exchanged by treating with 0.1 N aqueous cadmium (pH = 5.5) or manganese nitrate solutions at 296K (pH= 5.8), using a solid/liquid ratio of 1/50. The ion loaded zeolites, were washed and dried at 378 K and then submitted to a sulfidation process with 1M  $\text{Na}_2\text{S}$  solution, at room temperature, during 12 h (S/L=1/50). In such a

process CdS and MnS clusters precipitate in the zeolite framework and Na-form of zeolite was regenerated. The atomic absorption method evidenced a S/Cd ratio of 3.51 and a S/Mn ratio of 1.1.

X-ray powder diffraction patterns for these materials showed that zeolite crystallinity was maintained during synthesis. Most notable was that no peaks for the bulk semiconductor phase were evident in the powder data.

The optical absorption spectra at 300 K were obtained using a SPECORD UV/VIS spectrophotometer in the wavelength range 300-800 nm. Luminiscence spectra were also obtained at room and liquid-nitrogen temperature with pulsed excitation ( $\lambda=337.1$  nm,  $\nu=72$  Hz,  $\tau=10^{-8}$  s, 1.6 kW). EPR measurements were performed at room temperature with a RADIOPAN spectrometer in X band.

Measurements of the electric resistance as a function of temperature were made in air, in the range of 293 - 794 K, by means of an experimental set-up using a KEITHLEY 6517A instrument. Pellets of 7mm diameter and 1mm thick were prepared by pressing the powdered samples at 10 tf/cm<sup>2</sup>.

### 3. Results and Discussion

#### 3.1. Optical absorption

The optical absorption spectra give the quantization effect as the estimation of band gap (Fig.1). It is evident that discrete CdS clusters interconnect electronically by quantum tunneling forming a semiconductor supercluster with behavior intermediate between that of discrete clusters and bulk semiconductor ( $E_g=2.76$  eV,  $E_g = 3.55$  eV). This suggests that using two types of zeolites as template can be built with the same (CdS)<sub>4</sub> building block two types of superclusters [12]. The data showed an orientational effect on the optical properties of CdS superclusters. The absorption edge changes as a function of cluster-cluster contact distance in the zeolite (from 450 nm, for CLI-CdS, to 350 nm, for LAU-CdS). Because strong coupling with the host lattice occurs through the interaction between Cd and framework oxygen, the phonon broadening becomes important. The partial occupancy of zeolite sites by Cd<sup>2+</sup> produces CdS supercluster size distributions in the zeolite lattice rather than the more desirable homogeneous semiconductor superlattice.

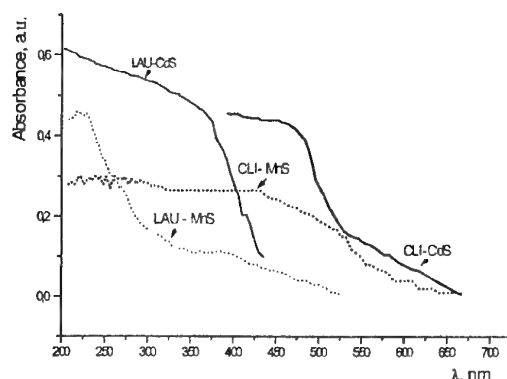


Fig. 1. Absorption spectra of MnS and CdS clusters in natural zeolites.

These are the first experimental data on MnS clusters encapsulated in zeolites. The S-S and Mn-Mn distances and atomic charges are responsible for the bandwidths [13]. Tappero and Lichanot investigated the geometry and electronic structure of bulk  $\alpha$ -MnS. The band structures and their associated densities of states indicated a large hybridization between the sulfur p and manganese d orbitals. The value of the gap was closed to 1.5 eV and was underestimated by 1.2 eV as regarding the experimental value of Sato et al. [14]. The  $\beta$  band structure (bandwidth = 3.81 eV) was ascribed to the 0.44 e charge transfer from S<sup>2-</sup> to Mn<sup>2+</sup> with respect to ideal ionic configuration. The optical spectrum of MnS-LAU shows three partially resolved quantum excitonic peaks (387 nm, 309 nm, 266 nm) while the MnS - CLI shows a plateau in the 318 - 427 nm region and an excitonic peak at 530 nm.

### 3.2. Photoluminescence

Photoluminescence of semiconductor clusters provide different energy states available between valence band and conduction band responsible for radiative recombination.

The room-temperature spectra of CdS doped zeolites are characterized by broad-band emission consisting of two main bands (Fig.2, tab.1)[15].

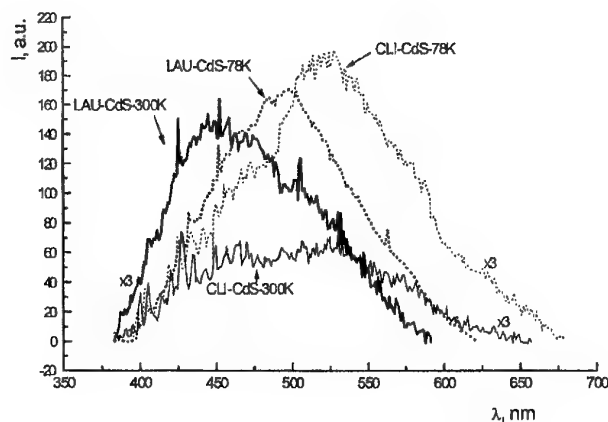


Fig. 2. Room- and low temperature emission spectra of CdS in natural zeolites .

For monodisperse particles with highly symmetric shapes, there exists sharp resonances in the optical region, corresponding to the natural modes of oscillation of the structure. When the wavelength approaches to the absorption edge, the local field intensity at the surface increases for small clusters and decreases for large particles. This is due to the sensitivity of the structural resonance peaks to the absorption. It is important to realize that although these sharp resonance peaks cannot be observed for an ensemble of particles with broad size distribution [16]. The local field effect is shown to be substantial for semiconductor clusters encapsulated in clinoptilolite. In order to investigate the main photoluminescence bands a background correction was carried out by a spline fit, and the corrected spectrum was deconvoluted into Gaussian components. The results are shown in Table 1.

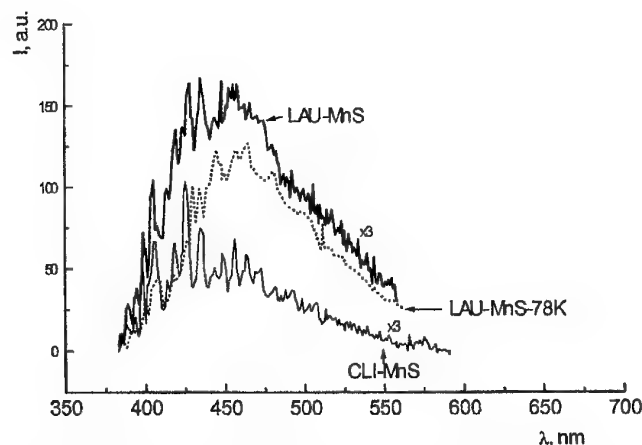


Fig. 3. Room- and low-temperature emission spectra of MnS in natural zeolites.

Table 1. The main emission bands of photoluminescence spectra.

Sample	Emission bands at 300K, nm	Emission bands at 78K	Sample	Emission bands at 300K, nm	Emission bands at 78K, nm
CLI-CdS	444 520	442 520 623	CLI-MnS	422 467	422 467
LAU-CdS	439 499	441 495	LAU-MnS	426 460 513	451 524

As the temperature is lowered, the emission intensity increases and the emission peak shifts to lower energies (Figs. 2, 3). The emission spectra revealed major peaks at 440, 500, 520 and 623 nm. The 440 nm emission was also observed in zeolite A, and attributed to sulfur related defect. The emission peaking at  $\sim 500$  nm is consistent with the dominance of fluorescence by transition coupling from the extended to the localized states. The localized states are presumable very closely spaced near the edge of the valence band and are populated by holes without a pump due to thermal activation. The higher energy emission peaking at ca 520 nm is consistent with an interaction of Lewis center with cadmium vacancies. The band at 623 nm observed at 78 K for CLI-CdS (Fig. 2) corresponds to the deep trap emission [17]. This band was also observed for CdS nanocrystallites stabilized by DNA and was attributed to cadmium atom defect sites in the cluster [18].

MnS clusters have 1:1 manganese-to-sulfur ratios and yield weakly emissive samples (Fig. 3). The blue band at 460 nm is attributed to the donor-acceptor pair transition in which the acceptor is related to the  $\text{Mn}^{2+}$  vacancy. Such vacancies should be compensated by the predominantly present  $\text{Na}^+$  in the zeolite channels or by the formation of  $\text{S}^-(\text{S}^{2+} + \text{hole})$ . The band at 510-520 nm was observed only in laumontite and its origin is still unknown. The red shift of MnS emission spectra, at 78 K, is negligible, suggesting a stronger interaction with the zeolite lattice and a better stability.

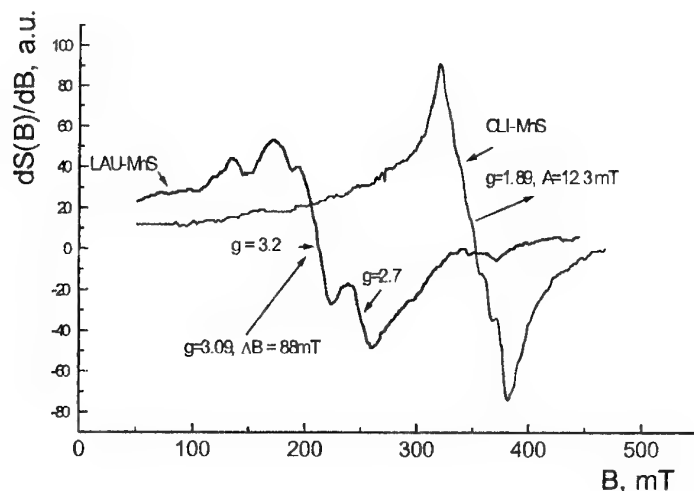


Fig. 4. Room temperature EPR spectra of LAU-MnS and CLI-MnS.

### 3.3. EPR

The EPR experiments clear evidence major differences in Mn species encapsulated in laumontite and clinoptilolite (Fig. 4). The EPR spectrum of CLI-MnS consist of a hyperfine sextet spectrum superposed on a broad background centered at about  $g = 1.89$  ( $\Delta B = 62$  mT,  $A = 12.3$  mT,  $\Delta B = 140$  mT). The unequal signal intensities of the hyperfine sextet demonstrate that the symmetry of Mn ions is lower than cubic phase. It is clear that at least a fraction of these sites are characterized by crystal field effects small enough to be treated as perturbations. The second is the broad background that is attributed to strong dipole-dipole interaction between Mn ions in clusters. The EPR spectrum of Mn-CLI evidenced only the hyperfine sextet at  $g = 1.89$ ,  $A = 8.7$  mT, characteristic for isolated  $\text{Mn}^{2+}$  ions in exchange positions. The MnS cluster formation determined modifications in the A value and in the intensity of hyperfine sextet spectrum and the appearance of the broad spectrum. The broad EPR spectrum can be related to the absorption peak at 530 nm ( $E_g = 2.34$  eV).

The MnS cluster formation in the laumontite channels affects only the linewidth of the EPR signal, which becomes larger (Fig. 4). In laumontite channels, Mn ions form polymeric species which gives EPR signals at low magnetic fields. Three of them, characterized by  $g = 2.7$ ,  $g = 3.0$  and  $g = 3.2$  contribute to the three excitonic peaks located at 266 nm, 387 nm and 309 nm.

### 3.4. The electrical conductivity

The electrical conductivity of zeolites in their cation forms and with semiconductor clusters was studied as a function of temperature (Fig. 5). The formation of semiconductor clusters into the zeolite channels determines the increase in electrical conductivity and the sharp decrease in the activation energy of electrical conductivity,  $\Delta E$  (Table 2).

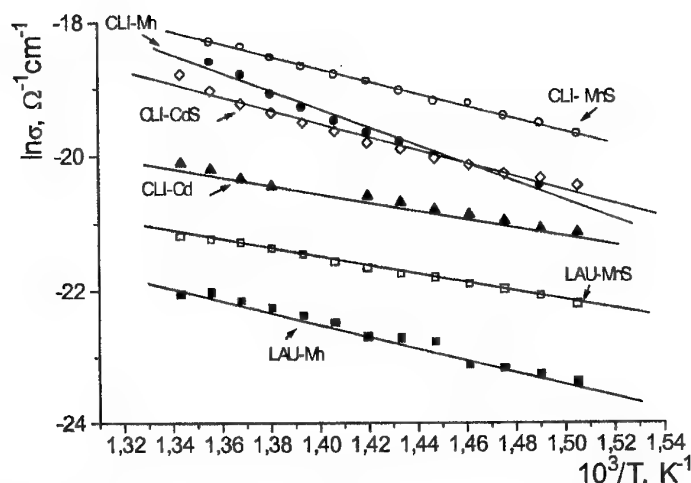


Fig. 7. The dependence of electrical conductivity of natural zeolites on the temperature and on the zeolite form.

Table 2. The values of the activation energy of electrical conductivity.

Sample	CLI-Mn	CLI-MnS	LAU-Mn	LAU-MnS	CLI-Cd	CLI-CdS
$\Delta E$ , eV	2.35	1.60	1.55	1.10	1.07	1.70

The differences in  $\Delta E$  values, calculated from the dependence  $\sigma = f(10^3/T)$ , can be related to the substitutional or interstitial Na impurities. The changes in electrical properties are due to systematic transformations in the density of electronic energy levels as a function of the size, known as quantum size effects.

## 4. Conclusions

Well-defined CdS and MnS clusters and superclusters have been synthesised within the pore structure of natural zeolites clinoptilolite and laumontite.

The ion-exchange method cannot fill up the zeolite channels, and disorder exists. The vacancies and imperfections break up the supercluster and introduce in homogeneities in the supercluster size distribution, which is the reason for the broad exciton absorption peak. For very small clusters the lattice structures and orbital hybridization may change in order to minimize surface dangling bonds and maximize bulk bonding. The appearance of the emission spectra specific to intrinsic defects of a well defined aggregate structure marks the onset of semiconductor properties. Phenomena such as trapping are connected with electronic states at the zeolite-semiconductor

interface. The MnS cluster formation into the zeolite channels was supported by optical and EPR spectra. Quantum confinement leads to changes in g factors, HFS constants and linewidths.

There is a strong dependence of the electrical conductivity on the dimensions of zeolite channels, and on local fields at the surface of the semiconductor clusters.

### References

- [1] Y. Wang, W. Mahler, *Opt. Commun.*, **61**, 233 (1987).
- [2] E. Helinski, P. Lucas, Y. Wang, *J. Chem. Phys.*, **89**, 3435 (1988).
- [3] G. B. Banfi, V. Degiorgio, D. Ricard, *Adv. Phys.*, **47**, 447 (1998).
- [4] J. Brus, *J. Phys. Chem.* **90**, 2555 (1986).
- [5] O. Terasaki, K. Yamazuki, J. M. Thomas, T. Ohsuna, D. Watanabe, J. V. Sanders, J. C. Barry, *Nature*, **58**, 330 (1987).
- [6] K. Koyama, Y. Takeuchi, *Z. Kristallogr.* **145**, 216 (1977).
- [7] F. Iacomi, E. Popovici, M. Alexandroaei, A. Barbat, *An. St. Univ. "Al. I. Cuza" Iasi*, **XXXII**, sIb, Fizica 99 (1986).
- [8] D. W. Ming, F. A. Mumpton, *Natural Zeolites '93*, Occ. Prop. Use, New York (1995).
- [9] I. Bedelea, S. D. Stoici, *Zeoliti Naturali*, Ed. Tehn., Bucuresti (1984).
- [10] Yu. A. Barbnakov, M. S. Ivanova, V. P. Petranovskii, V. V. Poborchii, V. G. Soloviev, A. F. Ioffe, S. M. Kirov, *Zeolites and Related Microporous Materials: State of the Art 1994*, Studies in Surface Science and Catalysis, vol. 84, Eds. J. Weitkamp, H. G. Karge, H. Pfeifer, W. Holde-rich, Elsevier Science B. V. 575 (1994).
- [11] E. Popovici, F. Iacomi, G. Singurel, E. Trif, Al. Nicula, *Anal. Letters*, **21(10)**, 1901 (1988).
- [12] N. Herron, Y. Wang, M. M. Eddy, G. D. Stucky, D. E. Cox, K. Moller, T. Bein, *J. Am. Chem. Soc.*, **111**, 530 (1989).
- [13] R. Tappero, A. Lichanot, *Chem. Phys.* **236**, 97 (1998).
- [14] H. Sato, T. Mihara, A. Furuta, Y. Ueda, H. Namatame, M. Taniguchi, *J. Elect. Spect. And Related Phenomena*, **78**, 87 (1996).
- [15] Y. Wang, N. Herron, *J. Phys. Chem.* **95**, 52 5(1991).
- [16] Y. Wang, *J. Phys. Chem.*, **95**, 119 (1991).
- [17] Y. Wang, N. Herron, *J. Phys. Chem.*, **92**, 4988 (1988).
- [18] J. L. Coffey, S. R. Bigam, R. F. Pinizzotto, H. Yang, *Nanotechnology*, **3**, 69 (1992).

## DIFFRACTION IN LASER INDUCED GRATINGS ON THIN $\text{As}_2\text{S}_3$ FILMS

A. Petris, V. I. Vlad

Institute of Atomic Physics, NILPRP - Dept. of Lasers and The Romanian Academy – CASP,  
Bucharest, Romania

We present an experimental study of the diffraction in laser induced phase gratings on thin amorphous  $\text{As}_2\text{S}_3$  films. A simplified model of the energy-band structure of this material has been used to understand the light induced changes of the absorption coefficient and refractive index. The results of the diffraction experiments have been explained using the analytical predictions of the Raman-Nath and Bragg diffraction theories. The results of our study indicate a strong variation of the absorption and refractive properties of the  $\text{As}_2\text{S}_3$  and a high efficiency of the laser induced phase gratings.

(Received July 20, 2001; accepted September 11, 2001)

*Keywords:* Amorphous chalcogenides, Phase gratings, Raman-Nath diffraction, Bragg diffraction

### 1. Introduction

The large change of the refractive index produced by illumination with green light at the band-gap energy, the possibility to obtain samples of large size, good spatial resolution, and the possibility to erase the recorded gratings by heating, make  $\text{As}_2\text{S}_3$  a promising material for holography, optical recording, optical phase conjugation, optical image processing, all-optical switching, integrated optics, etc. [1-5]

The investigation of the light diffraction on the holographic gratings induced in amorphous chalcogenides is important for a better understanding of the various photo-induced effects that occur in these materials and also for their applications.

We have experimentally studied the diffraction on phase gratings induced in thin amorphous  $\text{As}_2\text{S}_3$  films. In the Raman-Nath regime ("thin" gratings), the restrictions imposed by the Bragg diffraction condition are not present, and many diffraction orders can appear in the diffraction spectrum of the reading beam. The number and intensity of the diffraction orders depend on the grating phase modulation index (related to the non-linearity of the process).

The gratings have been induced using an Ar laser (514.5 nm wavelength). At this incident wavelength, the absorption coefficient and the refractive index are both modulated in a complex, amplitude and phase grating. The light-induced change of the absorption coefficient and its temporal evolution was experimentally studied. In order to discriminate between the contribution to diffraction produced by the amplitude and the phase gratings, a He-Ne laser beam has been used for probing. In this case, the complex grating acts almost as a pure phase grating [3]. We have studied the dynamics of the phase grating, by monitoring the temporal evolution of the various diffraction orders intensities of the He-Ne reading beam.

For low modulation of the phase grating, the diffraction spectra have been explained using the analytical predictions of the Raman-Nath diffraction theory. For high modulations of the phase grating, our experimental results show an intermediary regime between Raman-Nath and Bragg, and the Bessel function approximation of the Raman-Nath model cannot give anymore an accurate prediction of the diffraction orders intensities. Our study indicates a strong variation of the absorption and refractive properties of the  $\text{As}_2\text{S}_3$  films and the high efficiency of the laser induced phase grating.

## 2. Experimental results

### 2.1. The experimental setup

The experimental arrangement set-up for the study of the diffraction on phase gratings induced in thin amorphous  $\text{As}_2\text{S}_3$  films is shown in Fig. 1.

We have used samples of  $\text{As}_2\text{S}_3$  thin films (thickness,  $d = 5.4 \mu\text{m}$ ), thermally evaporated in vacuum on glass substrate.

The linear polarized  $\text{Ar}^+$  laser beam ( $\lambda = 514.5 \text{ nm}$ ,  $h\nu = 2.41 \text{ eV}$ ) is separated with the beam splitter BS in two beams of equal intensity which are symmetrically incident and superimposed in the  $\text{As}_2\text{S}_3$  film. The modulation index of the grating is, in this case,  $m = 1$ . The full angle between the interfering beams (in air) is  $\beta = 13^\circ$ , leading to a spatial period of the grating,  $\Lambda = 2.35 \mu\text{m}$ . For grating probing, a He-Ne beam ( $\lambda = 632.8 \text{ nm}$ ,  $h\nu = 1.96 \text{ eV}$ ), close to the normal incidence (non-coplanar with the Ar beams) was used. The power of the diffraction orders has been measured with a silicon photo-detector, connected to a x-y recorder. The temporal evolutions of the power of the zeroth (non-diffracted light), of the first, the second and the third diffraction orders of the He-Ne reading beam were measured.

In order to ensure a good separation between the diffraction orders, the reading He-Ne laser beam was slightly tilted with respect of the plane of the self-diffraction orders of the Ar laser beams.

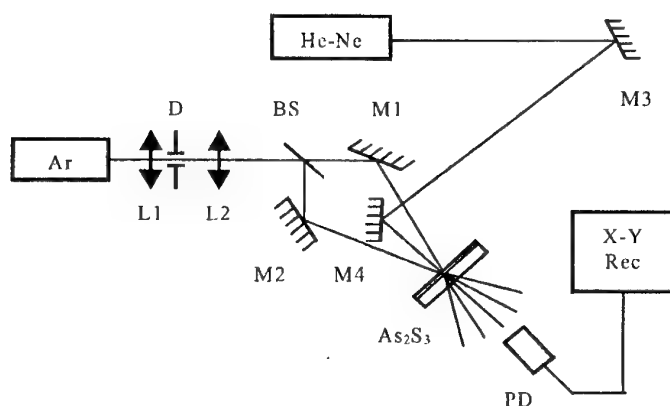


Fig. 1. The experimental setup for study of diffraction on thin  $\text{As}_2\text{S}_3$  gratings.

### 2.2. Absorption measurements

We have investigate the change in the absorption coefficient,  $\Delta\alpha$ , and its dynamics, produced by illumination with a single beam of the  $\text{Ar}^+$  laser. The light-induced absorption was measured at two average intensities ( $I_1 = 3.5 \text{ W/cm}^2$  and  $I_2 = 0.45 \text{ W/cm}^2$ ) of the gaussian laser beam. The temporal dependence of the  $\text{As}_2\text{S}_3$  transmission is shown in Fig. 2.

### 2.3. Diffraction measurements

The diffraction gratings have been recorded using two  $\text{Ar}^+$  laser beams ( $\lambda = 514.5 \text{ nm}$ ) of equal intensity,  $I = 0.45 \text{ W/cm}^2$ .

In Fig. 3 is shown the temporal evolution of He-Ne diffraction orders, recorded for different time scales: (a) 200 s, (b) 400 s, (c) 2000 s. It was obtained by writing the grating several times, in different positions on the thin film, and by recording, each time, the temporal evolution of one diffraction order of the probing beam only. The sensitivity of the measuring chain was kept constant for all diffraction orders. Some differences in the evolution of different diffraction orders and their relative magnitude, due to writing of the grating in different positions and fluctuations of Ar laser beam (the evolution of each grating was monitored for several tens of minutes), could be present.



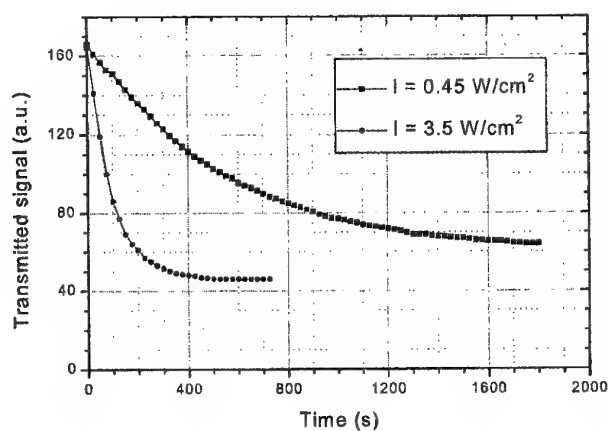
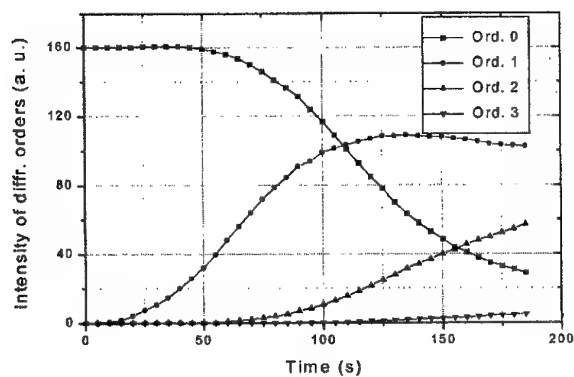
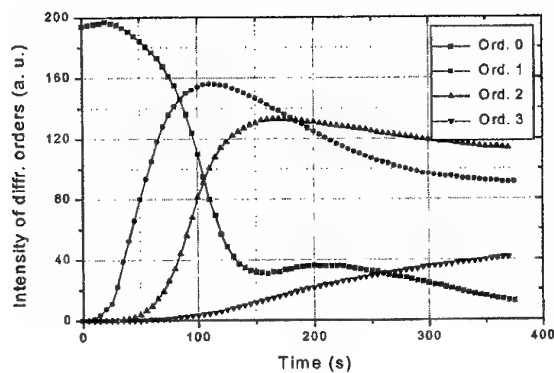


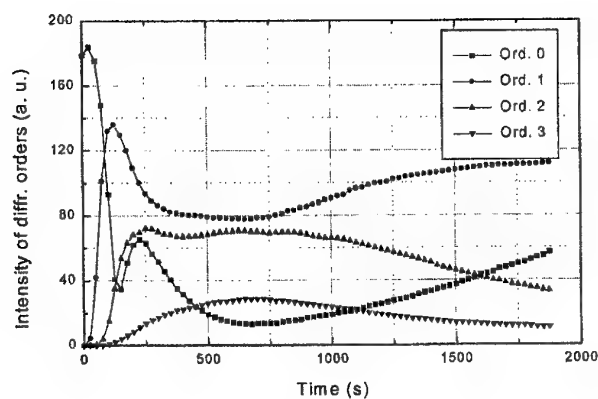
Fig. 2. The temporal dependence of the  $\text{As}_2\text{S}_3$  transmission ( $\lambda = 514.5 \text{ nm}$ ).



(a)



(b)



(c)

Fig. 3. The temporal evolution of He-Ne diffraction orders, recorded for different time scales: (a) 200 s, (b) 400 s, (c) 2000 s. The intensity of the writing Ar laser beams was  $0.45 \text{ W/cm}^2$ .

### 3. A simplified three-level model of the energy-band structure of $\text{As}_2\text{S}_3$ [Kwon, Kwak and Lee, [5]]

The change of the absorption coefficient and the refractive index of  $\text{As}_2\text{S}_3$  illuminated with the green line of the Ar laser can be explained using the simplified model of the energy-band structure proposed by Kwon, Kwak and Lee [5].

The complex energy-band structure of the  $\text{As}_2\text{S}_3$  is simplified to the energy-level diagram shown in Fig. 4.

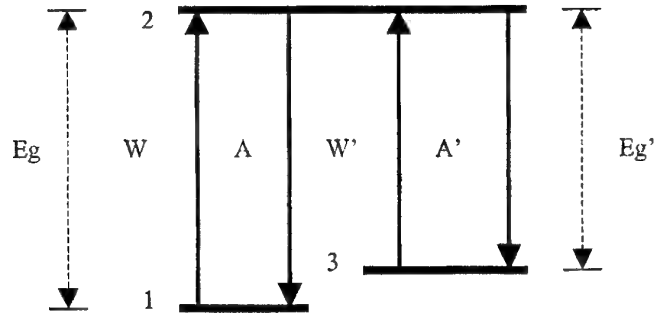


Fig. 4. A simplified model of energy-band structure of amorphous  $\text{As}_2\text{S}_3$ : level 3 - the photo-darkening state; A, A' - the spontaneous transition rates, W, W' - the pump rates.

All the valence electrons are assumed to be initially in the potential well 1. By illumination with the green line ( $\lambda = 514.5 \text{ nm}$ ,  $h\nu = 2.41 \text{ eV}$ ), valence electrons are excited to the conduction band 2 through the energy gap,  $E_g = 2.39 \text{ eV}$ . Some of the excited electrons relax to the initial state 1, while others relax to the photo-darkening state 3. The pump rates  $1 \rightarrow 2$  and  $3 \rightarrow 2$  are W and W', respectively, while the transition rates  $2 \rightarrow 1$  and  $2 \rightarrow 3$  are A and A', respectively. The transition rate  $3 \rightarrow 1$  is nearly zero at room temperature, but the transition  $3 \rightarrow 2 \rightarrow 1$  is allowed. For electrons trapped in the photo-darkening state 3, both the absorption coefficient and the refractive index are changed because of the reduced band-gap energy  $E'_g$ . Solving the rate equations for the three-level system, the temporal evolution of the absorption coefficient and the refractive index were obtained [5].

The absorption coefficient is:

$$\alpha(t) = N_1(t) \cdot \sigma + N_3(t) \cdot \sigma' = \alpha_0 + (\alpha_\infty - \alpha_0) \cdot \left[ 1 - \exp\left(-\frac{\alpha_0}{\alpha_\infty} W' t\right) \right], \quad (1)$$

where:  $N_1(t)$ ,  $\sigma$  and  $N_3(t)$ ,  $\sigma'$  are the populations and the absorption cross sections of the states 1 and 3, respectively,  $\alpha_0$  and  $\alpha_\infty$  are constant (independent of the incident intensity) and can be obtained from the experimental transmission:

$$T(t) = \exp[-\alpha(t)d] = \exp(-\alpha_0 d) \cdot \exp\left\{-\alpha_1 d \left[ 1 - \exp\left(-\frac{\alpha_0}{\alpha_\infty} W' t\right) \right]\right\}, \quad (2)$$

where  $\alpha_1 = \alpha_\infty - \alpha_0$ ,  $W' = S' I$ ,  $S'$  is a constant dependent on the  $\sigma'$ , and  $I$  is the incident light intensity.

The refractive index takes a similar form:

$$n(t) = N_1(t) \cdot k + N_3(t) \cdot k' = n_0 + (n_\infty - n_0) \cdot \left[ 1 - \exp\left(-\frac{\alpha_0}{\alpha_\infty} W' t\right) \right]. \quad (3)$$

where  $k$  and  $k'$  are the contribution to the refractive index of the electrons in states 1 and 3, respectively.

#### 4. Considerations on laser beam diffraction on phase gratings

The diffraction regime on phase gratings is determined [6,7] by the phase correlation of the diffraction orders,  $Q = 2\pi\lambda d/(n_0\Lambda^2)$ , and by the amplitude of the phase modulation,  $\Delta\Phi = 2\pi\Delta n d/\lambda \cos\theta$  ( $\lambda$  is the incident light wavelength,  $d$  is the grating thickness,  $n_0$  is the refractive index,  $\Lambda$  is the grating period,  $\Delta n$  is the modulation amplitude of the refractive index, and  $\theta$  - the incidence angle of the probing beam).

In the Raman-Nath diffraction regime ( $Q \leq 0.5$  and  $Q\Delta\Phi \leq 1$ , "thin" grating), many diffraction orders can appear. The intensity of the  $l$ -th diffraction order,  $I_l$  is given by [8-11]:

$$I_l = T \cdot I_{inc} \cdot J_l^2(\Delta\Phi) \quad (4)$$

where  $T$  is the transmission of the grating,  $I_{inc}$  is the intensity of the incident beam and  $J_l$  is the first kind Bessel function of the  $l$ -th order.

In the Bragg diffraction regime ( $Q \geq 10$  and  $Q/\Delta\Phi \geq 10$ , "thick" grating), one diffraction order can appear only, when the Bragg condition is satisfied. Its intensity is [8-10]:

$$\theta = \theta_B : \quad I_1 = T \cdot I_{inc} \cdot \sin^2 \left( \frac{\pi \Delta n d}{\lambda \cos \theta_B} \right) = T \cdot I_{inc} \cdot \sin^2 \left( \frac{\Delta\Phi_B}{2} \right) \quad (5)$$

when the reading beam is incident at the Bragg angle. When the incidence angle of the reading beam deviates with  $\Delta\theta$  from the Bragg angle, the intensity of the diffraction order becomes:

$$\theta = \theta_B \pm \Delta\theta : \quad I_1 = T \cdot I_{inc} \cdot \frac{\sin^2 \left[ \left( (\Delta\Phi_B/2)^2 + \chi^2 \right)^{1/2} \right]}{1 + \chi^2 / (\Delta\Phi_B/2)^2}, \quad (6)$$

where the parameter

$$\chi = \frac{\pi d \cdot \Delta\theta}{\Lambda} \quad (7)$$

is a measure of the deviation from the Bragg condition.

In the transition region between Raman-Nath and Bragg diffraction, the intensity of the diffraction orders is given by solving numerically [8,12] the set of coupled wave equations:

$$2 \frac{\partial U_l(\Delta\Phi)}{\partial z} + U_{l+1}(\Delta\Phi) - U_{l-1}(\Delta\Phi) = i\rho l^2 U_l(\Delta\Phi) \quad (8)$$

where  $U_l$  is the amplitude of the beam diffracted in the  $l$ -th diffraction order and  $\rho = Q/\Delta\Phi$ .

#### 5. Discussion of the experimental results

##### 5.1. Absorption measurements

The experimental transmission of the As<sub>2</sub>S<sub>3</sub> thin film (corrected for Fresnel reflections on the interfaces), was fitted with the Eq. (2), in order to obtain the pump rate  $W'$ , the values of  $\alpha_0$ ,  $\alpha_\infty$  and, consequently, the temporal evolution of the absorption coefficient,  $\alpha(t)$ . The results of the fitting procedure ( $\alpha_0 = 10 \text{ cm}^{-1}$ ,  $\alpha_\infty = 2355 \text{ cm}^{-1}$ ,  $W' = 1.75 \text{ s}^{-1}$  for  $I_1 = 3.5 \text{ W/cm}^2$  and  $W' = 0.21 \text{ s}^{-1}$  for  $I_2 = 0.45 \text{ W/cm}^2$ ) and the corresponding curves  $\alpha(t)$  are shown in Fig. 5.

##### 5.2. Diffraction measurements

In our diffraction experiments, with the He-Ne reading beam and the experimental parameters,  $\lambda = 632.8 \text{ nm}$ ,  $d = 5.4 \text{ }\mu\text{m}$ ,  $n_0 = 2.42$ ,  $\Lambda = 2.35 \text{ }\mu\text{m}$ , one can calculate  $Q = 1.6$ . In this case, the diffraction regime is the intermediary one, closer to the Raman-Nath regime. This is confirmed by the three diffraction orders that are observed in the diffraction spectrum.

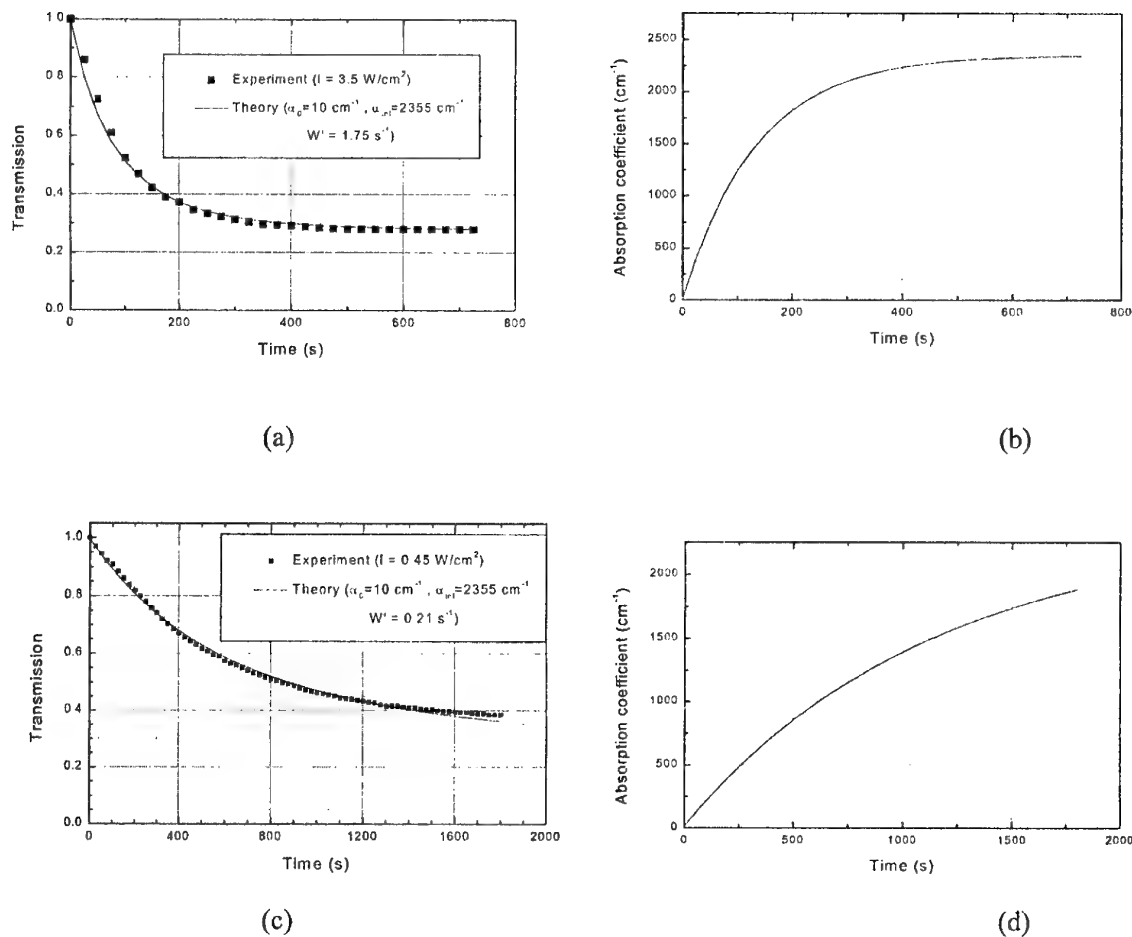


Fig. 5. The time-dependent absorption of  $\text{As}_2\text{S}_3$  film, for  $I=3.5 \text{ W/cm}^2$  (a, b) and  $I=0.45 \text{ W/cm}^2$  (c, d).

The diffraction experimental results (normalized to the value of the transmission of  $\text{As}_2\text{S}_3$  sample, for the He-Ne laser beam) have been compared with the results of the Raman-Nath diffraction theory and using the parameters determined from the absorption measurements ( $\alpha_0=10 \text{ cm}^{-1}$ ,  $\alpha_\infty=2355 \text{ cm}^{-1}$ ,  $W'=0.21 \text{ s}^{-1}$ ). Due to the fact that the maximum intensity in the interference pattern is four times larger than the intensity of each incident writing beam, the value of the pump rate was considered  $W'=0.84 \text{ s}^{-1}$ . The results of this comparison, considering  $n_0 = 2.42$  (from literature, [13]) and  $n_\infty=2.51$  (for a good correspondence of the temporal evolutions of the diffraction orders), are shown in Fig. 6.

The experimental results are satisfactorily described by the Eq. (4) only for small refractive index modulation of the  $\text{As}_2\text{S}_3$  grating (at the beginning of the grating recording). The discrepancy becomes large for high refractive index modulation, which could be explained by the diffraction in the intermediary regime, at the end of grating recording (when the phase modulation is  $\Delta\Phi = 4.8$ , the product  $Q\Delta\Phi = 7.7$ , and Eq. (4) is no longer valid).

The value of the maximum diffraction efficiency in the first order,  $\eta_D = 75\%$  (Fig. 6b), is more than two times larger than the maximum efficiency predicted by the Raman-Nath theory ( $\eta_{D, \max} = 33.9\%$ ), for a thin grating. Therefore, as high efficiency can be explained only by volume gratings (Bragg or intermediary diffraction regimes). The experimental results and the Bragg diffraction efficiency in the first order, considering the angular deviation  $\Delta\theta = 4^\circ$  between the angle of incidence of the probing beam and the Bragg angle ( $\theta_B=7^\circ45'$ ), are shown in Fig. 7.

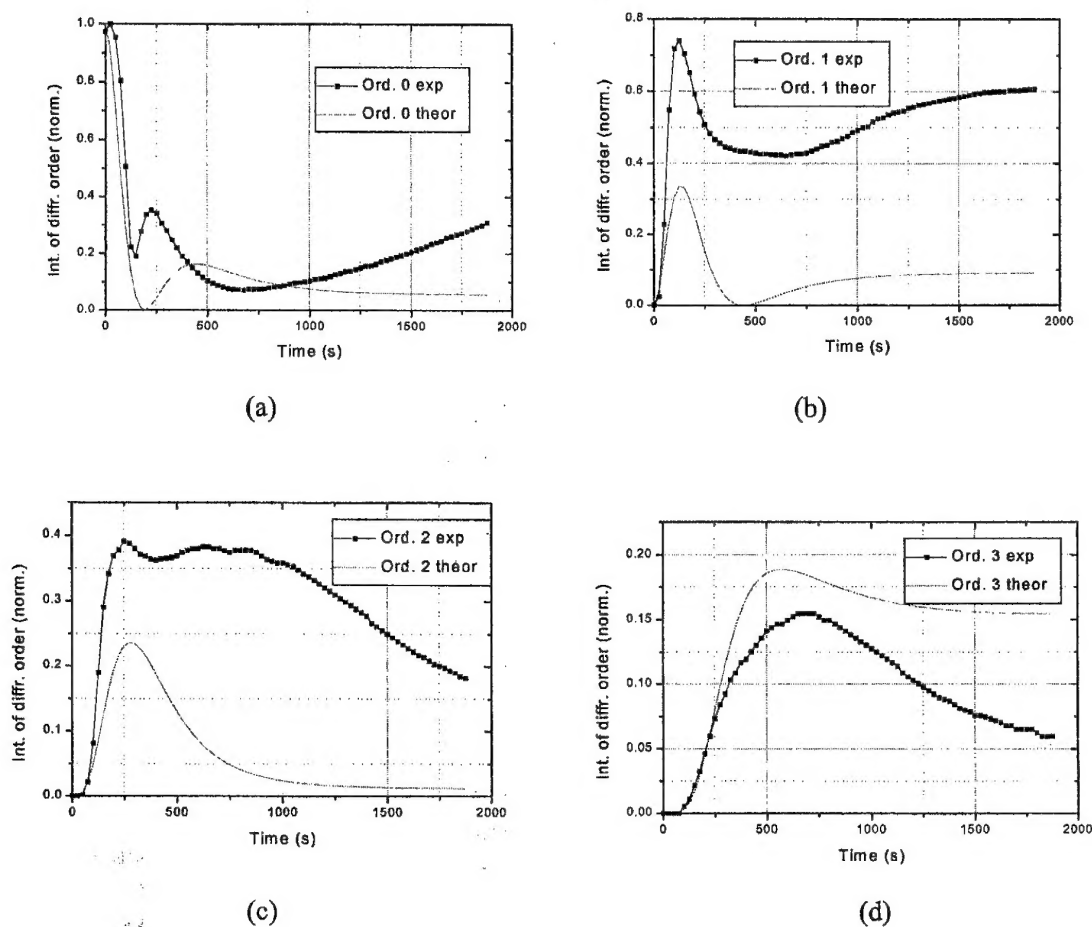


Fig. 6. Comparison between the diffraction experimental results and the Raman-Nath theory, using the temporal dependence of the refractive index predicted by the Eq. (3);  $W=0.84 \text{ s}^{-1}$ ;  $n_o=2.51$

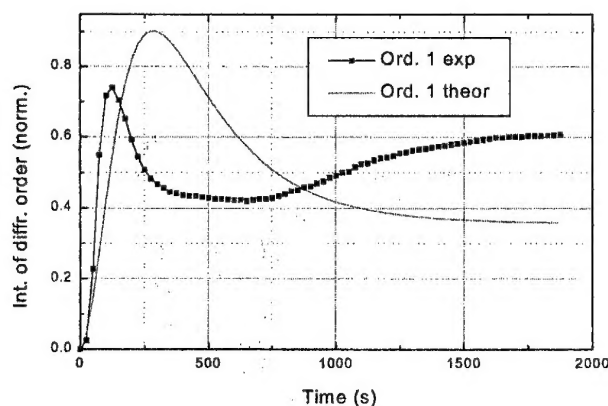


Fig. 7. The Bragg diffraction efficiency in the first order, considering the angular deviation  $\Delta\theta=4^\circ$  between the angle of incidence of the probing beam and the Bragg angle ( $\theta_B=7^\circ45'$ ).

From the Figs. 6 and 7 it is clear that an accurate description of the diffraction experimental results, for the entire range of phase modulations, can be obtained only by solving numerically the set of coupled wave equations (Eq. (8)). This will be done in a future paper.

From experimental diffraction and absorption results, and using the Eq. (3), it was possible to estimate the temporal dependence of the refractive index change (Fig. 8).

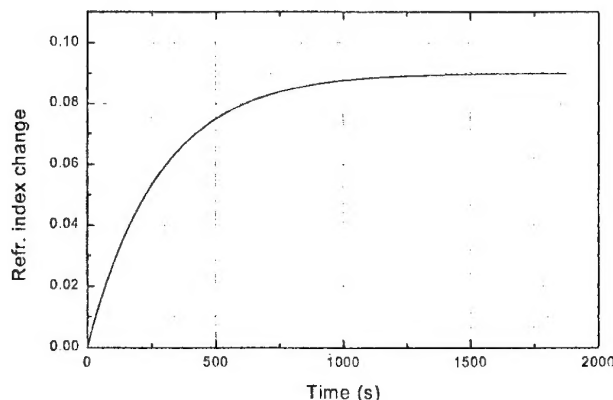


Fig. 8. The temporal dependence of the refractive index change obtained from the experimental results.

## 6. Conclusions

The results of an experimental study of diffraction on thin  $\text{As}_2\text{S}_3$  gratings have been presented. The absorption of  $\text{As}_2\text{S}_3$  thin film increases monotonically with exposure and saturates at the same value  $\alpha_\infty$ , independent of the light intensity, in the range of incident intensities used in this work ( $I = 0.45 - 3.5 \text{ W/cm}^2$ ). The refractive index increases monotonically with exposure and saturates at the same value  $n_\infty$ , in this range of intensities. For weak exposures, the diffraction on thin gratings satisfies the Raman-Nath formalism. For large phase modulations, the diffraction takes place in an intermediary regime (between Raman-Nath and Bragg) and the diffraction efficiency can reach 75%. Our experiments can be satisfactorily explained in the frame of a simplified three-level model of the energy-band structure of  $\text{As}_2\text{S}_3$ .

## References

- [1] A. Andriesh, M. Bertolotti (eds), *Physics and Applications of Non-Crystalline Semiconductors in Optoelectronics*, Kluwer Academic Publishers, Dordrecht, Boston, London (1997).
- [2] C. H. Kwak, Y. L. Lee, S. G. Kim, *JOSA B*, **16** (4), 600 (1999).
- [3] O. Salminen, N. Nordman, P. Riihola, A. Ozols, *Opt. Commun.* **116**, 310 (1995).
- [4] J. Teteris, O. Nordman, *Opt. Commun.* **138**, 279 (1997).
- [5] J. H. Kwon, C. H. Kwak, S. S. Lee, *Opt. Lett.* **10** (11), 568 (1985).
- [6] M. G. Moharam, T. K. Gaylord, R. Magnusson, *Opt. Commun.* **32** (1), 19 (1980).
- [7] M. G. Moharam, T. K. Gaylord, R. Magnusson, *Opt. Commun.* **32** (1), 14 (1980).
- [8] M. Born, E. Wolf, *Principles of Optics*, Pergamon Press, 1966.
- [9] J. P. Woerdman, *Philips Res. Repts. Suppl.*, No. 7 (1971).
- [10] P. Hariharan, *Optical holography*, Cambridge University Press, 1984.
- [11] H. J. Eichler, P. Gunther, D. W. Pohl, *Laser Induced Dynamic Gratings*, Springer Verlag, 1986.
- [12] A. Petris, V. I. Vlad, L. Voicu, R. Negres, *Proc. SPIE* **2461**, 251 (1995).
- [13] A. L. Dawar, P. K. Shishodia, G. Chauhan, J. C. Joshi, C. Jagadish, P. C. Mathur, *Appl. Optics* **29** (13), 1971 (1990).

## INSTRUCTIONS FOR AUTHORS

### Journal Scope

The Journal of Optoelectronics and Advanced Materials appears quarterly and publishes review papers, research papers and short communications in the field of optoelectronics and new advanced materials: optoelectronic devices, crystals of relevance in optoelectronics, amorphous and glassy materials, nanostructured materials, functional and smart materials. Theoretical papers are encouraged. Papers dealing with biomaterials and optoelectronic applications for medical purposes are accepted. An important aim of the Journal is to bring together the specialists from related fields: optoelectronics and materials.

### Submission of papers

Authors are invited to send the manuscripts in British English, firstly by e-mail and then by regular mail. Two hard copies and an electronic record on a 3 1/2 inches floppy disk are required.

Review papers are limited to 20 pages. Regular papers are limited to 10 pages. Short communications are limited to 4 pages. Excepting short communications, every paper must have an abstract with maximum 200 words. At least three keywords, which characterize the subject of the work, must be specified.

One full page of the Journal contains 54 rows with 95 characters/row (font size 11).

The following structure of a paper is recommended: 1. Introduction, 2. Experimental (Theory, Modeling, ...), 3. Results, 4. Discussion, 5. Conclusions.

References will be consecutively numbered in the text and collected at the end of the paper in the following style for journals, proceedings and books, respectively:

[1] N. Rivier, *Phil. Mag.*, **40**, 859 (1979).

[2] S. R. Ovshinsky, *Proc. 7-th Intern. Conf. Liq. Amorph. Semic.*, Edinburgh, Ed. W. E. Spear, Institute of Physics, Bristol, UK, 1978, p. 519.

[3] N. F. Mott, E. A. Davis, *Electron Processes in Non-Crystalline Materials*, Clarendon Press, Oxford (1979).

Figures and tables are recommended to be introduced in the text with their legends.

The editor will send every manuscript to two referees for a critical examination. The comments of the referees and the decision of the Editorial Board regarding the publication will be sent to the corresponding authors.

The manuscripts accepted for publication will be published in maximum three months. The corresponding author will receive one free copy of the issue of the Journal where the paper was printed and 10 reprints without charge. The authors can order additional reprints.

All rights are reserved by "Journal of Optoelectronics and Advanced Materials". Any reproduction or dissemination of the information herein, even as excerpts of any extent, is permitted only by written consent of the Editor-in-Chief.

The manuscripts must be sent to the following address:

### **JOURNAL OF OPTOELECTRONICS AND ADVANCED MATERIALS**

1 Atomistilor St., P.O. Box MG. 5  
76900 BUCHAREST-MAGURELE, ROMANIA  
Phone: +40-1-493.02.92; +40-1-493.00.47 ext.195  
Phone/Fax: +40-1-420.10.01  
E-mail: [review@inoe.inoe.ro](mailto:review@inoe.inoe.ro); [redactie@alpha2.infim.ro](mailto:redactie@alpha2.infim.ro)

Subscriptions for **JOURNAL OF OPTOELECTRONICS AND ADVANCED MATERIALS** can be requested at the above address.

Subscription payment will be made to the following accounts:

2511.1-401.1/ROL (Romanian lei): 50699113623 - TREZORERIE Jud. ILFOV;

2511.1-401.19/USD (US dollars): Romanian Trade Bank, BCR UNIREA 55101

Subscription for 2001 (four issues):

500 000 ROL (for Romania); 100 USD (for other countries).

**ISSN 1454-4164**

All rights reserved.

No part of this publication may be reproduced, stored in a retrieval system or transmitted in any form or by any means, electronic, mechanical, photocopying, recording or otherwise, without the written permission of the Editorial Board.

© INOE & INFM

Edited by:

**NATIONAL INSTITUTE  
FOR OPTOELECTRONICS**

Phone: +40-1-493.02.92. Fax: +40-1-420.10.01  
E-mail: inoe@inoe.inoe.ro

**NATIONAL INSTITUTE  
OF MATERIALS PHYSICS**

Phone: +40-1-493.00.47. Fax: +40-1-493.02.67  
E-mail: joam@alpha1.infm.ro

With the support of: Ministry of Education and Research,  
Consulting College for Research-Development and Innovation



ISSN 1454-4164